Salisbury, M.H., Shinohara, M., Richter, C., et al., 2002
Proceedings of the Ocean Drilling Program, Initial Reports Volume 195

3. SITE 1200[1]

Shipboard Scientific Party[2]

PRINCIPAL RESULTS

Site 1200 is located in the Mariana arc, a nonaccretionary convergent margin with a pervasively faulted forearc. The Mariana system contains numerous large mud volcanoes, which are composed principally of unconsolidated flows of serpentine muds with clasts of serpentinized mantle peridotite. Site 1200 is situated on the knoll of South Chamorro Seamount, the only known site of active blueschist mud volcanism in the world with associated megafaunal assemblages. The primary objectives at Site 1200 were to establish a long-term geochemical observatory and to obtain core samples to examine geological and biological processes associated with subduction materials from great depth.

Hole 1200A was cored with the rotary core barrel (RCB) to a depth of 147.2 meters below seafloor (mbsf) and recovered serpentinized ultramafic clasts and minor amounts of the host serpentine matrix. Hole 1200B was washed down to 98 mbsf and had to be abandoned because of hole stability problems before coring could be initiated. Hole 1200C is cased to 202.3 mbsf and instrumented with a long-term borehole observatory equipped with a reentry cone, a thermistor string with pressure cells, and two osmotic water samplers. Three holes, 1200D, 1200E, and 1200F were cored with the advanced hydraulic piston corer/extended core barrel (APC/XCB) to a maximum depth of 54.4 mbsf and recovered soft serpentine matrix with hard rock clasts.

The clasts consist of serpentinized ultramafic rocks embedded in serpentine mud. Most clasts are angular to subangular, whereas the larger clasts are subangular to subrounded. Harzburgites are the dominant original rock type, with minor dunites and a few lherzolites. The degree of serpentinization varies between 40% and 100% (average = ~70%), and loss on ignition (LOI) values vary between 11% and 18% (average = 14%). Based on preliminary geochemical analyses, it is likely that the serpentinized ultramafic rocks represent portions of the forearc mantle

[1]Examples of how to reference the whole or part of this volume.
[2]Shipboard Scientific Party addresses.

Ms 195IR-103

wedge that suffered 20%–25% melt extraction (overlapping with the ultramafic rock assemblages found on Conical Seamount during Ocean Drilling Program [ODP] Leg 125). The average Si/Mg ratio is 0.92, and the average Mg number is 92.3.

Relative to depleted mantle values, two trends are distinguished: one of Sr and Na enrichments and the other of Ca and Al depletions. In general, geochemical data from Site 1200 are well correlated with the values obtained for serpentinites from Site 780 (Conical Seamount summit) during Leg 125 (Shipboard Scientific Party, 1990c).

All holes at Site 1200 are characterized by a succession of silty clay–sized serpentine containing dispersed clasts or clast-poor serpentine diamicton with clast-rich intervals, all belonging to the same lithostratigraphic unit.

This unit is characterized by two distinct poorly sorted facies with dispersed clasts. Facies I is predominant and is composed of silty clay serpentine with dispersed clasts and clast-poor serpentine diamicton. Facies II is present in two short intervals in Hole 1200E and is characterized by clast-rich serpentine diamicton. With the exception of the increased clast content, the two facies are identical; however, no calcareous intervals occur within recovered intervals of clast-rich diamicton.

Core variability is evident in color reflectance data. All cores were dark blue gray to black when first split but became lighter in color once exposed to the aerobic laboratory environment. Calcareous intervals oxidized rapidly after cores were split, revealing hues of light yellowish brown, light bluish gray, and light pink. Recorded calcareous intervals and the location of clasts coated with a calcareous precipitate and calcareous nodules correlate well with microfossil content and abundance. Although most of the mud consisted of serpentine minerals, examination of the grit fraction revealed a rich population of high-pressure, low-temperature rocks and minerals from the décollement, including glaucophane, white mica/crossite/chlorite, talc, and chlorite schists.

Well-preserved and diversified subtropical assemblages of planktonic foraminifers and calcareous nannofossils were found in the top 0.1–0.3 m of Holes 1200D, 1200E, and 1200F, indicating that the surface of the summit is blanketed with calcareous microfossil-bearing deposits. Benthic foraminifers in small quantity and low diversity are also present in all holes. Samples farthest away from Hole 1200A contain more abundant, diversified, and better-preserved microfossil faunas. The downcore sections of these three holes are virtually barren of microfossils, except for a peculiar interval between 11 and 13 mbsf in Hole 1200D. This interval contains abundant and diversified calcareous microfossils comparable to those in the core tops. The major difference is that these fossils were overgrown by calcite on the original structures. All the fossils are late Quaternary in age.

Pore waters from Site 1200 reveal two distinct phenomena: a deep-sourced fluid that is believed to be upwelling from the top of the subducting slab 25–30 km below the seafloor and a new and exotic extremophile microbial community at 0–20 mbsf that has reduced sulfate in this fluid to zero and produced high alkalinity (up to 130 meq/kg) and dissolved sulfide in the process, possibly by oxidizing the C_1–C_6 hydrocarbons detected in headspace gas samples. The deep fluid is similar in many ways to that sampled on Conical Seamount to the north during Leg 125. It has a pH of 12.5, making it, along with the Conical Seamount fluids, the most alkaline pore water ever recovered from the deep sea. Relative to seawater, it is depleted in chloride, Mg, and Ca and

greatly enriched in alkalinity, Na and Na/Cl, K, sulfate, and light hydrocarbons.

Ultramafic rocks were easily demagnetized by alternating-field techniques and yielded mostly stable magnetic directions. The stable magnetization represents a chemical remanent magnetization acquired by magnetite particles as they formed during serpentinization. As expected from their emplacement history, the serpentine muds did not display a stable magnetic component. Thermal demagnetizations reveal Curie temperatures of 585°C, which suggests that the dominant magnetic mineral is pure magnetite. Koenigsberger ratios (mean = 2.4) indicate that the in situ magnetization of the ultramafic clasts is dominated by remanent magnetization rather than an instantaneous magnetization induced by the Earth's magnetic field.

The results of the physical properties measurements show that the material recovered from South Chamorro Seamount is very similar to that recovered from Conical Seamount during Leg 125 (Fryer, Pearce, Stokking, et al., 1990). The average bulk density of the clasts is 2.50 g/cm^3; the average grain density of the clasts is 2.66 g/cm^3. The average bulk density of the matrix is 1.87 g/cm^3; the average grain density of the matrix is 2.64 g/cm^3, nearly identical to that of the clasts. The hydraulic conductivity and diffusivity of the matrix were measured during a consolidation test in a Manheim squeezer cell. The initial results of the tests showed the matrix to have a hydraulic conductivity ranging between 10^{-11} and 10^{-10} m/s. These values are comparable in magnitude and range to those of clays and silts.

BACKGROUND AND OBJECTIVES

Background

Serpentine mud volcanism in the Mariana forearc region provides an opportunity to investigate slab-derived pore fluids and metamorphism of the subducted plate and overlying suprasubduction zone mantle and to determine the pressure and temperature conditions of the subduction zone at depths (up to ~30 km) that are impossible to reach by drilling. Previous drilling during Leg 125 on Conical Seamount, another serpentine mud volcano, showed that these features are bringing materials and pore fluids from the region of the décollement between the subducting Pacific Ocean lithosphere and the overlying wedge of the forearc plate (Fryer, 1992b; Mottl, 1992).

Site 1200 is located at the summit of one of the Mariana forearc serpentine mud volcanoes. The target site is a 200-m-high tumescent knoll on South Chamorro Seamount and lies at 13°47′N, 146°00′E, at a water depth of ~2930 meters below sea level (mbsl), ~125 km east of Guam in the western Pacific Ocean (Figs. **F1, F2**). It is situated ~85 km from the trench, where the depth to the slab is ~26.5 km, based on Isacks and Barazangi (1977). Pore fluids collected in gravity cores from this seamount exhibit a strong slab signal (Fryer et al., 1999). It is the only known site of active blueschist mud volcanism in the world and hosts the only documented megafaunal assemblages associated with serpentine/blueschist mud volcanism (Fryer and Mottl, 1997).

F1. Bathymetry of the Southern Mariana forearc, p. 64.

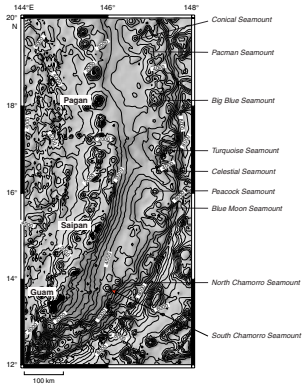

F2. Location of Site 1200, p. 65.

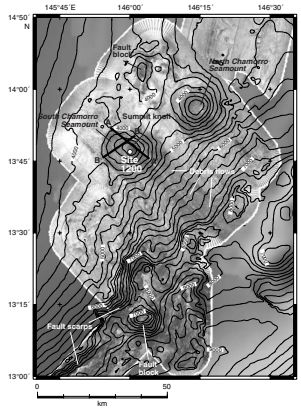

Objectives

The objectives of drilling at South Chamorro Seamount were to (1) examine the processes of mass transport and geochemical cycling in the subduction zones and forearcs of nonaccretionary convergent margins; (2) ascertain the spatial variability of slab-related fluids within the forearc environment as a means of tracing dehydration, decarbonation, and water-rock reactions in subduction and suprasubduction zone environments; (3) study the metamorphic and tectonic history of nonaccretionary forearc regions; (4) investigate the physical properties of the subduction zone as controls over dehydration reactions and seismicity; and (5) investigate biological activity associated with subduction zone material from great depths.

To achieve these objectives, drilling at Site 1200 was designed to recover sufficient material to permit petrologic and mineralogic characterization of the serpentine mud flow units, characterize their pore fluid compositions, collect any biological material contained therein, and establish a cased reentry hole for deploying downhole instrumentation for a long-term observatory at South Chamorro Seamount.

Downhole instrumentation for deployment in Hole 1200C included a downhole thermistor string, pressure sensor, and osmotic fluid sampler sealed with a circulation obviation retrofit kit (CORK). This installation will provide a long-term record of (1) the rebound of temperatures toward formation conditions after the emplacement of the seal; (2) possible temporal variations in temperatures and pressures due to lateral flow in discrete zones, regional and/or local seismicity, and short-term pressure effects; and (3) composition of the circulating fluids obtained with the osmotic fluid sampler. Data from the downhole instruments will be collected during a *Jason/DSL 120* cruise that is tentatively scheduled for 18 months after completion of Leg 195.

OPERATIONS

Guam Port Call

Leg 195 began in Guam harbor with the first line ashore at the fueling depot at 1600 hr on 2 March 2001. Upon completion of refueling activities, the ship was moved to Ammunition Berth Hotel for the remainder of the port call.

Port call activities, aside from the normal loading and off-loading of freight, included the loading of International Ocean Network (ION) equipment directly shipped from Japan and the equipment stored in Guam after Leg 191. In addition, special hardware required to support the installation of a CORK at Site 1200 was loaded. The night before the departure, Catermar hosted a barbecue on the dock for the entire ship's complement as an ice breaker.

Transit to Site 1200 (Proposed Site MAF-4B) and Station-Keeping Testing

At 1300 hr on 7 March, the *JOIDES Resolution* left the dock and got under way at full speed for the first automated station-keeping (ASK) test site. After only 36 min under full steam, the ship suffered a massive power failure at 1405 hr that left the ship in not-under-command condition. Minimum propulsion was returned at 1415 hr by switching to

manual engine control governors. The vessel was able to return to port for repair and readjustment of the electronic engine control governors. First line was ashore at 1617 hr at Berth 5 in Guam harbor, where system repairs immediately commenced.

At 0700 hr on 8 March 2001, the ship officially departed Guam for the second time. The vessel transited 54 nmi to a deepwater (~6300 m) test site, arriving on location at 1235 hr. This commenced a 48-hr sea trial of the ASK system. At 0209 hr on 9 March, the vessel departed the deepwater location and transited 40 nmi to an area selected as a site for shallow-water (<300 m) sea trials. The shallow-water testing was concluded, and the beacon was retrieved at 0845 hr on 10 March. The vessel got under way for the Guam pilot station, where the ASK test engineers departed. By 1130 hr on 10 March, the ship was under way at full speed for Site 1200 (proposed Site MAF-4B). The transit of 95 nmi was completed in 9.5 hr at an average speed of 10 kt.

Site 1200 (Proposed Site MAF-4B)

At 2100 hr on 10 March, the vessel arrived at the first location of Leg 195, and the thrusters and hydrophones were lowered. A positioning beacon was not immediately deployed, and the ship maintained station keeping by using the Global Positioning System. A brief 12-hr camera survey of the site was conducted to spot a locality that showed evidence of fluid migration to the surface (see **"Video Camera Survey,"** p. 9). At 0710 hr on 11 March, the first positioning beacon was deployed. When this beacon failed to respond to actuation commands, the ship was moved 200 m upcurrent and at 0832 hr a second beacon was deployed. A total of 15.25 hr was spent investigating the site and identifying prospective drilling locations, of which 1.5 hr was spent conducting a 23-m jet-in test at the future reentry hole location ("C" in Fig. **F3;** Table **T1**).

Hole 1200A

After returning to the locality identified for the first coring attempt (Fig. **F3**), the vibration-isolated television (VIT) was recovered and the first pilot hole, Hole 1200A, was spudded with the RCB system at 2200 hr on 11 March. The seafloor was tagged at a depth of 2921.0 meters below rig floor (mbrf). Coring continued through Core 195-1200A-10R to a depth of 89.4 mbsf (Table **T1**). Recovery was poor, with little recovery of the serpentine mud matrix material surrounding the hard ultramafic clasts typical of the site. Because of steadily increasing torque, a short wiper trip was made before the top of the bottom-hole assembly (BHA) went below the seafloor. Coring continued through Core 195-1200A-13R to a depth of 118.3 mbsf, where once again the rotating torque increased. During recovery of Core 195-1200A-13R, the top drive stalled and the drill string became stuck. After 30 min the pipe was worked free and RCB coring resumed. Core 195-1200A-16R was cored to a depth of 147.2 mbsf, where a repeat of the earlier stuck-pipe incident occurred. Once again, high torque and lost rotation resulted in a stuck drill string. The pipe was worked free, and another wiper trip to 30 mbsf was initiated. The drill string drag during the trip was fairly constant, except for a zone around 45 mbsf that continued to be troublesome. It was apparent that the hole could not be salvaged, and the drill string was pulled out of the hole. The seafloor was cleared at 1535 hr, ending Hole 1200A. One wash barrel "ghost" core (195-1200A-17G) recovered 2.66 m.

F3. Video camera survey tracks, p. 66.

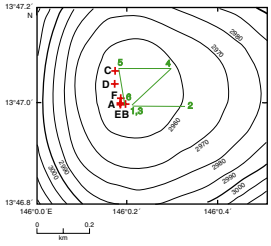

T1. Coring summary, p. 145.

Hole 1200B

The ship was offset 25 m to the east, and Hole 1200B was spudded at 1640 hr on 13 March, with the seafloor tagged at a depth of 2922.0 mbrf. Our intention was to drill ahead with an RCB wash barrel in place to 147.2 mbsf, the total depth (TD) achieved in Hole 1200A. By 0615 hr on 14 March, the hole had been advanced to a depth of 98.0 mbsf. As in Hole 1200A, the penetration rate was variable as the bit alternately encountered soft serpentine mud and then hard clasts. Overall, the average rate of penetration (ROP) for the interval was 11.0 m/hr.

Once again, high torque and overpull began to plague the hole. Regardless of consistent mud sweeps and multiple reaming attempts, the hole would not clean up. At 0645 hr on 14 March, it was decided to abandon further drilling/coring efforts and the drill string was pulled out of the hole. Overpulls of up to 120 kilopounds (kips) were required before finally clearing the seafloor at 0730 hr. The wash barrel was recovered, and at 1430 hr on 14 March the bit cleared the rig floor, ending Hole 1200B.

Because of the difficulties in drilling Holes 1200A and 1200B to the target depth, a variance from the Pollution, Prevention, and Safety Panel was requested to allow setting the 10.75-in surface casing string in the planned reentry hole to a depth of 250 mbsf (hole depth = ~270 mbsf), more than 100 m beyond the cored depth of 147.2 mbsf. This request was approved expeditiously because the formation at this site was not likely to change with depth.

Hole 1200C

The ship was offset 125 m north and ~25 m west to the location where the jet-in test had been conducted. The reentry cone had previously been assembled and pre-positioned onto the moonpool doors. The 20-in casing shoe joint had already been precut and the casing shoe welded in place. Two joints of 20-in casing were connected to the 20-in casing hanger, and this assembly was lowered and latched into place using the Dril-Quip (DQ) running tool.

An 18.5-in tricone mill-tooth bit with an underreamer dressed with 22-in cutter arms was made up to an 8.25-in positive displacement mud motor. Rig-floor testing of this assembly was initiated at 10 strokes per minute (spm), and the underreamer arms began to open up at 15 spm.

Hole 1200C was spudded at 0450 hr on 15 March, as the bit tagged the seafloor at a depth of 2943.0 mbrf. Progress was slow and variable, but the casing kept advancing using steadily increasing weight on bit up to 25 kips and total flow rates as high as 150 spm using two mud pumps. After 18.25 hr, the reentry cone base reached the seabed, placing the 20-in casing shoe at 23.7 mbsf and the bit at 25.9 mbsf. The DQ running tool was released, and the drilling assembly was tripped back to the ship, where it cleared the rig floor at 0530 hr on 17 March.

The next BHA consisted of the same 18.5-in tricone drill bit and underreamer combination but without the mud motor. The BHA was tripped to the seafloor, and after deploying the VIT, Hole 1200C was reentered for the first time at 1720 hr. The drilling assembly advanced smoothly. Penetration rates varied from 3 to 10 m/hr as the hole was advanced. All drilling parameters remained consistent, and no problems were experienced throughout the course of drilling. At 0130 hr on 18 March, the hole reached a TD of 3083.0 mbrf (140 mbsf). A sepiolite mud sweep was pumped while on bottom, followed by a wiper trip to

20.0 mbsf and back to TD. Hole conditions were good, and the driller indicated no overpull, drag, or torque problems during the trip. Eight meters of soft fill at the bottom was circulated out with another sepiolite mud sweep. The hole was displaced with 215 bbl of sepiolite, the top drive was set back, and the drill string was recovered back aboard ship, clearing the rig floor at 1130 hr on 18 March.

Hole 1200C was reentered for the second time at 2337 hr with the DQ running tool and nine joints of 16-in casing and a casing hanger. While the casing string was being washed/lowered into the hole, however, the casing shoe encountered an obstruction 6 m off the bottom, which prevented the casing hanger from landing. After three futile hours, the string was recovered back to the ship and one joint of casing was removed from the string.

The shortened string was run back into the hole, and the hanger was landed at 2100 hr on 19 March without incident. With the 16-in casing shoe placed at a depth of 107.4 mbsf, the casing string was cemented in place. The cementing equipment was laid out, and the drill string was recovered. The DQ tool was laid out, and the 18.5-in bit and underreamer were replaced with a 14.75-in bit. The drill string was run back in, and the fourth reentry was made at 1329 hr on 20 March. The cement column was drilled out, and the hole was deepened to 152.0 mbsf. The drill string was recovered, and an underreamer dressed with 20-in cutter arms was placed above the 14.75-in bit. The drill string was run back in, and the fifth reentry was made at 1015 hr on 21 March. Drilling resumed, and after advancing to 266.0 mbsf at 2245 hr on 22 March, the ROP went to zero. A wiper trip to the seafloor was initiated. At a depth of 237.0 mbsf, the pipe became stuck but was worked free within 15 min using 50 kips of overpull. The pipe trip continued to the 16-in casing shoe at 107.0 mbsf, and then the hole was washed/reamed back to 257.0 mbsf. The 9 m of soft fill was easily circulated out of the hole, but further deepening proved futile and the drill string was recovered for inspection. The bit was found to be in good condition with only a few chipped/broken teeth, but the underreamer was missing two out of three cutters.

Four joints of 10.75-in screened/perforated casing totaling 53.5 m in length were made up. The lowermost joint was terminated with a conventional cementing float shoe. The screened joints were followed by 14 joints of standard 10.75-in casing. At 2210 hr on 23 March, Hole 1200C was reentered, and by 0300 hr on 24 March, the casing had been advanced to a depth of 224.0 mbsf. Progress beyond this point was prevented, and the 10.75-in string was pulled out of the hole and tripped back to the drill ship, where it was decided to remove three joints of casing.

By 1458 hr on 24 March, the string had been tripped back to bottom and the casing was run in the hole without incident. The casing hanger was landed, latch engagement was verified, and the DQ tool was released by 1610 hr. The shortened casing string placed the shoe at 202.8 mbsf, with the screened interval extending from 202.3 to 148.8 mbsf.

Prior to withdrawing the drill string from the hole, the water sampler temperature probe was deployed in an attempt to sample some of the borehole fluids. Water sample and temperature data were collected from a depth of 30 mbsf, and the tool was recovered back to the ship.

Hole 1200C CORK Deployment

The CORK assembly (see "Borehole Instrumentation," p. 46), with six joints of 5.5-in drill pipe used as a stinger, was run in the hole at 0954 hr on 25 March, and the drill string was lowered to 53.0 mbsf. This left the CORK temporarily shy of landing out by ~8 m.

The thermistor string was deployed with two osmotic fluid samplers and an aluminum pin used in the shackle connecting the sinker bar weight. This "weak link" was designed to corrode over time, allowing the thermistor string and osmotic samplers to be recovered at a future date without having to recover the sinker bar weight.

At 1300 hr on 25 March, the thermistor/osmotic sampler assembly was slowly run into the hole, and at 1430 hr, the data logger was landed in the CORK body. One hour was taken at this point to calibrate the seafloor pressure sensor with the internal CORK pressure sensor. At 1530 hr, the drill string was pressured up and the data logger was latched into the CORK assembly. After using the wireline jars to shear the overshot shear pin, the wireline was recovered.

At 1630 hr, the CORK setting go-devil was deployed and the CORK was landed in the reentry cone structure. The drill string was pressured up, but before reaching the specified 1000-psi setting pressure, the shear pins on the internal bypass feature sheared at ~900 psi. The go-devil was recovered, redressed with a solid plug, and redeployed. Once landed, the drill string was pressured up to 1000 psi and held for 2 min. The standpipe was bled off and the drill string picked up, verifying that the CORK was not latched in. The CORK was landed once again, and the drill string was pressured up to 1500 psi and held for 3 min. The CORK latch mechanism still did not engage, so the drill string was pressured up a third time. This time, pressure was increased to 2000 psi for 5 min and then to 2500 psi for another 5 min. After bleeding off the pressure at the standpipe, the pipe was raised, and CORK latch verification was achieved at 2000 hr on 25 March.

The remotely operated vehicle (ROV)/submersible platform halves were moved onto the moonpool doors and bolted and welded around the drill string. At 2200 hr on 25 March, the platform was lowered into the water and released. This was followed immediately with the VIT. At 2315 hr, the platform was observed resting properly in place over the reentry cone/CORK body. The active heave compensator contributed greatly to a successful CORK landing and releasing operation. While the coring line was run in to retrieve the CORK setting go-devil, the VIT was retrieved and the drill string was recovered. The rig floor was cleared at 0500 hr on 26 March, ending operations at Hole 1200C.

Hole 1200D

The vessel was offset 40 m south of Hole 1200C. The VIT was deployed during the pipe trip to enable location of an appropriate spud position. Hole 1200D was spudded at 1415 hr on 26 March. Water depth was identified as 2942.0 mbrf, based on a visual tag with the drill bit, and the VIT was recovered. APC coring was initiated and continued to a depth of 44.4 mbsf using the APC advance-by-recovery method. When hard clasts were encountered, an XCB center-bit assembly was deployed to drill through clasts until breaking out into soft material. Then APC coring was resumed. This occurred a total of four times, between Cores 195-1200D-4H and 5H, 5H and 6H, 9H and 10H, and immediately after 10H. For microbiological contamination control, Whirl-

Pak microspheres were deployed, starting with Core 195-1200D-4H, and perfluorocarbon tracers (PFT) were pumped starting with Core 1H. After Core 195-1200D-10H was terminated by a hard clast, the XCB center bit was used to deepen the hole. After advancing 9 m the ROP fell to zero, and it was feared that the XCB cutting shoe/center bit had failed. Once recovered, the XCB barrel was found to be intact, with the cutting structure unharmed. This suggests that the drill bit was pushing a hard clast downhole ahead of the bit. As a result, the decision was made to abandon Hole 1200D. The hole was displaced with heavy mud. The top drive cleared the seafloor at 1230 hr on 27 March, officially ending Hole 1200D.

Hole 1200E

The ship was moved back to the coordinates of Hole 1200A, and at 1515 hr on 27 March, Hole 1200E was spudded using a visual seafloor tag depth of 2922.0 mbrf. APC coring was initiated and continued using the advance-by-recovery method through Core 195-1200E-6H, to a depth of 25.9 mbsf. The Davis-Villinger temperature probe (DVTP) was unsuccessfully deployed in an attempt to recover a temperature measurement. APC coring continued through Core 195-1200E-7H to a depth of 32.5 mbsf, where the XCB coring system was deployed to drill through a hard clast. Two XCB cores were recovered after some very slow drilling to a depth of 50.4 mbsf. Core 195-1200E-10H was recovered using the APC, advancing the hole to 56.4 mbsf. At this depth, a second DVTP temperature measurement was attempted, again without success.

The scientific objectives for this hole had been accomplished, and the drill string was thus pulled clear of the seafloor, officially ending Hole 1201E at 1115 hr on 28 March.

Hole 1200F

The ship was offset 20 m north, and Hole 1200F was spudded at 1315 hr on 28 March. Coring proceeded until the time allocated for operations at Site 1200 expired. Hole 1200F reached a depth of 16.3 mbsf, with the recovery of APC Cores 195-1200F-1H through 3H. An Adara temperature measurement taken with Core 195-1200F-3H was excellent. No PFT tracers or Whirl-Paks were used during the operations at this hole. The drill string was recovered back to the ship, and all BHA components were laid out. The bit cleared the rotary table at 2315 hr on 28 March. The ship was secured for transit while the positioning beacons were released and recovered. At 0200 hr on 29 March, the ship was under way for the Guam pilot station.

Video Camera Survey

A camera survey was conducted at Site 1200 prior to drilling. The objective was to locate the sites of active vent fluid springs (position 1 in Fig. F3), as identified by the presence of carbonate encrustations and chimneys and by the presence of mussel beds and other megafauna (snails, worms, and galatheid crabs).

The VIT was deployed while pipe was tripped to a depth of ~2920 m. The bottom was first observed at ~0615 hr. When the first positioning beacon failed to respond to actuation commands, the ship was moved 200 m upcurrent (east) and a second beacon was deployed (position 2

in Fig. F3). The ship was then moved farther west to the starting reference position (positions 1 and 3 in Fig. F3) to begin the survey, and as it moved, white patches (carbonate encrustations) were observed ~50 m from the east end of the beacon drop line. At 44 m east of the reference position, the seafloor was fissured.

When the ship had returned to the reference starting position (positions 1 and 3 in Fig. F3), we began a traverse on a heading of 045° for 200 m (to position 4 in Fig. F3). The seafloor is covered with rock clasts and serpentine mud along this traverse, and the depth increased slightly before decreasing to a shallower area of small (1–2 m) crags of serpentine mud with numerous rock clasts. This texture persisted over most of the traverse. At a distance of 94 m along the traverse from the reference starting point, the seafloor had fine fissures and fewer clasts. At ~190 m from the starting point, the seafloor became rockier and deepened by a few meters.

At position 4 (Fig. F3), the ship began an east-to-west transect for another 200 m to position 5 (Fig. F3). During this traverse, the seafloor rose slightly at first to ~2882 m then dropped off a few meters for the rest of the transect. Depth increased consistently, although only slightly, to a maximum depth of 2903 m. The summit depression appears to have a north-south elongation. The area within the depression, especially at the western end of the transect, has fewer and smaller rock clasts. As the ship reached the western end of the line, the seafloor had higher albedo and fewer rock clasts and, thus, was deemed appropriate for the reentry hole (Hole 1200C).

The next line of the survey was run southward to latitude 13°47.00′N along ~146°48.00′E (position 6 in Fig. F3). At 13°47.0120′N, white specks (interpreted as shells of dead mussels) were observed scattered over the seafloor. At ~13°46.9987′N, we observed white patches of carbonate encrustations and high albedo patches interpreted to be fresh exposures of serpentine mud. The marker left at the end of *Shinkai 6500* dive 351 was observed shortly afterward, and beds of live mussels, holes where cores had been taken previously, and white carbonate encrustations and small chimney structures were observed at ~13°47.0027′N, 146°00.1751′E. The bottom was tagged at a depth of 2920.7 m.

It was decided to conduct the jet-in test for the reentry hole near position 5 (Fig. F3) and then to return to the Shinkai springs site to drill the pilot hole. The ship was moved back to the jet-in test site at 13°47.0705′N, 146°00.1754′E, and the jet-in test was initiated. Mud emanating from the jet-in hole was high albedo serpentine mud initially, but turned dark shortly after the test began. This suggested that the oxidized lighter serpentine mud was present to a meter or so beneath the seafloor and was underlain by darker reduced mud. The jet-in test was completed at ~1500 hr.

The ship was moved back to the location of the spring site that was chosen for Hole 1200A, and after a box survey, the area of white carbonate chimneys was detected at a depth of 2921 m at 1932 hr. Shortly afterward, areas of patchy carbonate, the *Shinkai 6500* marker, and the mussel beds were relocated. The position for Hole 1200A was chosen to be within the Shinkai springs area but offset from the mussel beds in an effort to preserve these communities for future studies while optimizing the potential for recovery of cores that would yield good pore fluids for geochemical studies.

LITHOSTRATIGRAPHY

Five holes were cored at Site 1200. Unconsolidated serpentine successions were recovered from Holes 1200D, 1200E, and 1200F. All holes are characterized by a succession of silty clay–sized serpentine with dispersed clasts to clast-poor serpentine diamicton with clast-rich intervals that all belong to the same lithostratigraphic unit (Fig. F4).

Unit I

Interval: Sections 195-1200D-1H-1 through 10H-CC; 195-1200E-1H-1 through 10H-CC; and 195-1200F-1H-1 through 3H-CC
Depth: 0–44.4; 0–56.4; and 0–16.3 mbsf
Age: late Quaternary (<0.46 Ma)

Unit I extends through all recovered serpentine sections at Site 1200. It is characterized by poorly sorted material with dispersed clasts. Two distinct sedimentary facies are identified (Fig. F4). Facies I is composed of silty clay–sized serpentine with dispersed clasts and clast-poor serpentine diamicton (Figs. F5, F6). The observation of silty clay–sized serpentine with dispersed clasts (<5% clasts >2 mm in size) (Fig. F3, p. 41, in the "Explanatory Notes" chapter) or clast-poor serpentine diamicton (5%–10% clasts >2 mm in size) seems to depend on the core-splitting technique rather than on changes in lithology. Thus, clasts are visibly less abundant in holes and intervals split using the soft-sediment wireline method (Hole 1200D [0–21.9 mbsf] and interval 195-1200E-1H-1, 0 cm, to 6H-CC, 40 cm [0–25.93 mbsf]). Small pebbles and granules are pushed into the sediment and not split in half by the wireline. The rock saw was used to split the remaining intervals of Hole 1200E (interval 195-1200E-7H-1, 0 cm, to 10H-CC, 33 cm [25.93–56.45 mbsf]) and Hole 1200F (0–16.3 mbsf). The rock saw enables small pebbles and granules to be split in half, resulting in an apparently higher concentration of clasts. Facies II is composed of clast-rich serpentine diamicton (10%–30% clasts >2 mm) (Fig. F7). It should be noted that this facies was only recognized and described in cores cut by the rock saw.

Facies I

Facies I is the predominant facies and is composed of silty clay–sized serpentine with dispersed clasts and clast-poor serpentine diamicton (Figs. F5, F6). White chrysotile fibers and fragments are visible throughout all described sections.

Downcore variability in sediment composition is evident in color reflectance data (Fig. F4). All sediment cores were dark blue gray to black when first split but lightened in color once exposed to the aerobic environment of the core lab. Calcareous intervals (Fig. F4) oxidized extremely rapidly after the cores were split, revealing hues of light yellowish brown, light bluish gray, and light pink (Fig. F8). Recorded calcareous intervals (195-1200D-1H-1, 10–120 cm [0.10–1.20 mbsf], 195-1200E-1H-1, 10–133 cm [0.10–1.33 mbsf], 195-1200E-3H-1, 0 cm, to 4H-CC, 36 cm [11.00–17.55 mbsf], and 195-1200F-1H-1, 10–142 cm [0.10–1.42 mbsf]) and the location of clasts coated with calcareous precipitates (intervals 195-1200D-1H-4, 98.5–101 cm [5.48–5.51 mbsf], 1H-5, 33 cm [6.33 mbsf], 2H-2, 21–23.5 cm [8.61–8.64 mbsf], and 195-1200E-1H-2, 44 cm [1.94 mbsf]) and calcareous nodules (Sample 195-

F4. Lithology, color reflectance, and calcareous intervals, p. 67.

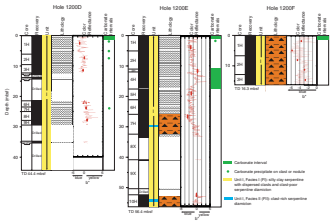

F5. Silty clay serpentine with dispersed clasts, p. 68.

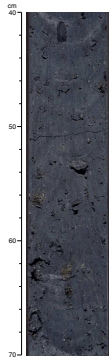

F6. Clast-poor serpentine diamicton, p. 69.

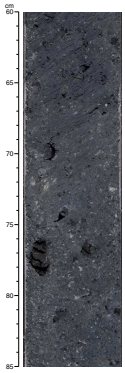

F7. Clast-rich serpentine diamicton, p. 70.

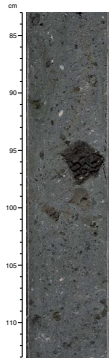

1200D-7H-1, 88 cm [24.38 mbsf]) correlate well with microfossil content and abundance (see "Biostratigraphy," p. 21).

Whole-core photography and color spectral analysis were completed as quickly as possible after splitting. A downcore trend from dark bluish gray to lighter greenish gray is an artifact of oxidation. Scraping core surfaces revealed the underlying dark blue-gray to black color of the material characteristic of its natural anoxic environment. Thin (<2 mm) bands of faint and diffuse greenish gray were observed in intervals 195-1200E-10H-1, 60–85 cm (53–53.25 mbsf), 195-1200F-1H-5, 16–22.5 cm, and 60–93 cm (6.16–6.22 and 6.60–6.93 mbsf), 2H-4, 35–49 cm (12.05–12.19 mbsf), and 3H-CC, 40–60 cm (16.01–16.21 mbsf). These color bands are not associated with a change in lithology, clast content, or texture. It is therefore surmised that they are not indicative of depositional processes but rather may represent intervals of "staining" from nearby altered clasts or differential oxidation rates.

Clasts identified in Facies I sediments are predominantly altered serpentinized ultramafic varieties (see "Smear Slide Analysis," p. 12, "X-Ray Diffraction," p. 14, and "Igneous and Metamorphic Petrology of Ultramafics," p. 16). The degree of alteration varies. Highly altered clasts range from green to greenish brown to red in color, are soft, and are easily fragmented. They are often present as a concentration of small (<2 mm) angular fragments in the footprint of a former large clast. Clast shape varies from rounded to angular (see "Structural Geology," p. 52).

Facies II

Facies II is composed of clast-rich serpentine diamicton and extends through intervals 195-1200E-7H-3, 68–97 cm, and 10H-2, 61–114 cm (29.58–29.87 and 54.51–55.04 mbsf) (Figs. F4, F7). With the exception of increased clast content, these sediments are identical to Facies I; however, no calcareous intervals are present within recovered intervals of clast-rich diamicton.

Smear Slide Analysis

Microscopic inspection of smear slide samples and two thin sections was conducted on the matrix of the serpentine deposits, including the clay-, silt-, and fine to medium sand–sized fractions. Some samples were wet sieved to obtain the fine sand fraction (grain diameter = 63–344 µm), which provided clean grains for optical mineral identification and photographic documentation. All smear slide samples and thin sections are dominated by serpentine minerals associated with small amounts of heavy minerals, whereas some samples also include authigenic phases (see "Site 1200 Smear Slides," p. 50).

Serpentine Minerals and Rock Fragments

Most serpentine species appear as silt- to sand-sized flaky particles, consisting of single crystals or microcrystalline aggregates (Figs. F9, F10A, F10B, F10E). Occasionally, they show hexagonal outlines or internal lamellae. They exhibit colors in various shades of dull green to greenish brown. No pleochroism is evident. They have low refractive indices (n = ±1.56) and low birefrigence with first-order interference colors (gray to yellow). Their optical character is biaxial negative with mostly low angles between the optic axes. From the optical features,

F8. Color variability in oxidized calcareous intervals, p. 71.

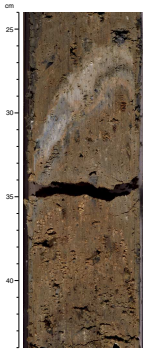

F9. Silty clay–sized serpentine matrix showing unsorted grain-size texture, p. 72.

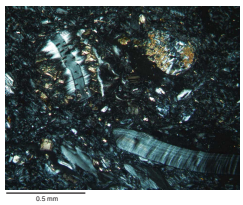

F10. Serpentine flakes, crysotile fibers, and zeolite-like material, p. 73.

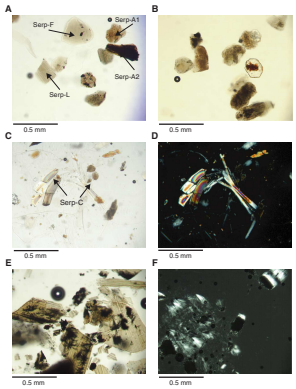

they represent members of the lizardite and/or antigorite groups. Because a reliable distinction between the two serpentine groups cannot be made, serpentine species were defined by their degree of alteration. Thus, fresh and translucent serpentines can be distinguished from dusky serpentines that include dispersed "dustlike" opaque particles that give the serpentines a dirty appearance. A third species consists of strongly altered serpentines that were replaced to a great extent by opaque materials. The latter species makes up the major constituent of the black serpentine muds frequently encountered in Holes 1200E and 1200F.

Chrysotile fibers were recognized as another distinct serpentine species, which is present in minor amounts throughout the investigated sections (Fig. F10C, F10D). Apart from their typical fibrous habit, they show pleochroism from greenish to brownish green and have slightly higher birefringence (multicolored first-order interference colors) than the other serpentine species.

Larger sand-sized clasts embedded in the silty matrix are frequently composed of rock fragments that were replaced pseudomorphously by serpentine minerals and brucite (Fig. F9). Distinction of serpentine and brucite arises from the brownish interference colors of the latter (Fig. F9). In addition to altered rock pieces, fresh rock fragments of greenschists and blueschists represent ubiquitous components of the serpentine muds (see detailed description in "Igneous and Metamorphic Petrology of Ultramafics," p. 16).

Accessory Minerals

In most samples, the serpentines are associated with low abundances of pale bluish amphiboles, particularly in the fine sand fraction (Fig. F11A). The elongated prismatic crystals show weak pleochroism between shades of blue and pinkish violet. Under crossed polarizers, internal zonation becomes visible (Fig. F11B). Moreover, they have low extinction angles and negative biaxial optical character, similar to common hornblendes. However, the distinct color and pleochroism features show affinities to amphiboles of the crossite to glaucophane group. Possibly, the blue amphiboles originate in deep blueschists that formed in the high-pressure, low-temperature environment of the Mariana subduction zone (Fryer et al., 1999).

Other identified accessory minerals are spinels, which appear as small isotropic grains of high relief and whiskeylike color, as well as garnet and greenish flakes of chlorite with anomalous interference colors.

Authigenic Minerals

The uppermost sections (0–1 mbsf) of Holes 1200D, 1200E, and 1200F include abundant authigenic aragonites. Exceptionally, they are also present farther downcore in Cores 195-1200E-1H through 3H, where they are associated with an interval of contorted and oxidized greenish silty clays and with parts of the underlying black silty clays. Aragonites appear as up to 1-mm-long lath-shaped crystals or form "mikado-like" bunches of small needles (Fig. F11C, F11D, F11E, F11F). Common features of both varieties are high refraction indices and high birefringence with high-order interference colors. Broken and rounded pieces of aragonite are present in trace amounts (one per smear slide) in other silty clay samples, where they likely represent reworked particles from the aragonite-bearing strata.

F11. Amphibole, aragonite laths and needles, and serpentine flakes, p. 74.

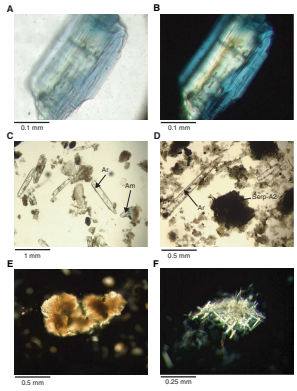

In Section 195-1200E-1H-2, black serpentine silty clays contain white millimeter-sized nodules exhibiting cauliflower structures. In smear slides, these concretions appear as radiating fibers attached to opaque nuclei (Fig. F10F). From its habit and according to X-ray diffraction (XRD) findings, this mineral likely represents a species of the zeolite group.

X-Ray Diffraction

To infer the source materials of framework clasts and fine-grained matrix in the serpentine mud deposits, XRD analyses were carried out on both rock pieces and mud samples on bulk powder mounts (Table T2). Similar to smear slides, the identification of distinct serpentine minerals by XRD is ambiguous and should be reexamined on shore by sophisticated X-ray microbeam or electron optical techniques.

Rock samples were taken from Hole 1200A, which was drilled with the RCB. Two major rock types can be distinguished from XRD results: altered harzburgites and strongly altered fine-grained ultramafic rocks (Fig. F12). Though dominated by serpentine, the harzburgites still include portions of the original rock-forming minerals olivine (forsterite), orthopyroxene (enstatite), and traces of clinopyroxene. Whereas brucite represents a subordinate mineral in the harzburgites, it is abundant in the fine-grained ultramafic rocks, which are otherwise dominated by serpentine minerals and contain few primary minerals. Some ultramafic rocks show signs of silica gel precipitation, as indicated by the presence of opal-CT (Fig. F12). Opal-CT is made up of recrystallized opal, including cristobalite and tridymite (Jones and Segnit, 1971). It thus represents a transitional phase between amorphous opal and microquartz and is usually formed under high-temperature conditions, but it may form discrete early diagenetic chert layers in shallowly buried deep-sea sediments that have not been affected by elevated temperatures (e.g., Bohrmann et al., 1994). One exotic greenschist fragment was analyzed, which shows no signs of serpentinization and consists of clinopyroxene and magnesium-rich chlorite (Fig. F12).

XRD measurements of silty clay samples support results from smear slide analyses and point to serpentine minerals and brucite as dominant constituents (Fig. F12). In contrast to the analyzed rock pieces, accessory amounts of amphibole, together with talc and chlorite, are evident in many samples. This assemblage indicates the presence of exotic greenschist and blueschist detritus within the serpentine muds.

The downcore semiquantitative distribution of minerals, as identified by XRD measurements, illustrates the distribution of aragonite in Holes 1200D, 1200E, and 1200F, as also deduced from smear slide analyses (Figs. F13, F14, F15). Aragonite is often associated with calcite. The downcore patterns suggest that aragonite/calcite and brucite tend to mutually exclude each other. Pore water conditions in the upper sediment layers may favor aragonite precipitation and brucite dissolution (cf. "Geochemistry," p. 29). From the top of Hole 1200D, fragments of a carbonate chimney consisted predominantly of calcite with minor aragonite.

Another mineral with a major XRD peak at 5.44 Å possibly represents the zeolite-like mineral found in one of the smear slides (Sample 195-1200E-1H-2, 116 cm). The XRD results, however, show that this authigenic mineral is actually encountered in most intervals composed of black serpentine silty clays. The only zeolite that shows a strong XRD peak near 5.44 Å is analcime (5.61 Å). This interpretation has to be re-

T2. XRD data for rock pieces and silty clay samples, p. 148.

F12. XRD patterns of rock pieces and silty clay–sized serpentine, p. 75.

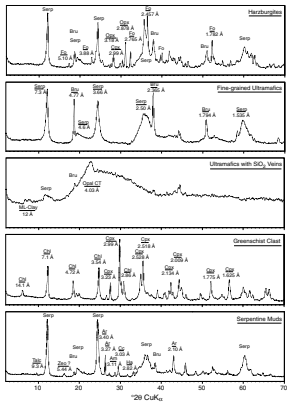

F13. Semiquantitative mineralogy of silty clay–sized serpentine, Hole 1200D, p. 76.

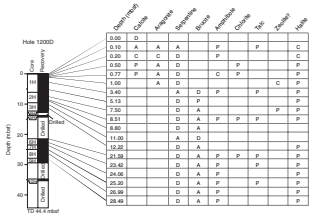

F14. Semiquantitative mineralogy of silty clay–sized serpentine, Hole 1200E, p. 77.

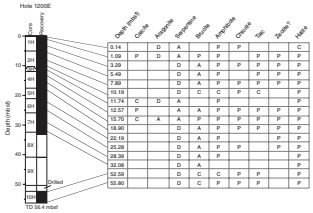

F15. Semiquantitative mineralogy of silty clay–sized serpentine, Hole 1200F, p. 78.

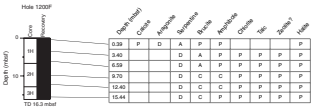

garded with caution because other diagnostic peaks of analcime at 3.43 and 2.93 Å seem to be suppressed in the Site 1200 XRD records. Halite was recognized as a minor component in all XRD samples as an artifact from sea salt remains in the sediment pore spaces.

Environmental Interpretation

The serpentine muds at Site 1200 show little variability in lithology, providing little insight into the depositional processes taking place on the knoll of South Chamorro Seamount. However, a few observations can be made. The overall poorly sorted nature of the muds is suggestive of a tectonically active area with a high rate of mud supply in a small area, consistent with the environmental setting of a mud volcano. The diamictic texture is consistent with the protrusion of unsorted serpentine mud onto the surface of the seamount and its transportation and deposition by debris flows on the flanks of the mud volcano. Clast-rich intervals are rare but may suggest crude bedding.

High abundances of aragonite and calcite and the absence of brucite in the near-surface muds point to geochemical pore water gradients that control the dissolution and precipitation of solid phases. These gradients are caused by rising pore fluids that originated at depth and mix with seawater near the surface. Where these pore fluids are released as springs, they give rise to the formation of carbonate chimneys at the seafloor, as observed at the top of Hole 1200A (see **"Geochemistry,"** p. 29). Moreover, the top layers of carbonate-bearing muds are mostly oxidized.

These observations lead us to conclude that the carbonate-rich and partly oxidized interval between 11.00 and 17.55 mbsf encountered in Hole 1200E may represent preserved paleosurface material, which was not affected by changing geochemical gradients while buried under younger material. This interval is characterized by deformed and folded color bands but is not associated with a change in lithology, texture, clast content, or clast concentration, which may suggest disaggregation and redeposition via debris flows or turbidity currents. Instead, sediment structures suggest downslope gravitational motion via slow creep or sliding. This process likely thickened the paleosurface deposits and protected them from chemical alteration during later burial. This might help to explain the presence of carbonate-bearing material, which was also found at depth on the flanks of Conical Seamount during Leg 125 (Shipboard Scientific Party, 1990b).

The interpretation of reworked "paleosurface" deposits suggests that these holes have been drilled into the flanks of the mud volcano, immediately adjacent to the present-day active-flow conduit. It is noted that camera surveys prior to drilling provided visual confirmation of conduit activity at the site of Hole 1200E; however, the conduit "pipe" may be oriented oblique to the drilled hole, enabling us to penetrate flank material downhole. It is also possible that calcareous material from the surface has been incorporated into material at depth by falling into fractures or crevasses observed at the surface by camera surveys during this leg (see **"Operations,"** p. 4) and earlier ROV and submersible surveys (Fryer et al., 1990). Serpentine mud volcano environments are very active and dynamic systems, and it is likely that the location of the active conduit changes over time. The data presented in this section confirm this complexity and extend our limited knowledge of the processes involved in fluid and sediment transport.

IGNEOUS AND METAMORPHIC PETROLOGY OF ULTRAMAFICS

The hard rocks recovered at Site 1200 are heavily serpentinized and tectonized harzburgite and dunite clasts. Of the ultramafic rocks, 98% are harzburgites and 2% are dunites. The maximum recovered thickness of a single clast is ~1 m. Overall, the degree of serpentinization varies positively with LOI. The petrography of the serpentinized ultramafic rocks has been determined through observation and description of 50 thin sections covering all representative rock samples collected at different depths in the cored holes. The samples have been selected on the basis of visual core description to characterize different textures, primary and secondary mineral phases, crystal content and size, and vein size. All observations are reported in the thin section description forms following the outlines illustrated in "Igneous Petrology," p. 10, in the "Explanatory Notes" chapter. Estimates of the primary mineralogy of the rocks are based on CIPW normative calculations (Table T3), as well as on visual and microscope observations and mineral-specific secondary textures (i.e., olivines commonly alter to mesh-textured serpentine, bastite is more common after orthopyroxene, etc.).

Clasts of similar serpentinized peridotites were recovered from the serpentine mud in Holes 1200D, 1200E, and 1200F (Fig. F16). The grit-sized fraction (0.1–1.5 cm) of the serpentine mud was inspected under a binocular microscope and handpicked for discrete lithologies. These lithologies are indicative of a high-pressure, low-temperature origin. Further microprobe and XRD analyses of the samples on shore will provide constraints on the pressure and temperature conditions.

Serpentinized and Tectonized Harzburgites

The colors of the harzburgites range from bluish gray (5B 5/1) to dark bluish gray (5B 4/1), and the grain size is highly variable, from fine to coarse grained (0.01–5 mm). The primary mineralogy includes olivine, orthopyroxene, clinopyroxene, and chromium spinel (Fig. F17). The relict amount of olivine = 0%–35%, whereas orthopyroxene = 0%–35%, clinopyroxene = 0%–5%, and Cr spinel = 1%–3%. Estimates of the original mineral phase contents range as follows: olivine = 35%–85%, orthopyroxene = 10%–50%, clinopyroxene = 0%–5%, and Cr spinel = 1%–3%. The serpentinized harzburgites generally display typical mesh and hourglass textures (when the serpentinization involves olivine), as well as bastitic texture (when orthopyroxene is the serpentinized mafic phase) (Figs. F18, F19). The mesh texture resembles a fisherman's net, where the rim of the net is serpentine and the empty space in the mesh center is occupied by fresh olivine (Fig. F20). In the hourglass texture, olivine is completely altered, leaving no distinction between the mesh rim and the mesh center, and a typical sweeping extinction appears when the stage is rotated. Bastitic texture consists of orthopyroxene pseudomorphs, partially or completely transformed to serpentine (Fig. F21).

Evidence of penetrative deformation is extensive in the harzburgite clasts. Olivine microgranulation is abundant in the majority of the samples, leaving residual anhedral and fine-grained (average diameter = 0.05 mm) relict olivine. Kink banding is common and clearly visible in the larger grains (Fig. F22). Orthopyroxene is mainly found as equant, subhedral grains (maximum length = 4 mm and average length = 1

T3. Major, minor, and trace elements, p. 150.

F16. Serpentinite clast in variably oxidized serpentine mud, p. 79.

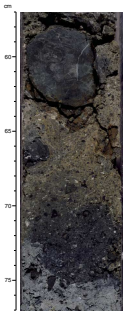

F17. Harzburgite sample showing the main mineral paragenesis, p. 80.

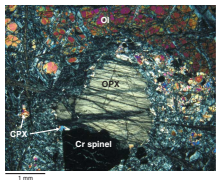

F18. Fresh harzburgite–dunite transition, p. 81.

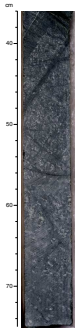

F19. Harzburgite intersected by a large "Frankenstein"-like chrysotile vein, p. 82.

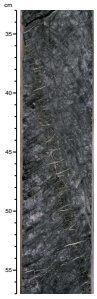

mm). As a result of extensive shearing, the orthopyroxene cleavage planes are often bent and exhibit undulatory extinction (Fig. F23). Clinopyroxene is present in association with or in proximity to orthopyroxene grains (Fig. F24). It also appears as small (0.2-mm-long axis), very thin, elongate exsolution lamellae parallel to (100) within orthopyroxene. Chromium spinel to magnesiochromite was identified by its translucent dark red color. Generally, it occurs as euhedral to anhedral crystals (Fig. F25).

The degree of harzburgite serpentinization is highly variable and ranges from 40% to 100% (average = ~75%). In some cases, the composition of the rock is impossible to infer from petrographic observation, due to pervasive serpentinization that obscures the primary mineralogy. In these cases, we used the chemical composition to classify the sample. Limited onboard XRD analyses indicate that lizardite is the most common serpentine group mineral, usually accompanied by brucite (Fig. F26). Where the original shape of the orthopyroxene grains is preserved, we identified bastitic serpentine pseudomorphs after orthopyroxene (Figs. F18, F19). Clinopyroxene and Cr spinel are the minerals least affected by serpentinization, but sometimes the latter is partially or even completely altered to magnetite. Frequently, magnetite is also present in veins as dustlike aggregates or rarely as small euhedral crystals, sometimes included in clinopyroxene. Amphiboles are found as orthopyroxene alteration products. They appear to have tremolite and/or anthophyllite composition and are usually <1% of the rock by volume.

Several generations of veins with variable size, mineralogy, and morphology are common in the harzburgites recovered at this site (Figs. F27, F28). Usually, a central vein with lizardite (antigorite?) mineralogy is crosscut by subsidiary fine veins of chrysotile (Fig. F29). Other veins contain secondary chlorite, magnetite, and associated scattered amphiboles. Magnetite is concentrated in the central part of the veins, in close association with chlorite and amphibole. Zones with a brownish tint in the thin sections may represent alteration of serpentine to clay minerals or brucite to hydromagnesite. Sample 195-1200A-11R-1 (Piece 5) contains not only the veining patterns and mineralogy described above, but also an additional vein with a quartz(?) ± brucite(?) ± serpentine(?) ± carbonate(?) and mica assemblage. This same vein material shows sutured grain contacts and local undulatory extinction, making the petrographic identification of this mineral assemblage difficult. In a few harzburgite samples (e.g., Sample 195-1200A-16R-1 [Piece 11B]), we observe almost completely serpentinized, rounded olivine grains included as chadacrysts within relatively fresh orthopyroxene grains, suggesting a cumulate origin (Fig. F30).

Serpentinized and Tectonized Dunites

The colors of the dunites range from very dark gray (N3) to dark bluish gray (5B 4/1), and the grain size is usually fine (0.01–1 mm). The primary mineralogy consists of olivine, orthopyroxene, and Cr spinel. The preserved amount of olivine = 3%–40%, orthopyroxene = 0%–1%, and Cr spinel = 1%–3%, whereas clinopyroxene is present only in trace amounts (<1%). The estimated primary mineral contents are olivine = 90%–98%, orthopyroxene = 0%–8%, Cr spinel = 1%–4%, and trace amounts of clinopyroxene (<1%). Since extensive deformation is present in all dunite samples, they may also be classified as serpentinized ultramafic mylonites. Microgranulation and kink banding in oliv-

F20. Hourglass and mesh textures, p. 83.

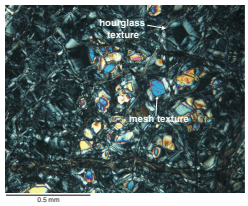

F21. Orthopyroxene with bastitic texture, p. 84.

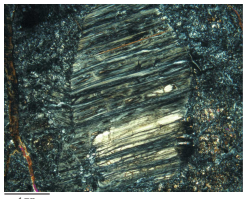

F22. Kink banding in olivine, p. 85.

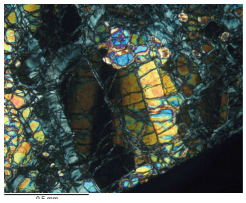

F23. Tectonized orthopyroxene showing undulatory extinction, p. 86.

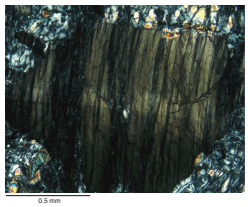

F24. Clinopyroxene included in orthopyroxene, p. 87.

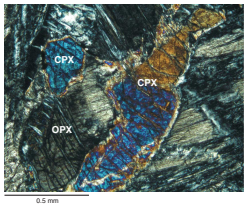

ine, bent cleavage planes and undulatory extinction in orthopyroxene, and granoblastic textures are widespread in all samples.

The recovered dunite clasts are all extensively serpentinized (60%–100%) and show mesh textures with hourglass extinction where olivine has been replaced by serpentine and brucite. The dunites are crosscut by several vein generations composed mainly of serpentine group minerals, chlorite, and magnetite (Fig. F28). Scattered amphibole grains (tremolite?) are present in small amounts. High concentrations of magnetite are seen in some veins. A brownish tint in the thin sections may be caused by alteration of serpentine to clay minerals.

Serpentinized and Tectonized Lherzolite

Only one lherzolite was recovered at this site. It is visually indistinguishable from harzburgite, having the same color, texture, and mineralogy. The only difference from the harzburgites is in the clinopyroxene content, as determined from thin section estimates and CIPW normative calculations. The relict mineralogy of the lherzolite sample (195-1200A-10R-1 [Piece 6A]) consists of olivine, orthopyroxene, and clinopyroxene in a 2:3:1 ratio. Based on the petrography, we estimate the original mineralogy of the sample as 67% olivine, 25% orthopyroxene, and 7% clinopyroxene. The opaque mineral, ~1% of the rock by volume, is Cr spinel. The estimated clinopyroxene content is also confirmed by the elevated Ca and Al content (see "Geochemistry of Serpentinites," p. 20) relative to the harzburgites (in the absence of carbonate minerals). The CIPW calculation gave 82% olivine, 11% orthopyroxene, and 7% clinopyroxene. The sample shows mesh and hourglass serpentine textures and contains a few thin veins of chlorite and serpentine. The degree of serpentinization is ~70%.

Sieved Grit-Sized Fraction from Holes 1200A and 1200B

A quantity of wash-core material contaminated by drilling muds was recovered from Hole 1200B. We wet sieved a portion of this material using 60-µm mesh sieves and dried the sample in an oven for several hours at 100°C. Then the material was further sieved to separate the >0.1-cm fraction. The largest fraction included grains of rock material, mineral fragments, and crystals that ranged from 0.1 to ~1.5 cm in size (grit). The grit was inspected under a binocular microscope and handpicked for discrete lithologies.

Whereas most of the sieved material consists of serpentine, it also contains several distinct lithologies of metabasites. These include crossite/white mica/chlorite schist (Fig. F31), chlorite schist (Figs. F32, F33), white mica schist, amphibole schist, glaucophane schist (Fig. F34), and, possibly, jadeite schist. Glaucophane schist (Fig. F35) is ~1% by volume, and the proportion of metabasic grit (including glaucophane schist) in relation to the remaining material is ~12% by volume. These lithologies are indicative of a high-pressure, low-temperature origin (Fryer et al., 1999). We interpret these small rock fragments as derivatives of metamorphosed basic rocks from the descending slab.

There is also a trace amount (<1%) of aragonite crystals in the grit-sized fraction (Fig. F11). These are commonly found at the seafloor, where rising pore fluids from the slab interact with seawater to precipitate carbonates. In gravity cores collected in 1997 (Fryer et al., 1999), there is a higher proportion of aragonite proximal to the mudline. The

F25. Cr spinel crosscut by serpentine veins, p. 88.

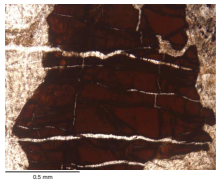

F26. Brucite showing reddish brown interference colors, p. 89.

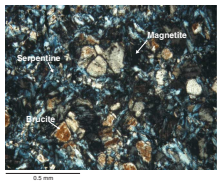

F27. Harzburgite showing a "Frankenstein"-like chrysotile serpentine vein, p. 90.

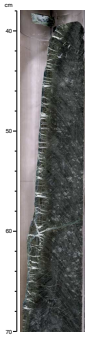

F28. Serpentinized dunite forming dark bands where completely altered, p. 91.

F29. Central vein of serpentine crosscut by finer veins of chrysotile, p. 92.

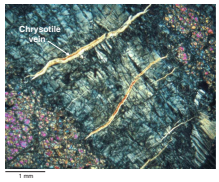

percentage of aragonite in the cores drops off with penetration to a level similar to that observed in the wash cores at the bottom of the gravity cores (0.10–0.20 mbsf in most cases) (see "Lithostratigraphy," p. 11).

The >0.1-mm-fraction of the sediment contains ~1% disaggregated grains of blue (sodic) amphibole (Fig. F36). Analyses of similar grains recovered in gravity cores from the same locality (Fryer et al., 1999) showed a crossitic composition, indicative of high-pressure, low-temperature metamorphism. The mineral grains show progressive zoning with blue rims and lighter blue-green cores. This suggests relatively rapid ascent within the rising serpentine muds at the site, as suggested by Fryer et al. (1999). The rationale for this interpretation is that if the grains had been in contact with rising fluids having the extreme compositions observed in the pore water analyses (see "Geochemistry," p. 29) for geologically significant periods, they would probably show retrograde metamorphic effects. None of the materials studied by Fryer et al. (1999) and Todd and Fryer (1999) have ever shown any mineral zoning indicative of retrograde effects. The mineral grains that we observe in the materials from Site 1200 also show no retrograde effects.

Although the wash core cannot be assigned a specific depth, we are confident that the lithologies present in the wash core are representative of the interval drilled in Hole 1200B. We also recovered serpentine muds in Section 195-1200A-15R-CC, and a portion was sieved and inspected for comparison with the wash core and the gravity cores described by Fryer et al. (1999). The materials in Section 195-1200A-15R-CC are similar in lithology and in proportions to those of the wash core sample and to the gravity cores investigated by Fryer et al. (1999) and Todd and Fryer (2000). We thus have data indicating that the high-pressure, low-temperature lithologies discussed above are present at Site 1200 to a depth of at least 147 mbsf.

We also have data suggesting that there is not much variation in the lithology of the serpentine matrix material. P. Fryer (pers. comm., 2001) has recovered pebble- to cobble-sized rock fragments of schists from dredges on South Chamorro Seamount, but the percentage of these compared to the other dredge samples recovered is <<1%. The lack of larger-sized rock fragments in the material drilled in Hole 1200A suggests that the metabasites are preferentially smaller pieces. The abundance of phyllosilicate minerals in the schists may contribute to the comminution of the protoliths as they rise from the source region. Pressure release as the rock fragments rise may cause the protolith to become more friable as the phyllosilicates expand. The continuous mechanical interactions within the rising muds may cause grinding and breakup of these more friable rocks into small fragments. We also note that the angularity of the serpentinized peridotites varies in a general way among the rocks that were recovered from cores in Hole 1200A. The smaller fragments are generally more angular than the larger ones, suggesting active breakup as the material rose in the conduit of the mud volcano.

The discovery of glaucophane schist in the grit-sized fraction of the serpentine mud from this site (Fig. F35) provides the strongest evidence yet obtained for the deep (slab) origin of the muds that are currently actively protruding at the summit knoll of South Chamorro Seamount. Unlike Conical Seamount, where only two metabasite fragments were found in six holes drilled, the site at South Chamorro Seamount provides a significant proportion of metabasites that allow the investigation of the paragenesis of the slab-derived lithologic fraction. It will be

F30. Poikilitic texture where orthopyroxene encloses olivine grain, p. 93.

F31. Mica-chlorite schist, p. 94.

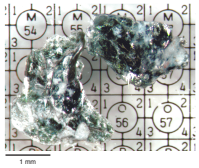

F32. Tremolite-rich chlorite schist in serpentine mud, p. 95.

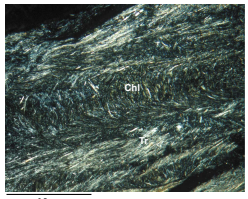

F33. Serpentine mud containing fragments of chlorite schist and altered serpentinite, p. 96.

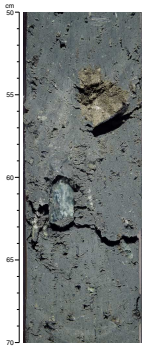

F34. Schists recovered from the wash material, Hole 1200B, p. 97.

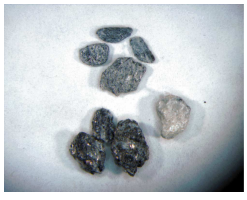

possible to determine the pressure and temperature ranges of the metabasites by shore-based investigations using microprobe techniques and micro-X-ray diffraction.

Preliminary examination of grit from the core catcher samples as well as leftover muds from physical properties (10-cm-long whole-round sections of the cores from Holes 1200D, 1200E, and 1200F) show a diverse assemblage of lithologies similar to those recovered from the wash material. However, the total volume of metabasite grit is less in these cores (5%–8%) than in the wash material (12%). The coarse mica schists are less abundant in Holes 1200D, 1200E, and 1200F (Fig. **F37**). There is a predominance of crossite/chlorite/white mica schist in all of the holes. In Section 195-1200D-8H-CC, an *Orbulina universa* test was found that has been completely replaced by and filled in with a magnetic mineral (iron sulfide). Fossils of various types and ages occur scattered throughout the cores (see **"Biostratigraphy,"** p. 21). The cores in the upper portion of Hole 1200D and most of the cores from Holes 1200E and 1200F were black, apparently from a reducing environment (they change color rapidly upon exposure to air) (Fig. **F38**). The replacement of the test by iron sulfide is, thus, not surprising. The surfaces of the grit-sized pieces of serpentinized ultramafic rocks were also black upon initial inspection.

Geochemistry of Serpentinites

Major, minor, and trace element contents of 27 representative samples of serpentinites from Site 1200 have been determined via ICP-AES analysis. The results are listed in Table **T3,** along with LOI and Mg number (= 100 × $Mg^{2+}/[Mg^{2+}+Fe^{2+}]$) values. Based on the olivine-orthopyroxene-clinopyroxene CIPW normative classification (Fig. **F39**) reported in Table **T3,** the serpentinite protoliths are dominantly harzburgites with minor dunites and one lherzolite, which is consistent with classification based on thin section observations. LOI values range from 11.3 to 18.2 wt%, with 14.2 wt% as the average for all serpentinites. The average Si/Mg ratio is 0.92, with both elements negatively correlated with the LOI values. The Mg-number values are high in all the rocks, ranging from 91.4 to 92.9. Our data reveal that the serpentinites are Mg rich, with Ni and Cr contents as high as 3700 and 3800 ppm, respectively. On average, the MgO, Ni, and Cr contents of the dunites are higher than in the harzburgites. Low CaO, Al_2O_3, and TiO_2 and high Ni contents (average Ni = 2645 ppm) confirm that most of the analyzed samples are highly residual. As in other suprasubduction zone mantle rocks (Pearce et al., 2000) the Mariana forearc serpentinites from South Chamorro Seamount preserve a record of extensive partial melting. To estimate the refractory nature of these mantle peridotites, we focused on the contents of CaO, Al_2O_3, and the Mg-number values. In both the CaO vs. Al_2O_3 and CaO vs. Mg-number diagrams (Fig. **F40**), the analyzed samples fall between the 15% and 30% melting lines, largely overlapping the fields of similar serpentinized ultramafic rocks from Conical and Torishima Seamounts drilled during Leg 125 (Ishii et al., 1992; Parkinson and Pearce, 1998; Savov and Ryan, unpubl. data). Thus, it appears that most ultramafic samples from Site 1200 have suffered 20%–25% melt extraction. The lherzolite sample shows a significantly lower degree of depletion, slightly higher than 15%. This is in agreement with its high clinopyroxene modal abundance (>5%) and 1 wt% higher CaO content relative to the average harzburgite.

F35. Glaucophane schist in serpentinite mud with serpentine and chlorite schist lithic fragments, p. 98.

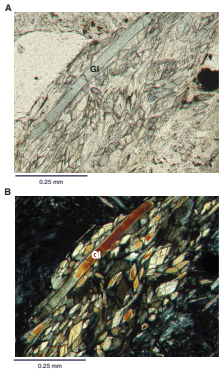

F36. Blue amphibole schist containing white mica and possibly chlorite, p. 99.

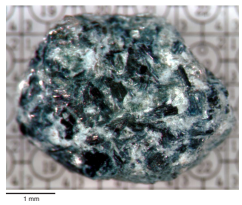

F37. Clast-poor blue serpentine mud, p. 100.

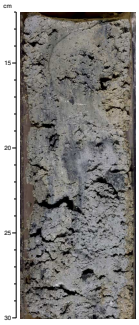

F38. Yellow-brown mud horizon reflecting the seawater-mud interaction, p. 101.

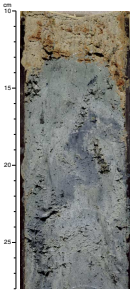

Overall, the trace element abundances of the South Chamorro serpentinites are similar to the values displayed by average serpentinites from Conical and Torishima Seamounts sampled during ODP Leg 125 at Site 780 (Fryer, Pearce, Stokking, et al., 1990), except for their higher Sr and Na and lower Ca and Al contents (Table T3).

BIOSTRATIGRAPHY

A total of six holes were drilled at Site 1200 on the summit of South Chamorro Seamount. Among the six holes, Holes 1200D, 1200E, and 1200F were drilled with the APC/XCB and yielded good recovery of serpentine mud in the depression on the summit. These three holes were examined for calcareous nannofossils. To further assess the nature of the nannofossil-bearing deposits, mud samples were also processed and examined for their foraminiferal contents.

In order to have a comprehensive account of the nature of the microfossil-bearing muds recovered at this site, this report includes a section documenting the foraminifers found in selected samples. A discussion of the depositional significance of both microfossil groups follows.

Calcareous Nannofossils

Hole 1200D

Rare but diversified and well-preserved calcareous nannofossils were found in the top 32 cm (0.32 mbsf) of Core 195-1200D-1H. The remainder of Core 195-1200D-1H is barren, except for traces of *Gephyrocapsa* in a poor state of preservation in Sample 195-1200D-1H-1, 51 cm (0.51 mbsf) (Table T4). Abundant *Emiliania huxleyi* is present continuously from the top of this hole to 0.32 mbsf, assigning the interval to Zone NN21 (<0.26 Ma). Besides *E. huxleyi, Gephyrocapsa oceanica, Umbellosphaera* spp., and *Umbilicosphaera sibogae* are the most common species. Other minor elements include *Syracosphaera* spp., *Helicosphaera carteri, Rhabdosphaera clavigera,* small *Reticulofenestra* spp., *Pontosphaera* spp., *Oolithotus fragilis,* small *Gephyrocapsa* spp., *Ceratolithus cristatus, Calcidiscus leptoporus,* and *Neosphaera coccolithomorpha* (roughly in descending order of abundance). These species are characteristic of upper water (0–100 m) communities of the subtropical Pacific (Okada and Honjo, 1973). The high abundance of umbelliforms (*Umbellosphaera tenuis, Umbellosphera irregularis,* and *R. clavigera*) and fewer placoliths indicates that the overlying surface water at this site is oligotrophic with low productivity (Young, 1994). The preservation of these dissolution-susceptible umbelliforms, together with the frequent occurrence of *Syracospheara* attests to the lack of differential dissolution and, therefore, good preservation of the assemblages. The absence of *Gephyrocapsa caribbeanica* in these samples further constrains the assemblages to Zone NN21, with an age younger than 0.27 Ma (Pujos, 1988).

Well to poorly preserved trace calcareous nannofossils were sporadically observed in the core catchers of Cores 195-1200D-1H to 6H (6.85–23.41 mbsf). The presence of *Coccolithus pelagicus, Reticulofenestra pseudoumbilicus,* and *Cyclicargolithus floridanus* appears to suggest that these specimens originated from pre-Quaternary sediments. However, the extreme rarity of nannofossils and the virtual absence of more definite and robust age-diagnostic markers (such as *Discoaster* and *Spheno-*

F39. CIPW normative compositions of serpentinites, p. 102.

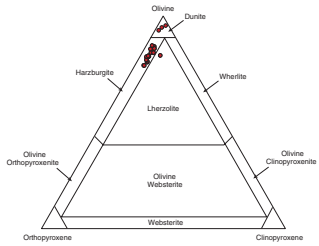

F40. Mantle peridotites from Conical, Torishima, and South Chamorro Seamounts, p. 103.

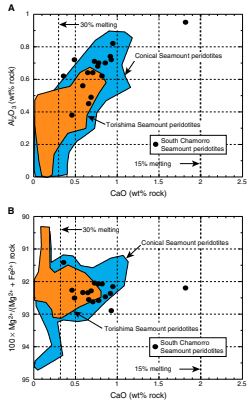

T4. Distribution of calcareous nannofossils, p. 152.

lithus, both common in low latitudes) hindered us from assigning firm ages to these samples.

Hole 1200E

Traces of well-preserved nannofossils were found in the core (Sample 195-1200E-1H-1, 0–10 cm). The assemblage is comparable to that found in the top of Hole 1200D and can be assigned to Zone NN21.

The rest of Core 195-1200E-1H and the entire Core 2H are virtually barren of nannofossils. In contrast, diversified but moderately preserved nannofossils in various degrees of abundance were recorded from several intervals of Cores 195-1200E-3H and 4H (11.11–13.07 mbsf) (Table **T4**). It is not clear whether the nannofossils persist throughout the entire 2-m section or are present sporadically in several separated intervals. These samples are characterized by a common and persistent occurrence of *Umbellosphaera* spp., *Umbilicosphaera sibogae,* and *Gephyrocapsa* spp., with less frequent *H. carteri, Syracosphaera* spp., and *R. clavigera*. Of great significance is the presence of abundant (~10%–20%) *G. caribbeanica,* which allows us to assign these samples to Zone NN20, with an age of 0.27–0.46 Ma. A high abundance of *G. caribbeanica* prior to the first occurrence of *E. huxleyi* has been documented quantitatively in the North Atlantic and the northeast Pacific (Su, 1996; Su et al., 2000). The acme of *G. caribbeanica* marks 0.268 Ma (Pujos, 1988).

Except for the great abundance of *G. caribbeanica* at the expense of *E. huxleyi,* the makeup of the assemblages is comparable to that found in the top sections of Holes 1200D and 1200F. Most of the specimens are overgrown with calcite, and thus, some of the specific diagnostic fine structures are obscured. The heavy encrustation of calcite on placoliths makes it difficult to identify whether *E. huxleyi* is present in the samples. Nevertheless, *Pseudoemiliania lacunosa* is still absent, constraining these samples to younger than 0.46 Ma in age.

Hole 1200F

The topmost interval of Core 195-1200F-1H (0–20 cm) contains rare, well to moderately preserved late Quaternary calcareous nannofossils (Table **T4**). *E. huxleyi* dominates the topmost two samples (195-1200F-1H-1, 0–0.5 cm, and 1H-1, 8.5 cm [0–0.085 mbsf]), probably because of the good preservation. Also common are members of *Umbellosphaera, Umbilicosphaera, Gephyrocapsa,* and *Syracosphaera*. Species of *H. carteri* and *C. leptoporus* are rare. With the addition of subordinate *O. fragilis* and *Pontosphaera* spp., the assemblages are similar to those found in the topmost section of Hole 1200D. Nannofossils occur continuously in the next two samples downsection (Samples 195-1200F-1H-1, 14 cm, and 1H-1, 20 cm), but the preservation deteriorates significantly. *E. huxleyi* is not identifiable, and dissolution-susceptible species, such as *Syracosphaera* spp. and *O. fragilis,* are absent. Except for the change induced by the poor preservation, the assemblage is comparable to that of the topmost samples of the section. Traces of nannofossils appear once again in Samples 195-1200F-1H-1, 66 cm, and 1H-1, 121 cm, consisting mainly of poorly preserved *U. sibogae* and *Umbellosphaera*. The absence of *P. lacunosa* once again suggests a late Pleistocene age (<0.46 Ma) for these samples.

Foraminifers

Hole 1200D

Abundant and well-preserved planktonic foraminifers were found in the topmost core (Sample 195-1200D-1H-1, 0–5 cm) (Table T5). Typical subtropical *Globigerinoides* plexus such as *Globigerinoides ruber, Globigerinoides sacculifer, Globigerinoides quadrilobatus,* and *Globigerinoides immaturus* dominate the faunal assemblage. Other common tropical-subtropical species are also present: *Orbulina universa, Globorotalia menardii,* and *Globigerinella aequilateralis,* with less common *Neogloboquadrina dutertrei, Sphaeroidinella dehiscens,* and *Zeaglobigerina rubescens*. The sample also contains rare (Table T5) *Globorotalia truncatulinoides,* which is age diagnostic of Zone N22 (Quaternary). Benthic foraminifers were also found in small quantities. The benthic foraminiferal assemblage shows a wide range of diversity; for instance, members of *Cibicidoides, Melonis, Fissurina, Lagena, Gyroidina,* and *Ehrenbergina* were found.

Comparable assemblages of planktonic foraminifers were found between 0.27 and 0.29 mbsf in the same section, but the abundance is much less and the preservation state also deteriorates. Only a few benthic foraminifers were spotted. The presence of *G. truncatulinoides* indicates that this sample belongs to Zone N22 (Quaternary). The rest of the hole is barren of foraminifers.

T5. Distribution of planktonic foraminifers, p. 154.

Hole 1200E

Only a few nannofossils were spotted in the smear slides of the topmost core (Sample 195-1200E-1H-1, 0–0.5 cm); however, a diversified planktonic foraminiferal assemblage was recovered. Despite lower abundance and poorer preservation, the assemblage is very similar to that of the top of Hole 1200D. *Globigerinoides* dominates the assemblage in association with other typical subtropical dwellers such as *G. menardii* and *O. universa* (Table T5). The abundance and diversity of benthic foraminifers decreases significantly compared to those from Hole 1200D. The rest of Cores 195-1200E-1H and 2H are barren of foraminifers.

Beyond our expectation, abundant planktonic foraminifers were found in Core 195-1200E-3H: Samples 195-1200E-3H-1, 12–17 cm (11.12 mbsf), 35–38 cm (11.35 mbsf), 77–82 cm (11.77 mbsf), and 3H-CC (12.06 mbsf). Foraminifers in the uppermost sample (195-1200E-3H-1, 12–17 cm [11.12 mbsf]) are more common and better preserved. This sample contains a few specimens of *Candeina nitida* and *G. truncatulinoides,* as well as a few well-preserved, orange, tiny *Z. rubescens*. The lower three samples show increasing degrees of differential dissolution. The lowermost sample (195-1200E-3H-CC [12.06 mbsf]) is so badly preserved that there is no sign of *Z. rubescens;* instead, *Globorotalia tumida,* the most resistant species, becomes common.

All four samples contain *G. truncatulinoides,* indicating a Quaternary age. A detailed examination of the makeup of the assemblages suggests changes related to surface-water conditions. All four samples contain more *G. menardii/G. tumida* and *G. truncatulinoides* and fewer *Pulleniatina obliquiloculata* than the other samples. The ratio of *G. menardii* to *P. obliquiloculata* has been used as an indication of the westward extent of eastern tropical Pacific water along the equator (Parker and Berger, 1971). Presumably, the western extension was strengthened during glacial periods. Indeed, it was found that increased abundances of *G. me-*

nardii relative to *P. obliquiloculata* occurred during glacial periods on the Ontong Java Plateau in the western equatorial Pacific (Yasuda et al., 1993). The increase of globorotalids in our record suggests that sediments in Core 195-1200E-3H were deposited during a cooler period than today.

Hole 1200F

Planktonic foraminiferal assemblages comparable to those in the top of Hole 1200E are also present in the top of Hole 1200F (Sample 195-1200F-1H-1, 14–19 cm [0.14 mbsf]), but in greater quantities (Table T5). A similar, moderately preserved assemblage was found in Sample 195-1200F-1H-1, 121–126 cm (1.21 mbsf); otherwise, downcore sections are barren. The Quaternary diagnostic species, *G. truncatulinoides,* is present in all foraminifer-bearing samples.

Discussion and Conclusions

The distribution of calcareous microfossils in the three examined holes is summarized in Figure F41. It appears that calcareous nannofossils and foraminifers are ubiquitous on the summit of the seamount, indicating that the surface of the summit is blanketed with recent pelagic biogenous sediments diluted by varying amounts of serpentine sediments. Holes that are farthest away from the active mud volcano conduit show less dilution with serpentine-bearing sediments and contain more abundant and diversified benthic foraminifers, such as those at the top of Hole 1200D. Apparently, the outflow of spring water and/or the outpouring of serpentine mud results in a hostile environment for benthic foraminifers.

Except for a few isolated nannofossils found in deep sections in Hole 1200D, all of the planktonic foraminiferal and nannofossil assemblages at Site 1200 are indicative of a late Quaternary age. Most samples contain good quantities of orange-pigmented *Z. rubescens* (except Sample 195-1200E-3H-CC because of strong dissolution/recrystallization), which indicates the freshness and young age of the samples (Parker and Berger, 1971). Nannofossils found in Core 195-1200E-3H appear to indicate an age older than 0.268 Ma, belonging to the upper part of Zone NN20, as indicated by the elevated abundance of *G. caribbeanica* (Fig. F42). The planktonic foraminifers in these samples consist of cooler subtropical dwellers, such as *G. truncatulinoides* and *G. menardii,* than samples from the first core and the uppermost cores of Holes 1200D, 1200E, and 1200F, implying cooler sea-surface conditions.

Detailed census data on nannofossil assemblages from Core 195-1200E-3H (Fig. F41) show a clear floral succession. The relatively high percentage of *G. caribbeanica* and decreased abundance of *Umbellosphaera* spp. in Sample 195-1200E-3H-1, 77–82 cm (11.77 mbsf), seems to indicate a cooler interval relative to others. Correspondingly, the planktonic foraminiferal assemblage also shows a relatively high frequency of *G. menardii* and *G. truncatulinodes* and an absence of *P. obliquiloculata,* indicative of a dominance of subtropical rather than tropical fauna. The succession shown by both foraminiferal and nannofossil assemblages attests strongly that these microfossils are in situ and represent a paleosurface deposit. At the same time, samples immediately below the top of Holes 1200D and 1200F (i.e., Samples 195-1200D-1H-1, 27–29 cm, and 195-1200F-1H-1, 14–19 cm) contain more warm-water dwellers such as *P. obliquiloculata* and fewer globorotalids

F41. Occurrence of nannofossils, p. 104.

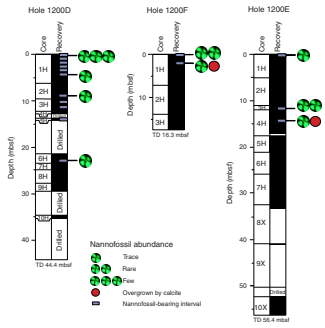

F42. Relative abundances of calcareous nannofossils, p. 105.

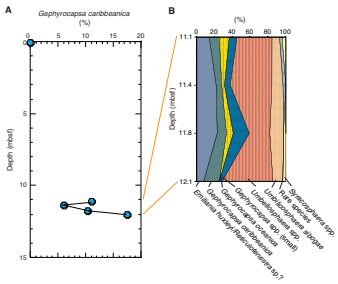

(Table T5). Such faunal and floral successions are evidence that these fossil horizons are in their original depositional sequence, reflecting climatic fluctuation during the late Quaternary. These fossil-bearing intervals were deposited when the mud volcano was more or less quiet. During these quiet periods, only small amounts of serpentine mud were brought to the seafloor surface; thus, the microfossil assemblages were less diluted and were preserved in their original depositional sequence.

The existence of paleosurfaces, where abundant calcareous microfossils are present, explains the high carbonate concentrations in the sediments at these intervals (see "Geochemistry," p. 29). However, preservation deteriorates rapidly downhole. Pore fluids apparently play an important role in dissolving the most susceptible delicate microfossils and in precipitating calcite on other robust ones. The tiny, orange *Z. rubescens* and other small, thin foraminiferal tests are considered to be the first victims of dissolution (Adelseck, 1978), whereas other less-susceptible forms were beneficiaries, exhibiting obvious signs of overgrown calcite. Microfossils in Core 195-1200E-3H display dramatic dissolution and overgrowth. For instance, pristine umbelliforms usually show faint shadows under crossed nicols, but the outgrowth of calcite causes them to show bright yellow birefringence. Planktonic foraminifers also show such distinct overgrowth to various degrees. Increased dissolution and overgrowth is manifested by the increasing dominance of *Globigerinoides conglobatus/G. immaturus* over *G. ruber* and the appearance of thick-tested *G. tumida* at the expense of *Z. rubescens* and *C. nitida*. Furthermore, in those intervals where foraminifers show moderate preservation (e.g., Samples 195-1200E-3H-1, 77–82 cm, and 195-1200F-1H-1, 121–126 cm), microscopic aragonite crystals are present, indicating oversaturation of Ca^{2+} and CO_3^{2-} in pore water and subsequent in situ precipitation. Nannofossils in these samples show significant recrystallization with excessive calcite on the surface as well as in the void spaces.

In summary, calcareous microfossils at Site 1200 suggest the following:

1. The summit of South Chamorro Seamount is blanketed with recent pelagic biogenous sediments mixed with serpentine sediments. Benthic foraminifers only survive in Hole 1200D, where dilution by serpentine mud and seepage of spring fluids is less intense (see "Lithostratigraphy," p. 11, and "Geochemistry," p. 29).
2. A paleosurface interval occurs at 11–13 mbsf in Hole 1200E. Microfossils in this interval may belong to Zone NN20, with an estimated age of 0.268–0.46 Ma. Microfossil assemblages in this interval show evidence of floral and faunal successions, indicating sequential in situ deposition during past cool and warm periods. This implies that there was a quiescent period of serpentine mud eruptions at Site 1200.
3. Microfossils in the buried paleosurface horizons show differential dissolution and overgrowth. Pore fluids that are oversaturated with carbonate ions play an important role in the dissolution and recrystallization of microfossils under chemical equilibrium. Most foraminifers and nannofossils are overgrown by recrystallized calcite at the expense of the most susceptible forms, such as *Z. rubescens,* which show evidence of dissolution.

PALEOMAGNETISM

The rock-magnetic and paleomagnetic investigations at Site 1200 were conducted to document the magnetic mineralogy, evaluate the potential contribution of serpentinized ultramafic rocks to the magnetic anomalies in forearc regions and the magnetic signatures of seamounts, investigate the magnetic properties of the serpentine sediments in comparison to the properties of the ultramafic parent rock, and potentially reorient the recovered rock fragments into a common reference frame. The process of serpentinization produces secondary magnetite by the alteration of primary olivine, orthopyroxene, clinopyroxene, and spinel. Because the composition and concentration of the iron oxide phase should be related to the degree of serpentinization, measurements of the magnetic properties of rocks and serpentine muds from Site 1200 may contribute to our understanding of the serpentinization process.

Magnetic properties and the potential contribution of serpentinized oceanic mantle rocks to magnetic anomalies have been examined by several investigators, including Stokking et al. (1990), Kelso et al. (1996), and Kikawa et al. (1996), and the magnetic properties of serpentinites from ophiolite complexes have been studied by Beske-Diehl and Banerjee (1980), Luyendyk and Day (1982), and Swift and Johnson (1984). However, with the exception of the study of Stokking et al. (1990), little is known about the magnetic properties of serpentinites in forearc settings.

Magnetic measurements (alternating-field [AF] demagnetization and magnetic susceptibility) were performed on 26 oriented ultramafic minicore and minicube samples from Hole 1200A, 4 unoriented samples originally taken for physical properties measurements, and 11 oriented cubes of serpentine sediment samples from Holes 1200D and 1200E. AF demagnetizations of discrete samples were routinely performed at steps of 0, 5, 10, 15, 20, 25, 30, 35, 40, 50, 60, 70, and 80 mT. The results of these measurements are displayed in Table T6. In addition, small rock chips were used to study thermal demagnetization of isothermal remanent magnetization (IRM), for IRM acquisition experiments, and measurements of the backfield coercivity of saturation remanence. To evaluate the significance and consistency of the characteristic remanent magnetization (ChRM) obtained from the ultramafic clasts, a 72-cm-long hard rock piece was stepwise demagnetized to 80 mT in 2-cm intervals.

T6. Rock-magnetic and paleomagnetic results, p. 155.

Rock-Magnetic Properties and Magnetic Mineralogy

Natural Remanent Magnetization and Susceptibility

The natural remanent magnetization (NRM) intensities of the ultramafic rocks range from 0.03 to 2.66 A/m (arithmetic mean = 0.49 A/m); values are displayed in Table T6 and Figure F43. These values are slightly higher but in a similar range as measurements reported in similar material from Conical and Torishima Forearc Seamounts by Stokking et al. (1990), which range from 0.01 to 0.59 A/m (arithmetic mean = 0.20 A/m). The volume magnetic susceptibilities of the serpentinites in Hole 1200A (Table T6; Fig. F43) range from 1.65×10^{-3} to 1.63×10^{-2} (arithmetic mean = 5.58×10^{-3}). These results are also very similar to the data from Conical Seamount (0.05×10^{-3} to 9.78×10^{-3}; arithmetic

F43. NRM, susceptibility, Koenigsberger ratio, and MDF plots, p. 106.

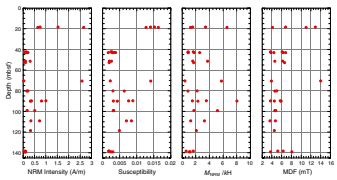

mean = 3.83×10^{-3}). Both the magnetic intensity and magnetic susceptibility are very high, and the positive linear correlation between both parameters (r = 0.73) suggests that both signals are dominated by the concentration variation of the magnetic carrier mineral.

The magnetic properties of the serpentine mud are similar to the properties of the parent rocks. The NRM intensity ranges from 0.15 to 0.95 A/m (arithmetic mean = 0.44 A/m), and volume magnetic susceptibilities vary between 2.32×10^{-3} and 1.18×10^{-2} (arithmetic mean = 6.81×10^{-3}).

Magnetic Carrier Mineral

The mineralogy of the phases that contribute to the magnetization and magnetic susceptibility was examined through magnetic studies, including AF demagnetization of the NRM and IRM, Curie temperature determinations, the acquisition of an IRM, and the measurement of the backfield coercivity of saturation remanence (B_{cr}).

Thermal demagnetization of a few selected rock chips shows a near-linear decrease of magnetic intensity between room temperature and ~500°C, above which the demagnetization rate increases (Fig. **F44**). All measured samples have Curie temperatures (T_c) of 585°C, which suggests that the dominant magnetic mineral is pure magnetite (T_c = 585°C). Minor substitution of other elements (e.g., Ti, Al, or Mg) decreases the Curie temperature of magnetite. No other sharp decrease in magnetization, which would suggest that another mineral is contributing to the NRM, occurs. Therefore, it is likely that very pure magnetite is the dominant carrier of remanence and susceptibility. The magnetite is predominantly a secondary mineral formed during serpentinization.

The samples that exhibit very uniform IRM acquisition behavior were saturated by 400 mT and have B_{cr} values of 12–58 mT (average = 25.3 mT) (Fig. **F45**), which are virtually identical to the B_{cr} values reported by Stokking et al. (1990) of 14–50 mT.

Koenigsberger Ratio

The Koenigsberger (Q_{NRM}) ratio compares the relative importance of the remanent magnetization with the magnetization induced in the formation by the Earth's magnetic field. Koenigsberger ratios were calculated using the following equation:

$$Q_{NRM} = M_{NRM}/(k \times H),$$

where

- k = the volume susceptibility and
- H = the value of the ambient geomagnetic field at Site 1200 (Merrill and McElhinny, 1983).

The value for H used is 31.83 A/m (40,000 nT). The Q_{NRM} ratio is used to determine whether the in situ magnetization of the crustal section is dominated by remanent magnetization ($Q_{NRM} > 1$) or an induced component parallel to the current field ($Q_{NRM} < 1$). The Koenigsberger ratios of the hard rock clasts (Table **T6;** Fig. **F43**) vary from 0.4 to 8.0 (mean = 2.4), indicating that the in situ magnetization of most of these rocks (26 out of 30) is larger than their induced magnetization. Thus, the in situ mag-

F44. Thermal demagnetization curves, p. 107.

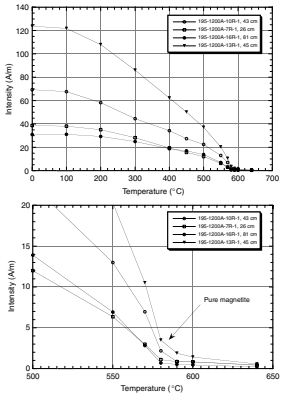

F45. IRM and backfield acquisition curves, p. 108.

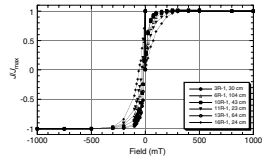

netization is dominated by remanent magnetization rather than an instantaneous magnetization induced by the Earth's magnetic field.

Demagnetization Character and Magnetic Remanence

The samples were easily demagnetized by AF techniques, as illustrated in Figures F46 and F47. The decay of remanent magnetization intensity during progressive demagnetization of most ultramafic clasts is very similar and displays little variability (Fig. F46). The median destructive field (MDF), the field required to reduce the NRM to one-half, is very low throughout the recovered section and ranges from 3.6 to 14.0 mT (average = 5.9 mT) (Table T6; Fig. F43). The MDF of the serpentine mud samples is extremely low and ranges from 2.5 to 3.7 mT (average = 2.8 mT). Subsequent to demagnetization, individual components of magnetization were identified for each sample using a least-squares fitting routine applied to each component of magnetization identified on a vector end point diagram.

Stable magnetic directions were determined for 17 of the 26 oriented hard rock samples and are displayed in Table T6. This component represents a chemical remanent magnetization acquired by magnetite particles as they formed during serpentinization (e.g., Stokking et al., 1990; Kelso et al., 1996). The stable component of magnetization decays to the origin of the vector end point diagrams in most cases. However, for a small number of samples, the stable component of magnetization did not decay to the origin. As expected from their emplacement history, serpentine muds did not display a stable magnetic component.

The AF demagnetization behavior of representative samples is illustrated in vector end point diagrams and shows three different types of behavior (Fig. F47). Type 1 samples have one single component of magnetization (Fig. F47A, F47B) that yields a stable magnetic direction, despite low MDF values. Type 2 samples display a ChRM with a soft overprint that is removed by a 10- to 15-mT field (Fig. F47C, F47D). It was not possible to determine a ChRM from Type 3 samples (Fig. F47E, F47F) or from serpentine muds (Fig. F47G, F47H). The results of the vector component analysis of the stable magnetizations are presented in Table T6.

Comparison between the demagnetization behavior of NRM and the saturation IRM (SIRM) was conducted to obtain initial information about the domain state of the magnetic carrier mineral (Fuller et al., 1988; Lowrie and Fuller, 1971; Stokking et al., 1990). The SIRM of serpentinized harzburgites is more stable during AF demagnetization than the NRM (Fig. F48), which suggests that multidomain magnetite dominates the magnetic properties. However, a certain number of pseudo-single domain–sized magnetite grains that are capable of carrying a stable magnetic remanence are apparently present, in addition to the multidomain magnetite.

The variability of the ChRM and the potential use of the ChRM to reorient individual rock pieces were investigated by stepwise demagnetization of one 72-cm-long piece of serpentinized harzburgite. The results of this test show a variation in declination between 150° and 330° and a variation in inclination between 38° and 84° at 20 mT over this short interval (Fig. F49). This demonstrates that the magnetization, which was acquired as a chemical remanent magnetization during serpentinization, was either acquired over a relatively long period of time or while the rock was being deformed and rotated. In addition, the degree of serpentinization within individual rock pieces can vary significantly (see

F46. Normalized NRM AF demagnetization curves, p. 109.

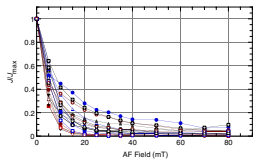

F47. AF demagnetization of serpentinized peridotite clasts and serpentine muds, p. 110.

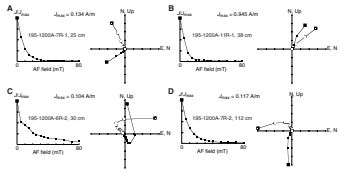

F48. AF demagnetization of NRM and saturation IRM of serpentinized harzburgite and serpentine sediments, p. 112.

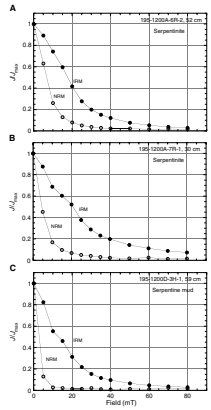

F49. Magnetic intensity, declination, and inclination in a single rock piece, p. 113.

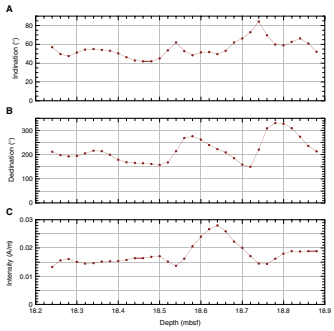

"Igneous and Metamorphic Petrology of Ultramafics," p. 16), which might contribute to the nonhomogenous magnetization. This result precludes the use of the ChRM as reorientation tool.

GEOCHEMISTRY

The first serpentine mud volcano drilled in the Mariana forearc was Conical Seamount, the summit and flanks of which were cored during ODP Leg 125 in 1989. The unusual interstitial waters recovered were inferred to be ascending from the décollement zone of the subducting Pacific plate, some 29 km below the seafloor (Mottl, 1992). The pore waters recovered from Site 1200 on the summit of South Chamorro Seamount are similar in many ways to those from summit Site 780 on Conical Seamount and doubtless have a similar origin, by dehydration and decarbonation of the crust of the downgoing slab (Fryer et al., 1999). The décollement is nearly as deep beneath South Chamorro Seamount, about 27 km, as beneath Conical Seamount. The South Chamorro Seamount fluids differ from those at Conical Seamount, however, in some significant ways, chiefly within the uppermost 20 mbsf. These differences apparently result from microbial activity within the shallow regions of the South Chamorro Seamount summit. There is also a macrofaunal community at the summit springs on South Chamorro Seamount (Fryer and Mottl, 1997), the likes of which was not seen during 21 dives in the manned submersible *Alvin* at Conical Seamount summit, in spite of the discovery of springs and chimneys there (Fryer, 1992a; Fryer et al., 1990, 1995). We detail here the chemistry of interstitial water, sediment, and headspace gas from Site 1200, which tell a coherent story about processes within and beneath the summit of South Chamorro Seamount.

Interstitial Waters

Interstitial waters were squeezed from serpentine mud from four of the six holes drilled at Site 1200 (Table T7). A fifth hole (1200C) yielded a single water sample from the open borehole at 30 mbsf and 2.69°C, which proved to be drill water (surface seawater), but that will be useful as a starting composition for long-term sampling by the osmotic sampler that was left in this cased, CORKed, and instrumented hole. The chlorinity of this sample is indistinguishable from that of two surface seawater samples taken on 18 and 23 March, which bracket the dates of sealing of this hole, and show no change in chlorinity over this time period. Only a single uncontaminated sample of interstitial water was recovered from Hole 1200A, but this sample from 71 mbsf proved to be the deepest we obtained. The other three holes produced multiple samples from which depth profiles could be constructed. Hole 1200E is located within 10 m of Hole 1200A and a spring identified by the presence of mussels, whelks, small tubeworms, galatheid crabs, and a dive marker left by M.J. Mottl on Dive 351 of the *Shinkai 6500* submersible in November 1996 (Fryer and Mottl, 1997). This spring was located during Leg 195 using the VIT camera mounted near the end of the drill string. As at Conical Seamount, the three known springs on the South Chamorro Seamount summit are cool, within a degree of the bottom-water temperature of 1.67°C. Temperature gradients estimated from Holes 1200E and 1200F are 0.0092 and 0.0724°C/m, respectively (Table T18), such that none of the interstitial water exceeded 3.0°C at the sam-

T7. Composition of interstitial water, p. 156.

pling depth (Table T7). Holes 1200F and 1200D are ~20 and 80 m north of Hole 1200E, respectively, and thus constitute a transect northward from the spring.

Chloride, Sulfide, Sodium, Alkalinity, and Sulfate: An Analytical Note

The data in Table T7 include chloride measured by ion chromatography (IC) as well as chlorinity measured by electrochemical titration with $AgNO_3$, which is normally a much more accurate and precise technique. A third column gives the preferred value for chloride; these values are those measured by IC except where titration chlorinity yielded smaller values. The reason for this somewhat unusual presentation is that many of the interstitial water samples from Site 1200 proved to have exceptionally high concentrations of dissolved sulfide, which would be present mainly as the bisulfide ion (HS^-) at pHs between 7.05 and 14 at 25°C. The high concentrations overwhelmed the technique intended to measure dissolved sulfide, colorimetry as methylene blue (Parsons et al., 1984). It was not feasible to bubble off this sulfide because of the risk of evaporation from the minuscule aliquots devoted to these analyses. From late in the sampling of Hole 1200E through Hole 1200F, therefore, we precipitated abundant dissolved sulfide from different aliquots using $HgCl_2$, $AgNO_3$, and Zn acetate to be measured on shore along with sulfur isotopic composition. In the meantime, we have estimated the dissolved sulfide concentration as the difference between chlorinity by titration and chloride by IC, as the latter measures only chloride and the former titrates bisulfide as well as chloride, bromide, and iodide (the usual contributors to chlorinity), according to the following reaction:

$$2AgNO_3 + 2HS^- = Ag_2S\downarrow + H_2S + 2NO_3^-.$$

Except for the 2 deep samples from Hole 1200A, 11 of the 17 samples from Hole 1200D farthest from the spring and the single uppermost samples from Holes 1200E and 1200F, chlorinity measured by titration exceeded chloride measured by IC, indicating the presence of dissolved sulfide (along with the putrid smell, the blackness of some of the core, and the abundant precipitate on addition of the reagents noted above, including a salt-and-pepper precipitate that formed during the chlorinity titration instead of the usual white AgCl precipitate).

We attempted to titrate the supernatant solution from above the Zn acetate precipitate (white colloidal ZnS) for chlorinity but determined that many ions co-precipitated with ZnS, including chloride, sulfate, Na, and K. Accordingly, the relatively imprecise (1%–2%) chloride data measured by IC proved to be our best estimate of the true chloride concentration for the 39 sulfide-bearing samples (of 54 total). Calculations of charge balance ($Na + K + 2Mg + 2Ca - Cl - 2SO_4$ – alkalinity) using the preferred chloride values and Na measured by IC showed that anions exceeded cations in 49 of 54 samples by an average of 2%. The charge imbalance results mainly from an overestimate of chloride; comparison with titration chlorinity from samples lacking dissolved sulfide suggests that the IC chloride data are too high by ~1%. Comparison of Na measured by IC with the Na concentration estimated from charge balance indicates that the IC Na values are too low by ~2%, almost half of which is due to the contribution from the overestimate of IC chlo-

ride to the calculated charge balance. For this reason, the calculated Na values are considered to be more accurate. Neither of these probable discrepancies from the true value is sufficiently large or certain to justify a correction, except that chloride measured by IC has been corrected downward by 1% in the calculation of dissolved sulfide concentrations only; without this correction, the concentrations of dissolved sulfide reported as near zero would become negative by 5 mmol/kg. Accordingly, the estimated uncertainty in the calculated bisulfide concentrations is 5 to 10 mmol/kg.

Bisulfide concentrations do not contribute to charge balance as calculated above because they are titrated by HCl and have already been counted in the alkalinity. The same is true for boron, which would be present entirely as borate ions ($B[OH]_4^-$) at a pH much greater than 9.3. Given the composition and high pH of the samples, the measured alkalinity results mainly from bisulfide, carbonate, and hydroxyl ions and their complexes, in that order, for the high-bisulfide samples, with a small contribution from borate. Oxidation of dissolved sulfide would potentially cause measured sulfate to be too high. To test for this possibility, we analyzed the supernatant solution from 18 samples from Holes 1200E and 1200D to which $AgNO_3$ had been added immediately upon recovery from the squeezer, prior to any exposure to the atmosphere. These supernatants yielded sulfate concentrations identical to those from the normal IC aliquots, indicating that sulfide oxidation had not affected the IC aliquots at the time of analysis and that the sulfate data reflect the actual concentration in the pore water at the time of sampling.

Results

The concentration of chloride in the interstitial water is lower than that in the bottom seawater by as much as 7% (Fig. F50) but not nearly as low as the minimum of 234 mmol/kg observed at Conical Seamount. Chloride exhibits a steep decrease within the uppermost 4.5 mbsf. Mottl (1992) interpreted the freshening and the steep surficial gradient at Conical Seamount to result from upward flow from great depth of an aqueous fluid derived from dehydration of the downgoing slab. The steepness of the surficial gradient implies upwelling at 1 cm/yr or more. The chloride maximum in Hole 1200D at 12 mbsf represents a significant deviation from an ideal one-dimensional advection-diffusion profile and probably results from lateral intrusion of seawater within the summit knoll; it corresponds to a depression in an otherwise ideal profile for Na (Fig. F50) that appears in both the Na calculated from charge balance and measured by IC. The chloride variations in Hole 1200D likewise appear in both the IC data, in replicate analyses, and in the chlorinity data determined by titration. Also reproducible was the chloride maximum in Hole 1200E at 20–25 mbsf, but this increase is within the imprecision of the IC method and is not matched by a deviation in Na. It is difficult to explain this latter maximum except as analytical imprecision.

Depth profiles of Na, Na/Cl, K, and B are near-ideal vertical advection-diffusion profiles that strongly support the inference of upwelling (Fig. F50). The curvature of the profiles implies that upwelling is fastest in Holes 1200E and 1200F near the spring and slowest in Hole 1200D farther away. As at Conical Seamount, these three elements, along with H_2O, are apparently strongly enriched in the upwelling deep slab–

F50. Cl, Na, K, and B in interstitial water, p. 114.

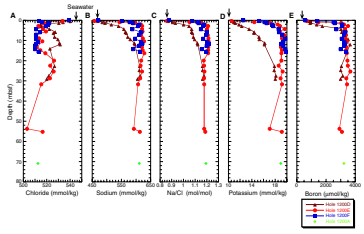

derived fluid. Except for H_2O, the degrees of the enrichments relative to seawater also agree well with those at Conical Seamount (Table T8).

The pH of the samples (Fig. F51), measured at 25°C, is as high as 12.5; along with the Site 780 samples from the Conical Seamount summit, these are the highest pH values ever measured in deep-sea pore water. The high pH results from equilibration of the solution with brucite and/or serpentine at low temperature, which requires an extremely low hydrogen ion concentration (i.e., high pH) at the low Mg concentrations observed. The depth profiles for pH resemble those for Na, K, and B and likewise indicate upwelling at different velocities for the three holes. The only major discrepancy from a typical advection-diffusion profile is the small maximum in pH at 4–9 mbsf in Holes 1200E and 1200F (which shows up better in a plot of hydroxyl ion vs. depth, not shown). This maximum corresponds to a similar maximum in alkalinity of 130 meq/kg at 3–16 mbsf (centered at 10 mbsf) in Hole 1200E near the spring (Fig. F51). At greater depths, alkalinity drops precipitously to 60 meq/kg, less than half the maximum and the same concentration to which alkalinity rises in distant Hole 1200D, without an intervening maximum. This value is also similar to the deep alkalinity at Site 780 on Conical Seamount (Table T8). The intermediate Hole 1200F shows a maximum of 112 meq/kg at 12 mbsf but did not penetrate deeply enough to exhibit the expected decline with increasing depth.

A shallow alkalinity maximum is a common feature in deep-sea pore waters where microbial sulfate reduction is oxidizing organic matter. It is typically accompanied not only by a decrease in sulfate but also by an increase in ammonium ions, which would dissociate to ammonia at the high pH of the Site 1200 solutions. All three features are found at Site 1200 (Fig. F51). Ammonia profiles with depth are quite similar to those for alkalinity, although the ammonia maximum at 3–16 mbsf in Hole 1200E is more clearly bimodal, with peaks at 2 and 9–13 mbsf. Below the maximum, ammonia decreases with depth to a concentration nearly identical to that in the deep pore water at Conical Seamount (Table T8). Sulfate decreases in all three holes and is essentially absent in Hole 1200E at the spring, between 2 and 20 mbsf. Below that depth, it increases back to seawater concentration. In the deepest sample, from 71 mbsf in nearby Hole 1200A, sulfate actually exceeds seawater concentration by 7% when adjusted to the chlorinity of ocean bottom water. Summit Site 780 at Conical Seamount also yielded sulfate-rich pore waters, with up to 1.7 times seawater concentration, even when uncorrected for seawater chlorinity. Sulfate in intermediate Hole 1200F decreases to nearly zero at 1 mbsf but then abruptly rebounds. It shows a second strong minimum at 14 mbsf. Distant Hole 1200D shows a pronounced minimum at 3 mbsf and a second minimum at 14 mbsf that would be even larger if this sample had not been contaminated by seawater during core recovery. At greater depth, sulfate rebounds to near seawater concentrations in this hole as well.

Microbial sulfate reduction produces dissolved sulfide that typically precipitates as metastable iron monosulfide minerals that eventually convert to pyrite. Dissolved sulfide, estimated as the difference between chlorinity measured by titration and chloride (adjusted) measured by IC, as discussed above, defines clearly bimodal maxima at the same depths as the extrema for alkalinity, ammonia, and sulfate (Fig. F51). These maxima reach very high concentrations in spring Hole 1200E and smaller maxima in successively more distant Holes 1200F and 1200D. Whereas the calculated concentrations have a large uncertainty (±5–10 mmol/kg), the shape of the profiles including the bimodality of

T8. Composition of pore water vs. seawater, p. 159.

F51. Composition of interstitial water, p. 115.

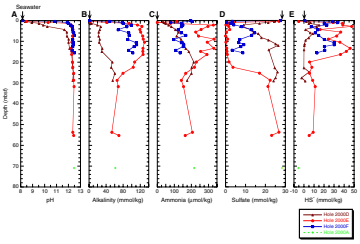

the peaks has been confirmed by semiquantitative estimates of the amount of ZnS and Ag_2S produced in the treated samples, as well as from the distribution of metal sulfide precipitates formed during colorimetric analyses for phosphate. The deepest sample, from 71 mbsf in Hole 1200A, shows no evidence of dissolved sulfide. At Conical Seamount summit, a single sample from 2.7 mbsf yielded a dissolved sulfide concentration of 2 mmol/kg (by methylene blue colorimetry), whereas samples from 3 to 35 mbsf in the same Hole 780D had concentrations below the detection limit of 0.25 mmol/kg.

Depth profiles of Mg, Ca, Sr, and Li are similar to one another (Fig. F52). All decrease sharply within 1–4 mbsf from the seawater value to low concentrations that persist to greater depth. The profiles are consistent with upwelling of a fluid that is highly depleted in these elements, with the fastest upwelling in Holes 1200E and 1200F near the spring and the slowest in Hole 1200D farther away. Depletion of these elements was also observed in the upwelling fluid at Conical Seamount (Table T8). The low concentration of Mg is typical of fluids in equilibrium with serpentine-bearing assemblages, such as the altered interstitial seawater recovered from serpentinite within Torishima Forearc Seamount, an inactive mud volcano in the Izu-Bonin forearc (Table T8). The low concentrations of Ca and Sr result from precipitation of $CaCO_3$ at the high observed alkalinity. Ca could not be detected by either titration or IC at the depth of the alkalinity maximum, but it rebounds to low values as the alkalinity decreases with depth. Ca and Sr in Hole 1200D, likewise, are higher where alkalinity is lower, except in the surficial carbonate precipitation zone discussed below. Li may be substituting for Mg and Fe in minerals of the serpentinite assemblage. It is the only one of the alkali elements to show depletion rather than enrichment relative to its concentration in seawater.

Mn is enriched near the seafloor as the sediment becomes reducing, but it decreases abruptly and drastically below 0.5–2 mbsf in the various holes (Fig. F52). As the sediment remains reducing below these depths, this drop is surprising. The decrease is probably not in response to carbonate precipitation, based on depth profiles from the inactive Torishima Forearc Seamount (Mottl, 1992); at the transition from pelagic sediment to serpentinite there, Mn plummets but Ca and Sr rise and alkalinity is little changed. Like Li, Mn may be substituting for Mg and Fe in minerals of the serpentinite assemblage.

Si and F (Fig. F53) both decrease sharply within the upper meter below the seafloor and then rebound just as sharply, especially in Holes 1200E and 1200F near the spring. Below that they fluctuate and decrease again to a minimum at ~15 mbsf in Hole 1200D and ~20 mbsf in Hole 1200E before converging toward intermediate concentrations in the deeper samples. The structure of these profiles, with multiple maxima and minima, indicates that these elements are highly reactive within the upper 20 mbsf and these reactions provide both sources and sinks at different depths. Al is generally low but appears to increase at depths below 20 to 30 mbsf.

Headspace and Core Liner Gas

The zone of complete sulfate reduction at 2–20 mbsf in Hole 1200E suggests the possibility of microbial methanogenesis within this zone. Samples of gas collected from the core liner immediately on recovery (Table T9) and from sediment plugs taken for headspace gas analysis (Table T10) show abundant methane as well as higher hydrocarbons,

F52. Mg, Ca, Sr, Mn, and Li in interstitial water, p. 116.

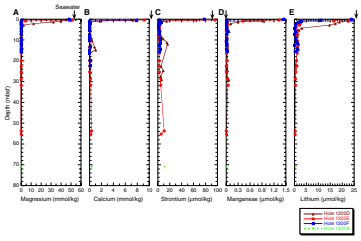

F53. Si, F, Fe, and Al in interstitial water, p. 117.

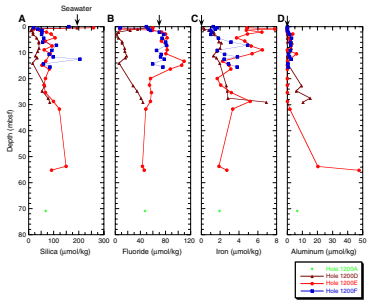

T9. Composition of gas pockets, p. 160.

T10. Composition of headspace gas, p. 161.

up to C_3 in the sediment, and C_6 in the core-liner gas, in each case the heaviest hydrocarbon detectable by the methods used. Whereas methane is generally in the range of 1–5 mM at this depth, there is no obvious peak in methane there (Fig. F54); instead, there are peaks above and below at the same depths as the extrema in dissolved sulfide, sulfate, and ammonia. There are small peaks in methane and ethane at 3 and 9–12 mbsf in Hole 1200E and much larger peaks at 1.5 and 14 mbsf in Hole 1200F; the latter depth produced the only detectable propane in the headspace gas samples. The C_1/C_2 ratio, moreover, increases with depth, suggesting selective consumption rather than production of methane at shallow depth.

The light hydrocarbon concentration range at South Chamorro Seamount is similar to that at Conical Seamount only when the hydrocarbon-rich flank Site 779 is included; there, the high concentrations are deeper than 200 mbsf. At the respective summit sites, South Chamorro Seamount has much higher methane and ethane at 1–20 mbsf (Fig. F54). The deeper fluids are more similar; methane is nearly identical, whereas ethane appears to be higher at Conical Seamount (Table T8). Another major difference is a larger and more rapid increase with depth in the C_1/C_2 ratio at South Chamorro Seamount, to 780 at 54 mbsf. At Conical Seamount summit Site 780, this ratio never exceeds 300, and at flank Site 779, it is higher in only two samples, from 227 and 266 mbsf.

F54. Hydrocarbons in interstitial water, p. 118.

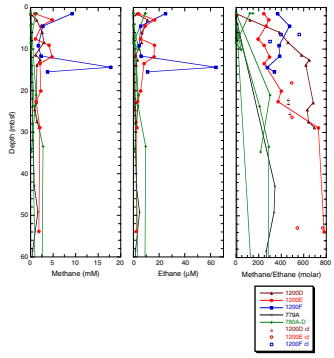

Sediment Chemistry

The steep gradients in pore water composition near the seafloor, where the deep upwelling fluid interacts chemically with overlying seawater, is a zone of intense reaction. The most obvious of these reactions is reflected in the bulk composition of the surficial sediment (Table T11). The H_2O that is bound into mineral structures is constant at 12–14 wt%, approximately the value in serpentine, over the depth interval sampled (Fig. F55). This percentage drops near the seafloor as other phases precipitate at this reaction front. Chief among them are aragonite, formed when the high-alkalinity, Ca-poor fluid from depth meets seawater, which has low alkalinity but plenty of Ca, and iron sulfides, formed from microbially produced dissolved sulfide. Bulk analyses of the serpentine mud show a large spike in $CaCO_3$ in the uppermost 2 mbsf to concentrations as high as 36 wt%. The same effect was seen at all the Conical Seamount sites (Mottl, 1992). At other depths $CaCO_3$ is <1%, except for two samples from 12 and 16 mbsf, which also have high sulfur. The presence of calcareous fossils at these two depths suggests that they represent a paleoseafloor surface that became enriched in $CaCO_3$ and S in the same manner as the present seafloor today but then was buried by serpentine mud protruded from the throat of the mud volcano. Calcareous fossils at this depth show the darkening typical of incipient pyritization. The sulfur content of the serpentine mud near the present seafloor spikes at 2.4 wt%, compared with concentrations of <0.01 wt% at greater depth. Between the surficial spike and the low values at depth, all three holes exhibit a plateau defined by an intermediate sulfur content of 0.2–0.3 wt%. This plateau extends as deep as 25 mbsf in Hole 1200E, but to only 5 mbsf in Hole 1200D. At Conical Seamount summit Site 780, by contrast, the highest S concentration measured in the mud was only 0.14 wt% and S generally was not detectable.

T11. CHNS and coulometric analysis, p. 162.

F55. CHNS and coulometric analyses, p. 119.

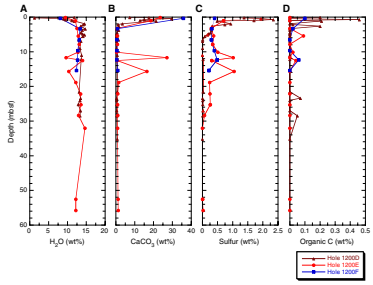

Organic carbon (Table T11; Fig. F55) was detectable in only 13 of the 49 samples of serpentine mud analyzed. Of these 13, nine had ≤0.1 wt%. The remaining four samples are all from the uppermost 2.7 mbsf of Hole 1200D, and the highest two values of 0.4–0.5 wt% are from the uppermost 0.75 mbsf. These organic carbon concentrations are lower than those from the summit Site 780 on Conical Seamount, which were typically 0.2 wt%, except for a similar enrichment to 0.56 wt% within the uppermost 2 mbsf.

Synthesis and Discussion of Chemical Data

The Deep Upwelling Fluid

The two major processes exhibited by the chemical data from Hole 1200A are upwelling of a fluid from a deep source and microbial sulfate reduction near the seafloor. Both processes are more active in Hole 1200E near the spring and become less so with increasing distance toward Hole 1200D. As was inferred by Mottl (1992) for Conical Seamount, the upwelling fluid can best be explained as originating at the décollement 26.5 km below South Chamorro Seamount summit by dehydration and decarbonation of the subducting Pacific plate. The upwelling fluid is quite similar to that at Conical Seamount for most components (Table T8), including its high pH; its enrichment in alkalinity, Na/Cl, K, B, ammonia, and hydrocarbons through C_6, all components that are virtually absent in depleted harzburgite and therefore require a different source; its depletion in Mg, Ca, Sr, and Li; and its low concentrations of Si, Mn, Fe, Ba, and phosphate. The South Chamorro Seamount fluid differs from that at Conical Seamount chiefly in its much higher chloride content, which is still 6% lower than in the ambient ocean bottom water, and its lower sulfate, which is still slightly higher than in seawater. As a result of its higher chloride, the South Chamorro Seamount fluid has more Na than seawater, whereas the Conical Seamount fluid has less, although both are highly enriched in Na relative to Cl and by approximately the same amount.

The deep fluids from Conical and South Chamorro Seamounts contrast markedly with the interstitial water recovered from Torishima Forearc Seamount, an inactive mud volcano in the Izu-Bonin forearc (Table T8) (Mottl, 1992). The Torishima Forearc Seamount pore water represents the end product of reaction between seawater and partially serpentinized harzburgite. Compared with the Conical and South Chamorro Seamount fluids, it is enriched rather than depleted in chloride, Na, Ca, and Sr and depleted rather than enriched in alkalinity, sulfate, K, and B. Its pH, at 9.6, is not nearly as high and its Na/Cl ratio is unchanged from seawater values. Its only resemblance to the slab-derived fluids is its low concentrations of Mg, Si, Fe, and Mn, and even then, Mn is considerably higher than at the active mud volcanoes. The Torishima Forearc Seamount pore water has lost some Li but not nearly as much as Conical and South Chamorro Seamounts. It also has substantially less ammonia, less methane by three orders of magnitude, and no higher hydrocarbons. The deep fluids at South Chamorro and Conical Seamounts certainly cannot have originated by simple reaction between ultramafic rock and seawater.

The deep fluids from South Chamorro and Conical Seamounts also differ from interstitial waters sampled from six other serpentine seamounts in the Mariana forearc that were gravity and piston cored in 1997 (Fryer et al., 1999). All these other seamounts are closer to the

Mariana Trench, such that the distance to the underlying décollement is correspondingly shallower, ranging from 16 to 25 km. Only the farthest from the trench, Big Blue Seamount, yielded pore waters depleted in Ca; the others showed large increases in Ca and decreases in alkalinity. Fryer et al. (1999) attributed this difference to depth-dependent decarbonation of the downgoing plate. If this interpretation is correct, it implies that the deep slab-derived fluids are continuously saturated with $CaCO_3$ during their ascent. If they originate deep enough that decarbonation reactions are active, they will be enriched at their source in carbonate alkalinity, which will drive down the Ca concentration, as in the South Chamorro and Conical Seamount fluids, by precipitation of $CaCO_3$. If not, they will be enriched in Ca, leached from noncarbonate rocks in the source region and during ascent, and become correspondingly poor in carbonate alkalinity. In either case, however, little $CaCO_3$ will actually form in the conduits, as one or the other of the components necessary to form $CaCO_3$ will always be in short supply. This supply shortage is only alleviated at the seafloor by the abundant Ca in seawater, which still cannot precipitate much carbonate from the shallower-sourced, alkalinity-poor fluids. Fryer et al. (1999) noted that only the most deeply sourced fluids, such as those at South Chamorro and Conical Seamounts, have produced $CaCO_3$ chimneys at the seafloor and the corresponding zone of aragonite precipitation in the surficial muds, as observed at Site 1200 (Fig. **F55**).

The much smaller decrease in chloride relative to seawater in the South Chamorro vs. Conical Seamount fluids could be explained if the conduits through which the deep fluids ascend were more mature (i.e., more pervasively altered) at Conical Seamount than at South Chamorro Seamount. Consider that these fluids ascend tens of kilometers through a matrix that consists mainly of partially serpentinized, depleted harzburgite. This rock is still undergoing serpentinization, which will consume H_2O and leave the remaining solution saltier, yet the fluid reaching the seafloor at both Conical and South Chamorro Seamount summits remains fresher than seawater, as measured by chloride content (but not by total equivalents of cations or anions, which are 4% higher in the South Chamorro Seamount deep fluid than in seawater vs. 47% lower in the Conical Seamount fluid). How fresh must surely be a function, in part, of how much serpentinization the fluid has effected during its ascent, which depends in turn on how much fresh harzburgite the fluid has encountered. A more thoroughly altered conduit, as hypothesized for Conical Seamount, would deliver a fresher fluid to the seafloor. In this scenario, the higher sulfate in the Conical Seamount fluid could also result from less reaction; perhaps the greater serpentinization accomplished by the South Chamorro Seamount fluid also involved greater loss of sulfate, presumably by reduction to sulfide. It is well known that serpentinization generates extreme reducing conditions by oxidation of ferrous iron in the primary ultramafic minerals to ferric iron in magnetite. As the deep fluids ascending beneath Conical and South Chamorro Seamounts appear to have little or no dissolved sulfide, this reaction product would have to have precipitated as pyrite or some other sulfide mineral within the conduit. Of course, this hypothesis does not explain how the fluids acquired their high sulfate content in the first place.

The ultimate freshness of the fluid must also be a function of its original salinity. We do not know the chlorinity of the fluid at its source, but if it originates by dehydration of various minerals, it is not incon-

ceivable that it is essentially fresh. The probable source of chloride is mixing with seawater-derived pore solutions, most likely by dewatering of sediment and basement pore solutions (as opposed to dehydration of minerals) at the décollement but possibly also by admixture of downwelled seawater during ascent. The biggest problem is in explaining the extreme enrichment in some other major components, especially Na, sulfate, and alkalinity. In both the South Chamorro and Conical Seamount fluids, Na is so enriched as to be nearly the only cation (along with a much smaller amount of K) and its concentration exceeds that of chloride by 20%–40% (Table T8), much more than the sum of cations exceeds chloride in seawater (11%). Sulfate is barely enriched at South Chamorro Seamount, but the sulfate-rich fluid at Conical Seamount requires a major source. Substantial (chiefly carbonate) alkalinity has been added to both fluids. The sources of these components are unknown in detail, but given the relative chemical simplicity of the depleted harzburgite in the overriding plate through which the solutions ascend and react, the only real candidate is the sediment and altered basalt at the top of the subducting plate.

Microbial Activity within the Shallow Subsurface

Although the composition of the deep upwelling fluids is generally similar, at 0–20 mbsf the compositions of the interstitial water, headspace gas, and surficial sediment at South Chamorro Seamount summit all differ considerably from those at Conical Seamount. All of the differences can be attributed to microbial activity within the uppermost 20 mbsf at Site 1200. This activity is remarkable, considering the prevailing pH of 12.5; this is clearly a community of extremophiles. The zone of zero sulfate at 2–20 mbsf in Hole 1200E requires that sulfate is being actively reduced at two depths, one just above the zone of sulfate exhaustion and the other just below it. The presence of two such zones is confirmed by the data from Holes 1200D and 1200F, which clearly show two sulfate minima, the first at 1–3 mbsf and the second at 14 mbsf. The sulfate maximum that lies between these minima in both holes will eventually be erased by diffusion unless it is externally supplied. In Hole 1200D this maximum lies at 12 mbsf, the same depth as the chloride maximum attributed earlier to a lateral incursion of seawater. In Hole 1200E, however, there is no evidence of such an incursion, and it is likely that this maximum is unsupported; the depth profile is thus non–steady state and implies that sulfate reduction was initiated relatively recently in this hole.

In most marine sediments, once dissolved sulfate goes to zero with depth, as in Hole 1200E, it stays there, as there is usually no deeper source of additional sulfate. The only previously identified exceptions are young ridge flanks, such as the eastern flank of the Juan de Fuca Ridge drilled during ODP Leg 168, where unaltered seawater downwells through basement outcrops and flows laterally, carrying a new supply of sulfate to the base of the sediment column, and settings such as Middle Valley, drilled during ODP Leg 139, in which previously deposited gypsum or anhydrite is redissolving in the sediment, thereby supplying sulfate to the interstitial water. Site 1200 represents a third case, in which sulfate is being supplied by upwelling of sulfate-rich water from a deep slab source. The two depths of sulfate reduction in the holes at Site 1200, therefore, each have a different source of sulfate; the upper level is supplied by downward diffusion of seawater sulfate, against advective upwelling, whereas the lower level is supplied by ad-

vection of sulfate from a deep source below. These different supplies should be reflected in the sulfur isotopic composition of the sulfide produced. Mottl and Alt (1992) found that the $\delta^{34}S$ of dissolved sulfate in the deep fluid from Conical Seamount Site 780 was 14‰ ± 1‰, considerably lighter than the value of 20.5‰ in seawater and suggestive of a contribution from a basaltic source. (By contrast, pore water from serpentinite within the inactive Torishima Forearc Seamount yielded $\delta^{34}S$ values as high as 31.2‰, suggestive of a residue from microbial sulfate reduction.)

The products of sulfate reduction by oxidation of organic matter include carbonate alkalinity, dissolved sulfide, and ammonia. These products tend to exhibit maxima corresponding to those of the sulfate minima (Fig. **F51**), confirming that there are upper and lower zones of microbial sulfate reduction. The simplified reaction is usually written as follows:

$$2CH_2O + SO_4^{2-} = H_2S + 2HCO_3^-.$$

This reaction produces two equivalents of (carbonate) alkalinity. At the high pH of the present solutions, the reaction is more appropriately written as follows:

$$2CH_2O + SO_4^{2-} + 3OH^- = 2CO_3^{2-} + HS^- + 3H_2O.$$

This reaction also produces a net of two equivalents of alkalinity, the difference between four equivalents of carbonate plus one of bisulfide alkalinity produced vs. three of hydroxyl alkalinity consumed. Because this reaction consumes hydroxyl, effectively producing hydrogen ions, it cannot cause the pH maximum observed in Holes 1200E and 1200F. The most likely hydroxyl-generating reactions involve dissolution of Fe-bearing minerals in the serpentinite, giving rise to the observed maximum in dissolved Fe within the uppermost 10 mbsf (Fig. **F53**). The likely candidates are magnetite and the ferrous silicate components in olivine and orthopyroxene. At high pH, these reactions are as follows:

$$4Fe_3O_4 + HS^- + 11H_2O = 12Fe^{2+} + SO_4^{2-} + 23OH^-,$$

$$Fe_2SiO_4 + 2H_2O = 2Fe^{2+} + SiO_{2(aq)} + 4OH^-, \text{ and}$$

$$FeSiO_3 + H_2O = Fe^{2+} + SiO_{2(aq)} + 2OH^-.$$

The dissolution of magnetite is probably the predominant reaction because secondary magnetite is abundant in the altered rock, and its dissolution produces by far the most hydroxyl ions per mole of starting phase. As this reaction involves reduction of Fe and oxidation of dissolved sulfide, it is almost certainly microbially mediated.

So far, we have assumed that the microbiota are consuming normal organic matter in the process of reducing dissolved sulfate. Yet, this is not normal deep-sea sediment; the organic carbon content of partially serpentinized, depleted harzburgite squeezed up from below is essentially zero. As noted earlier, it could not be detected in 36 of 49 samples analyzed. Values exceeding 0.1 wt% were found only in the uppermost 3 mbsf. What, then, are the microorganisms eating? The answer must be that the ultimate source is the C_1 through C_6 hydrocarbons supplied with the deep upwelling fluid. Whereas methane can be biogenic, these

higher hydrocarbons can only be thermogenic and, thus, must have a deep source. The reaction at high pH can be written as follows:

$$CH_4 + SO_4^{2-} + OH^- = CO_3^{2-} + HS^- + 2H_2O.$$

These simple hydrocarbons contain no nitrogen, however. This, too, must ultimately be supplied from depth, in the form of ammonia in the deep fluids. Once a microbial fauna has been established that utilizes these resources, it can intercept the organic carbon and nitrogen streaming in with the ascending fluid and effectively trap them within the ecosystem, where they can be recycled and continually enriched. This process may explain the enrichment in organic carbon in the uppermost sediment (Fig. **F55**). The molar ratio of organic carbon (methane) to nitrogen (ammonia) supplied by the deep fluid is ~8 at both Conical and South Chamorro Seamounts (Table **T8**). This compares with the Redfield ratio of 106/16 = 6.6, implying that the deep fluids represent a good food source for the microbiota. The CH_4/NH_3 molar ratio within the alkalinity maximum at 2–10 mbsf in Hole 1200E ranges from 4 to 16 and averages 11 (average = 10 for all of Hole 1200E). These values are similar to both the Redfield ratio and the ratio in the supply and are consistent with a deep source for C and N in this ecosystem.

Most of the dissolved sulfide generated by these reactions surely precipitates as the iron sulfides that blackened the cores from Holes 1200E and 1200F. The plateau of sulfur enrichment in the mud extends to 25 mbsf in Hole 1200E at the spring to at least 15 mbsf in Hole 1200F, but to only 5 mbsf in the distant Hole 1200D (Fig. **F55**). The highest sulfur enrichments, however, are restricted to the uppermost 2 mbsf, where the gradients in both dissolved sulfide (Fig. **F51**) and Fe (Fig. **F53**) are steepest, presumably because upwelling of the fluid compresses the gradients at the seafloor. (Mn gradients are also steepest in this chemically reduced interval, implying strong redox gradients.) This combination of dissolved species would precipitate abundant iron sulfides according to the following reaction:

$$Fe^{2+} + HS^- = FeS\downarrow + H^+.$$

Why are there such active communities of both micro- and macrobiota at the South Chamorro Seamount summit and apparently none at Conical Seamount? The macrofauna almost certainly depend on the microbiota for their existence. The overall fluid flow rates are not obviously dissimilar at the two sites, and the organic carbon and ammonia content of the fluids are virtually identical (Table **T8**), implying a similar food supply. Although the drill holes at Site 780 were not located at any known spring, upwelling velocities of 1 cm/yr were documented there from the curvature in the chlorinity-depth profiles (Mottl, 1992). On the other hand, even Hole 1200D, the most distant from the South Chamorro Seamount spring, has three times the concentration of methane within the uppermost 10 mbsf that Site 780 has on Conical Seamount (Fig. **F54**). (This higher methane, however, is probably more an effect of the microbial activity than a cause, if, in fact, these materials are recycled within the community.) At present, this question is unanswered. Perhaps the lower salinity of the Conical Seamount fluids (410 mmol/kg total equivalents of cations or anions compared with 604 mmol/kg in the bottom seawater and 630 mmol/kg in the South Chamorro Seamount deep fluid) inhibits microbial colonization and

growth. Perhaps there are similar communities on Conical Seamount that have just not been discovered yet. It is a large seamount, and 21 *Alvin* dives could cover only a small fraction of even its summit area.

PHYSICAL PROPERTIES

Hole 1200A

All whole-round core samples from Hole 1200A longer than 40 cm were run through the multisensor track (MST). RCB drilling in Hole 1200A recovered mainly hard rock sections with a diameter of ~5.75 cm, smaller than the nominal 6.6-cm core diameter. The reduced core diameter required corrections of the values measured by the MST. The values in the database do not reflect these corrections, but the data in the figures presented below have been corrected.

The natural gamma ray (NGR) count rates were corrected for the reduced sample volume using the following equation:

$$NGR_{corr} = [(6.6)^2/(5.75)^2] \times NGR_{meas}.$$

Gamma ray attenuation (GRA) bulk density values were corrected for the smaller core diameter using the following equation:

$$\rho_{corr} = (6.6/5.75) \times \rho_{meas},$$

where ρ = bulk density.

Magnetic susceptibility (MSL) measurements were made on the MST using the archive half of all of the split core sections from Hole 1200A at 2-cm sample intervals. The following equation is used to convert measured values from the MSL into SI volume susceptibility; a correction factor of 0.46, provided by the instrument manufacturer (Bartington), is used to account for the reduced core volume. Bartington provides correction factors that assume the sample is in the form of a cylinder. A Bartington correction factor of 0.46 assumes that the split core section has the same magnetic susceptibility as a cylinder with half the cross-sectional area of a full core with a diameter of 5.75 cm:

$$M_{corr} = (M_{meas}/0.46) \times 10^{-5},$$

where M = magnetic susceptibility.

The *P*-wave velocity logger (PWL) provided no sensible data in Hole 1200A because of the lack of acoustic coupling between the core and the liner.

Results from the corrected MST runs are presented in Figure **F56.** Index and physical properties measurements, made using discrete samples of clasts and, where possible, matrix material, are presented in Tables **T12** and **T13.**

Volume Magnetic Susceptibility

Volume magnetic susceptibility values derived from the MSL (Fig. **F56A**) show wide scatter, >1000 × 10^{-5} (SI units) along the length of most core sections. The scatter in susceptibility values could be the result of gaps in the core, which are not corrected for in our determination of volume magnetic susceptibility. These gaps will reduce the vol-

F56. Magnetic susceptibility, bulk density, and natural gamma radiation, Hole 1200A, p. 120.

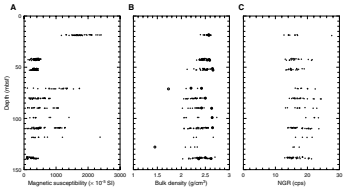

T12. Index properties of discrete samples, Hole 1200A, p. 163.

T13. Physical properties, Hole 1200A, p. 164.

ume magnetic susceptibility. The scatter is significantly lower in measurements from Cores 195-1200A-6R (41.40–51.10 mbsf), 7R (51.10–60.70 mbsf), and 16R (137.60–147.20 mbsf), which exhibit lower susceptibility values than other cores.

Density

The mean bulk density of the clasts from Hole 1200A, derived from index properties measurements, is 2.52 g/cm³. Density measurements made with the GRA are consistently less than or equal to index properties bulk density measurements from the same depth interval (Fig. F56B). The discrepancy between these two measurements is likely caused by the presence of fractures in the core. The index properties samples were taken from unfractured sections of clast material. Fractures present in cores from Hole 1200A result in a reduced apparent bulk density. Density measurements from the GRA of <2.0 g/cm³ have been deleted from Figure F56B because it is unlikely that any igneous or metamorphic rock has a density lower than this value (Telford et al., 1976). The index properties bulk density values represent the true bulk densities and represent the maximum values that the GRA would measure on complete, unfractured whole-round core.

P-Wave Velocity

P-wave velocity was measured on discrete samples of clast material, cut into ~2-cm cubes with faces oriented perpendicular to the x-, y-, and z-axis of the core (Fig. F57). Measured velocities range from 3.80 to 5.48 km/s (mean = 4.89 km/s). For each sample, with the exception of Sample 195-1200A-11R-1, 57 cm (89.97 mbsf), the difference in the velocity measured along each axis is considered below the error level. Sample 195-1200A-11R-1, 57 cm (89.97 mbsf), exhibits a >10% variation in velocity between the velocities measured parallel to each axis. This sample, which exhibited a distinct fabric, was identified as dunite and was the only sample of this lithology to be tested.

Figure F58 shows a plot of *P*-wave velocity vs. density for clasts from Hole 1200A. As shown by many investigations (e.g., Miller and Christensen, 1997), *P*-wave velocity tends to increase with density.

Thermal Conductivity

Thermal conductivity measurements were made on every clast piece in every core section and, where possible, in the matrix (Fig. F59A). Thermal conductivity values from the clasts vary between 1.66 and 2.85 W/(m·K) (mean = 2.21 W/[m·K]) (Fig. F59). Only a single thermal conductivity measurement could be made in the matrix material from Hole 1200A, and this gave a value of 0.37 W/(m·K) at a depth of 127.9 mbsf. Thermal conductivity values for the clast material from Hole 1200A are, on average, slightly lower than those obtained at ODP Site 780 (Shipboard Scientific Party, 1990a).

Holes 1200D, 1200E, and 1200F

MST measurements were performed on all whole-round core samples from Holes 1200D, 1200E, and 1200F. The results are presented in Figures F60, F61, and F62. Index and physical properties are presented in Tables T14, T15, and T16. APC core samples were affected by gas ex-

F57. *P*-wave velocity and mean velocity distribution, Hole 1200A, p. 121.

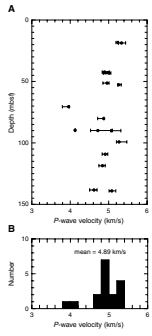

F58. *P*-wave velocity vs. bulk density, Hole 1200A, p. 122.

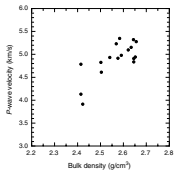

F59. Thermal conductivity, Hole 1200A, p. 123.

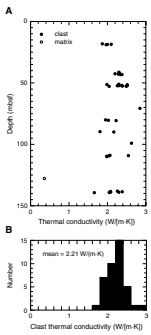

F60. MST results, Hole 1200D, p. 124.

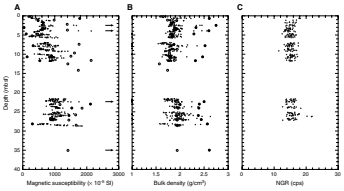

F61. MST results, Hole 1200E, p. 125.

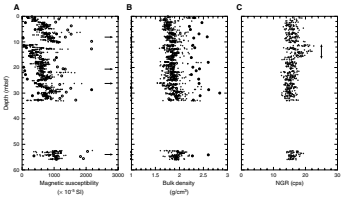

pansion within the core liner, forming gas voids up to 2 cm wide. The voids reduce magnetic susceptibility values by a small amount at a distance of ~10 cm on either side of the void. Removal of the effect of the voids proved difficult and largely unnecessary, and attempts to do so were abandoned. GRA density values are reduced almost to zero by the presence of a void, but only at a distance of up to ~2 cm from the void. The locations of wide (>0.5 cm) voids, visible through the core liner, were recorded and used to edit the data. Anomalously low density values (<1.0 g/cm^3 or obviously outside the local trend) were eliminated from the GRA data set by hand.

Although the core liners were mostly full, the PWL was unable to obtain *P*-wave velocity measurements. Discrete *P*-wave velocity measurements using insertion transducers (PWS1 and PWS2) on split core samples were also unsuccessful. This is attributed to high signal attenuation, probably caused by the occurrence of small gas-filled fractures.

Volume Magnetic Susceptibility

The volume magnetic susceptibility in Holes 1200D, 1200E, and 1200F generally increases with depth, from ~100 × 10^{-5} to ~1000 × 10^{-5} (mean = 779 × 10^{-5}). However, there are distinct drops in susceptibility in Holes 1200E and 1200F at ~11 mbsf. The drop in susceptibility coincides with an increase in gamma ray counts in Hole 1200E. A similar anomaly is not observed at the same depth in Hole 1200F.

In addition to the MSL measurements, discrete volume magnetic susceptibility measurements were made on the same clast and matrix samples used for index properties measurements (Tables **T14, T15**). The volume magnetic susceptibility for discrete samples is calculated using the grain volume. A Bartington MS1B meter, calibrated to measure volume susceptibility for a 10-cm^3 sample, was used to obtain three measurements for each sample, from which the mean was calculated. The susceptibility values are corrected for the dry sample volume (V_{samp}) using the following equation:

$$M_{corr} = (10/V_{samp}) \times M_{meas},$$

where M = volume magnetic susceptibility.

The volume magnetic susceptibility of discrete matrix samples varies between 255 × 10^{-5} and 2541 × 10^{-5} (mean = 1347 × 10^{-5}). The clast material exhibits a wider range of magnetic susceptibilities than the matrix, between 30 × 10^{-5} and 13,738 × 10^{-5} (mean = 2220 × 10^{-5}). The magnetic susceptibility of discrete matrix samples is higher than the whole-core susceptibility. Whole-core measurements include a water volume of ~27%, which contributes little to the magnetic susceptibility; the MST volume magnetic susceptibility values should be increased by nearly 40% to be comparable to the values obtained for discrete matrix samples that contain no water.

Although there may be a systematic relationship between magnetic susceptibility and clast lithology (Table **T14**), the number of samples for many lithologies is too small for meaningful statistical analysis. However, the distribution of matrix and clast susceptibilities (Fig. **F63**) shows that, with the exception of a few clasts with extremely high magnetic susceptibilities, the dominant carrier minerals of the magnetic susceptibility are concentrated in the matrix material of the serpentine muds. This is consistent with shipboard observations of increased mag-

F62. MST results, Hole 1200F, p. 126.

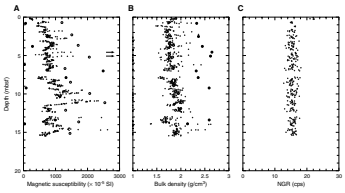

T14. Index properties of clast material, Holes 1200D, 1200E, and 1200F, p. 165.

T15. Index properties of matrix material, Holes 1200D, 1200E, and 1200F, p. 166.

T16. Physical properties, Holes 1200D, 1200E, and 1200F, p. 167.

F63. Distribution of magnetic susceptibility, Holes 1200D, 1200E, and 1200F, p. 127.

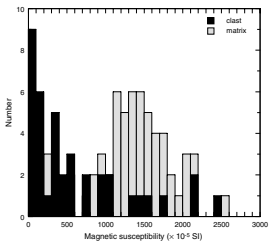

netite along fragile serpentine-filled veins in the clasts from Site 1200 (see "Structural Geology," p. 52).

Density

Bulk density measured by the GRA densitometer increases from ~1.75 at the seafloor to ~2 g/cm³ at 50–60 mbsf. The mean bulk density derived from index properties measurements on matrix material is 1.87 g/cm³, consistent with the whole-core bulk density measurements. The mean bulk density of clast material is 2.45 g/cm³, significantly higher than the matrix density. The grain density derived from index properties samples is similar for both clast and matrix samples (Fig. F64). The mean grain density for both the clast and matrix material is the same (2.64 g/cm³), which is consistent with the matrix being formed by the mechanical deformation of clast material.

F64. Distribution of grain density, Holes 1200D, 1200E, and 1200F, p. 128.

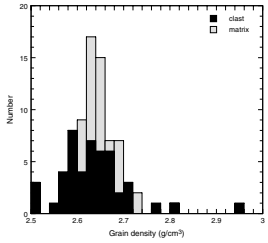

Natural Gamma Ray

Natural gamma ray emissions are nearly constant for all holes at ~15 counts per second. However, there is one notable gamma ray anomaly around 11–17 mbsf in Hole 1200E that coincides with a carbonate interval (see "Lithostratigraphy," p. 11); the top of this interval coincides with a drop in magnetic susceptibility in Holes 1200E (Fig. F61) and 1200F (Fig. F62).

F65. Peak shear strength, Holes 1200D, 1200E, and 1200F, p. 129.

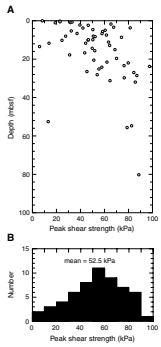

Shear Strength

The shear strength of the matrix material was measured once per section on the working half within 30 min of splitting the core. The measured peak shear strengths exhibit wide scatter (Fig. F65). A weak zone at a depth of 11–12 mbsf coincides with the low magnetic susceptibility and high gamma ray count shown in Figure F61. A mean value of 52.5 kPa is determined from all measurements. Disturbance from XCB coring and core splitting may explain the anomalously low (<30 kPa) strength measured in the sample at 52 mbsf. Water used to wash the split core faces was observed in the core liner during these measurements.

F66. Thermal conductivity, Holes 1200D, 1200E, and 1200F, p. 130.

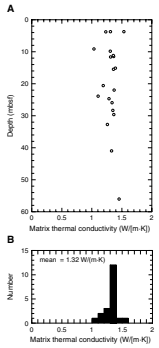

Thermal Conductivity

Thermal conductivity measurements range from 1.04 to 1.54 W/(m·K) (mean = 1.32 W/[m·K]) and show little scatter (Fig. F66). There appears to be a small increase in thermal conductivity with depth, but it is poorly constrained because of the limited number of measurements.

F67. Formation factor and porosity, Holes 1200D, 1200E, and 1200F, p. 131.

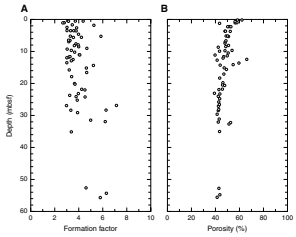

Formation Factor

The formation factor was determined from resistivity measurements made using a Wenner four-probe array with a 13.3-mm probe spacing. The probes were inserted to their full 15-mm length into the split core surface to provide consistent apparent resistivity measurements but not absolute values. Pore water was assumed to have the same electrolytic properties as surface seawater.

Formation factors range from 2.68 to 7.14 (mean = 3.97) (Fig. F67A), which is relatively high for sediments. The trend of the data shows that

the formation factor increases slightly with depth, consistent with the decrease in porosity with depth (Fig. F67B). The increase in porosity at a depth of 11–12 mbsf is yet another indicator of the change in material properties that occurs at that depth.

Hydraulic Conductivity and Specific Storage

Hydraulic conductivity (K) and specific storage (S_s) were determined for cylindrical samples of matrix material extracted from the whole-round core. We determine hydraulic conductivities between 1.1×10^{-11} and 2.8×10^{-10} m/s and specific storage values between 6.0×10^{-5} and 5.8×10^{-4} m^{-1} (Table T17), consistent with measurements using sediments with a similar grain size and distribution (Mitchell, 1976). Tests for hydraulic conductivity anisotropy were made by making measurements on samples extracted parallel and perpendicular to the core axis. A value of $K_{xx}/K_{zz} = 1.15$ suggests that any hydraulic conductivity anisotropy is relatively small and may not be significant given the small number of samples tested.

T17. Hydraulic conductivity and specific storage, Holes 1200D and 1200E, p. 169.

To test the effect of different axial loads on these flow parameters, two subsamples from Sample 195-1200D-1H-4, 120–130 cm, were tested with axial loads of 6.3 and 62.8 MPa. The tenfold increase in load decreased the hydraulic conductivity by more than one-third and decreased storage by more than one-fifth, as a result of the material becoming more consolidated.

It is important to note that in this type of test, the pore pressure gradients are very large and the sample passes through a large range of consolidation states. For example, in the case of Sample 195-1200D-1H-4, 120–130 cm, the initial void ratio of 1.4 is reduced to 0.66 at the end of the loading test. Our measurements of hydraulic conductivity and specific storage represent weighted average values obtained over a range of consolidation states.

Temperature Measurements

In situ temperature measurements were made in Hole 1200E using the DVTP and in Hole 1200F using the Adara temperature probe. The temperature records are shown in Figure F68. The typical temperature sequence first shows the temperature decrease as the temperature tool is lowered in the water column. The tool is lowered to the seafloor to the mudline, where it is allowed to reach equilibrium for >10 min. The temperature tool is then pushed into the sediments and held at a constant depth for another 10 min. Here, the temperature quickly increases in response to frictional heating and subsequently decays. This middle series is the temperature decay curve used to find the sediment temperature. Finally, the tool is removed from the sediments to the mudline, where it remains for 10 min, after which it is returned to the surface. This portion of the temperature sequence also shows a step increase in temperature, followed by a fast decrease and then slow increase as the tool is raised to the surface. Shown on the figures are the seafloor or mudline temperature (T_{ml}) and the estimated sediment temperature at depth (T_{sed}).

F68. Temperature, Holes 1200E and 1200F, p. 132.

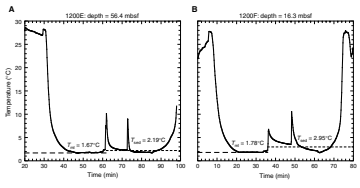

The sediment temperatures at depth were determined using the curve fitting programs CONEFIT for data collected with the DVTP and TFIT for data collected with the Adara temperature probe. The estimates of sediment temperatures can vary by several degrees, depending on the

value of the thermal conductivity of the sediment and the region of the decay curve chosen for the estimation. The sediment temperatures shown in Figure F68 were found using only the latter portions of the temperature decay curves.

Using the values of the mudline temperatures, the sediment temperatures at depth, and the depth of the measurement, the thermal gradient was calculated. Those values are shown in Table T18. A weighted bulk thermal conductivity = 1.38 W/(m·K) was calculated from the mean values of the clast and matrix thermal conductivities (2.21 and 1.32 W/[m·K], respectively) and their relative abundance (7% clast and 93% matrix), as estimated from the recovery data. Because there was negligible variation of the thermal conductivity with depth (see Fig. F66), the integrated thermal resistivity was not calculated. Instead, the heat flow was calculated directly using the following equation:

T18. In situ temperature, depth, thermal gradient, and heat flow, p. 170.

$$q = -K \times (\Delta T/\Delta z),$$

where

q = heat flow (W/m²),
K = thermal conductivity, and
$\Delta T/\Delta z$ = thermal gradient.

It should be noted that these values of heat flow assume that all heat flow is due to conduction.

When compared to the global average of ~50 mW/m² (Garland, 1979), the heat flow in Hole 1200E is lower (q = 13 mW/m²), whereas that in Hole 1200F is higher (q = 99 mW/m²). Hole 1200E is located within several meters of fissures in the mud volcano. Fluid flow is likely occurring in these fissures, and the thermal gradient in Hole 1200E might be suppressed by advective transport of heat by the fluid. Hole 1200F is located farther from the fissures where the thermal gradient might not be suppressed. However, this interpretation is complicated by the absolute temperature values in Holes 1200A and 1200E. Higher temperatures at both the mudline and within the sediment would be expected if heat were being transported advectively. This is not the case. The mudline temperature in Hole 1200F (1.78°C) is larger than that in Hole 1200E (1.67°C). This difference may be caused by use of the Adara temperature probe in Hole 1200F, whereas the DVTP was used in Hole 1200E, and so direct comparisons may not be valid.

MICROBIOLOGY

Microbiological samples were successfully collected from APC Holes 1200D and 1200E. Microbiological whole-round core samples were collected adjacent to pore water geochemical whole-round samples in all cases. A total of 18 samples was collected from Hole 1200D and 21 samples from Hole 1200E, with a higher sampling frequency near the surface. The maximum sampled depth was 28.9 and 55.3 mbsf, respectively, in Holes 1200D and 1200E. All microbiological samples were subjected to a series of tracer tests to determine the presence and extent of possible contamination to the exterior and interior of whole-round cores. For both holes, adjacent in situ pore water chemistry and fluorescent microspheres (Cores 195-1200D-5H through 9H and throughout

Hole 1200E) were used to detect contamination of samples. In Hole 1200D, PFT was also used as an additional chemical tracer (Smith et al., 2000a, 2000b). All three methods of detection positively demonstrated the contamination of a single whole-round core sample from Hole 1200D, showing relatively low alkalinity, interior fluorescent beads, and interior elevated levels of PFT, respectively (Sample 195-1200D-5H-1, 20–30 cm). All other microbiological samples showed either no direct contamination in terms of pore water chemistry and/or fluorescent microspheres or no detectable levels of PFT. These results demonstrate the potential for the collection of uncontaminated core samples to be used in microbiological research by drilling of deep ocean sediments.

Subsamples from all microbiological samples were collected and processed using a laminar flow hood. These included (1) the preservation of subsamples for molecular biological analyses by quick freezing with liquid nitrogen and then maintenance at –70°C; (2) toothpick scrapings stored at 4°C in sterile phosphate buffered saline for determination of the abundance and distribution of microorganisms by direct counting fluorescence microscopy, along with morphological characterizations by light microscopy; (3) the preservation of subsamples in 2.5% glutaraldehyde for scanning electron microscopy and, potentially, transmission electron microscopy; (4) the preservation of subsamples for flourescent in situ hybridization probing; (5) the aseptic cryopreservation of subsamples placed in 30% glycerol solution and quick freezing in liquid nitrogen for use with multiple enrichment culture procedures; and (6) the preservation of subsamples in serum vials stored at 4°C under nitrogen-flushed headspace, also for use in enrichment culture under anaerobic conditions, which was done for subsamples from Hole 1200D only.

BOREHOLE INSTRUMENTATION

Fluid circulation in the oceanic crust and through the seafloor occurs in passive continental margins, accretionary and nonaccretionary prisms, mid-ocean ridges, and ridge flanks. The placement of constraints on the physical and chemical nature of crustal fluid flux can be done by direct observation, measurements on cored material, and by downhole measurements and sampling. Downhole measurements and sampling have proven to be the best method for deep, high-pressure environments. In areas where the natural flux is large, numerous Deep Sea Drilling Project and ODP holes have been drilled. Unfortunately, flow into the formations being drilled is induced by nonhydrostatic formation conditions and/or the differential pressures resulting from density differences between the warm, low-density formation fluid and the cold, higher-density drilling fluid in these boreholes. CORK installations are designed to prevent this flow and to monitor in situ temperature and pressure conditions as drilling disturbances decay and natural conditions return. Borehole fluid samples representing formation fluids over extended time intervals can also be obtained without requiring CORK removal (Davis et al., 1992). CORKs have been deployed in ODP holes during Legs 139 (Juan de Fuca Ridge), 156 (Barbados accretionary prism), 168 (Juan de Fuca Ridge), 174B (Mid-Atlantic Ridge), and 195 (South Chamorro Seamount) to further understanding of fluid budgets. The CORK deployed in Hole 1200C will be the first to permit study of a nonaccretionary prism environment.

Total fluid budget determination at accretionary active margins has been hindered by the presence of laterally heterogeneous and transient flow processes, with the former resulting from different flow rates and compositions along the strike of the margin and the latter resulting largely from the valvelike influence of the sediments of the accretionary complex. Because the hydraulic flow properties of sediments vary with fluid pressure and fluid pressure varies as a function of fluid production rate and transient hydrologic properties, the accretionary system acts in a nonlinear transient manner as both a seal and a relief valve on the fluid flow system.

A total fluid budget should be more readily determined at nonaccretionary active margins because the heterogeneous and transient effects from the sediments of the accretionary prism do not have to be considered, resulting in hydrologic flow systems that operate on longer timescales, approaching steady-state flow. This hypothesis must be tested by determining the physical nature of fluid flow in nonaccretionary settings. Fluid budgets can then be constructed to determine whether the expected long-term flow is consistent with observations or if the flow is transient.

CORK

Design

The design used for the CORK in Hole 1200C incorporated most of the features used in previously CORKed holes, as documented by Davis et al. (1992). These features include the following:

1. A seal inside a modified casing string that prevents flow of seawater or formation fluid into or out of the borehole and that is capable of withstanding positive and negative pressures with magnitudes of up to the local difference between lithostatic and hydrostatic pressure.
2. Temperature measurement throughout the well bore.
3. Measurement of fluid pressure inside the well bore and at the seafloor with sensors of high stability, sensitivity, and dynamic range. This is necessary because small signals can be superimposed on large (potentially lithostatic) absolute pressures, and natural changes can occur over long periods of time.
4. A device to record the above data for up to 5 yr and capable of being downloaded by an ROV.
5. Deployment and recovery capability by research vessels other than a drill ship.
6. Redundant continuous fluid sampling at depth with samplers that can be recovered in 1.5 to 2 yr.
7. Use of equipment from previous experiments to minimize costs.

Components

The components used to meet the above objectives were a data logger, two pressure transducers, a thermistor cable, an extension cable, a spectra rope, two osmotically pumped fluid samplers, a weak point, and a sinker bar (Fig. F69; Table T19). These components were joined and, in some cases, fabricated on board the *JOIDES Resolution* while the hole was being drilled. The spectra rope, thermistor cable, and extension were joined with electrical tape, tie wraps, and wax string at ~5-m inter-

F69. Configuration of CORK installed in Hole 1200C, p. 133.

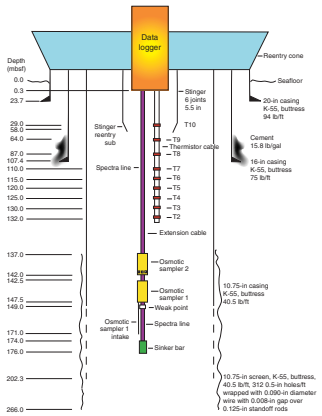

T19. String configuration and installation comments, p. 171.

vals to prevent the tape from unraveling and the tie wraps from sliding down the cable as the rope stretched under tension. It was important that the rope, thermistor cable, and extension cable be permitted to stretch independently, since each had a different stretch coefficient. The measured pH of 12.5 was of some concern because no one knew how the various cable components would withstand 1.5 yr in this corrosive environment.

Data Logger

The data logging unit is contained in a 4130 alloy mild steel pressure case that provides the upper CORK seal when latched into the landing collar (Fig. **F70**). Because the landing collar is constructed of the same material as the pressure case, the possibility of corrosion is minimized. The instrument hardware is mounted on an aluminum chassis within the 50-mm (2.5 in) inside diameter (ID) pressure case. Padded bulkheads and soft mounts at the top and bottom of the chassis provide longitudinal shock absorption.

Analog to digital conversion and 16 channels of voltage and resistance may be recorded by the data logger at intervals of 10 s or greater. Data are stored in 2 MB of solid-state memory, permitting data accumulation for a period of up to 5 yr with 1-hr sampling. For Hole 1200C, 15 channels, set for 1-hr sampling, were utilized: date and time, borehole pressure, seafloor pressure, internal temperature, resistances of the nine thermistors of the thermistor string, and two fixed, low temperature–coefficient resistors. Power is provided by four lithium thionyl chloride "C" cells, which will run the instrument for up to 5 yr under typical operating conditions. Additional backup power for memory is provided by a separate lithium cell.

Data retrieval and programming commands are performed over a 9600-baud three-wire RS-232 link. The external data communication link is provided by a four-contact, coaxial underwater mateable connector mounted on the top of the data logger (Ocean Design Inc.; "O.D. Blue") (Fig. **F70**). Power can be supplied to the data logger via this connection from an external source. The electrical connection can be established with a specially designed, gravity-driven, self-centering "top-hat" mounted on a submersible or ROV.

F70. CORK component identification, p. 134.

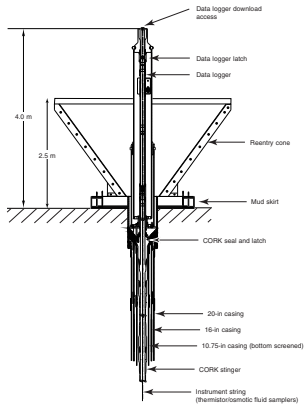

Pressure Transducers

Temperature-compensated quartz pressure transducers with a total range of 40 MPa (at 4000 mbsl) were employed to measure the seafloor and borehole fluid pressures (Paroscientific Model 8B 4000-2) (Davis et al., 1992).

Thermistor Cable

The thermistor cable string consists of 164 m of 12 twisted pairs of polypropylene insulated No. 20 American wire gage (AWG) wires with a nominal wall thickness of 0.016 in wrapped in an outer armor of Kevlar. Breakouts for the thermistors are underwater connectors (SeaCon MAW2-HC). The lower end of the cable is sealed to prevent fluid seepage into the data logger electronics.

This cable was originally deployed in Hole 1024C in 1996 during ODP Leg 168 prior to being recovered by the *Atlantis* (Woods Hole Oceanographic Institution) in September 1999. Because the hole temperatures were low (~30°C), because recovery resulted in no cable damage (aside from cutting off the T1 breakout), and because subsequent testing indicated good insulation and conductivity, the cable was con-

sidered to be in good condition for use in Hole 1200C. Because it was too short for the projected hole depth, extensions were fabricated to enable emplacement of thermistors at the desired depths while permitting the use of the existing breakouts. Because of hole problems, the actual hole depth obviated the need for the extensions.

Thermistors and Installation

The thermistors (Thermometrics SP100) were molded into MAW2-HC connectors. The thermistor cable had breakouts at depths of 29, 64, 99, 134, 139, 144, 149, 154, and 159 m of the paired conductors molded to 1N2 cables, which were in turn molded to MAW2-HC connectors. The breakouts were taped with 2-in electrical tape, with care taken to place the molded connections and thermistors against the cable body to prevent thermistor damage. Hydraulic hose (1.25 in ID) protected the installation, which was secured with electrical tape, nylon cord, and wax string (to prevent the tape from unraveling).

Spectra Rope and Weak Point

The spectra rope had been used during earlier CORK recoveries and was of suitable length for this deployment and design. This rope was used to make two separate lines with galvanized thimbles at each end. Rope 1 (149 m long) was fastened to the bottom of the data logger, tied off at each osmotic sampler, and terminated at the weak point. Rope 2 (25 m long) was fastened to the other end of the weak point and terminated at the sinker bar (Table **T20;** Fig. **F69**). The addition of a weak point was a change implemented to address the possibility of hole fill preventing sampler recovery. In Hole 1200C, both osmotic samplers were deployed above the screen, inside casing, with the weak point located at the top of the screen and the intake for the lower sampler located inside the screened section of casing (Fig. **F69**). The weak point consisted of a galvanized shackle (galvanization was removed to increase rate of corrosion) with an aluminum pin whose design had been tested to failure between 2 and 2.8 T. With no corrosion protection, it is thought that the weak point will most likely break prior to the recovery attempt.

T20. Spectra rope specifications, p. 172.

Osmotically Pumped Fluid Samplers

Developed by Hans Jannasch (Monterey Bay Aquarium Research Institute) to provide a long-term nonelectronic sampler without moving parts, osmotic samplers can continuously collect borehole fluids for up to 5 yr. Constructed primarily of polyvinyl chloride and Teflon tubing, they are driven by molecular diffusion of water through a rigid semipermeable membrane that separates a saturated salt solution from distilled water. The resulting osmotic pressure is used to pull water through one membrane at a rate of ~4 µL/hr at 20°C. Because the rate of flow increases with increasing temperature, the precise rate of flow is determined by the number of membranes and the operating temperature. Osmotic pumps draw from a distilled water reservoir, which is connected to a small-bore Teflon tube (1.1 mm ID) that is open at the sampling port. The length of the tubing is determined by the pump rate and deployment time (Davis, Fisher, Firth, et al., 1997). Although diffusion tends to integrate samples with different compositions, the characteristic distance for molecular diffusion should be <0.5 m for the expected 1.5- to 2-yr duration in Hole 1200C.

Each osmotic sampler in Hole 1200C has five membranes, with the operating temperature to be determined from the thermistor string

data. Because the two samplers will be deployed for 1.5 to 2 yr (recovery is expected in spring 2003), each one had 4000 ft of Teflon tubing. The top sampler (osmotic sampler 2) sampling port is located at a depth of 142 mbsf and the lower sampler (osmotic sampler 1) has a 1.1-mm ID sampling tube that extends below the weak point into the screened section 3 m above the sinker bar to a depth of 171 mbsf (Fig. F69).

The samplers (7.62 cm outer diameter) pass through the CORK and over the spectra cable (Fig. F69). The deepest thermistor is located just above osmotic sampler 2 so that temperature, and thus rate of pumping, will be known for the life of the experiment. Samples will be analyzed for the major and some minor seawater ions. The stable isotopic compositions of H, O, C, B, and Cl will also be measured.

Deployment

Deployment was conducted in eight phases. In order, they were as follows:

1. Drilling and placement of the reentry cone and surface casing (20 in);
2. Drilling, placement, and cementation of the intermediate casing string (16 in);
3. Drilling ahead and placement of the combination 10.75-in casing and screen;
4. Running of the stinger and CORK body to the seafloor;
5. Placement, seating, and latching of data logger–thermistor string assembly into the CORK body and unlatching the wireline from the data logger;
6. Calibration of pressure sensors;
7. Seating and latching of the CORK body into reentry cone; and
8. Release of CORK body from drill string.

An overview of the deployment methodology as stated by Davis, Mottl, Fisher, et al. (1992) is found below. A description of the first three steps can be found in "Hole 1200C," p. 6, in "Operations." A detailed description of the last five steps can be obtained from the ODP Drilling Services Department. Figure F71 provides a visual representation of the last five steps, and Figure F70 shows the final result. Figures F72 and F73 provide insight on the drill string equipment used.

Six sections of 5.5-in drill pipe (58 m), referred to as the stinger, were attached to the bottom of the CORK prior to deployment. The stinger is used to keep the CORK centered in the reentry cone during deployment of the thermistor string/data logger. It also serves to add weight (8500 lb, in this case) to the string to prevent heave from prematurely unlatching the running tool from the CORK. The CORK running tool, which, "jays," or latches onto the CORK, was attached to the end of the drill string (Fig. F72). Once the running tool was "jayed" onto the CORK, a hydraulic latch-setting hose was made up between the running tool and the CORK.

The CORK was then lowered to the seafloor on the drill string. Once the reentry cone was located, the CORK was positioned with the stinger in the cone throat such that the CORK could not land or latch in the cone as the ship heaved (Fig. F71A). Because the coring line used to deploy the thermistor string/data logger was not heave compensated, the drill string was held in this position while the thermistor string/data logger assembly was deployed.

F71. CORK deployment sequence, p. 135.

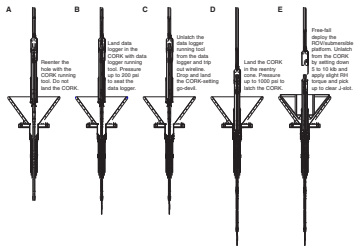

F72. CORK tools, p. 136.

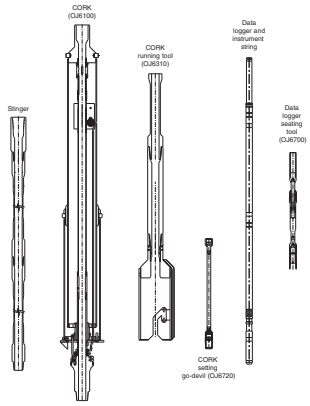

F73. Data logger seating tool operation, p. 137.

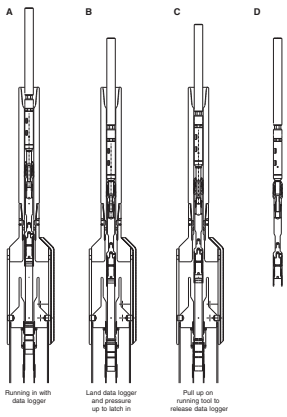

The data logger, thermistor string, osmotic fluid samplers, and sinker bar were placed in the drill pipe and attached to the logger seating tool (Fig. F73A), and the assembly was lowered down the drill string with the coring line. The sinker bar and thermistor string passed through the CORK, the stinger, and into the cased and screened borehole below. The data logger was then seated and latched inside the CORK (Fig. F73B). After the data logger latch-in was confirmed, the data logger seating tool was unlatched from the data logger and retrieved (Fig. F73C, F73D).

Once the wireline was out of the drill pipe, a CORK-setting go-devil was pumped down the drill string (Fig. F71C). The heave compensator was activated, and the drill string was lowered until the CORK with logger assembly landed in the 10.75-in casing hanger. The go-devil landed in the CORK running tool and blocked circulation, allowing the drill string to become pressurized. The pressure was channeled to a latch-setting piston via the hydraulic setting hose. When activated, the setting piston drove a latch ring into mating grooves in the 10.75-in casing hanger (Fig. F71D). The CORK must be latched in place to prevent it from being pumped out of the reentry cone should a positive pressure differential be present in the borehole.

After verifying that the CORK was latched in, a submersible ROV platform was deployed. Consisting of a central sleeve and a horizontal plate with holes that covers the reentry cone, it allows a vehicle to rest stably beside the CORK. The platform is fabricated in two halves. Prior to deployment, the halves were positioned around the drill string and bolted and welded together. Using the drill string as a guide, the platform was then free-fall deployed, automatically centering itself over the CORK as it landed on the reentry cone rim (Fig. F71E).

After verification by camera that the platform was in place, the running tool was "unjayed" from the CORK by setting down, rotating the drill string clockwise, and then lifting up. Removal of the running tool from the CORK resulted in the hydraulic setting hose automatically disconnecting. Thirteen hours after deployment began, the drill string was recovered and the instrumented borehole seal installation was complete (Figs. F69, F70, F71E; Table T21).

T21. Installation event times, p. 173.

Submersible/ROV Operations

CORK data logger downloads can be performed by a submersible or ROV. Also, because CORKs have two internal hydraulically controlled systems (a differential pressure vent and data logger latch), hydraulic power supplied by a submersible or ROV permits removal and replacement of the thermistor string/data logger without requiring the capabilities and expense of a drill ship. The procedure is (1) a wireline is connected to the data logger, (2) the vent and the latch are hydraulically opened in sequence, and (3) the data logger/thermistor string is removed using the attached wireline. By reversing the unlatching sequence, replacement of the data logger or other instrumentation can be performed (Davis, Mottl, Fisher, et al., 1992).

An ROV data download for Hole 1200C is tentatively scheduled for spring 2003. It is hoped that funding and ship time can be obtained to recover the osmotic samplers, thermistor string, and data logger and redeploy the data logger during that visit.

CORK Recovery

Only a drill ship is capable of recovering the main body of a CORK through the use of a pulling tool attached to the end of the drill string. Lowering the pulling tool over the CORK mechanically activates the differential pressure vent to open, and the pulling tool "jays" onto the CORK release sleeve. Lifting the drill string engages the CORK release sleeve, which releases the CORK latch ring. The release sleeve then engages the CORK itself, which is free to be pulled out of the reentry cone.

The CORK and the submersible/ROV platform is then picked up until it is sufficiently clear of the reentry cone to prevent heave from reseating it. Because only the stinger (the drill pipe attached below the CORK) is positioned in the reentry cone throat and casing at this time, the heave compensation can be deactivated and wireline equipped with a mechanical latch can be lowered down the drill string to retrieve the thermistor string and data logger. Once this assembly is retrieved and the CORK with the submersible/ROV platform is recovered with the drill string, the borehole is open for further operations (Davis, Mottl, Fisher, et al., 1992).

Hydrologic Disturbance from Exploratory Holes

Prior to drilling the CORK hole, single-bit exploratory Holes 1200A and 1200B were drilled to determine what procedures were needed to successfully drill the CORK borehole. Because Holes 1200A and 1200B collapsed, as anticipated, they were not cemented. We believe that the low hydraulic conductivity of the formations will prevent communication between these holes and the CORK without grouting these exploratory holes. Drilled to a depth of 145 mbsf, Hole 1200A was the deepest and poses the greatest threat of communication with Hole 1200C, the CORK hole. The distance between Holes 1200A and 1200C is ~100 m, and Hole 1200C has a total depth of 266 mbsf, with the screened section between 149 and 203 mbsf and no bridge plug present. Hole 1200B, before collapse, had a total depth of 98 mbsf and was located near Hole 1200A. The distances between Holes 1200D, 1200E, and 1200F from Hole 1200C are 52, 137, and 111 m, respectively (Fig. **F3**). Because each of these holes penetrated <30 mbsf, none should pose a risk to Hole 1200C.

STRUCTURAL GEOLOGY

General Comments

The serpentine muds of the various drill holes at Site 1200 are classified as silty-clay serpentine or clast-poor diamictite, depending on the grain size of the matrix and the relative abundance of clasts (see **"Lithostratigraphy,"** p. 11). These are nongenetic terms based on grain size and aptly describe the serpentine muds from a sedimentological point of view.

Based on the internal characteristics of the serpentine mud and the geologic environment in which serpentine volcanoes form, the genetic term "tectonic mud breccia" will be used in this chapter to describe serpentine mud containing mostly angular clasts, regardless of clast abundance (in contrast to the classification scheme used to formally describe the cores at Site 1200). These breccias are the product of tectonic and

geochemical processes that have changed solid ultramafic rocks to their present state. A proposed summary of the tectonic history recorded in these rocks, from earliest to latest events follows:

1. Plastic deformation of upper mantle peridotites, possibly accompanying partial melting event(s);
2. Later "cold fracturing" of these peridotites by planar joints, followed by minor serpentinization along these discrete fractures;
3. Pervasive partial serpentinization of peridotite by influx of large amounts of water along grain boundaries; accompanying the volume increase associated with this serpentinization the earlier-formed veins were stretched apart and became deposition sites for secondary veinlets of fibrous chrysotile (see **F29**);
4. Later brecciation of the partially serpentinized peridotite, as zones of weakness (fault zones?) formed passageways along which lower-density, water-saturated serpentine mud could begin to rise buoyantly through more dense surrounding rocks; the chrysotile-rich planar veins that occupied zones of weakness in the serpentinized peridotite controlled initial fragment shapes;
5. During ascent of the serpentine muds, larger blocks of serpentinite fragmented into smaller pieces through mechanical abrasion, depressurization fracturing during decompression, and volume expansion associated with continuing serpentinization; the ascent velocity of the tectonized serpentine mud breccia likely accelerated as serpentinization continued and the bulk density of the serpentine mud breccia was lowered by lessening amounts of relict ultramafic minerals in entrained serpentinite blocks; and
6. Extrusion of serpentine mud breccia onto the seafloor resulted in the reduction of upward velocities as the breccia was able to move horizontally as well as vertically within the accumulating "serpentine volcano;" likely, larger dense fragments could no longer be buoyed upward within the "volcanoes" and are concentrated near the base of South Chamorro Seamount; injection of new mud breccia at the base of this seamount results in continued shearing throughout the edifice as new material penetrates preexisting breccia and as gravitational stresses within the weak seamount result in the outward flow of material.

History Of Tectonism and Serpentinization

As the serpentine mud breccia rose from depth beneath the Mariana forearc, it incorporated large amounts of partially serpentinized ultramafic rocks, which were torn from wall rocks surrounding the conduit and were carried upward in an ascending matrix of serpentine mud. Structures preserved within the rocks recovered from Site 1200 provide information about the tectonic history of the ultramafic rocks that underlie the forearc and also about the history of their serpentinization.

Early Metamorphism and Deformation

The relict minerals of the original ultramafic rock (especially olivine) commonly show kink banding (see **"Igneous and Metamorphic Petrology of Ultramafics,"** p. 16). Orthopyroxenes show undulatory extinction. These features are also typical of the serpentinized peridotites studied at Conical Seamount during Leg 125 (Girardeau and Laga-

brielle, 1992) and suggest that metamorphism and shearing affected a large area of the mantle that was later to become the Mariana forearc.

Regional Fracture Event

Subsequent to the above metamorphism but before any serpentinization had occurred, regional brittle deformation occurred and a set of tectonic fractures developed in the mantle beneath this area. This was possibly due to flexing of the upper mantle at the initiation of the Mariana arc system (Fryer, 1996). These fractures appear to be oriented at high angles to one another, but stereographic analyses of multiple joints in different clasts failed to reveal any systematic relationships.

First Serpentinization Event

The above fractures likely served as pathways along which small amounts of water percolated from below, forming narrow, widely spaced serpentine veins and veinlets (those seen in serpentinite clasts are mostly <10 mm wide). These serpentine veins contain abundant fine magnetite grains, especially at their centers, which give the veins a "striped" appearance parallel to their walls (Fig. F74). Fine birefringent mineral grains (brucite?) are also present in these veins, intermixed with serpentine. Serpentine mineral crystals in these veins are typically fine grained and intergrown in mosaic patterns. The distribution of these veins in recovered serpentinite clasts suggests that little water was available at this time, as no more than 1%–2% of the peridotite was serpentinized during this event.

F74. Veins formed during the first serpentinization event, p. 138.

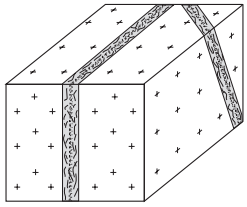

Second Serpentinization Event

Subsequent to formation of the first vein set along discrete fractures, large volumes of water (likely derived from subducted oceanic crust and sediment) penetrated the obducted mantle beneath the Mariana forearc and massive serpentinization occurred. This serpentinization process was pervasive, as water percolated along intergrain boundaries and not along discrete fractures as in the first event. Samples of serpentinite cored in Holes 1200A and 1200B suggest that peridotites were 60%–100% serpentinized during this second event, typically leaving residual "bastite" crystals of disaggregated orthopyroxene in a matrix of nearly completely serpentinized olivine.

Large volume increases accompanied this second serpentinization event, as high-density olivine and orthopyroxene were hydrated to serpentine. The serpentine veins formed in the first minor serpentinization event could not increase in volume, however, and were subjected to dilatory stresses when the surrounding peridotite expanded. Expansion of the enclosing rock in directions normal to the vein planes had no effect, but dilation in directions parallel to the veins caused dilation fractures to form in an irregular boxwork pattern across vein planes (Fig. F75). Serpentine-rich fluids migrated into these open fractures, depositing narrow veinlets of uncontaminated chrysotile (Fig. F76). A similar mechanism was proposed by Fryer, Pearce, Stokking, et al. (1990) to explain the origin of these secondary veins (termed "Frankenstein" veins) in serpentinite from Conical Seamount during Leg 125. At Site 1200, the veins consisting of pure greenish white fibrous chrysotile formed by solution precipitation rather than in situ replacement and are restricted in their occurrence to within and near the first-generation

F75. Veins formed during the second serpentinization event, p. 139.

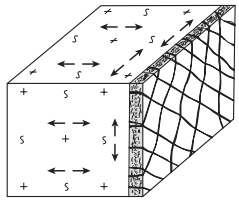

F76. Clast margin showing second-generation chrysotile veinlets, p. 140.

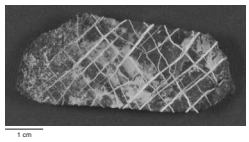

banded veins. These crosscutting veinlets are <1 mm thick with fiber axes perpendicular to the veins. Thicker secondary veins must have formed by this same process elsewhere, however, as indicated by the common occurrence of chrysotile asbestos fibers up to 12 mm long in the serpentine mud breccia. Such wide fibrous veins would be zones of weakness in massive serpentinite and would not be preserved within clasts but instead form the margins of some clasts, indicating fracture boundaries (Fig. F77).

F77. Serpentinized clast showing second-generation chrysotile veinlets, p. 141.

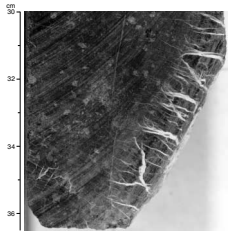

Tectonic Shearing of Serpentine Mud

The ascent and flow of fragment-laden serpentine mud is a tectonic process, and examination of impregnated mud thin sections at finest microscopic scales reveals that these muds are laden with microscopic angular fragments (see Fig. F9). For this reason, they are referred to as "tectonic breccias" in this chapter. The muds commonly display subparallel alignment of silt-sized serpentine platelets. These zones appear to be highly irregular and may reflect internal flow processes that indicate a swirling of mud around suspended clasts. These same zones, however, could possibly be a consequence of core disturbance.

Morphology of Breccia Fragments

The South Chamorro serpentine mud volcano formed by the upward migration (protrusion) of low-density, low-viscosity serpentine mud breccia (see "Physical Properties," p. 40) through obducted mantle and onto the seafloor. This serpentine mud breccia contains angular and subangular rock fragments at all scales—from microscopic to blocks more than a meter across. These fragments (also called "clasts" elsewhere in text) mostly consist of serpentinized and partially serpentinized peridotites but also include mineral fragments from the original peridotites (olivine, orthopyroxene, magnetite, and chrome spinel) as well as sparse clasts of chlorite schist and other aluminosilicate metamorphic assemblages. The shapes of these clasts vary systematically with their grain size and are important characteristics of this unique tectonic breccia.

F78. Hole 1200A serpentinite clasts, p. 142.

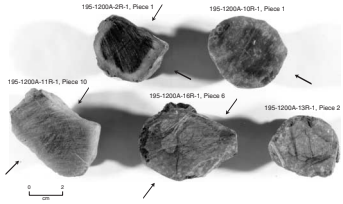

Brecciation Processes

The initial disintegration of massive serpentinite appears to have been controlled by the presence of weak asbestos-rich serpentine veins formed along an older joint set, and many smaller clasts are seen to have their shapes initially determined by these joints (Fig. F78). The external shapes of the large serpentinite blocks cored in Holes 1200A and 1200B cannot be known directly, but the common occurrence of chrysotile veins on the external faces of many clasts (Fig. F77) suggests that these blocks were also bounded by veins.

Fragmentation of larger blocks into smaller ones likely occurs during contact between blocks during ascent and results in an abundance of angular clasts <25 mm in maximum dimension (Fig. F79; also see the "Appendix," p. 60).

F79. Size, sphericity, and roundness of clasts, p. 143.

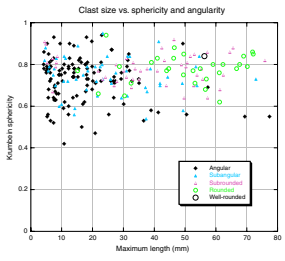

Sizes of Clasts within the Breccia

Clasts within the breccia have a seriate size distribution, from fractions of millimeters to more than a meter in maximum dimension. Be-

low a few millimeters in size, grains mostly consist of individual minerals rather than rock assemblages.

Shapes of Clasts within the Breccia

There are two measures of shape that need to be considered when evaluating the morphology of clasts within the breccia: roundness, which is the degree of angularity of grain corners, and sphericity, which measures the equality of the length axes of a clast. Thus, a perfect cube would have low roundness but high sphericity, whereas an elongate clast with well-rounded corners would have high roundness but low sphericity. Sphericity was measured using methods outlined in Krumbein (1941).

Roundness was determined by visual reference to the "roundness charts" given by Carver (1971). In Figure F79, sphericity is plotted against maximum clast length values measured for 250 clasts from Site 1200. Although there is no apparent correlation between clast size and sphericity, the degree of roundness (shown by symbols for each clast) does vary with clast size, as smaller clasts tend to be more angular than larger ones. This apparent correlation between roundness and size is also shown in Figure F80, where the shapes of randomly selected clasts of different sizes are compared, although it should be noted that some clasts may have been rounded by the drilling process.

F80. Serpentinite clast shape as a function of size, p. 144.

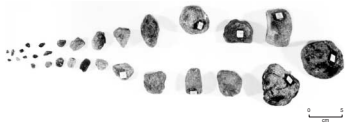

Significance

The distribution of clast shapes in the serpentine mud breccia is quite different from that in most clastic sedimentary rocks, where clasts are in grain-to-grain contact with one another and most clasts are rounded to a similar degree, regardless of clast size. The distribution of clast shapes in these tectonic mud breccias can therefore be used as a "signature" for these deposits and may be useful in establishing correlations with related deposits found elsewhere. Sedimentary serpentinite deposits, found worldwide where deep-sea continental margin accretionary terranes are exposed on land (Lockwood, 1971), have been suggested to be derived from serpentinite protrusions such as those of the Mariana forearc (Fryer, 1996). If they are related, analyses of clast morphologies in subaerial deposits might be useful to establish or to reject correlations with the Mariana protrusions.

REFERENCES

Adelseck, C.G., Jr., 1978. Dissolution of deep-sea carbonate: preliminary calibration of preservational and morphologic aspects. *Deep-Sea Res. Part A,* 25:1167–1185.

Beske-Diehl, S.J., and Banerjee, S.K., 1980. Metamorphism in the Troodos ophiolite: implications for marine magnetic anomalies. *Nature,* 285:563–564.

Bohrmann, G., Abelmann, A., Gersonde, R., Hubberten, H., and Kuhn, G., 1994. Pure siliceous ooze, a diagenetic environment for early chert formation. *Geology,* 22:207–210.

Carver, R.E., 1971. *Procedures in Sedimentary Petrology:* New York (Wiley).

Davis, E.E., Becker, K., Pettigrew, T., Carson, B., and MacDonald, R., 1992. CORK: a hydrologic seal and downhole observatory for deep-ocean boreholes. *In* Davis, E.E., Mottl, M.J., Fisher, A.T., et al., *Proc. ODP, Init. Repts,* 139: College Station, TX (Ocean Drilling Program), 43–53.

Davis, E.E., Fisher, A.T., Firth, J.V., et al., 1997. *Proc. ODP, Init. Repts.,* 168: College Station, TX (Ocean Drilling Program).

Davis, E.E., Mottl, M.J., Fisher, A.T., et al., 1992. *Proc. ODP, Init. Repts.,* 139: College Station, TX (Ocean Drilling Program).

Fryer, P., 1992a. Mud volcanoes of the Marianas. *Sci. Am.,* 266:46–52.

————, 1992b. A synthesis of Leg 125 drilling of serpentine seamounts on the Mariana and Izu-Bonin forearcs. *In* Fryer, P., Pearce, J.A., Stokking, L.B., et al., *Proc. ODP Sci. Results,* 125: College Station, TX (Ocean Drilling Program), 593–614.

————, 1996. Evolution of the Mariana convergent plate margin system. *Rev. Geophys.,* 34:89–125.

Fryer, P., and Mottl, M.J., 1997. *Sinkai 6500* investigations of a resurgent mud volcano on the southeastern Mariana forearc. *JAMSTEC J. Deep Sea Res.,* 13:103–114.

Fryer, P., Mottl, M., Johnson, L., Haggerty, J., Phipps, S., and Maekawa, H., 1995. Serpentine bodies in the forearcs of Western Pacific convergent margins: origin and associated fluids. *In* Taylor, B., and Natland, J. (Eds.), *Active Margins and Marginal Basins of the Western Pacific*. Geophys. Monogr., Am. Geophys. Union, 88:259–279.

Fryer, P., Pearce, J.A., Stokking, L.B., et al., 1990. *Proc. ODP, Init. Repts.,* 125: College Station, TX (Ocean Drilling Program).

Fryer, P., Saboda, K.L., Johnson, L.E., Mackay, M.E., Moore, G.F., and Stoffers, P., 1990. Conical Seamount: SeaMARC II, *Alvin* submersible and seismic-reflection studies. *In* Fryer, P., Pearce, J.A., Stokking, L.B., et al., *Proc. ODP, Init. Repts.,* 125: College Station, TX (Ocean Drilling Program), 69–80.

Fryer, P., Wheat, C.G., and Mottl, M.J., 1999. Mariana blueschist mud volcanism: implications for conditions within the subduction zone. *Geology,* 27:103–106.

Fuller, M., Cisowski, S., Hart, M., Haston, R., Schmidtke, E., and Jarrard, R., 1988. NRM:IRM demagnetization plots: an aid to the interpretation of natural remanent magnetization. *Geophys. Res. Lett.,* 15:518–521.

Garland, G.D., 1979. *Introduction to Geophysics*: Philadelphia (Saunders).

Girardeau, J., and Lagabrielle, Y., 1992. Deformation history of peridotites from the Mariana forearc, Conical Seamount, Leg 125. *In* Fryer, P., Pearce, J.A., Stokking, L.B., et al., *Proc. ODP, Sci. Results,* 125: College Station, TX (Ocean Drilling Program), 519–532.

Isacks, B.L., and Barazangi, M., 1977. Geometry of Benioff zones: lateral segmentation and downwards bending of the subducted lithosphere. *In* Talwani, M., and Pitman, W.C., III (Eds.), *Island Arcs, Deep Sea Trenches, and Back Arc Basins*. Maurice Ewing Ser., Am. Geophys. Union, 1:94–114.

Ishii, T., Robinson, P.T., Maekawa, H., and Fiske, R., 1992. Petrological studies of peridotites from diapiric serpentinite seamounts in the Izu-Ogasawara-Mariana forearc, Leg 125. *In* Fryer, P., Pearce, J.A., Stokking, L.B., et al., *Proc. ODP, Sci. Results,* 125: College Station, TX (Ocean Drilling Program), 445–485.

Ishiwatari, A., 1985. Igneous petrogenesis of the Yakuno ophiolite (Japan) in the context of the diversity of ophiolites. *Contrib. Mineral. Petrol.,* 89:155–167.

Jones, J.B., and Segnit, E.R., 1971. The nature of opal, I. Nomenclature and constituents phases. *J. Geol. Soc. Australia,* 18:57–68.

Kelso, P.R., Richter, C., and Pariso, J.E., 1996. Rock magnetic properties, magnetic mineralogy, and paleomagnetism of periodotites from Site 895, Hess Deep. *In* Mèvel, C., Gillis, K.M., Allan, J.F., and Meyer, P.S. (Eds.), *Proc. ODP, Sci. Results,* 147: College Station, TX (Ocean Drilling Program), 405–413.

Kikawa, E., Kelso, P.R., Pariso, J.E., and Richter, C., 1996. Paleomagnetism of gabbroic rocks and peridotites from Sites 894 and 895, Leg 147, Hess Deep: results of half-core and whole-core measurements. *In* Mèvel, C., Gillis, K.M., Allan, J.F., and Meyer, P.S. (Eds.), *Proc. ODP, Sci. Results,* 147: College Station, TX (Ocean Drilling Program), 383–391.

Krumbein, W.C., 1941. Measurement and geologic significance of shape and roundness of sedimentary particles. *J. Sedimentol. Petrol.,* 11:64–72.

Lockwood, J.P., 1971. Sedimentary and gravity slide emplacement of serpentinite. *Geol. Soc. Am. Bull.,* 82:919–936.

Lowrie, W., and Fuller, M., 1971. On the alternating field demagnetization characteristics of multidomain thermoremanent magnetization of magnetite. *J. Geophys. Res.,* 76:6339–6349.

Luyendyk, B.P., and Day, R., 1982. Paleomagnetism of the Samail ophiolite, Oman: 2. The Wadi Kadir gabbro section. *J. Geophys. Res.,* 87:10903–10917.

Merrill, R.T., and McElhinny, M.W., 1983. *The Earth's Magnetic Field: Its History, Origin, and Planetary Perspective:* London (Academic Press).

Miller, D.J., and Christensen, N.I., 1997. Seismic velocities of lower crustal and upper mantle rocks from the slow-spreading Mid-Atlantic Ridge, south of the Kane Transform Zone (MARK). *In* Karson, J.A., Cannat, M., Miller, D.J., and Elthon, D. (Eds.), *Proc. ODP, Sci. Results,* 153: College Station, TX (Ocean Drilling Program), 437–454.

Mitchell, J.K., 1976. *Fundamentals of Soil Behavior:* New York (Wiley).

Mottl, M.J., 1992. Pore waters from serpentine seamounts in the Mariana and lzu-Bonin forearcs, Leg 125: evidence for volatiles from the subducting slab. *In* Fryer, P., Pearce, J.A., Stokking, L.B., et al., *Proc. ODP, Sci. Results,* 125: College Station, TX (Ocean Drilling Program), 373–385.

Mottl, M.J., and Alt, J.C., 1992. Data report: Minor and trace element and sulfur isotopic composition of pore waters from Sites 778 through 786. *In* Fryer, P., Pearce, J.A., Stokking, L.B., et al., *Proc. ODP, Sci. Results,* 125: College Station, TX (Ocean Drilling Program), 683–688.

Okada, H., and Honjo, S., 1973. The distribution of oceanic coccolithophorids in the Pacific. *Deep-Sea Res. Part A,* 20:355–374.

Parker, F.L., and Berger, W.H., 1971. Faunal and solution patterns of planktonic foraminifera in surface sediments of the South Pacific. *Deep-Sea Res. Part A,* 18:73–107.

Parkinson, I.J., and Pearce, J.A., 1998. Peridotites from the Izu-Bonin-Mariana forearc (ODP Leg 125): evidence for mantle melting and melt-mantle interactions in a supra-subduction zone setting. *J. Petrol.* 39:1577–1618.

Parsons, T.R., Maita, Y., and Lalli, C.M., 1984. *A Manual of Chemical and Biological Methods for Seawater Analysis:* New York (Pergamon Press).

Pearce, J.A., Baker, P.F., Edwards, S.J., Parkinson, I.J., and Leat, P.T., 2000. Geochemistry and tectonic significance of peridotites from the South-Sandwich arc-basin system, South Atlantic. *Contrib. Mineral. Petrol.,* 139:36–53.

Pujos, A., 1988. Spatio-temporal distribution of some Quaternary coccoliths. *Oceanol. Acta,* 11:65–77.

Shipboard Scientific Party, 1990a. Site 778. *In* Fryer, P., Pearce, J.A., Stokking, L.B., et al., *Proc. ODP, Init. Repts.,* 125: College Station, TX (Ocean Drilling Program), 97–114.

————, 1990b. Site 779. *In* Fryer, P., Pearce, J.A., Stokking, L.B., et al., *Proc. ODP, Init. Repts.,* 125: College Station, TX (Ocean Drilling Program), 115–145.

———, 1990c. Site 780. *In* Fryer, P., Pearce, J.A., Stokking, L.B., et al., *Proc. ODP, Init. Repts.,* 125: College Station, TX (Ocean Drilling Program), 147–178.

Smith, D.C., Spivack, A.J., Fisk, M.R., Haveman, S.A., Staudigel, H., and ODP Leg 185 Shipboard Scientific Party, 2000a. Methods for quantifying potential microbial contamination during deep ocean coring. *ODP Tech. Note,* 28 [Online]. Available from World Wide Web: <http://www-odp.tamu.edu/publications/tnotes/tn28/INDEX.HTM>. [Cited 2001-03-02]

———, 2000b. Tracer-based estimates of drilling-induced microbial contamination of deep sea crust. *Geomicrobiol. J.,* 17:207–219.

Stokking, L.B., Merrill, D.L., Haston, R.B., Ali, J.R., and Saboda, K.L., 1990. Rock magnetic studies of serpentinite seamounts in the Mariana and Izu-Bonin regions. *In* Fryer, P., Pearce, J.A., Stokking, L.B., et al., *Proc. ODP Sci. Results,* 125: College Station, TX (Ocean Drilling Program), 561–579.

Su, X., 1996. Development of late Tertiary and Quaternary coccolith assemblages in the Northeast Atlantic. *GEOMAR Rep.,* 48.

Su, X., Baumann, K.-H., and Thiede, J., 2000. Calcareous nannofossils from Leg 168: biochronology and diagenesis. *In* Fisher, A., Davis, E.E., and Escutia, C. (Eds.), *Proc. ODP, Sci. Results,* 168: College Station, TX (Ocean Drilling Program), 39–49.

Swift, B.A., and Johnson, H.P., 1984. Magnetic properties of the Bay of Islands ophiolite suite and implications for the magnetization of oceanic crust. *J. Geophys. Res.,* 89:3291–3308.

Telford, W.M., Geldart, L.P., Sheritt, R.E., and Keys, D.A., 1976. *Applied Geophysics:* Cambridge (Cambridge Univ. Press).

Todd, C., and Fryer, P., 1999. Blueschist mud volcanism in the Mariana forearc: sampling the subducted slab. *Geol. Soc. Am. Abstr. Progr.,* 31:7.

Yasuda, M., Berger, W.H., Wu, G., Burke, S., and Schmidt, H., 1993. Foraminifer preservation record for the last million years: Site 805, Ontong Java Plateau. *In* Berger, W.H., Kroenke, L.W., Mayer, L.A., et al., *Proc. ODP, Sci. Results,* 130: College Station, TX (Ocean Drilling Program), 491–508.

Young, J.R., 1994. Functions of coccoliths. *In* Winter, A., and Siesser, W.G. (Eds.), *Coccolithophores:* Cambridge (Cambridge Univ. Press), 63–82.

APPENDIX

Dimensional Characteristics of Serpentinite Clasts, Hole 1200A

Clast number	Size measurement (mm)			Roundness and sphericity measurements		
	Long axis (L)	Middle axis (M)	Short axis (S)	Carver/Krumbein Roundness	Krumbein plots M/L	Krumbein plots S/M
1	14.1	6.4	5.6	0.3	0.45	0.88
2	14.3	7.8	5.5	0.3	0.55	0.71
3	8.3	7.6	5.1	0.4	0.92	0.67
4	8.0	4.6	3.4	0.2	0.58	0.74
5	10.6	6.4	3.6	0.2	0.60	0.56
6	10.8	8.5	8.0	0.3	0.79	0.94
7	12.0	7.7	6.9	0.4	0.64	0.90
8	10.8	4.2	2.1	0.1	0.39	0.50
9	17.4	11.3	6.3	0.1	0.65	0.56
10	8.6	6.8	6.5	0.6	0.79	0.96
11	8.0	6.4	3.5	0.4	0.80	0.55
12	10.7	8.9	4.9	0.3	0.83	0.55
13	8.8	6.0	4.6	0.1	0.68	0.77
14	7.8	5.6	3.7	0.2	0.72	0.66
15	7.1	4.4	3.4	0.5	0.62	0.77
16	5.6	3.1	1.8	0.1	0.55	0.58
17	6.2	4.3	3.3	0.2	0.69	0.77
18	5.3	3.0	1.6	0.2	0.57	0.53
19	14.7	10.9	7.7	0.4	0.74	0.71
20	10.8	8.1	7.4	0.1	0.75	0.91
21	8.1	6.5	5.0	0.6	0.80	0.77
22	8.3	5.5	6.6	0.5	0.66	1.20
23	9.0	5.6	4.1	0.2	0.62	0.73
24	10.0	5.3	4.2	0.3	0.53	0.79
25	7.7	5.1	3.8	0.1	0.66	0.75
26	31.3	20.6	13.3	0.4	0.66	0.65
27	25.9	21.4	12.3	0.4	0.83	0.57
28	22.5	17.2	14.6	0.3	0.76	0.85
29	27.7	21.6	18.5	0.5	0.78	0.86
30	37.7	27.8	15.4	0.3	0.74	0.55
31	32.1	24.9	24.8	0.4	0.78	1.00
32	20.1	12.8	11.7	0.2	0.64	0.91
33	32.6	19.9	17.8	0.5	0.61	0.89
34	23.4	16.2	12.9	0.3	0.69	0.80
35	24.2	16.6	14.2	0.5	0.69	0.86
36	17.7	13.0	12.4	0.2	0.73	0.95
37	21.6	13.7	9.2	0.4	0.63	0.67
38	21.9	15.3	14.2	0.5	0.70	0.93
39	39.1	34.7	23.4	0.7	0.89	0.67
40	20.9	17.0	12.5	0.3	0.81	0.74
41	15.2	10.5	10.0	0.8	0.69	0.95
42	31.0	23.7	23.3	0.6	0.76	0.98
43	27.9	19.7	14.9	0.5	0.71	0.76
44	33.2	26.2	22.7	0.6	0.79	0.87
45	32.8	23.4	16.9	0.2	0.71	0.72
46	29.4	18.7	12.0	0.3	0.64	0.64
47	23.3	16.4	13.0	0.5	0.70	0.79
48	18.1	12.7	8.0	0.3	0.70	0.63
49	18.5	13.3	11.7	0.3	0.72	0.88
50	37.7	31.4	21.7	0.5	0.83	0.69
51	30.2	26.9	15.2	0.6	0.89	0.57
52	37.2	23.1	20.1	0.3	0.62	0.87
53	15.6	12.5	10.8	0.2	0.80	0.86
54	31.0	21.3	18.3	0.6	0.69	0.86
55	42.5	37.4	33.4	0.5	0.88	0.89
56	52.8	34.6	28.2	0.6	0.66	0.82
57	49.6	40.8	36.4	0.7	0.82	0.89
58	53.9	35.9	33.8	0.5	0.67	0.94
59	56.3	46.5	40.4	0.9	0.83	0.87
60	49.5	38.3	26.6	0.7	0.77	0.69
61	55.7	41.6	29.5	0.6	0.75	0.71
62	53.2	35.7	28.0	0.7	0.67	0.78
63	66.7	55.0	38.5	0.7	0.82	0.70

Appendix (continued).

Clast number	Size measurement (mm)			Roundness and sphericity measurements		
	Long axis (L)	Middle axis (M)	Short axis (S)	Carver/Krumbein Roundness	Krumbein plots M/L	Krumbein plots S/M
64	64.5	58.6	45.0	0.6	0.91	0.77
65	41.0	37.6	25.2	0.7	0.92	0.67
66	53.9	31.9	30.8	0.4	0.59	0.97
67	53.5	44.6	31.6	0.3	0.83	0.71
68	44.7	36.1	25.8	0.7	0.81	0.71
69	61.1	53.6	30.4	0.8	0.88	0.57
70	59.1	54.0	33.3	0.7	0.91	0.62
71	41.0	32.8	23.7	0.6	0.80	0.72
72	54.9	40.4	36.0	0.8	0.74	0.89
73	44.0	31.6	27.8	0.7	0.72	0.88
74	62.3	49.2	40.5	0.8	0.79	0.82
75	49.7	28.1	23.3	0.5	0.57	0.83
76	43.3	34.9	29.2	0.5	0.81	0.84
77	72.1	57.6	54.9	0.8	0.80	0.95
78	65.6	55.9	53.2	0.6	0.85	0.95
79	56.9	39.9	32.2	0.7	0.70	0.81
80	50.3	40.1	30.9	0.5	0.80	0.77
81	67.7	60.0	39.3	0.7	0.89	0.66
82	46.4	44.4	37.8	0.6	0.96	0.85
83	18.3	12.7	12.3	0.1	0.69	0.97
84	32.0	22.5	20.5	0.2	0.70	0.91
85	12.3	9.7	7.3	0.2	0.79	0.75
86	22.8	18.0	10.6	0.1	0.79	0.59
87	73.0	61.5	33.6	0.4	0.84	0.55
88	20.5	14.1	12.9	0.1	0.69	0.91
89	13.8	10.6	7.3	0.2	0.77	0.69
90	13.7	9.6	7.8	0.1	0.70	0.81
91	41.3	26.4	12.2	0.1	0.64	0.46
92	32.5	24.7	15.0	0.7	0.76	0.61
93	22.3	16.5	13.9	0.1	0.74	0.84
94	49.1	31.3	27.5	0.4	0.64	0.88
95	29.3	21.0	15.7	0.2	0.72	0.75
96	7.5	7.0	6.4	0.1	0.93	0.91
97	13.7	7.8	6.4	0.1	0.57	0.82
98	11.3	9.4	7.7	0.3	0.83	0.82
99	16.5	8.2	4.2	0.1	0.50	0.51
100	7.9	6.3	3.0	0.2	0.80	0.48
101	7.4	5.9	5.4	0.2	0.80	0.92
102	7.3	6.3	3.6	0.4	0.86	0.57
103	7.6	6.6	4.2	0.4	0.87	0.64
104	5.3	5.1	4.0	0.2	0.96	0.78
105	5.3	4.4	3.4	0.5	0.83	0.77
106	6.1	5.4	3.7	0.1	0.89	0.69
107	7.4	4.8	3.0	0.2	0.65	0.63
108	7.6	5.3	2.7	0.2	0.70	0.51
109	7.4	4.4	1.7	0.1	0.59	0.39
110	5.5	4.9	2.9	0.1	0.89	0.59
111	5.7	3.2	2.6	0.2	0.56	0.81
112	5.1	4.2	2.7	0.2	0.82	0.64
113	4.5	3.8	2.9	0.4	0.84	0.76
114	4.2	3.3	2.7	0.2	0.79	0.82
115	14.0	10.0	8.5	0.1	0.71	0.85
116	15.5	12.7	9.1	0.2	0.82	0.72
117	13.5	10.5	9.0	0.1	0.78	0.86
118	12.3	9.3	7.9	0.1	0.76	0.85
119	9.5	8.8	7.5	0.1	0.93	0.85
120	12.2	7.3	3.6	0.1	0.60	0.49
121	11.1	8.4	6.4	0.1	0.76	0.76
122	7.1	6.5	4.5	0.5	0.92	0.69
123	9.2	4.9	3.8	0.3	0.53	0.78
124	5.8	5.3	3.9	0.2	0.91	0.74
125	8.4	5.5	3.7	0.2	0.65	0.67
126	11.0	6.5	4.4	0.1	0.59	0.68
127	4.9	4.3	4.1	0.5	0.88	0.95
128	6.8	5.5	4.7	0.2	0.81	0.85
129	6.0	5.0	3.5	0.4	0.83	0.70
130	8.0	5.5	2.9	0.1	0.69	0.53

Appendix (continued).

Clast number	Size measurement (mm)			Roundness and sphericity measurements		
	Long axis (L)	Middle axis (M)	Short axis (S)	Carver/Krumbein Roundness	Krumbein plots M/L	Krumbein plots S/M
131	4.3	4.0	2.9	0.1	0.93	0.73
132	6.5	5.4	3.9	0.1	0.83	0.72
133	6.4	3.2	1.9	0.1	0.50	0.59
134	6.5	4.9	3.3	0.1	0.75	0.67
135	6.3	5.4	3.6	0.1	0.86	0.67
136	6.3	5.4	3.2	0.1	0.86	0.59
137	5.8	4.7	2.3	0.1	0.81	0.49
138	5.1	4.0	3.0	0.2	0.78	0.75
139	5.7	4.2	3.6	0.4	0.74	0.86
140	6.0	4.8	3.6	0.1	0.80	0.75
141	5.2	4.1	3.3	0.1	0.79	0.80
142	4.5	4.3	3.5	0.5	0.96	0.81
143	4.8	4.6	3.4	0.3	0.96	0.74
144	4.3	3.0	2.9	0.1	0.70	0.97
145	23.1	20.8	13.0	0.4	0.90	0.63
146	26.1	17.9	13.6	0.3	0.69	0.76
147	16.4	14.6	9.7	0.1	0.89	0.66
148	14.9	9.6	6.3	0.1	0.64	0.66
149	26.9	17.1	11.0	0.1	0.64	0.64
150	27.0	17.4	14.6	0.6	0.64	0.84
151	9.3	7.3	5.4	0.2	0.78	0.74
152	27.6	22.4	14.7	0.4	0.81	0.66
153	25.3	11.6	9.7	0.2	0.46	0.84
154	29.4	21.8	17.1	0.2	0.74	0.78
155	10.2	8.5	5.8	0.1	0.83	0.68
156	14.1	10.5	8.9	0.1	0.74	0.85
157	14.0	13.3	10.3	0.2	0.95	0.77
158	10.3	6.4	6.3	0.1	0.62	0.98
159	33.1	24.3	17.5	0.5	0.73	0.72
160	18.4	16.0	11.3	0.2	0.87	0.71
161	31.3	26.8	21.6	0.4	0.86	0.81
162	17.9	13.7	11.9	0.1	0.77	0.87
163	14.0	9.4	8.3	0.1	0.67	0.88
164	12.3	6.5	5.1	0.1	0.53	0.78
165	37.4	17.1	12.6	0.3	0.46	0.74
166	18.1	16.5	16.1	0.2	0.91	0.98
167	46.3	43.3	28.4	0.7	0.94	0.66
168	48.8	38.6	31.5	0.5	0.79	0.82
169	17.0	13.3	9.1	0.3	0.78	0.68
170	53.0	43.8	40.0	0.6	0.83	0.91
171	9.3	5.6	6.4	0.2	0.60	1.14
172	35.0	24.3	19.4	0.1	0.69	0.80
173	28.7	25.3	16.3	0.7	0.88	0.64
174	35.1	25.4	17.6	0.2	0.72	0.69
175	54.6	48.1	36.4	0.4	0.88	0.76
176	18.6	13.0	10.4	0.1	0.70	0.80
177	18.2	12.4	10.3	0.2	0.68	0.83
178	26.8	22.4	11.9	0.1	0.84	0.53
179	50.7	40.2	34.0	0.6	0.79	0.85
180	35.6	27.2	21.1	0.5	0.76	0.78
181	18.3	13.9	8.1	0.1	0.76	0.58
182	30.1	23.3	9.0	0.2	0.77	0.39
183	20.9	9.2	5.0	0.1	0.44	0.54
184	55.3	42.5	34.3	0.5	0.77	0.81
185	22.8	17.4	16.0	0.2	0.76	0.92
186	49.4	28.3	16.7	0.4	0.57	0.59
187	27.1	19.0	13.6	0.2	0.70	0.72
188	12.6	12.2	9.5	0.1	0.97	0.78
189	43.9	27.1	24.1	0.5	0.62	0.89
190	14.1	11.1	8.6	0.1	0.79	0.77
191	16.9	9.4	7.0	0.1	0.56	0.74
192	9.9	7.4	5.7	0.2	0.75	0.77
193	16.0	13.1	11.0	0.1	0.82	0.84
194	17.8	10.4	9.3	0.2	0.58	0.89
195	18.3	15.0	10.9	0.3	0.82	0.73
196	26.0	18.2	13.8	0.2	0.70	0.76
197	19.9	17.4	11.3	0.1	0.87	0.65

Appendix (continued).

Clast number	Size measurement (mm)			Roundness and sphericity measurements		
	Long axis (L)	Middle axis (M)	Short axis (S)	Carver/Krumbein Roundness	Krumbein plots M/L	Krumbein plots S/M
198	21.3	15.3	11.3	0.4	0.72	0.74
199	15.3	13.8	12.0	0.3	0.90	0.87
200	9.1	6.2	5.6	0.1	0.68	0.90
201	18.1	17.4	7.8	0.2	0.96	0.45
202	77.4	45.2	22.1	0.2	0.58	0.49
203	19.9	16.3	7.6	0.1	0.82	0.47
204	57.2	47.4	43.9	0.5	0.83	0.93
205	70.2	50.3	47.4	0.7	0.72	0.94
206	41.5	40.4	31.6	0.4	0.97	0.78
207	46.5	44.6	33.3	0.7	0.96	0.75
208	24.4	24.2	20.7	0.7	0.99	0.86
209	31.8	25.8	24.4	0.2	0.81	0.95
210	56.6	44.9	22.3	0.8	0.79	0.50
211	61.2	37.2	23.8	0.7	0.61	0.64
212	50.5	30.0	14.7	0.2	0.59	0.49
213	61.3	37.2	31.6	0.5	0.61	0.85
214	62.4	44.0	36.6	0.6	0.71	0.83
215	52.6	37.6	33.8	0.7	0.71	0.90
216	57.3	33.2	25.5	0.6	0.58	0.77
217	26.2	24.5	18.5	0.2	0.94	0.76
218	44.4	32.3	24.5	0.4	0.73	0.76
219	41.9	40.4	15.8	0.3	0.96	0.39
220	31.2	24.8	19.4	0.1	0.79	0.78
221	23.0	22.2	19.8	0.2	0.97	0.89
222	39.0	19.5	15.6	0.2	0.50	0.80
223	41.9	37.4	16.3	0.3	0.89	0.44
224	27.4	20.5	13.7	0.2	0.75	0.67
225	35.1	24.6	19.5	0.6	0.70	0.79
226	31.5	27.0	20.0	0.1	0.86	0.74
227	23.4	21.7	21.6	0.3	0.93	1.00
228	19.8	19.0	15.3	0.1	0.96	0.81
229	38.8	35.8	20.0	0.3	0.92	0.56
230	51.7	46.6	34.4	0.5	0.90	0.74
231	33.8	30.3	17.9	0.6	0.90	0.59
232	27.0	17.8	16.8	0.1	0.66	0.94
233	69.4	38.8	20.3	0.1	0.56	0.52
234	21.0	12.6	12.3	0.1	0.60	0.98
235	24.8	20.2	18.0	0.4	0.81	0.89
236	26.3	25.8	17.4	0.1	0.98	0.67
237	49.3	45.0	39.2	0.2	0.91	0.87
238	31.0	23.6	18.4	0.3	0.76	0.78
239	71.9	58.7	55.8	0.7	0.82	0.95
240	30.4	16.4	15.2	0.7	0.54	0.93
241	21.9	12.7	11.0	0.8	0.58	0.87
242	75.9	58.6	53.6	0.5	0.77	0.91
243	57.4	42.8	25.0	0.2	0.75	0.58
244	36.6	15.8	12.4	0.2	0.43	0.78
245	12.6	12.2	7.5	0.1	0.97	0.61
246	15.3	10.5	9.2	0.1	0.69	0.88
247	69.0	57.8	48.2	0.7	0.84	0.83

Note: This table is also available in **ASCII format.**

Figure F1. Bathymetry of the Southern Mariana forearc (500-m contour intervals).

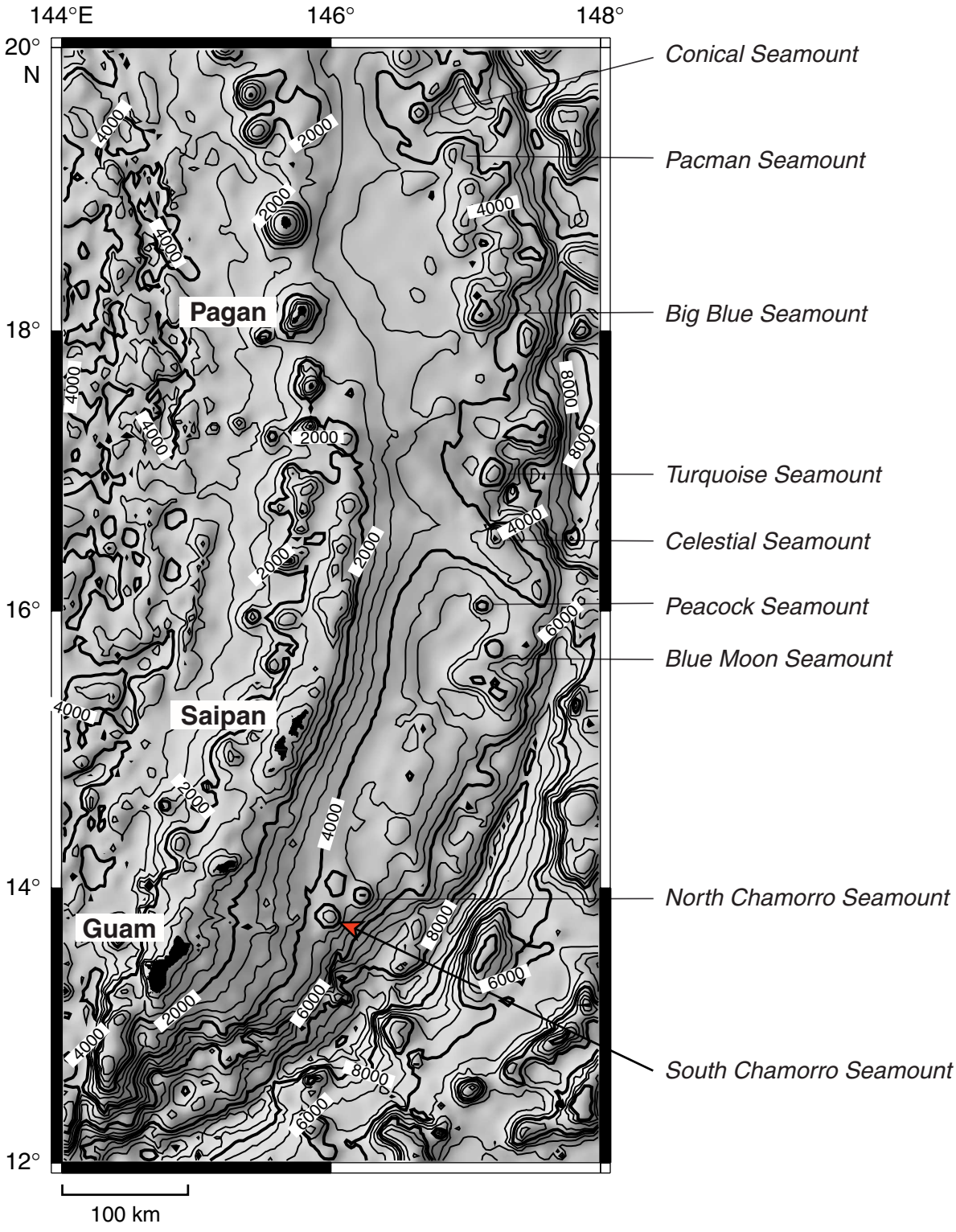

Figure F2. Location of Site 1200 (HMR-1 side-scan imagery).

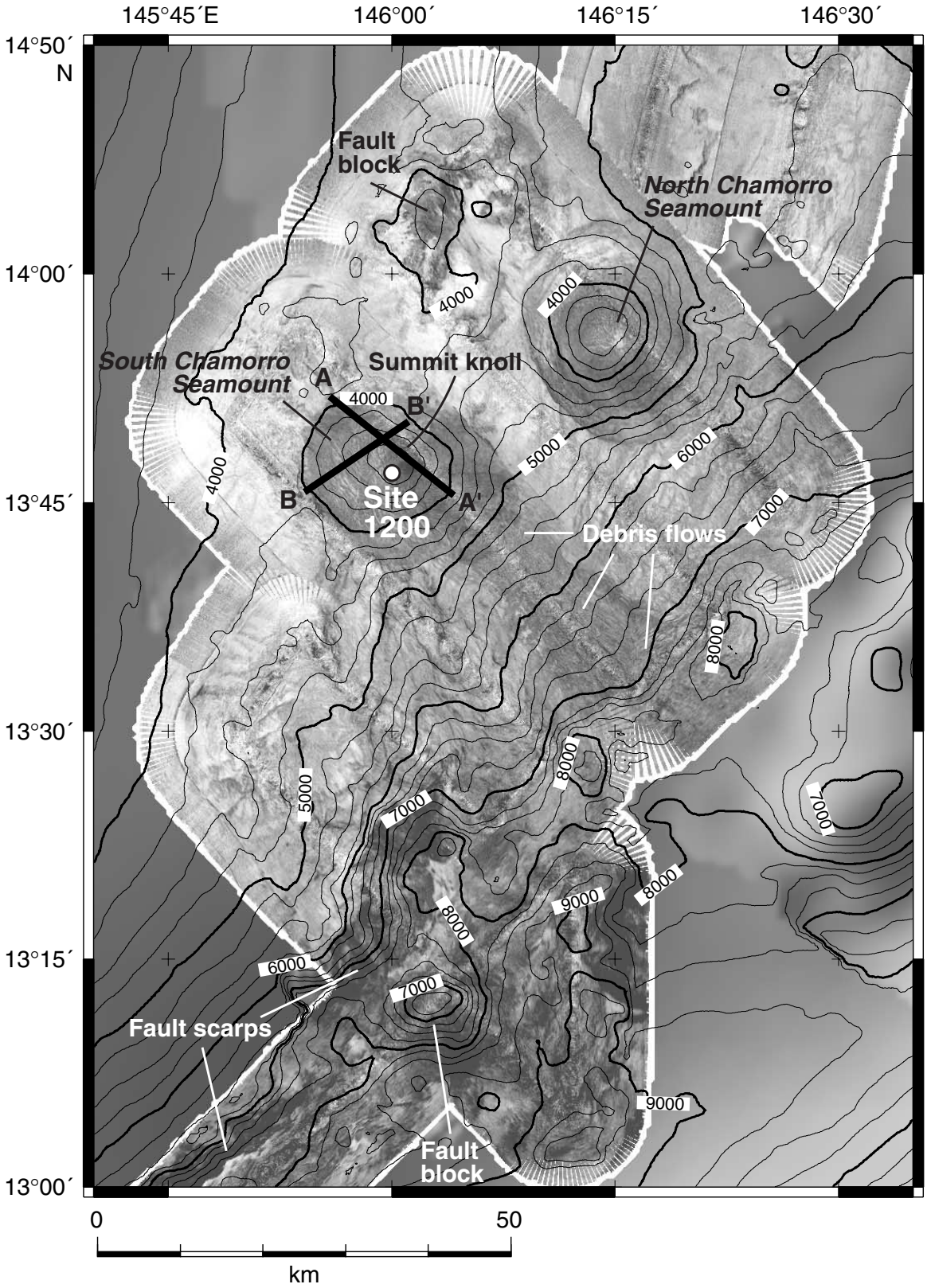

Figure F3. Video camera survey tracks with location points referenced in the text and positions of Site 1200 holes.

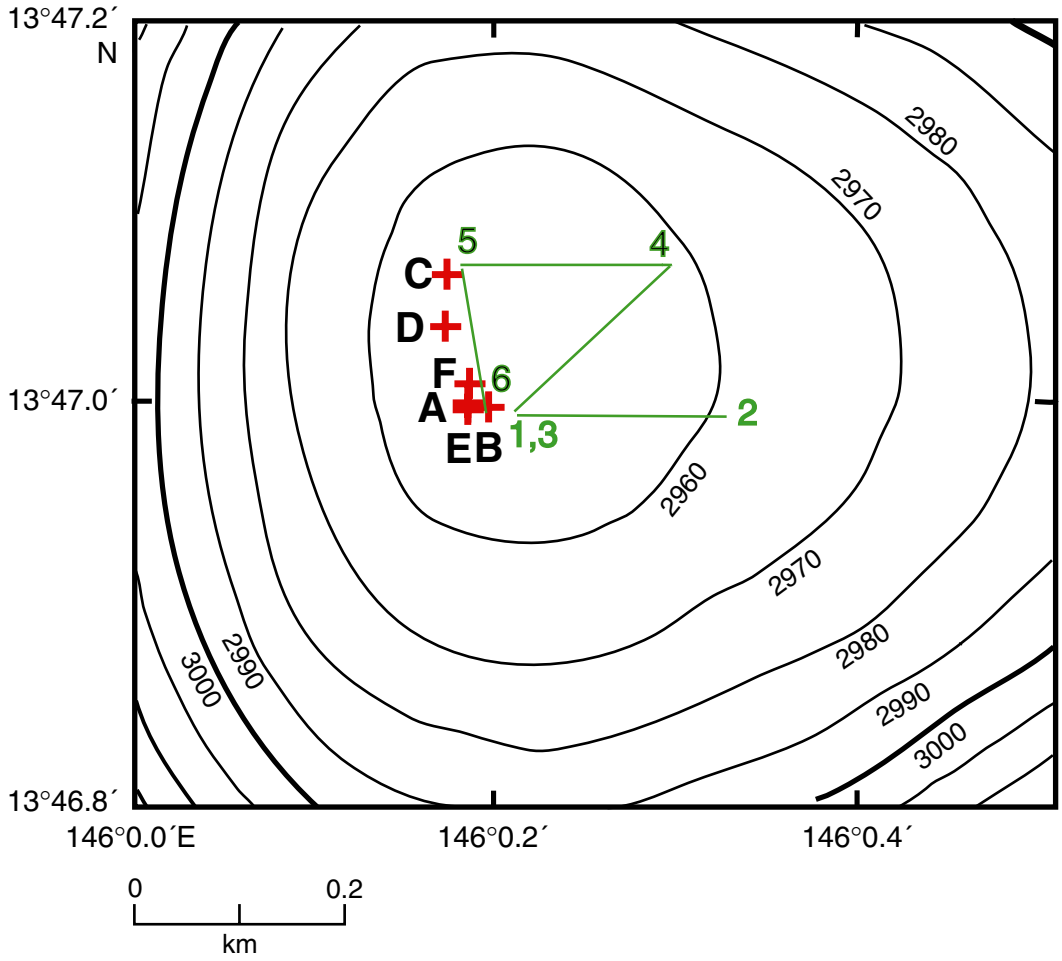

Figure F4. Summary figure for Site 1200 including lithology, color reflectance, and calcareous intervals. Yellow intervals in the "Unit" column indicate intervals of Facies I. Light blue intervals in the same column indicate intervals of Facies II. Color reflectance parameter b* measures the amount of reflectance in the blue vs. yellow spectra. Carbonate intervals were identified using 10% HCl acid tests at regularly spaced intervals. Color reflectance values correlate well with carbonate intervals; however, the overall heterogeneity of the material produces spectral peaks in non-calcareous intervals. TD = total depth. See Figure **F4,** p. 42, in the "Explanatory Notes" chapter for a key to the lithology symbols.

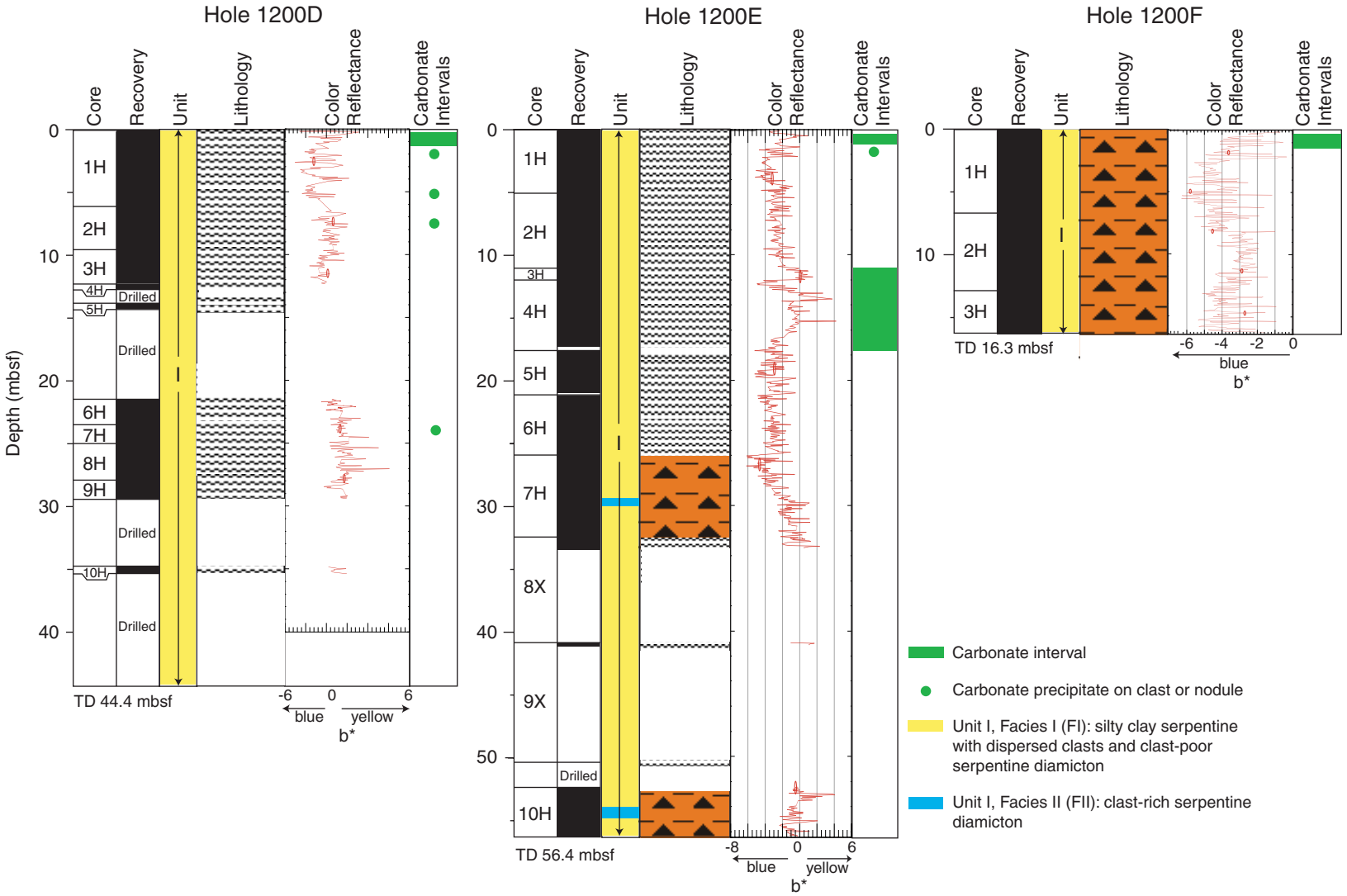

Figure F5. Silty clay serpentine with dispersed clasts typical of Facies I (interval 195-1200E-6H-2, 40–70 cm).

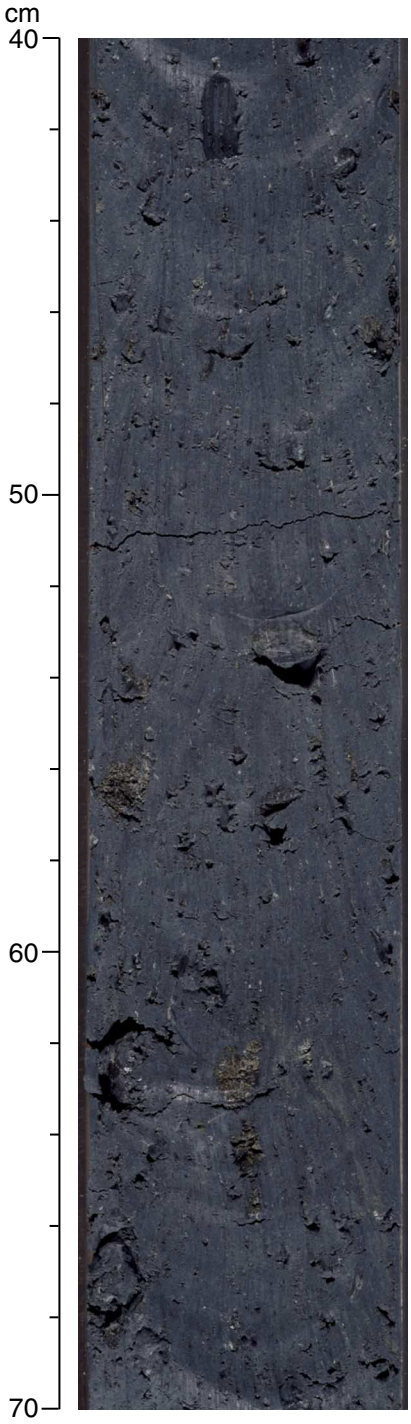

Figure F6. Clast-poor serpentine diamicton typical of Facies I (interval 195-1200E-7H-1, 60–85 cm).

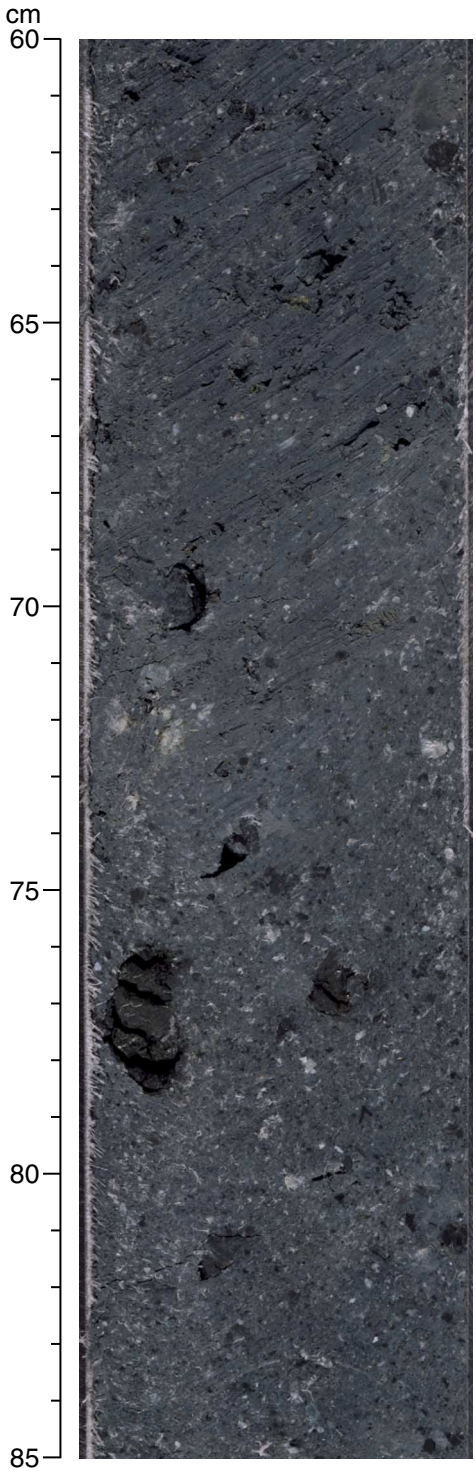

Figure F7. Clast-rich serpentine diamicton characteristic of Facies II (interval 195-1200E-10H-2, 83–113 cm).

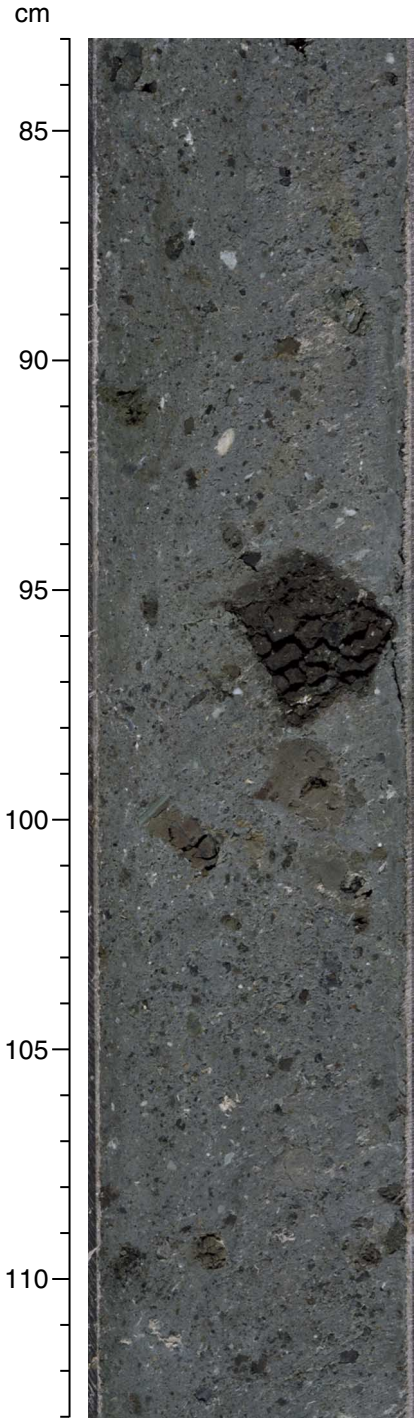

Figure F8. Color variability within oxidized calcareous intervals (interval 195-1200E-4H-3, 24–44 cm).

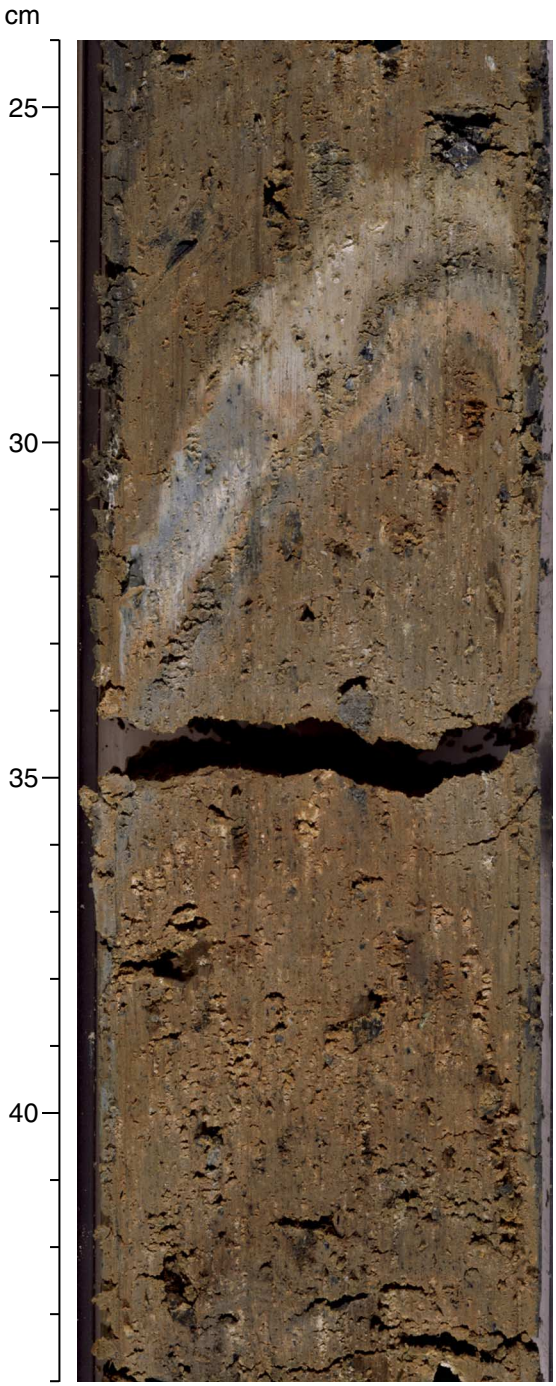

Figure F9. Thin section of silty clay–sized serpentine matrix showing typical unsorted grain-size texture (Sample **195-1200F-1H-4, 34–36 cm**) (crossed polarizers; 10× magnification). The groundmass consists of silt-sized serpentine flakes. Larger embedded sand-sized grains consist of serpentine flakes or represent altered lithoclasts (upper left and right) that were replaced pseudomorphously by serpentine (white and gray interference colors) and brucite (brown interference colors).

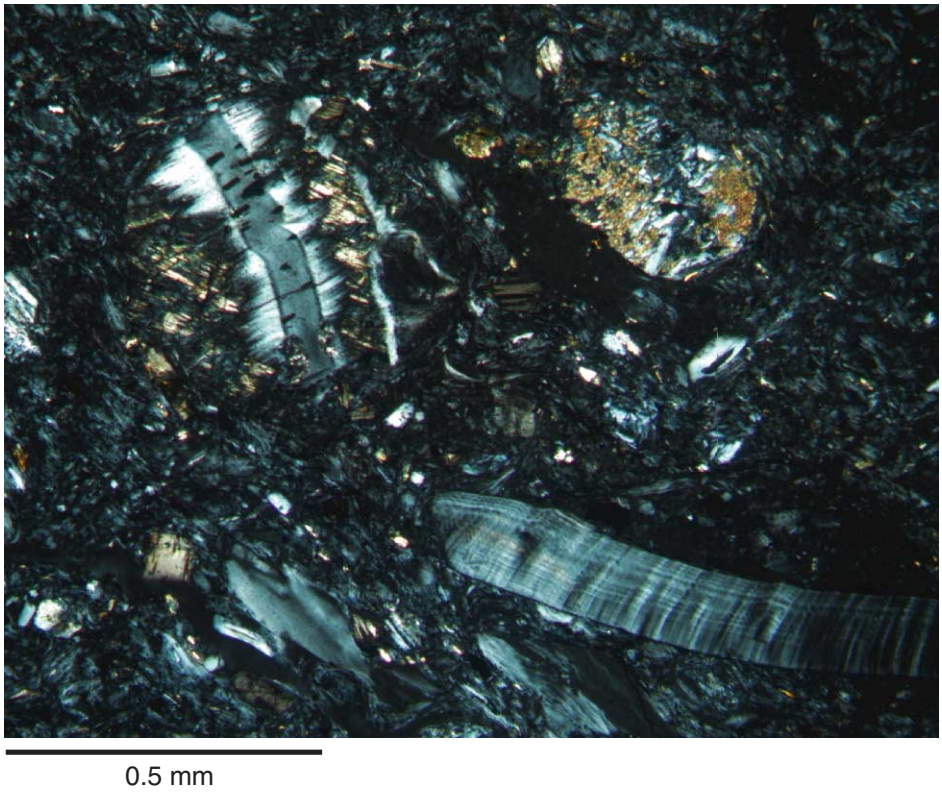

Figure F10. Major constituents of silty clay–sized serpentine encountered in smear slides of the fine-sand fraction (63- to 344-µm grain size). **A.** Four species of flaky serpentine minerals comprising fresh and translucent flakes (Serp-F), dusky and slightly altered flakes (Serp-A1), strongly altered serpentines that were replaced by opaque material (Serp-A2), and serpentines with internal lamellae (Serp-L). **B.** Serpentine flakes with one specimen exhibiting a euhedral hexagonal outline. **C.** Chrysotile fibers (Serp-C) under plane-polarized light. **D.** Chrysotile fibers (Serp-C) under crossed polarizers. **E.** Detail of Serp-L species. **F.** Authigenic zeolite-like mineral from a concretionary nodule in black serpentine silty clay.

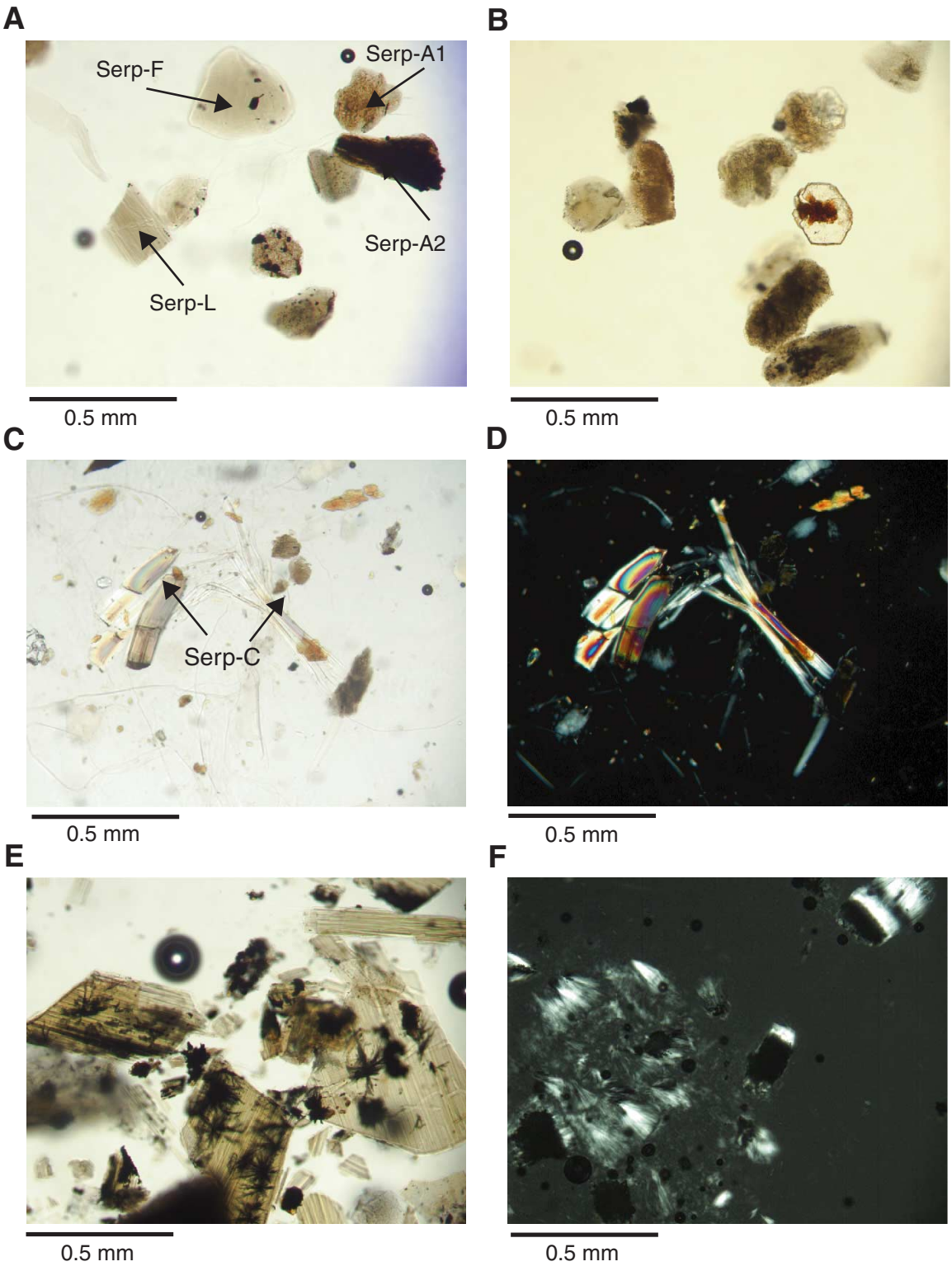

Figure F11. Major constituents of silty clay–sized serpentine encountered in smear slides of the fine-sand fraction (63- to 344-µm grain size). **A.** Pale bluish amphibole under plane-polarized light. **B.** Pale bluish amphibole under crossed polarizers, revealing internal zonation. **C, D.** Elongated authigenic aragonite laths (Ar), blue amphibole (Am), and serpentine flakes (Serp-A2). **E, F.** Bunches and "mikado"-like clusters of tiny aragonite needles.

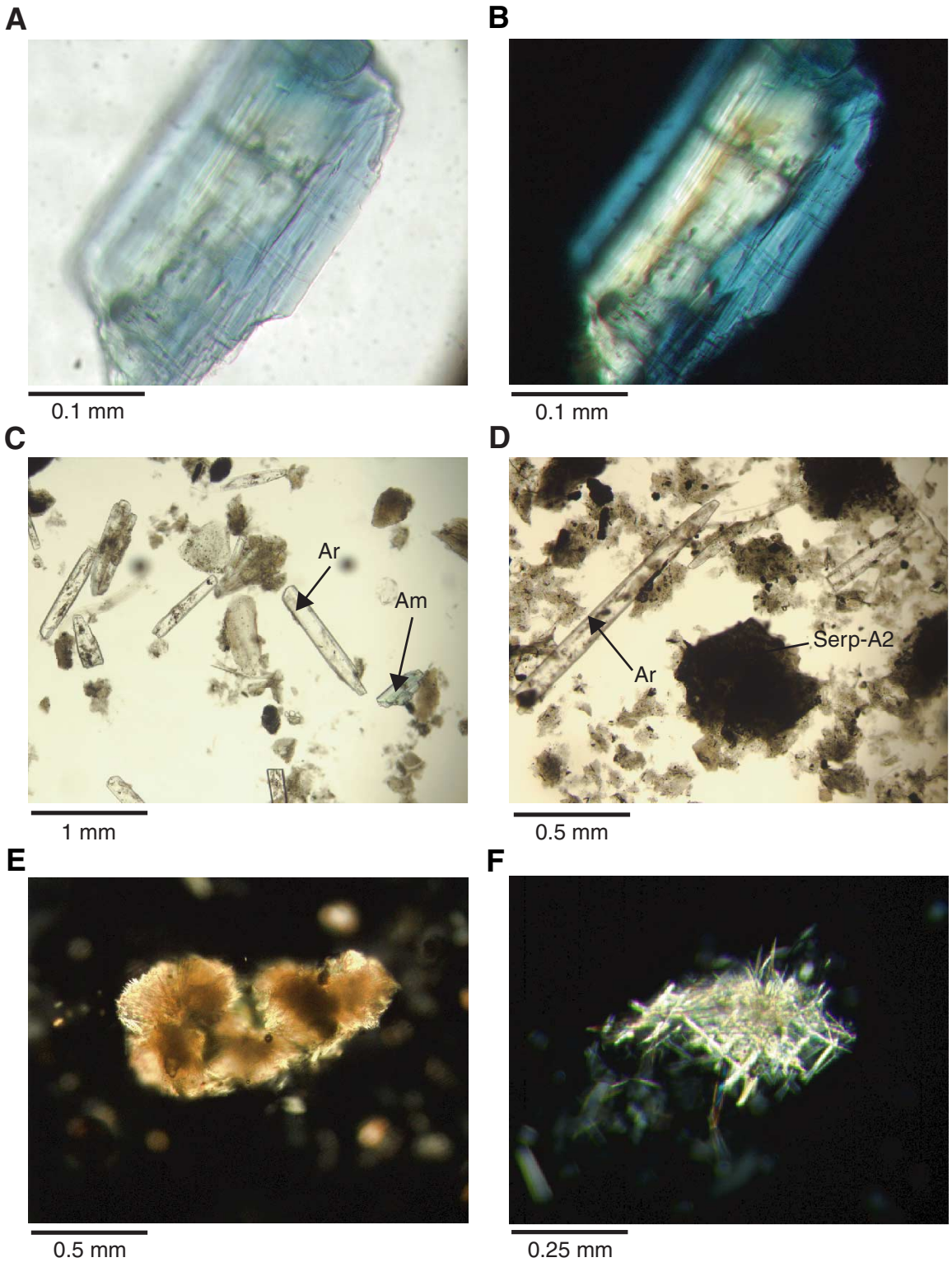

Figure F12. Typical XRD patterns of rock pieces and silty clay–sized serpentine measured on bulk powder mounts. Serp = serpentine minerals, Bru = brucite, Opx = othopyroxene, Cpx = clinopyroxene, Fo = forsterite, ML = mixed-layer clay mineral, Chl = chlorite, Ar = aragonite, Cc = calcite, Am = amphibole, Zeo? = suspected analcime, Ha = halite.

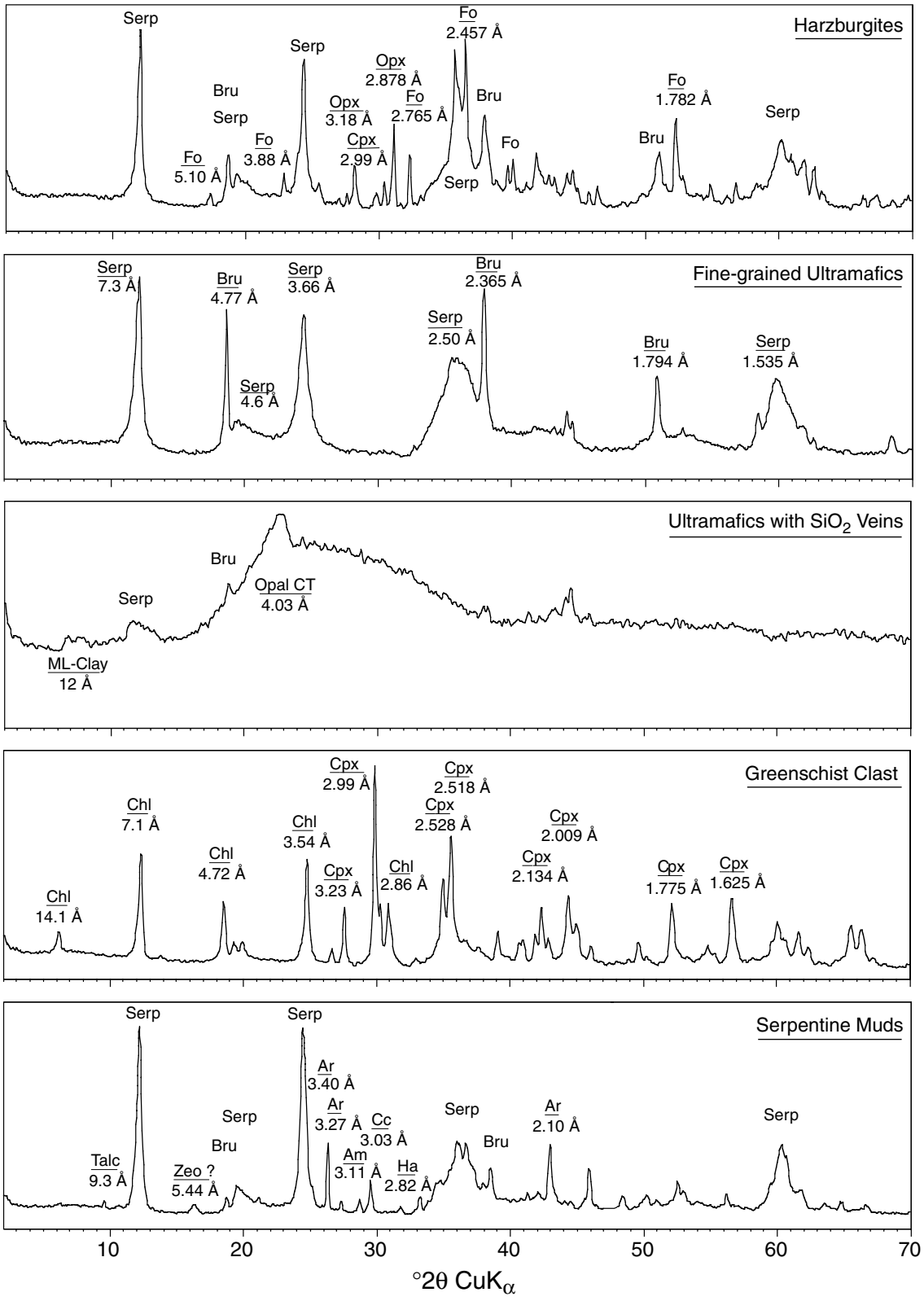

Figure F13. Downhole changes in semiquantitative mineralogy of silty clay–sized serpentine in Hole 1200D, as inferred from XRD analyses of bulk powder mounts. Abundance: D = dominant (50%–100%), A = abundant (20%–50%), C = common (5%–20%), P = present (1%–5%). TD = total depth.

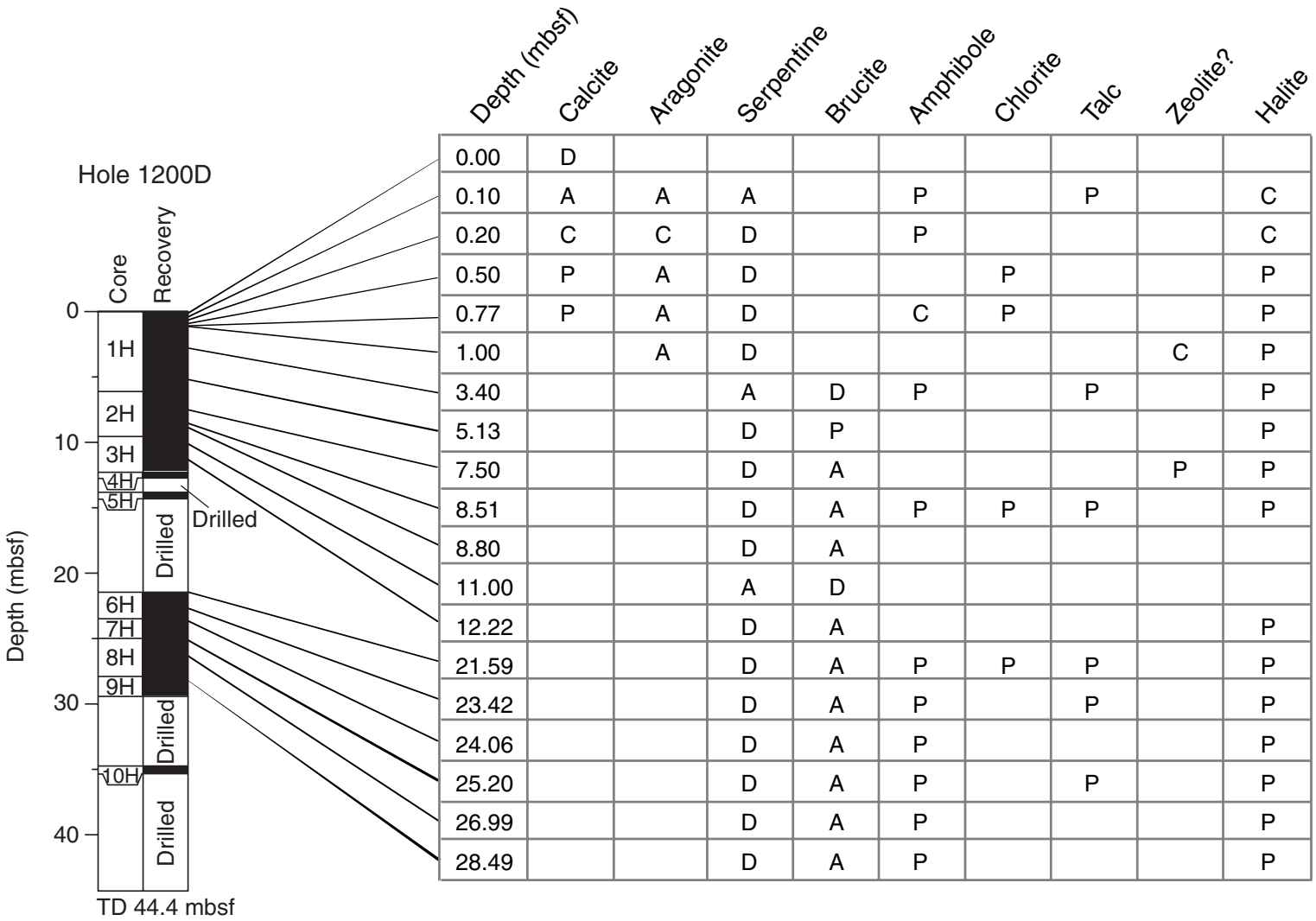

Depth (mbsf)	Calcite	Aragonite	Serpentine	Brucite	Amphibole	Chlorite	Talc	Zeolite?	Halite
0.00	D								
0.10	A	A	A		P		P		C
0.20	C	C	D		P				C
0.50	P	A	D			P			P
0.77	P	A	D		C	P			P
1.00		A	D					C	P
3.40			A	D	P		P		P
5.13			D	P					P
7.50			D	A				P	P
8.51			D	A	P	P	P		P
8.80			D	A					
11.00			A	D					
12.22			D	A					P
21.59			D	A	P	P	P		P
23.42			D	A	P		P		P
24.06			D	A	P				P
25.20			D	A	P		P		P
26.99			D	A	P				P
28.49			D	A	P				P

Figure F14. Downhole changes in semiquantitative mineralogy of silty clay–sized serpentine in Hole 1200E, as inferred from XRD analyses of bulk powder mounts. Abundance: D = dominant (50%–100%), A = abundant (20%–50%), C = common (5%–20%), P = present (1%–5%). TD = total depth.

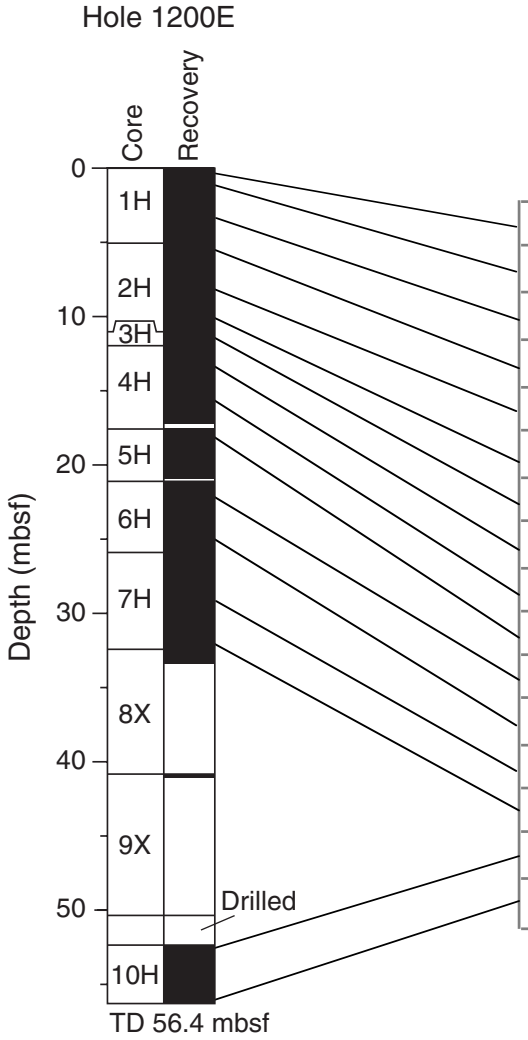

Depth (mbsf)	Calcite	Aragonite	Serpentine	Brucite	Amphibole	Chlorite	Talc	Zeolite?	Halite
0.14		D	A		P	P			C
1.09	P	D	A	P	P		P	P	P
3.29			D	A	P	P	P	P	P
5.49			D	A	P		P	P	P
7.89			D	A	P	P	P	P	P
10.19			D	C	C	P	C		P
11.74	C	D	A		P				P
12.57	P		A	A	P	P	P	P	P
15.70	C	A	A	P	P	P	P	P	P
18.90			D	A	P	P	P	P	P
22.19			D	A	P			P	P
25.28			D	A	P	P		P	P
28.39			D	A	P				P
32.08			D	A					P
52.59			D	C	C	P	P		P
55.80			D	C	P	P	P		P

Figure F15. Downhole changes in semiquantitative mineralogy of silty clay–sized serpentine in Hole 1200F, as inferred from XRD analyses. Abundance: D = dominant (50%–100%), A = abundant (20%–50%), C = common (5%–20%), P = present (1%–5%). TD = total depth.

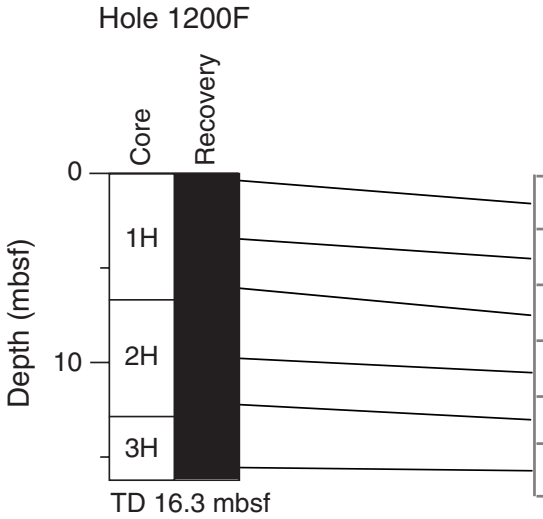

Depth (mbsf)	Calcite	Aragonite	Serpentine	Brucite	Amphibole	Chlorite	Talc	Zeolite?	Halite
0.39	P	D	A	P	P				P
3.40			D	A	P	P	P	P	P
6.59			D	A	P	P	P	P	P
9.70			D	C	C	P	P	P	P
12.40			D	C	C	P	P	P	P
15.44			D	C	P	P	P	P	P

Figure F16. Color photograph of large serpentinite clast included in matrix of variably oxidized yellow-brown to blue colored serpentine mud (interval 195-1200E-1H-1, 57–77 cm).

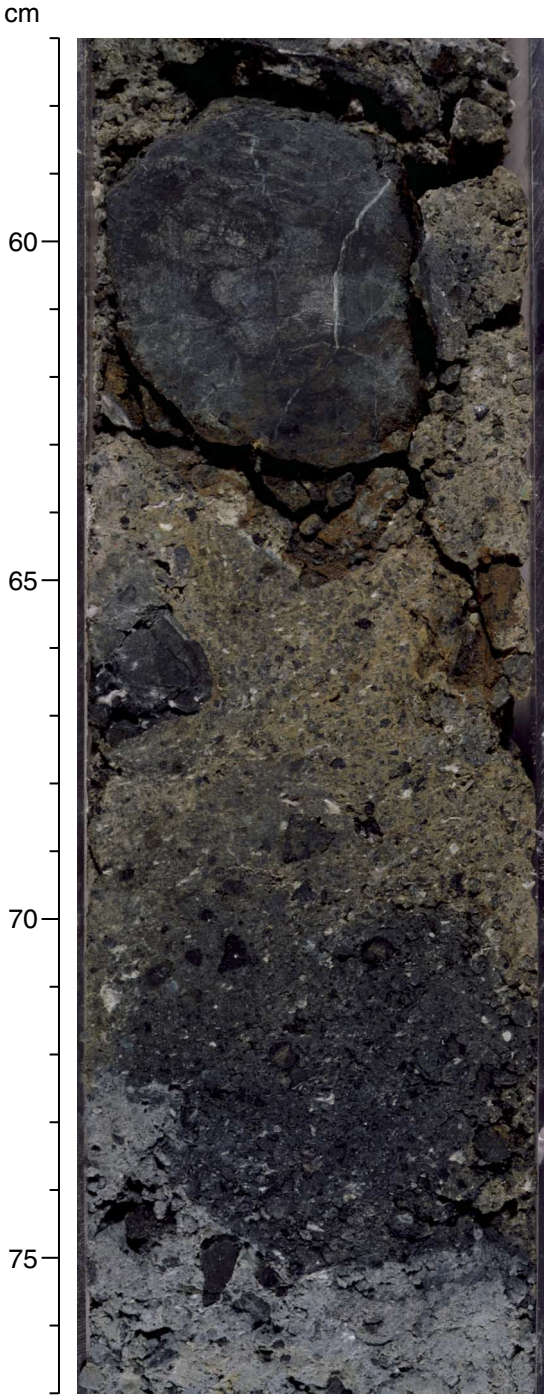

Figure F17. Photomicrograph in cross-polarized light of harzburgite sample showing the main mineral paragenesis (Sample 195-1200A-12R-1, 25–27 cm) (cross-polarized light). Ol = olivine, OPX = orthopyroxene, CPX = clinopyroxene, Cr spinel = chromium spinel.

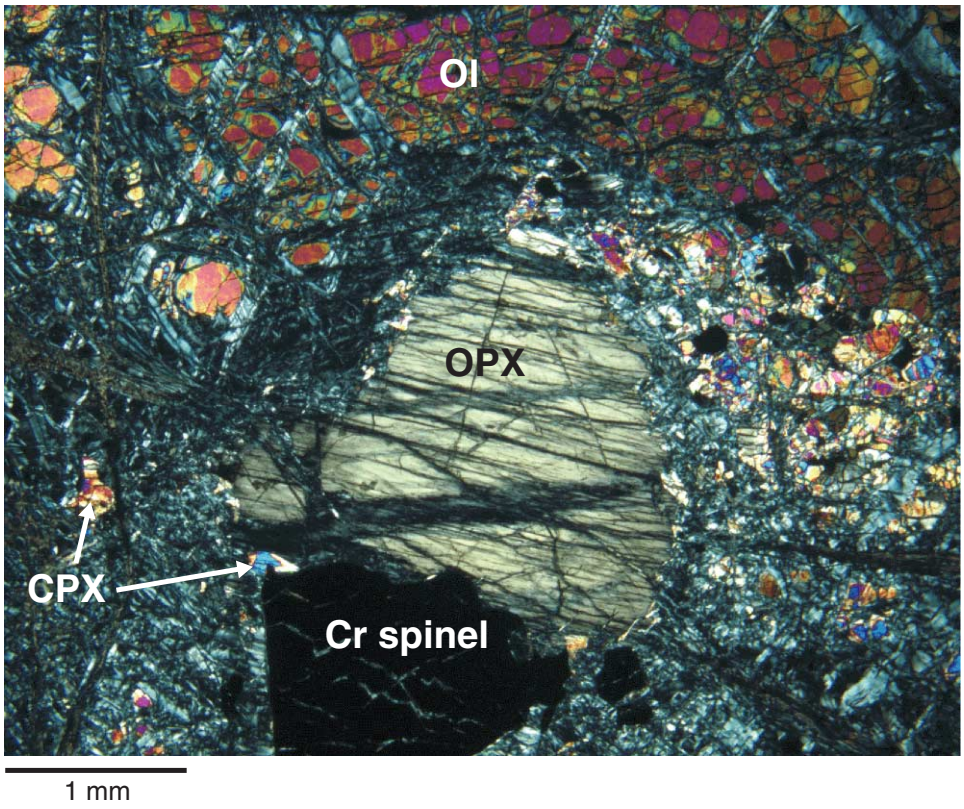

Figure F18. Color photograph of fresh harzburgite–dunite transition. Orthopyroxene grains in the harzburgite are altered to form typical bastitic texture (interval 195-1200A-3R-1, 36–75 cm).

Figure F19. Color photograph of coarse-grained harzburgite intersected by a large "Frankenstein"-like chrysotile vein. Orthopyroxene grains in the harzburgite are altered to form typical bastitic texture (interval 195-1200A-7R-1, 33–57 cm).

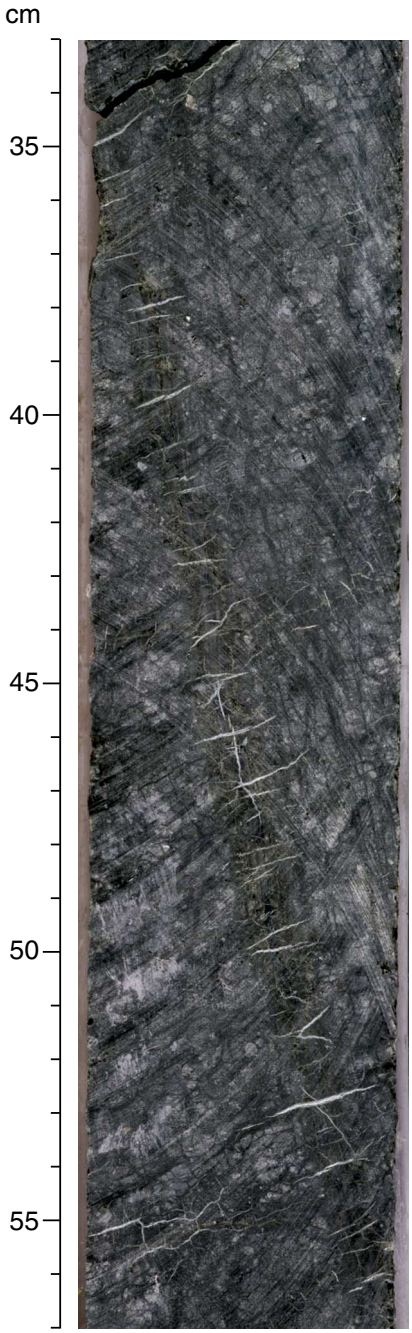

Figure F20. Photomicrograph of hourglass and mesh textures (Sample **195-1200A-14R-1, 22–25 cm**) (cross-polarized light).

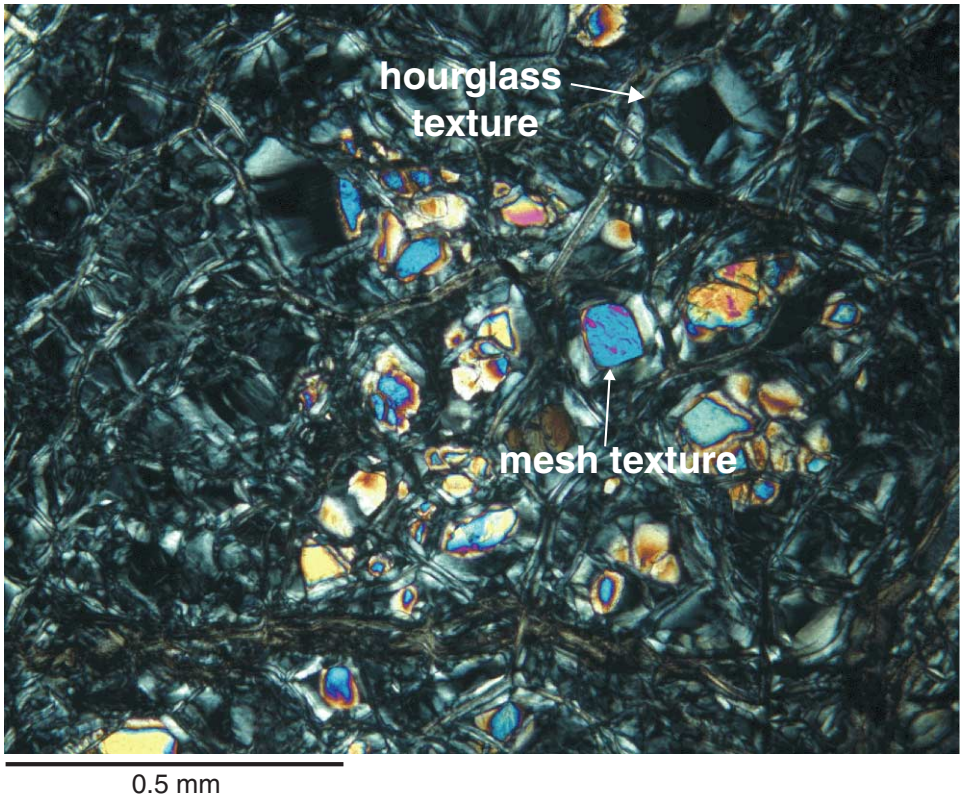

Figure F21. Photomicrograph of orthopyroxene with bastitic texture (Sample 195-1200A-13R-1, 89–92 cm) (cross-polarized light).

Figure F22. Photomicrograph of kink banding in olivine (Sample **195-1200A-12R-1, 25–27 cm**) (cross-polarized light).

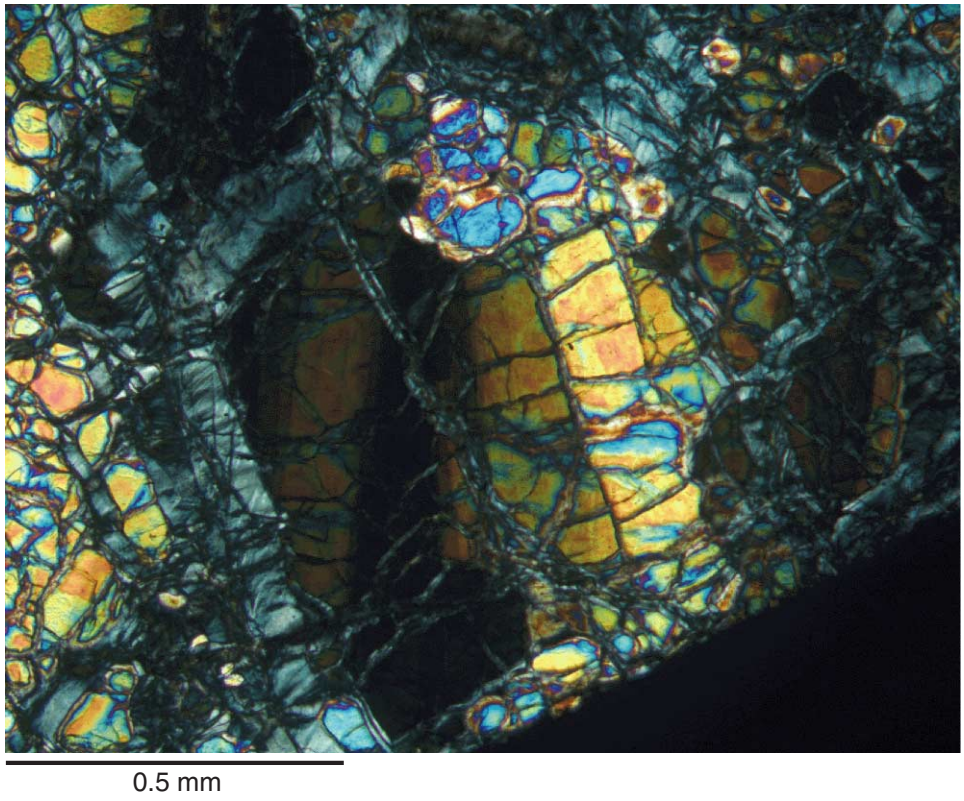

Figure F23. Photomicrograph of tectonized orthopyroxene showing undulatory extinction caused by plastic deformation (Sample **195-1200A-12R-1, 3–7 cm**) (cross-polarized light).

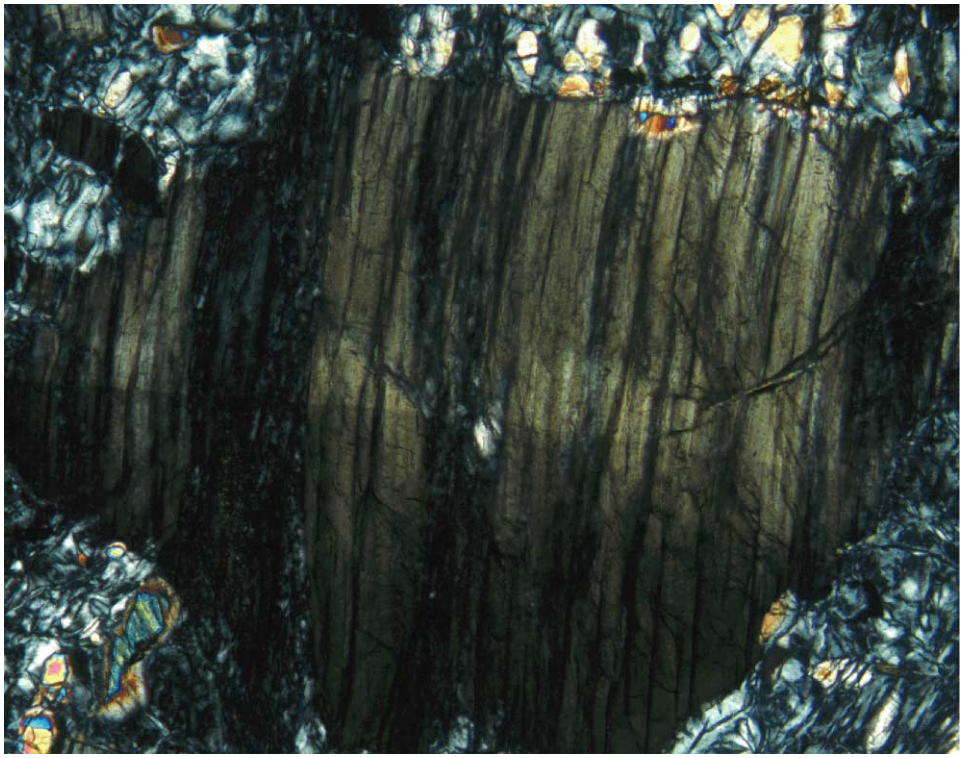

Figure F24. Photomicrograph showing clinopyroxene (CPX) included in orthopyroxene (OPX) (Sample 195-1200A-3R-1, 81–84 cm) (cross-polarized light).

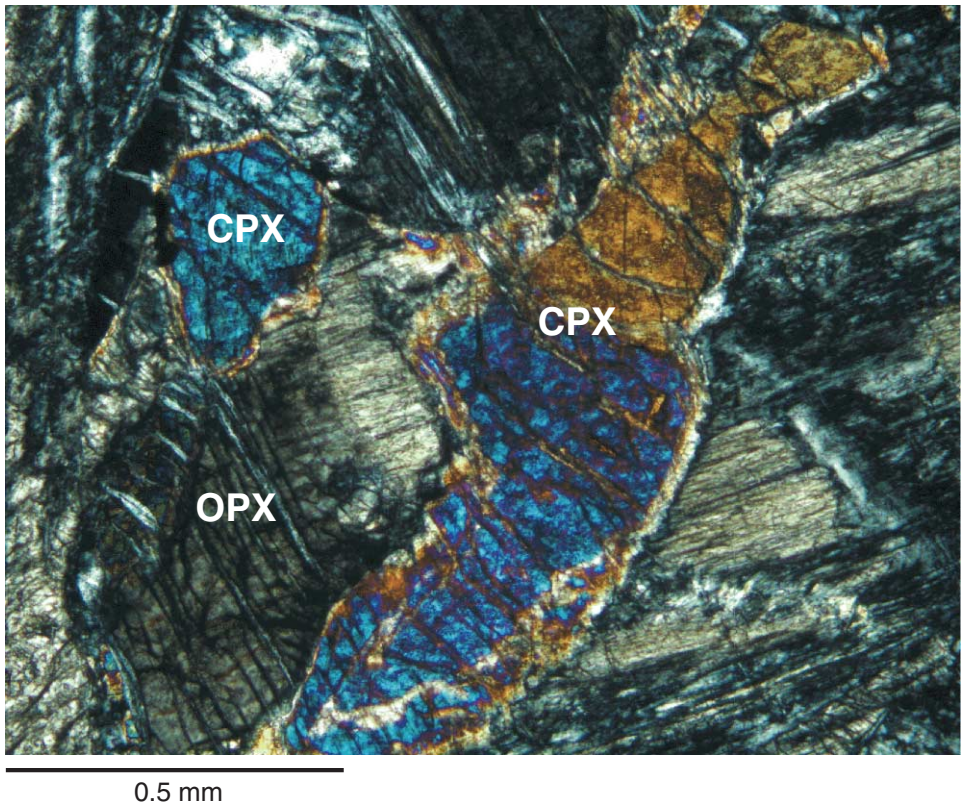

Figure F25. Photomicrograph showing Cr spinel with characteristic translucent dark red color, crosscut by serpentine veins (Sample **195-1200A-6R-1, 31–35 cm**) (plane-polarized light).

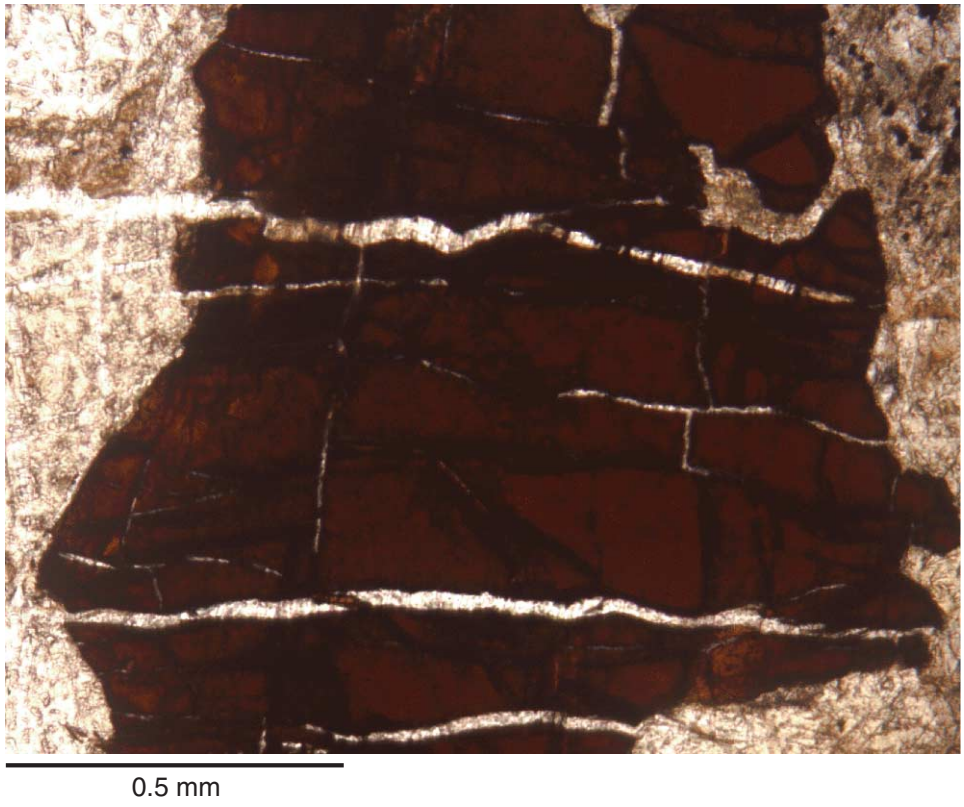

Figure F26. Photomicrograph of brucite showing anomalous reddish brown interference colors. The brucite is associated with magnetite and serpentine (Sample **195-1200D-1H-3, 89–93 cm**) (cross-polarized light).

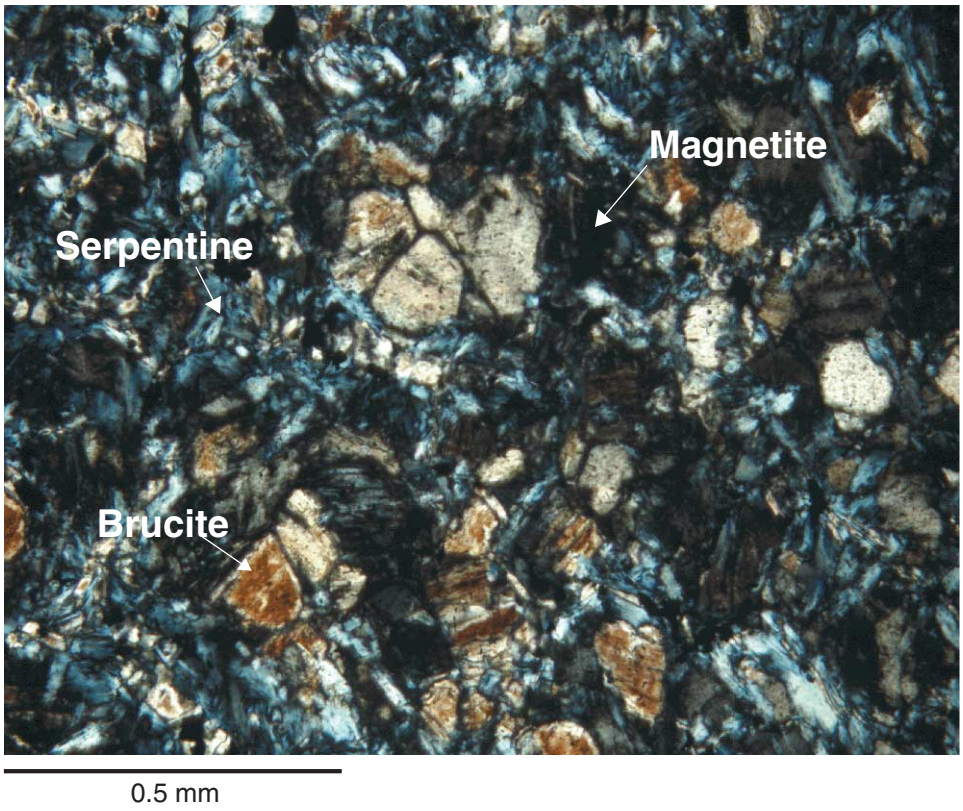

Figure F27. Color photograph of medium-grained harzburgite showing a "Frankenstein"-like chrysotile serpentine vein along the clast edge. The vein is intersecting another set of earlier serpentine veins (interval 195-1200A-6R-1, 38–70 cm).

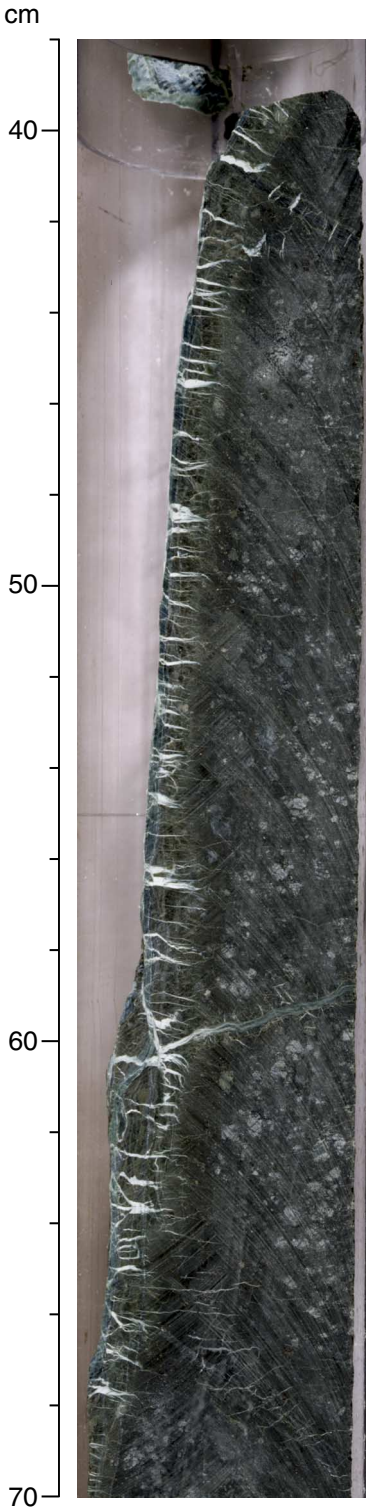

Figure F28. Color photograph of variably serpentinized dunite forming dark bands where completely altered. The banding of the sample is crosscut by later white chrysotile veins (interval 195-1200A-13R-1, 10–17 cm).

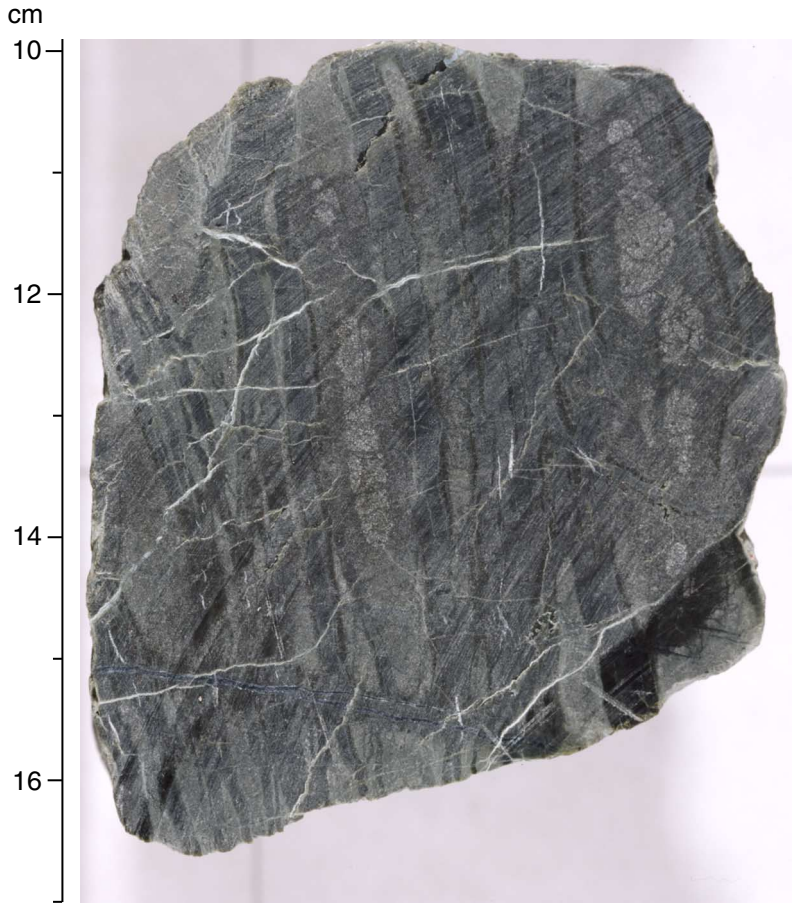

Figure F29. Photomicrograph showing a wide central vein of serpentine crosscut by subsidiary finer veins of chrysotile (Sample **195-1200A-7R-2, 27–29 cm**) (cross-polarized light).

Figure F30. Photomicrograph showing remnant of poikilitic texture where orthopyroxene encloses former olivine grain (Sample **195-1200A-12R-1, 3–7 cm**) (cross-polarized light).

Figure F31. Two pieces of mica-chlorite schist.

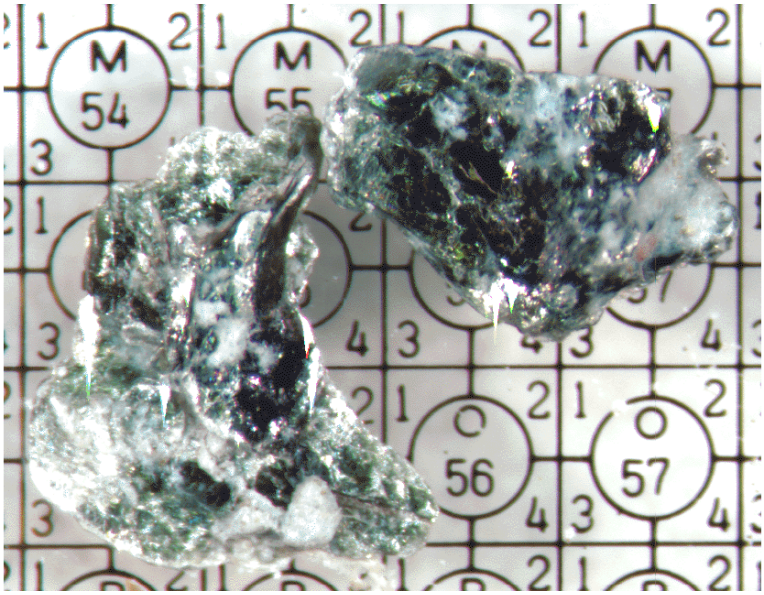

Figure F32. Photomicrograph of tremolite (Tr)-rich chlorite (Chl) schist found in serpentine mud (Sample 195-1200F-1H-4, 34–36 cm) (cross-polarized light).

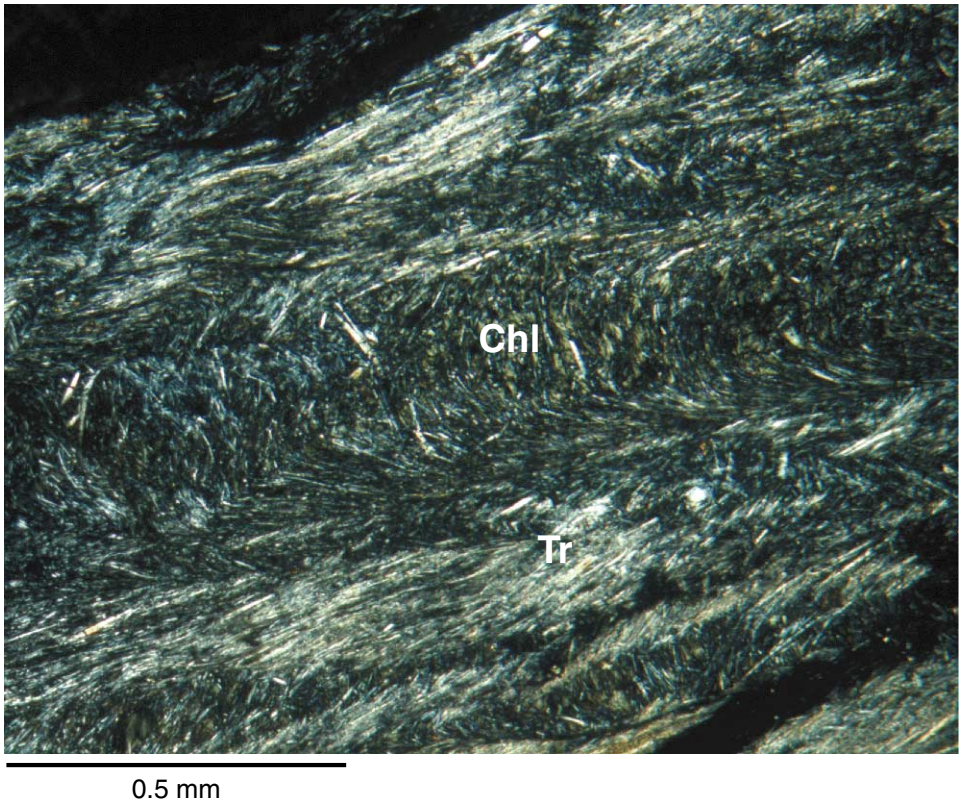

Figure F33. Color photograph of serpentine mud containing fragments of chlorite schist (60–63 cm) and extensively altered serpentinite (54–57 cm) (interval 195-1200D-8H-2, 50–70 cm).

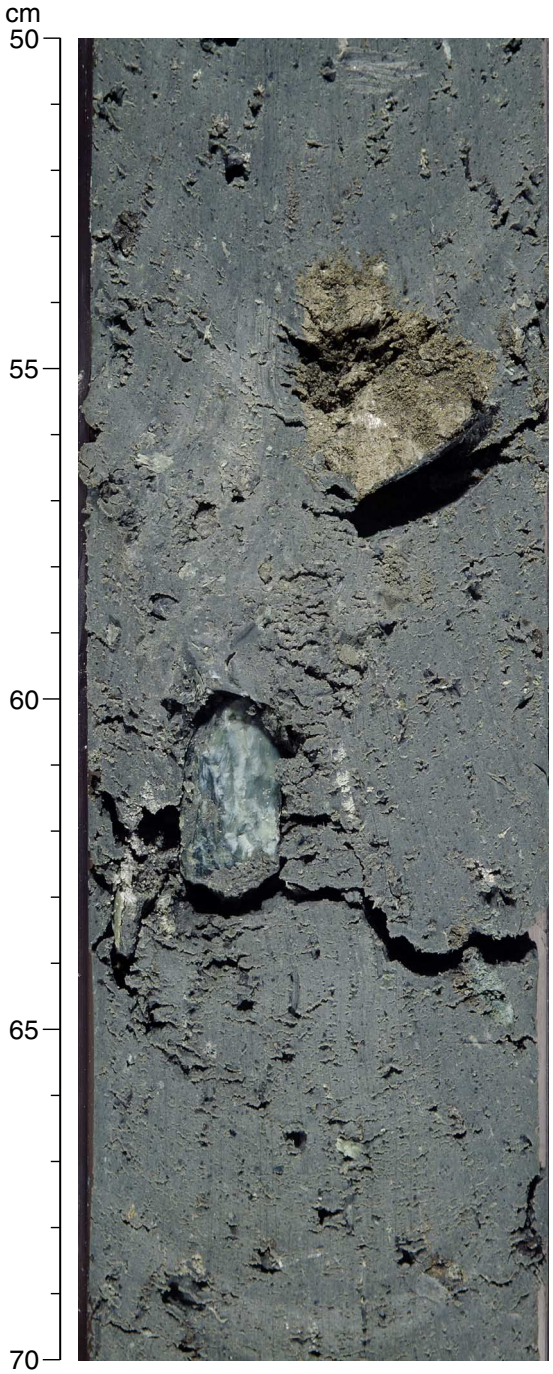

Figure F34. Image of three types of schists recovered from the wash material from Hole 1200B. The white mica schist on the right is 2 mm wide and 3 mm long. The three dark amphibole mica schists at the bottom are much coarser grained than the four Na-amphibole mica schists at the top of the picture.

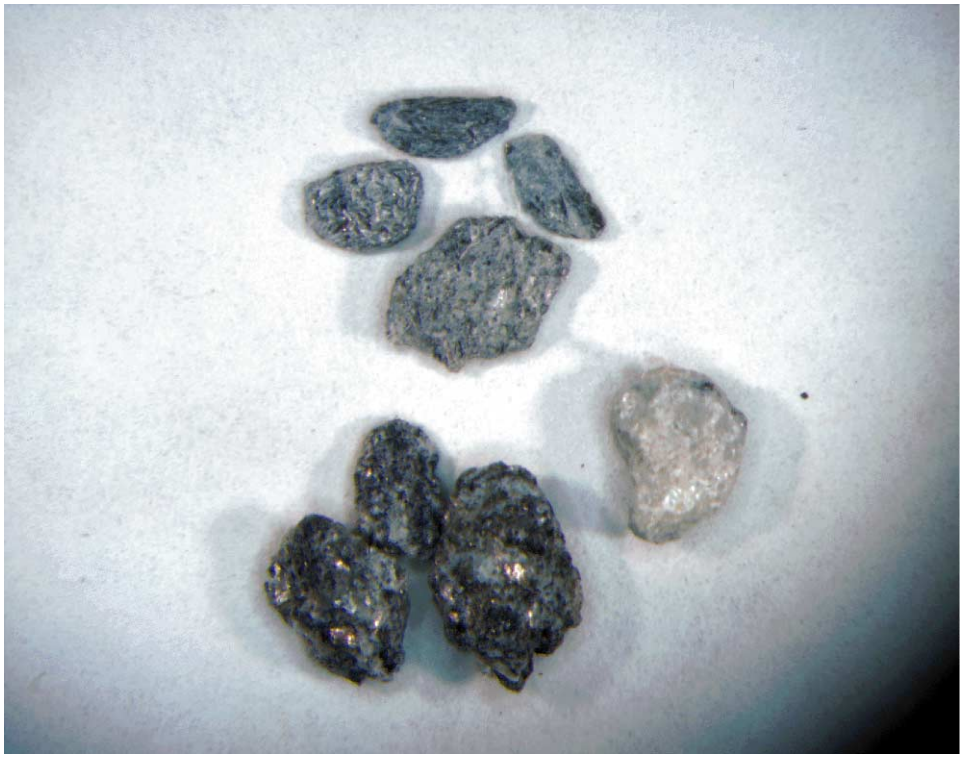

Figure F35. Photomicrograph of glaucophane (Gl) schist found in serpentine mud sample along with serpentinite and chlorite schist lithic fragments (Sample 195-1200F-1H-4, 34–36 cm) **A.** Plane-polarized light. **B.** Cross-polarized light.

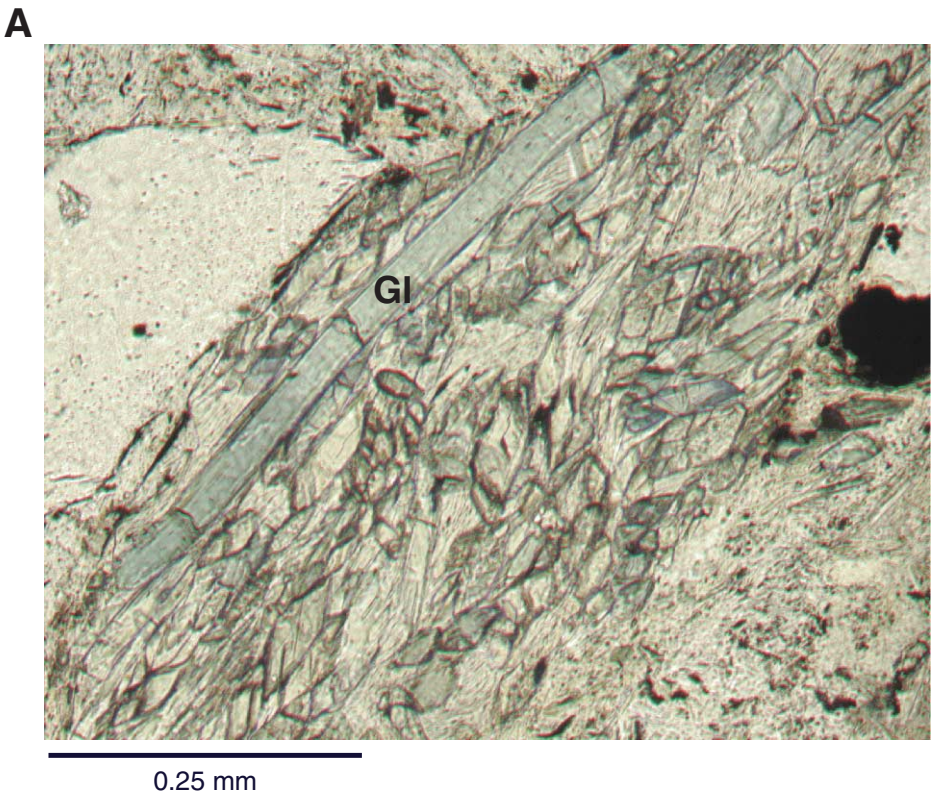

Figure F36. Image of a single piece of blue (sodic) amphibole schist containing white mica and possibly chlorite.

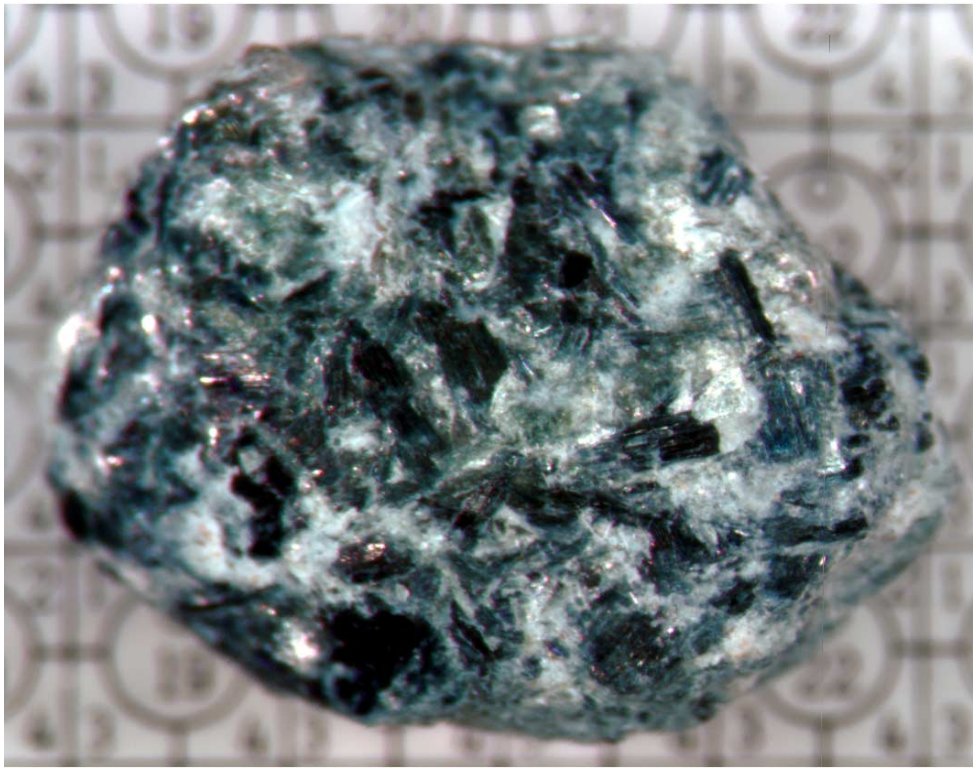

Figure F37. Color photograph of clast-poor blue serpentine mud (interval 195-1200E-1H-1, 12–30 cm).

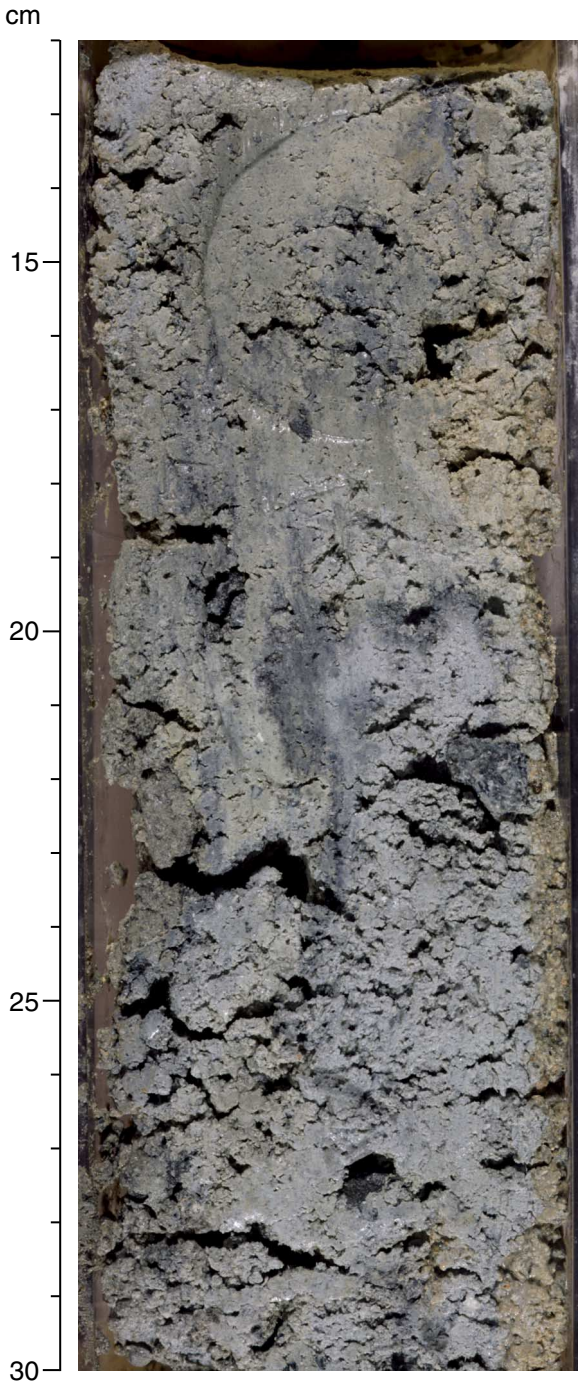

Figure F38. Color photograph of the uppermost section of Hole 1200D, where 4 cm of yellow-brown mud horizon on top reflects the seawater-mud interaction. Below this horizon, the mud is less affected by the seawater, as recorded by its blue color (interval 195-1200D-1H-1, 10–28 cm).

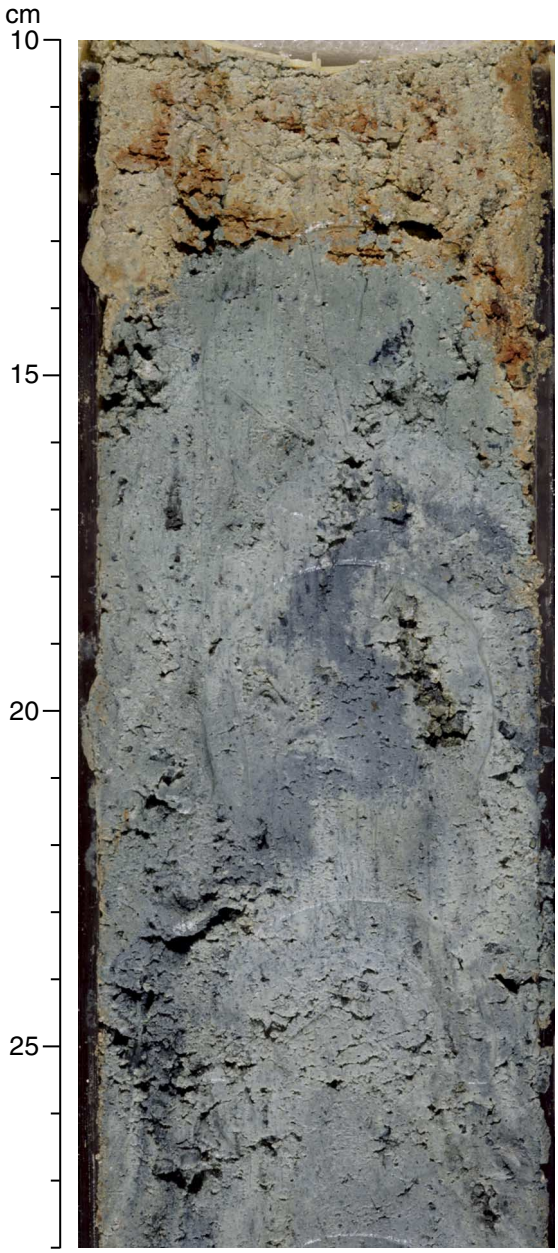

Figure F39. CIPW normative compositions of serpentinites from Site 1200 plotted in the International Union of Geological Societies (IUGS) classification system for ultramafic rocks. Most of the Site 1200 clasts are harzburgites or dunites.

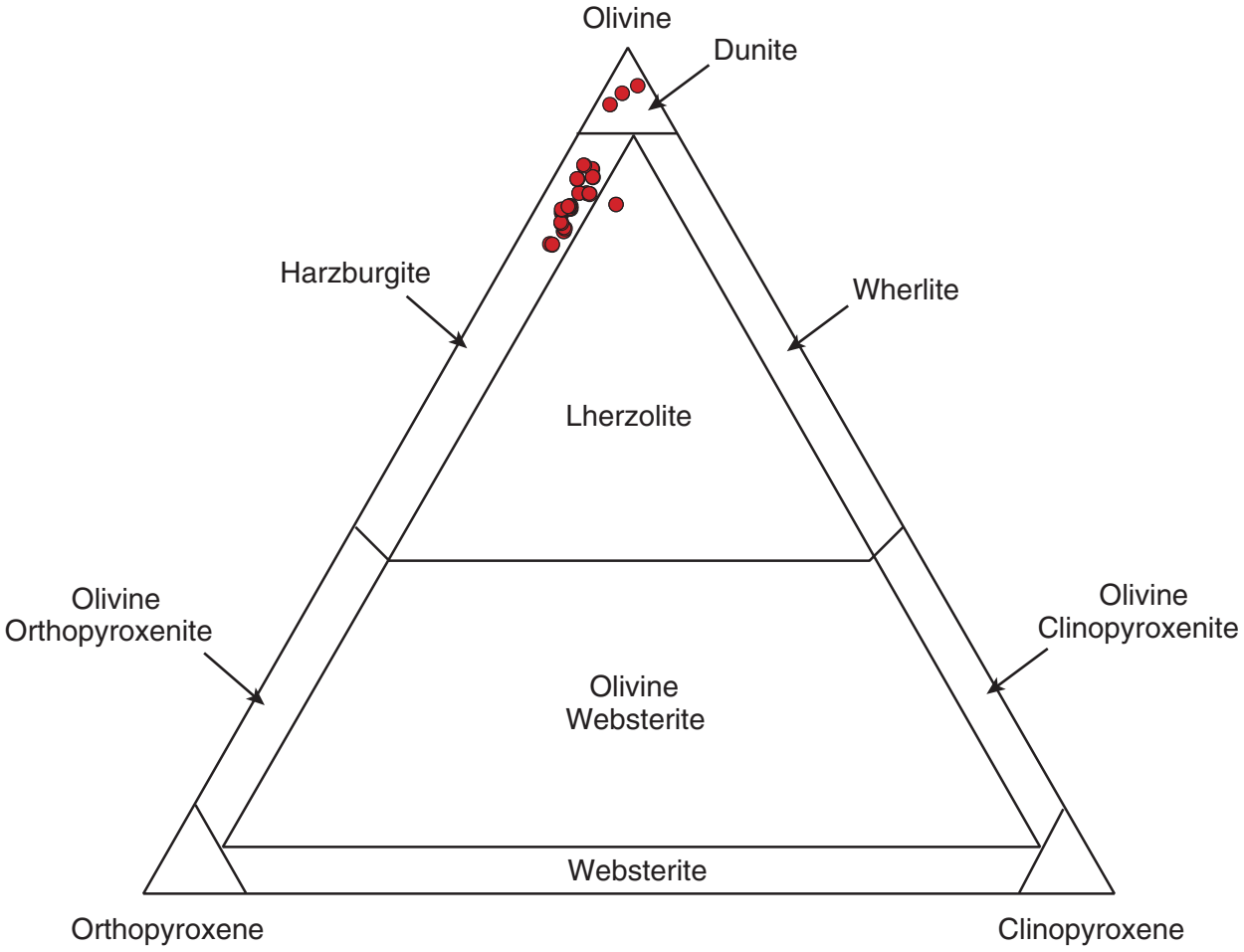

Figure F40. Mantle peridotites from Conical, Torishima, and South Chamorro Seamounts plotted in (**A**) CaO vs. Al_2O_3 and (**B**) CaO vs. $100 \times Mg^{2+}/(Mg^{2+}+Fe^{2+})$ diagrams after Ishiwatari (1985), showing different degrees of melting. Fields for Conical and Torishima Seamount peridotites are from Ishii et al. (1992), Parkinson and Pearce (1998), and I.P. Savov and W.B.F. Ryan (unpubl. data).

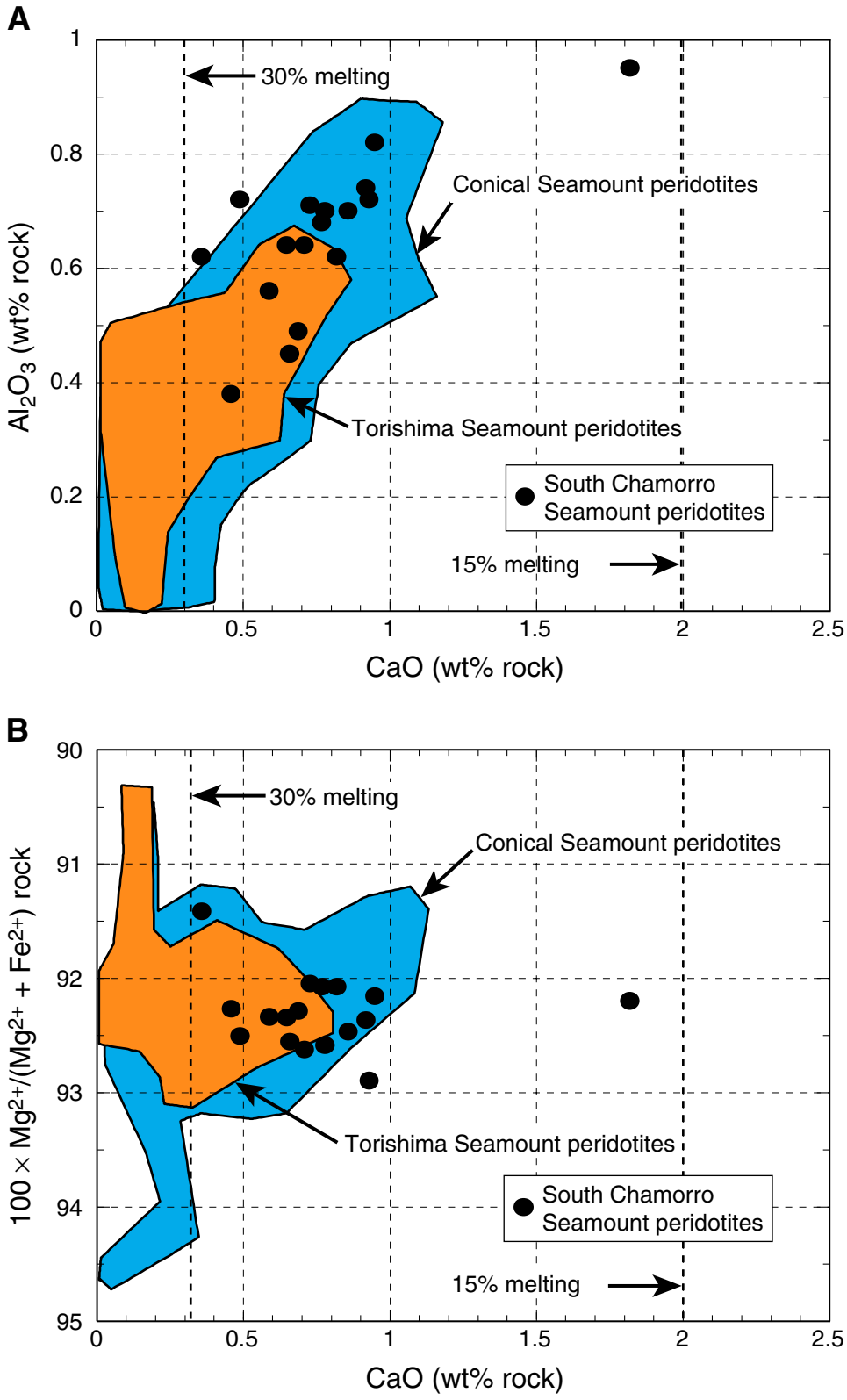

Figure F41. Occurrence of nannofossils in Holes 1200D, 1200E, and 1200F. The abundance of nannofossils ranging from common to trace are indicated by the number of nannofossil symbols presented next to the column. Calcite overgrowth is indicated by a solid red dot. Hole 1200D is the farthest from the active vents, and Hole 1200E is the closest. TD = total depth.

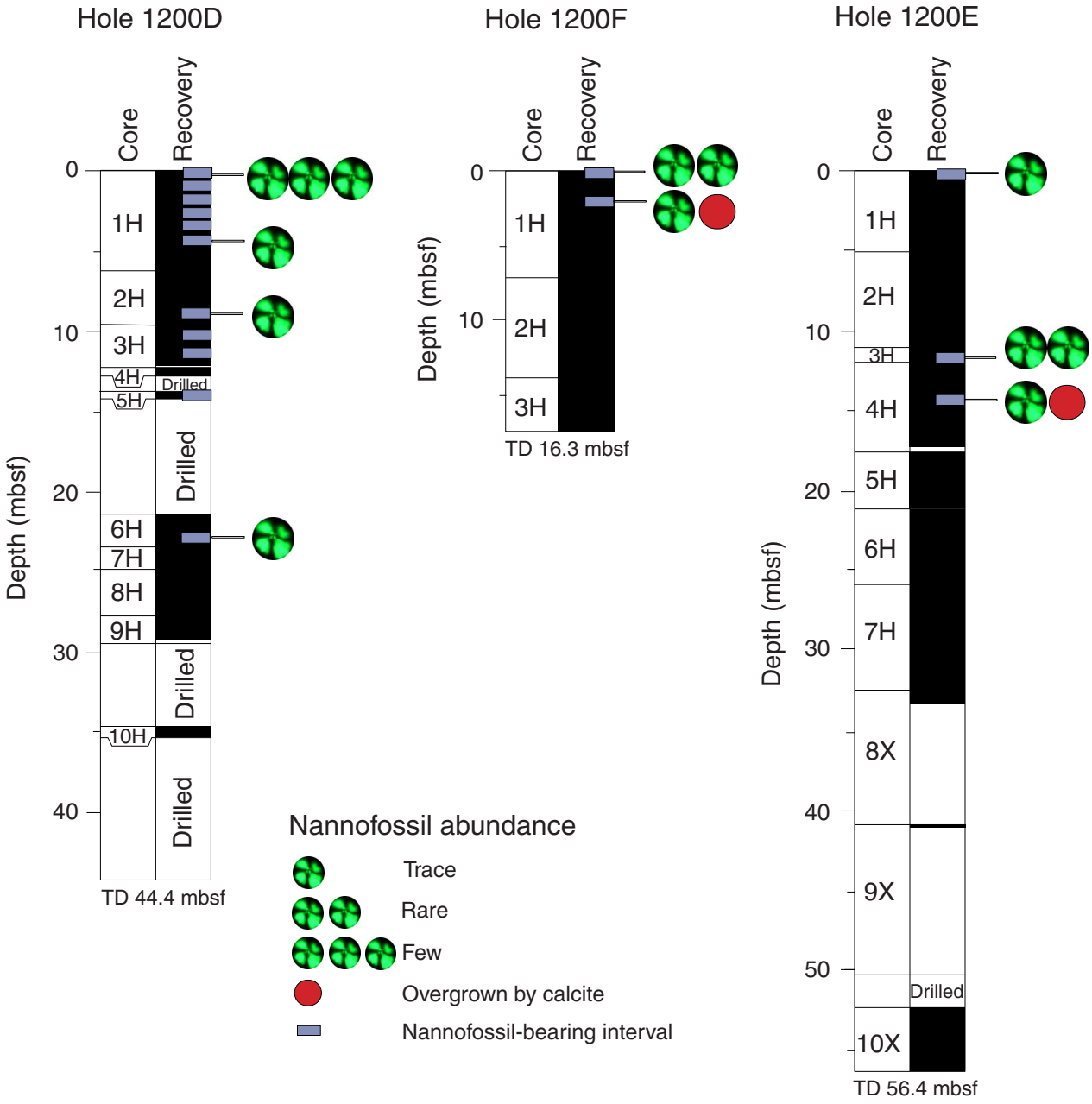

Figure F42. A. Abundance of *Gephyrocapsa caribbeanica* in Hole 1200E. **B.** Relative abundances of major calcareous nannofossil taxa in successive samples from Core 195-1200E-3H.

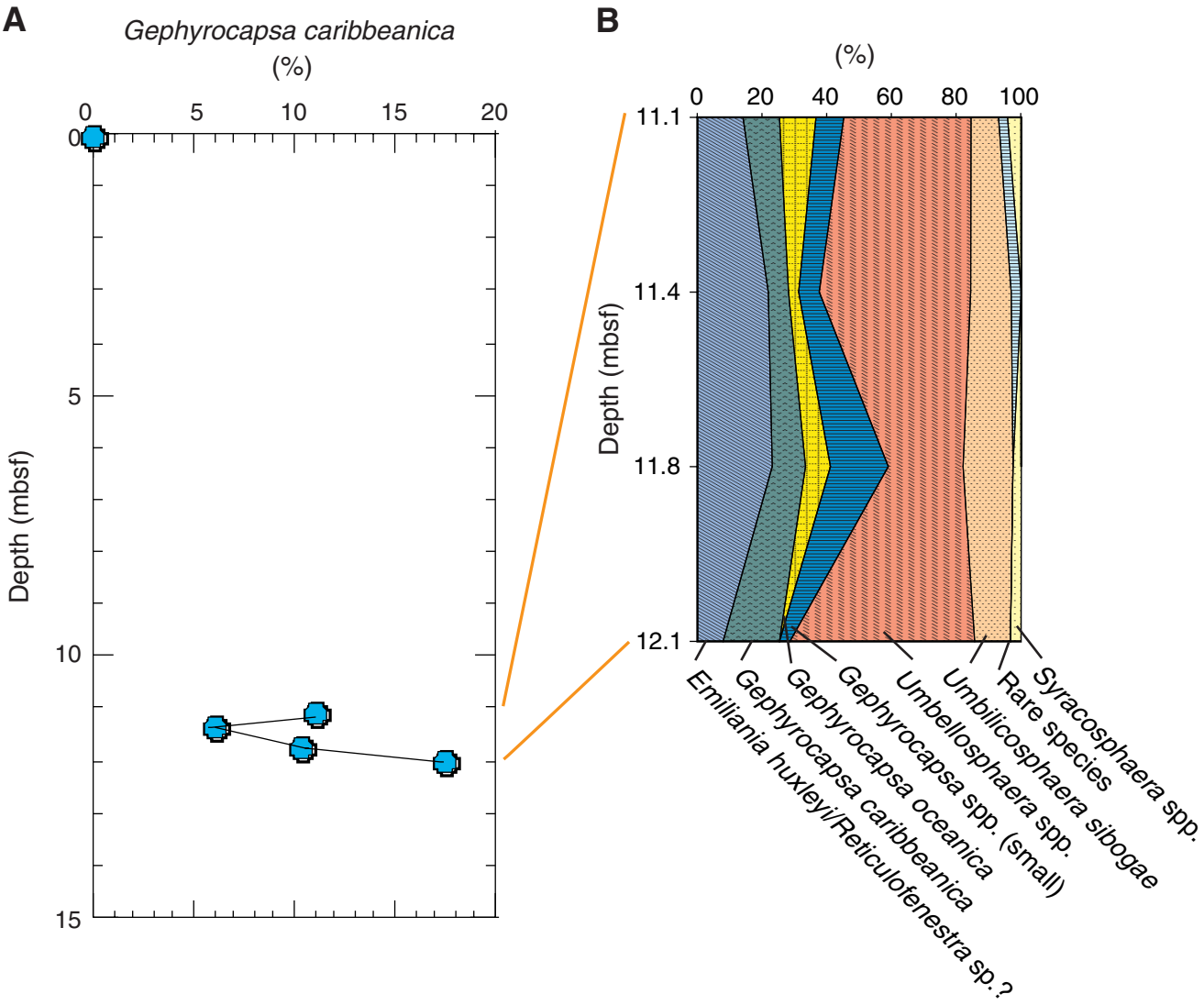

Figure F43. Plots of the intensity of NRM, susceptibility, Koenigsberger ratio, and MDF of ultramafic clasts vs. depth in Hole 1200A.

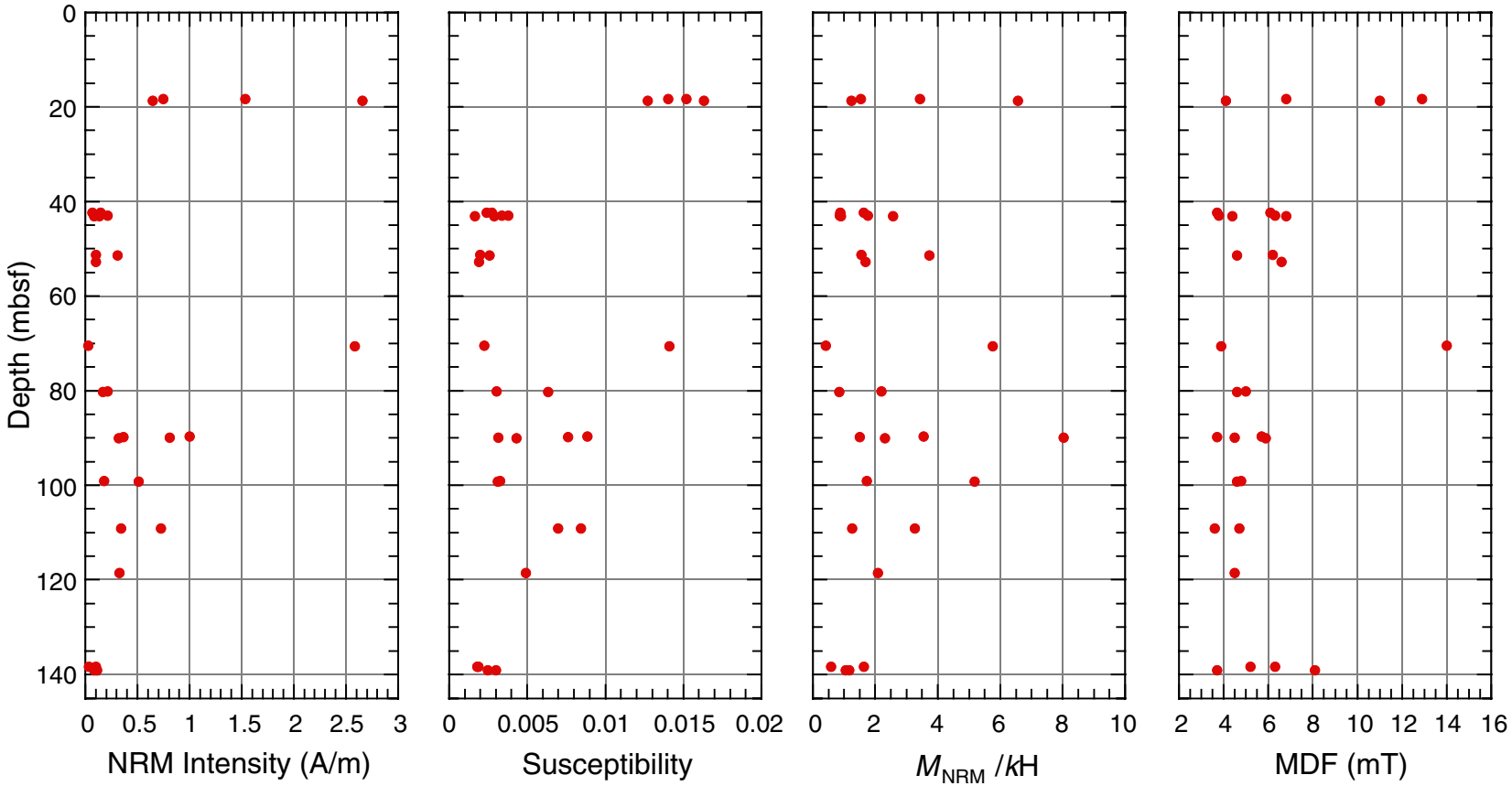

Figure F44. Thermal demagnetization curves of four samples from Hole 1200A. The decrease in magnetization at 585°C suggests that pure magnetite is the dominant magnetic carrier.

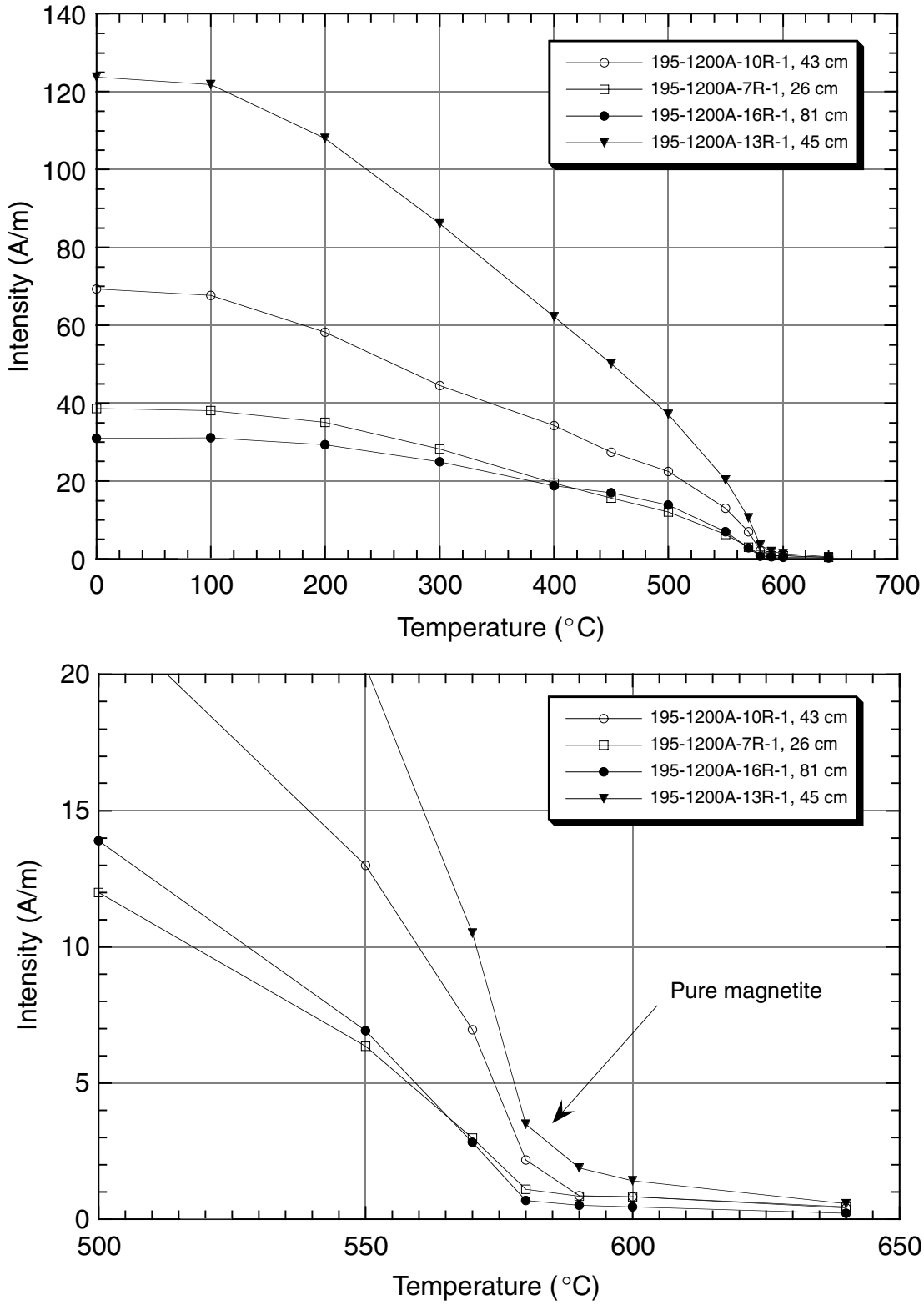

Figure F45. Isothermal remanent magnetization (IRM) and backfield acquisition curves for representative discrete samples from Site 1200. Samples saturate by 400 mT, and B_{cr} is between 25 and 75 mT.

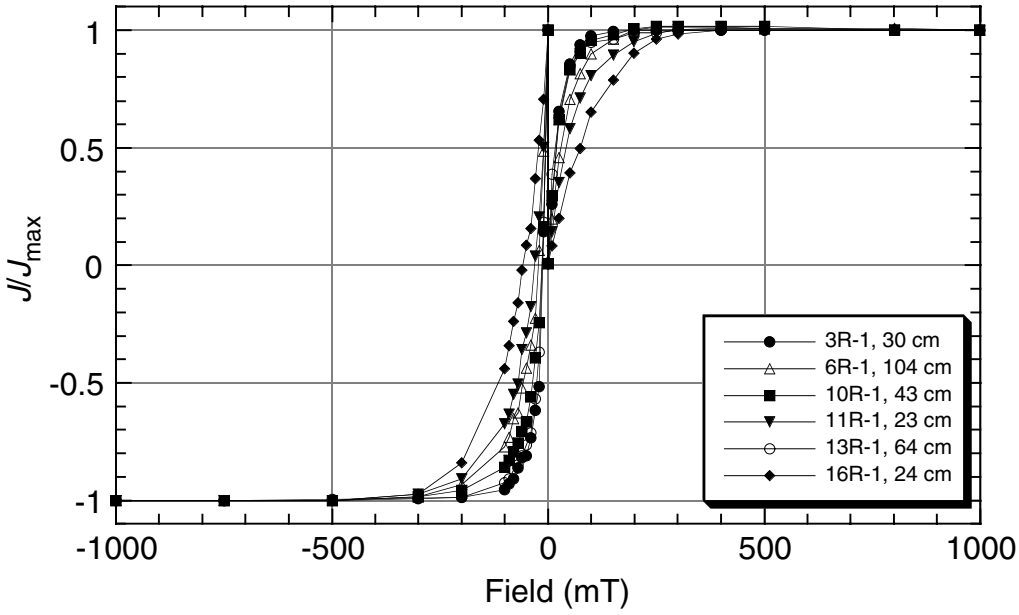

Figure F46. Normalized NRM AF demagnetization curves of representative samples from Hole 1200A show that the decay of the intensity of remanent magnetization during progressive demagnetization of most ultramafic clasts is very similar and displays very little variability.

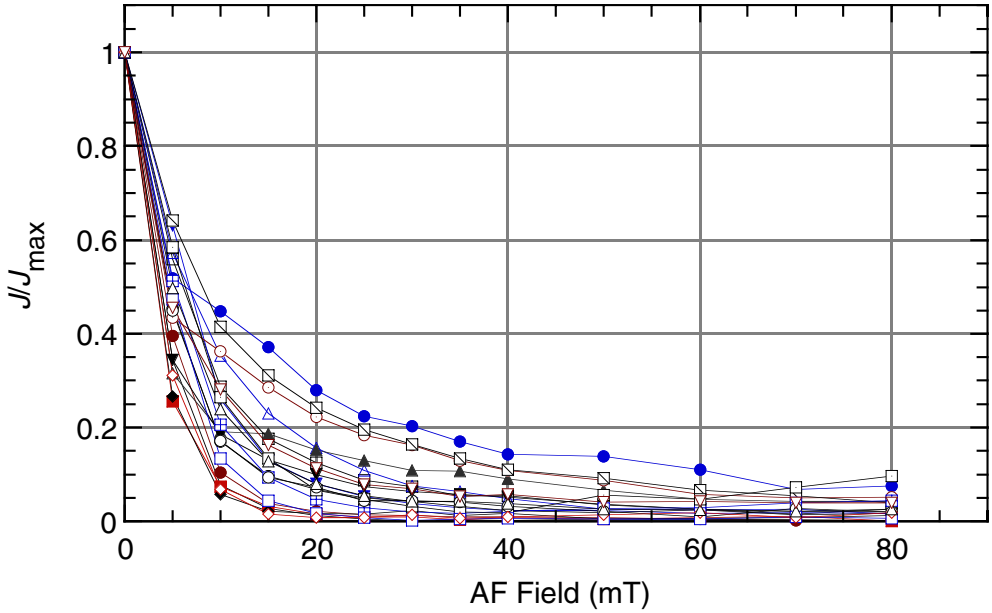

Figure F47. AF demagnetization behavior of serpentinized peridotite clasts (Hole 1200A) and serpentine sediments (Hole 1200D). Solid symbols = the horizontal component of remanence, open symbols = the vertical component. Intensity units are in A/m, demagnetization levels in mT. **A, B.** Intensity decay and vector end point diagrams (Type 1) (see **"Demagnetization Character and Magnetic Remanence,"** p. 28). **C, D.** Intensity decay and vector end point diagrams (Type 2). (Continued on next page.)

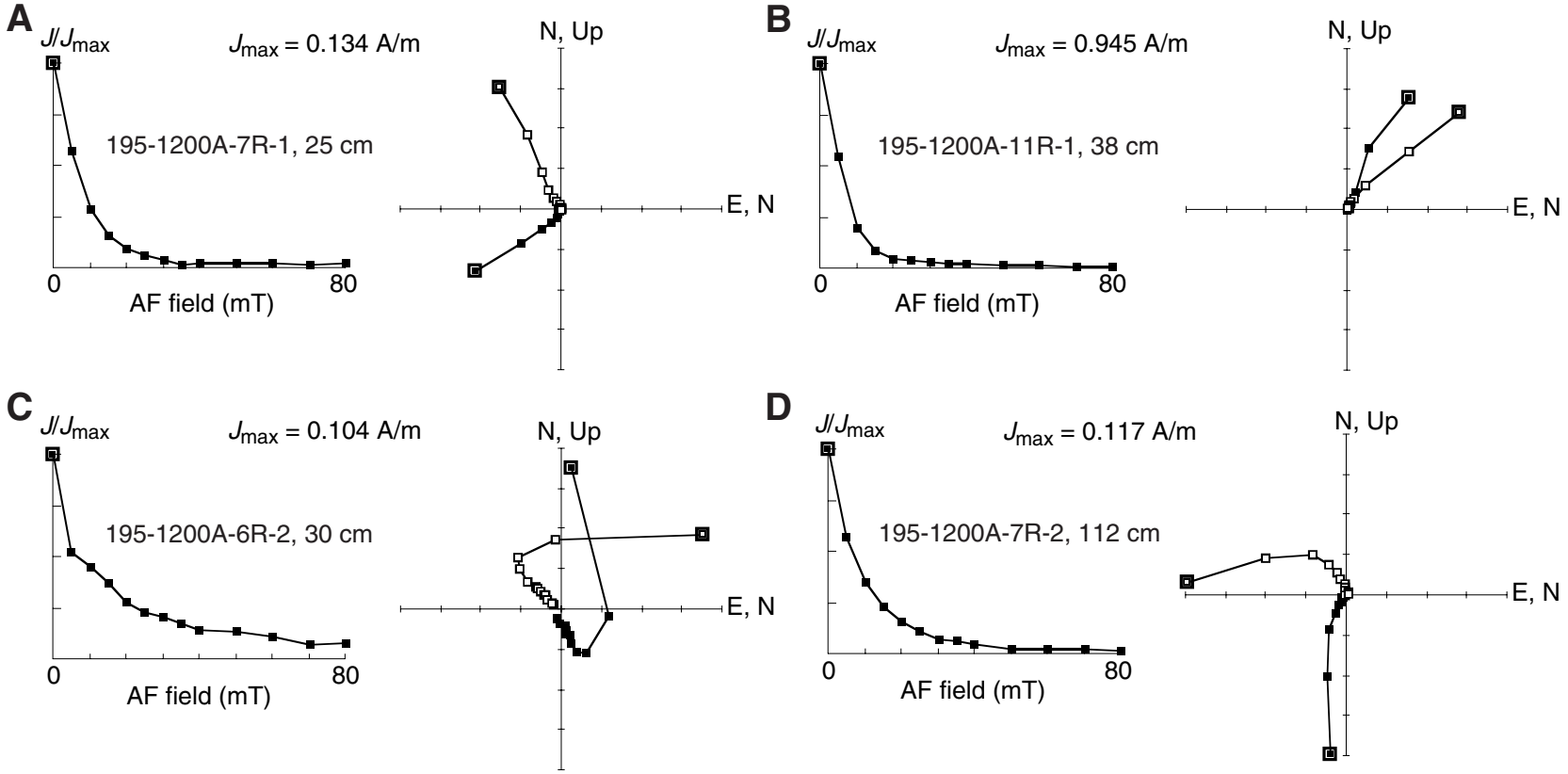

Figure F47 (continued). E, F. Intensity decay and vector end point diagrams (Type 3). **G, H.** Intensity decay and vector end point diagrams of serpentine muds.

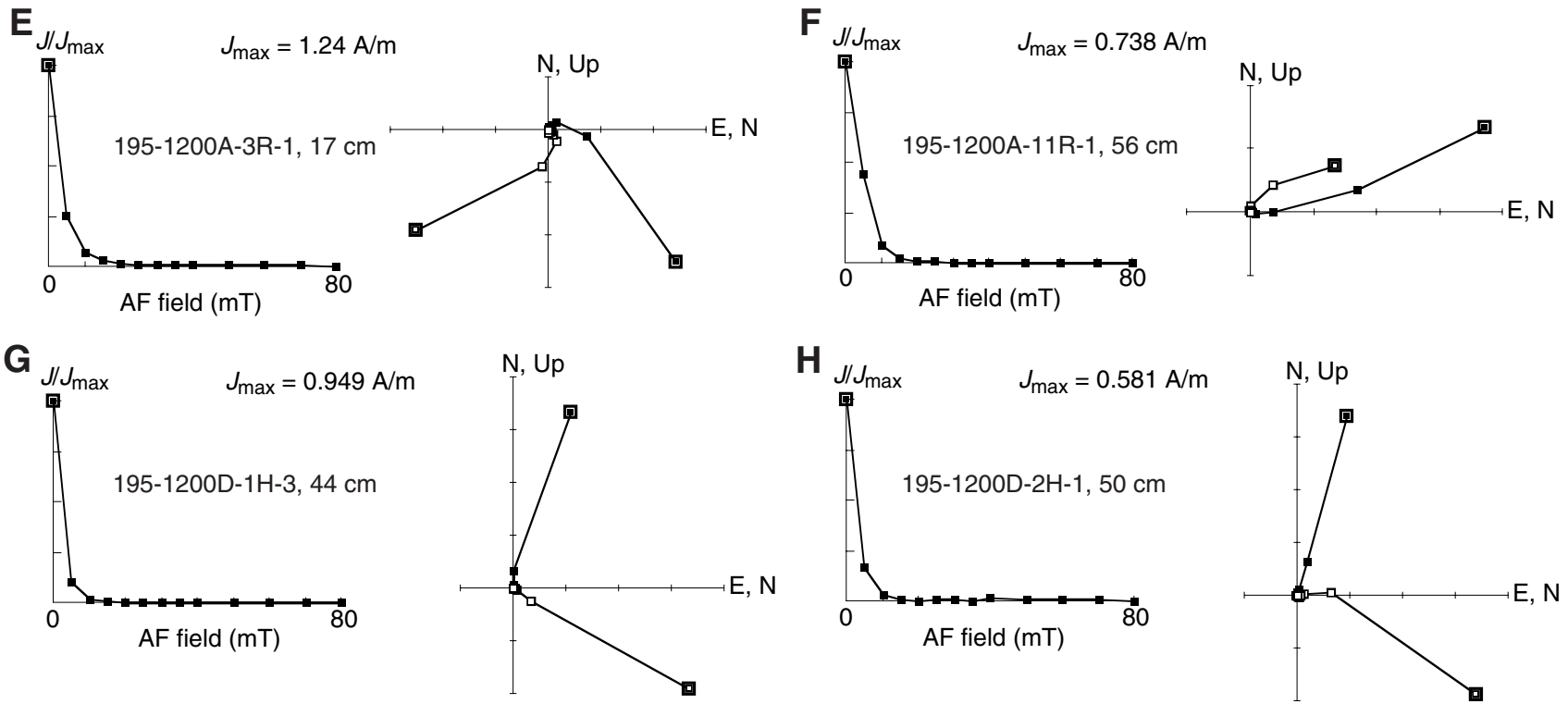

Figure F48. A–C. AF demagnetization behavior of NRM (open symbols) and saturation IRM (solid symbols) from samples of serpentinized harzburgite (Hole 1200A) and serpentine sediments (Hole 1200D).

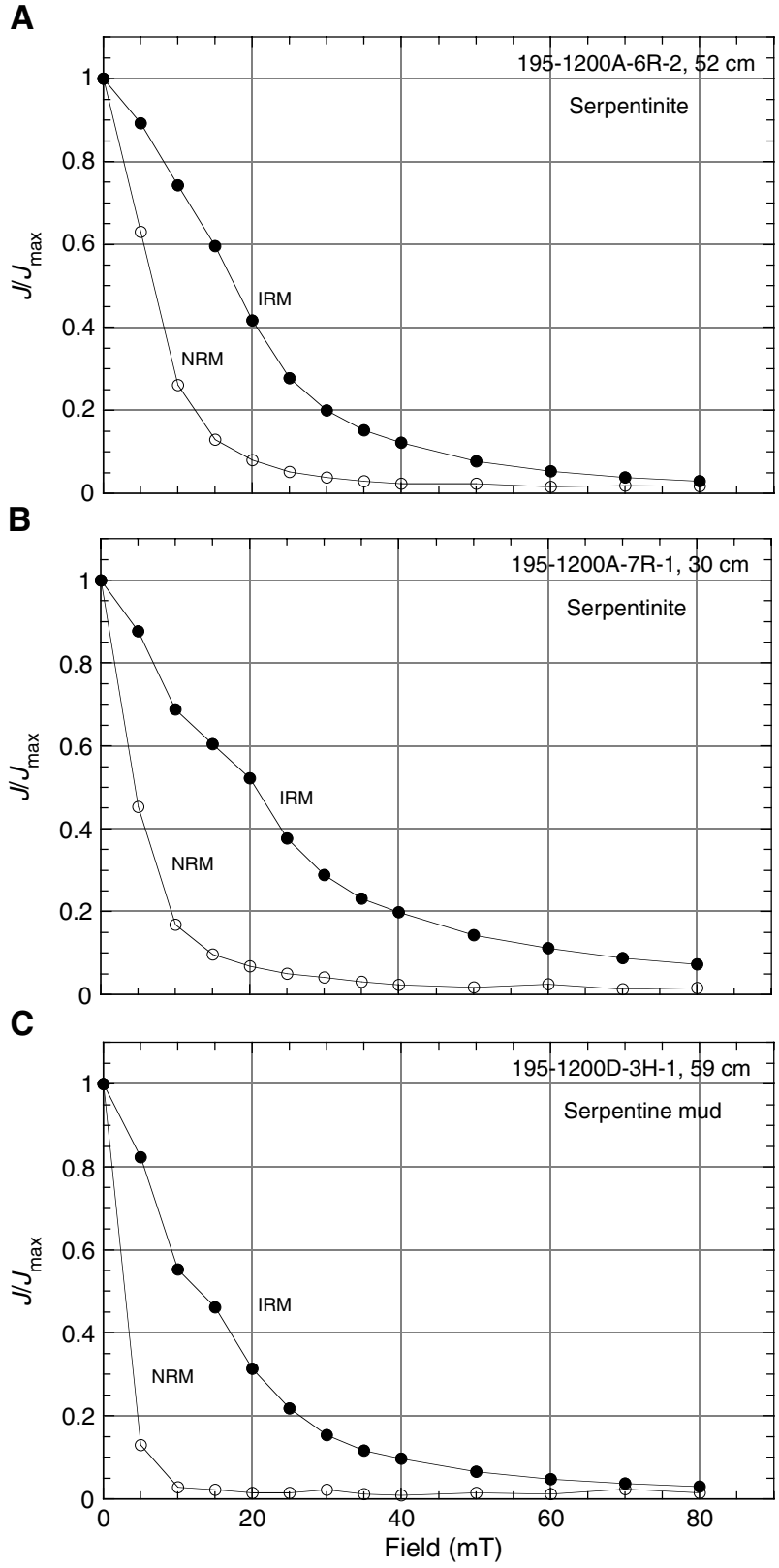

Figure F49. A–C. Magnetic intensity, declination, and inclination vs. depth in Sample 195-1200A-3R-1, 0–72 cm, at 20 mT, showing a considerable variability of the stable magnetization direction even within one piece.

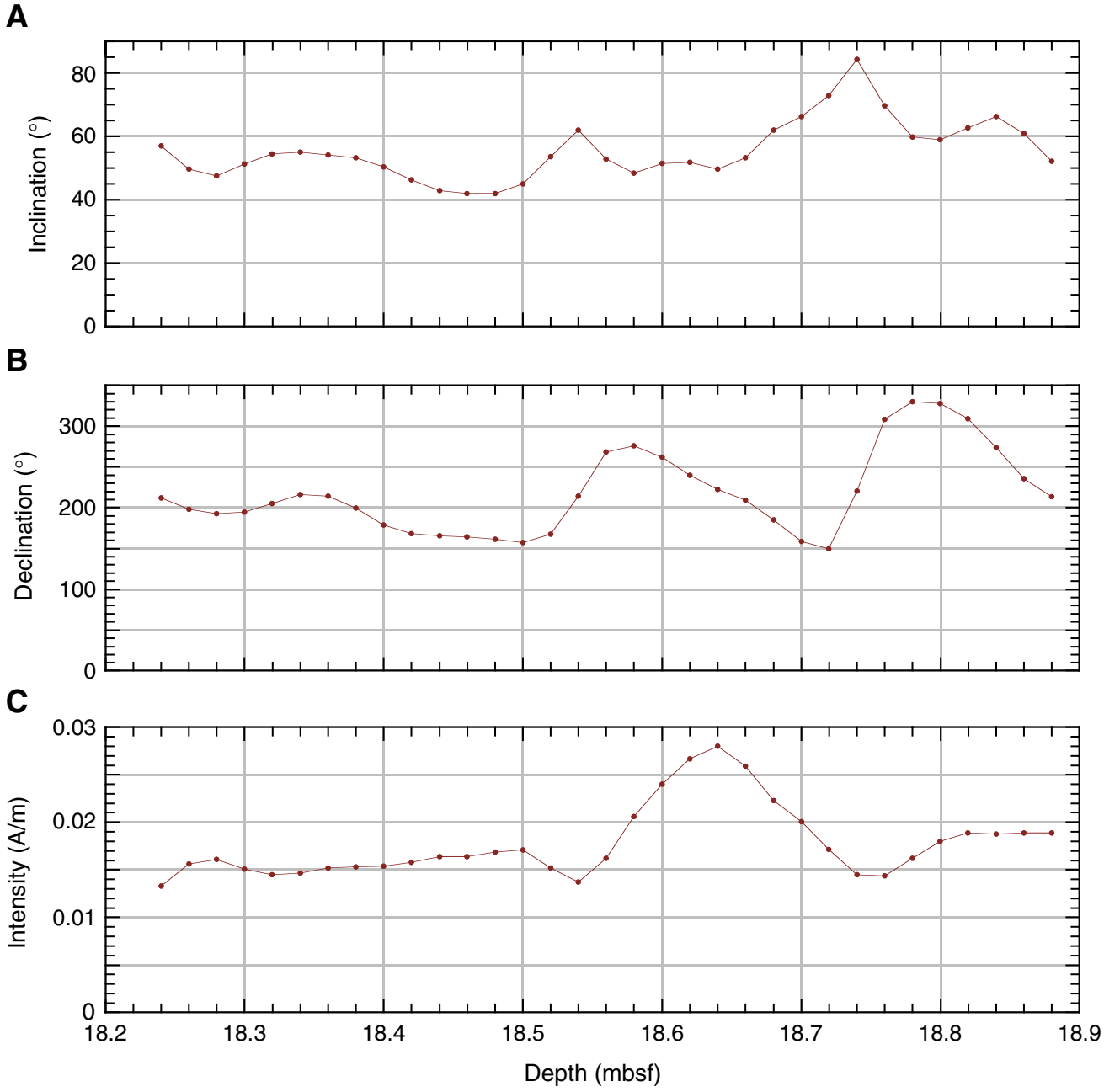

Figure F50. Composition of interstitial water. **A.** Chloride. **B.** Sodium. **C.** Na/Cl ratio. **D.** Potassium. **E.** Boron. Arrows indicate the concentration estimated for the ambient bottom seawater.

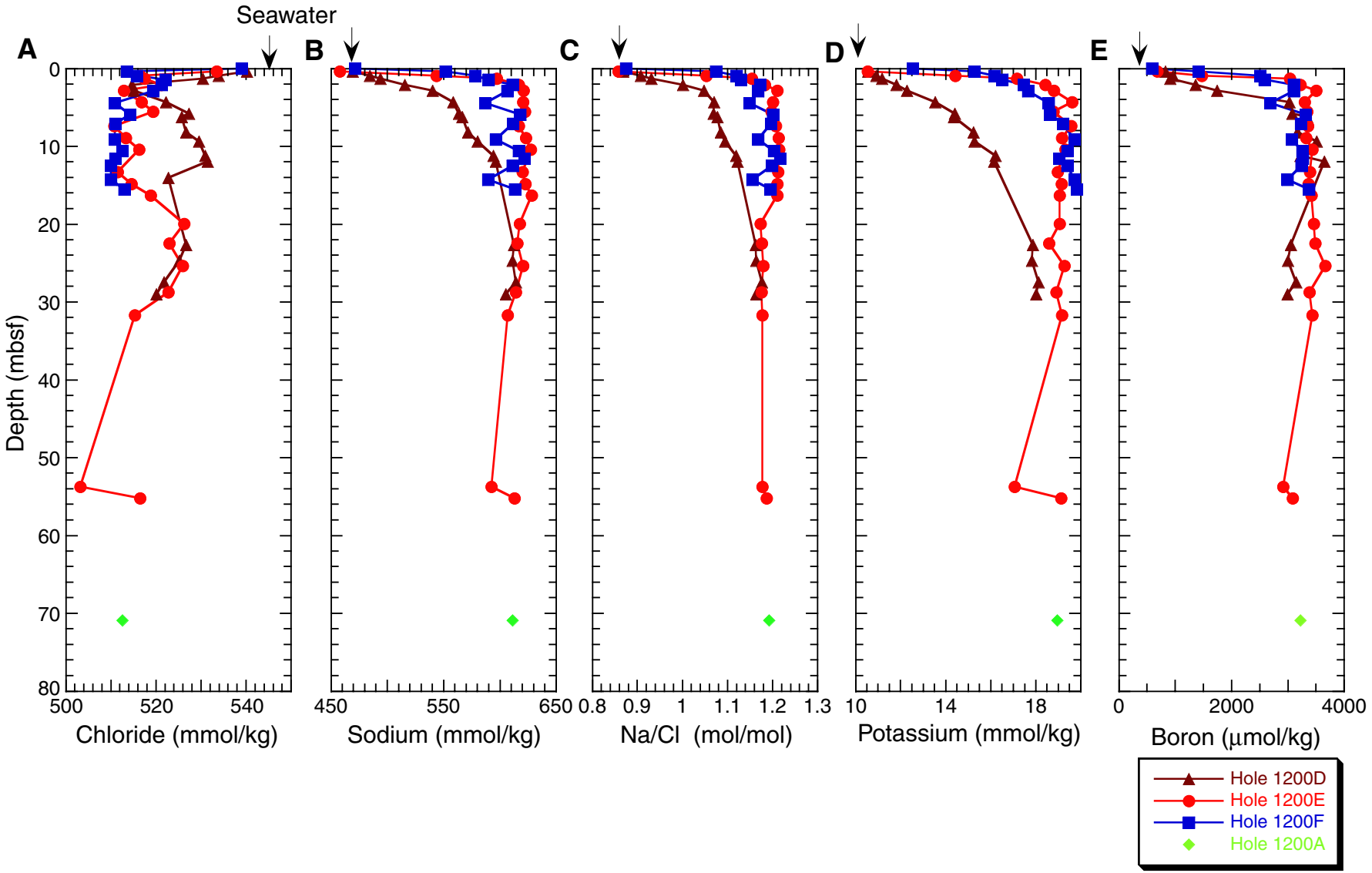

Figure F51. Composition of interstitial water. **A.** pH. **B.** Alkalinity. **C.** Ammonia. **D.** Sulfate. **E.** Hydrogen sulfide. Arrows indicate the concentration estimated for the ambient bottom seawater.

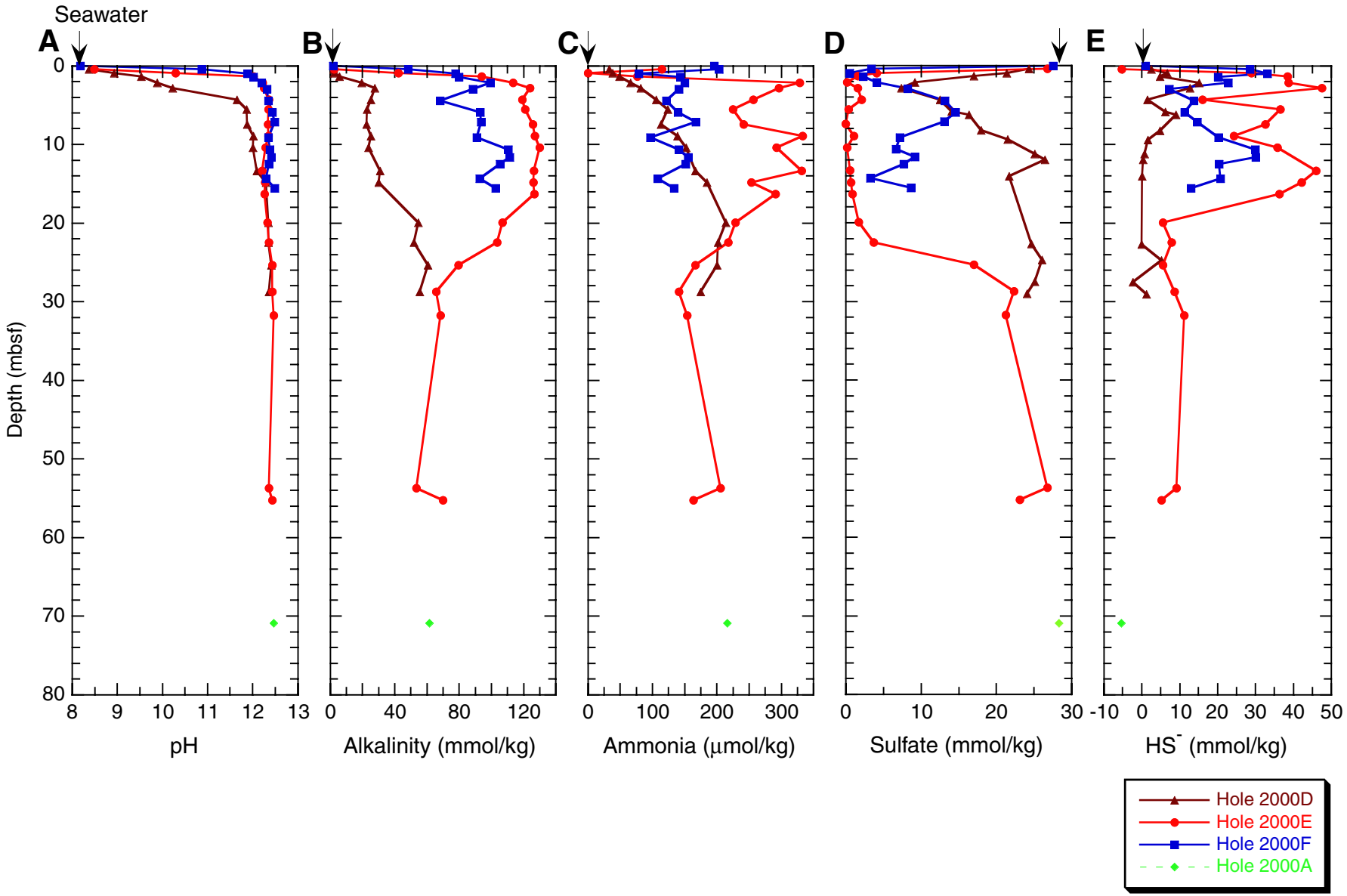

Figure F52. Composition of interstitial water. **A.** Magnesium. **B.** Calcium. **C.** Strontium. **D.** Manganese. **E.** Lithium. Arrows indicate the concentration estimated for the ambient bottom seawater.

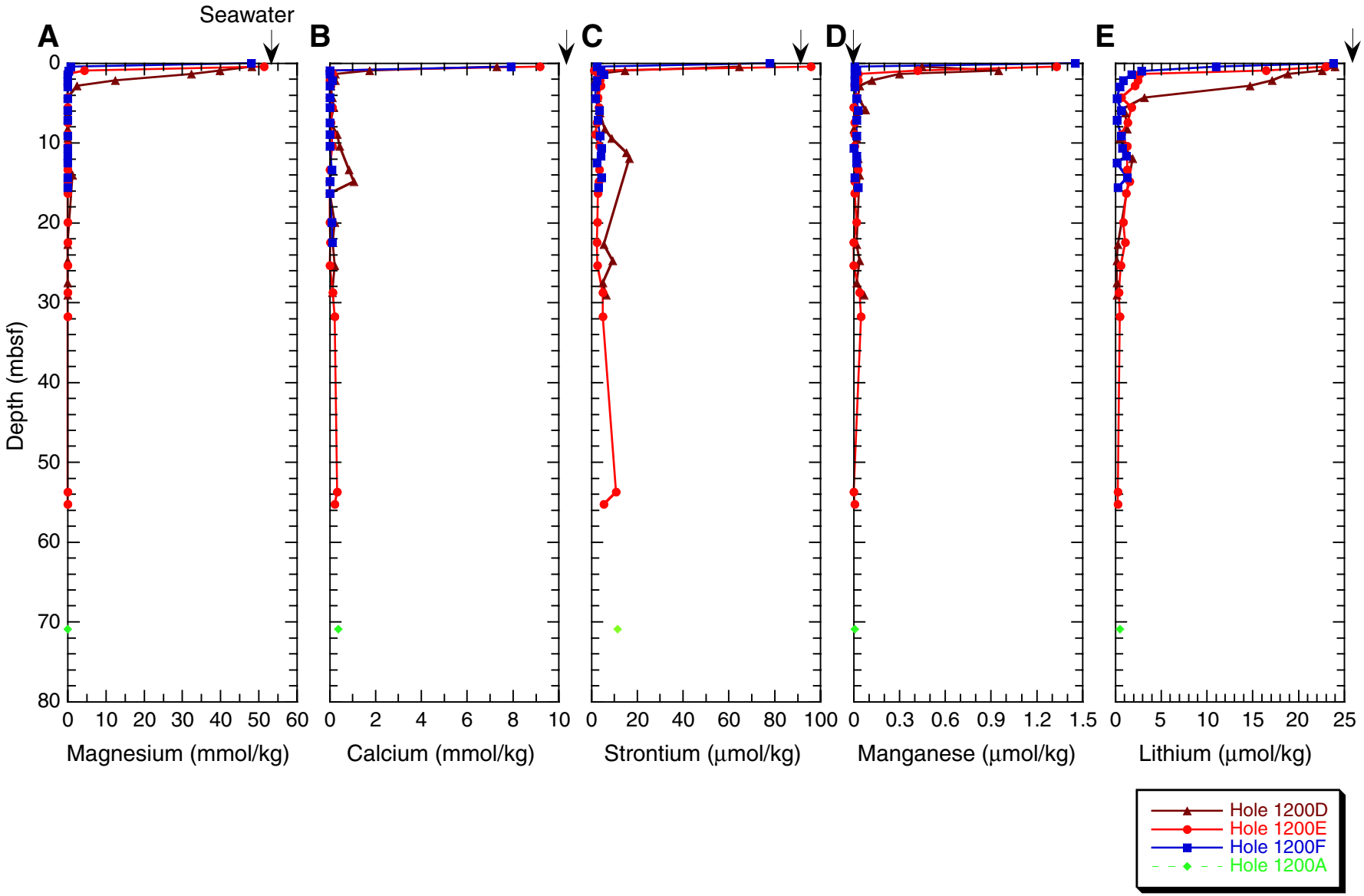

Figure F53. Composition of interstitial water. **A.** Silica. **B.** Fluoride. **C.** Iron. **D.** Aluminum. Arrows indicate the concentration estimated for the ambient bottom seawater.

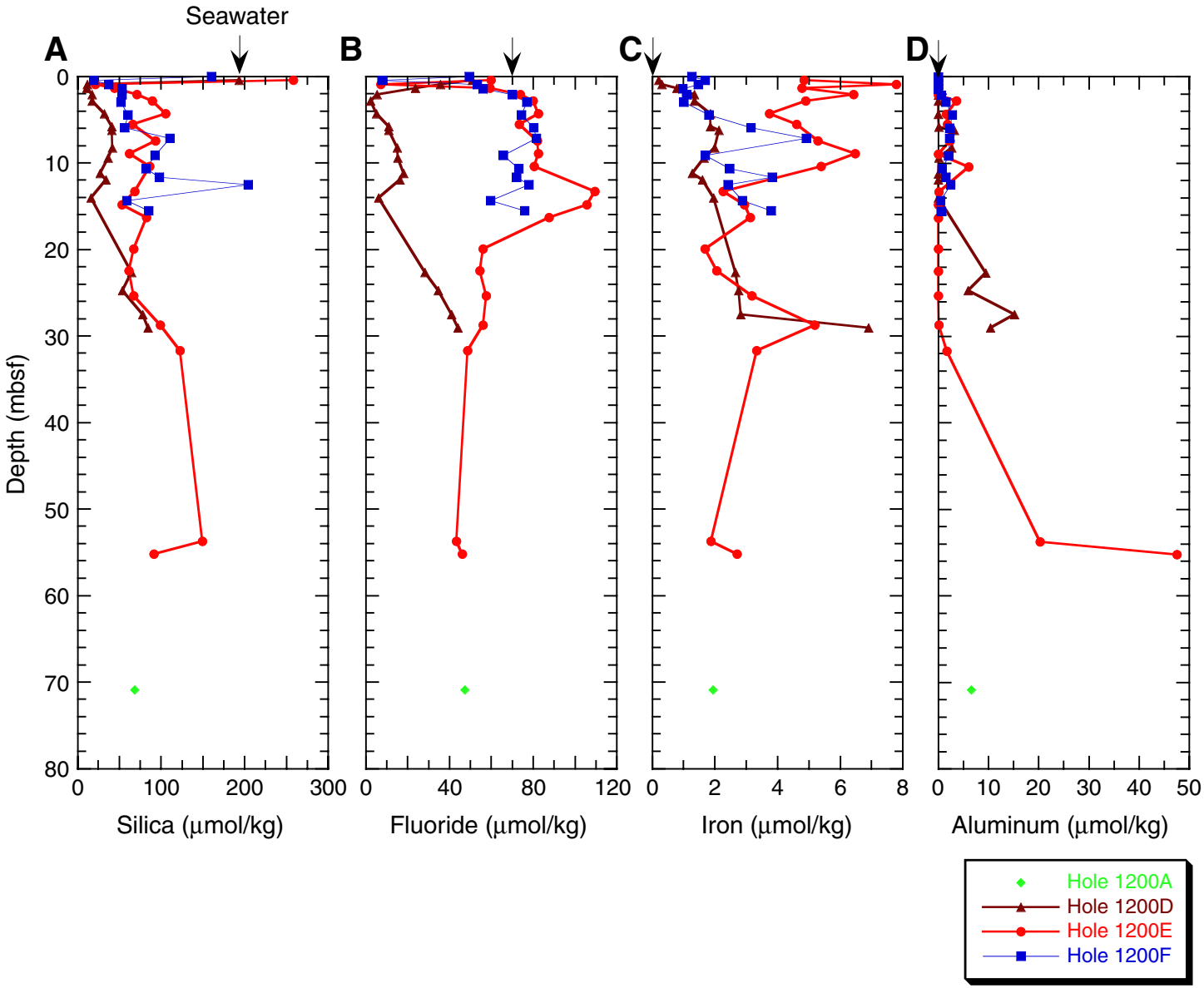

Figure F54. Hydrocarbon composition of interstitial water, compared with that from Leg 125 Sites 779 and 780 on Conical Seamount. cl = core-liner gas.

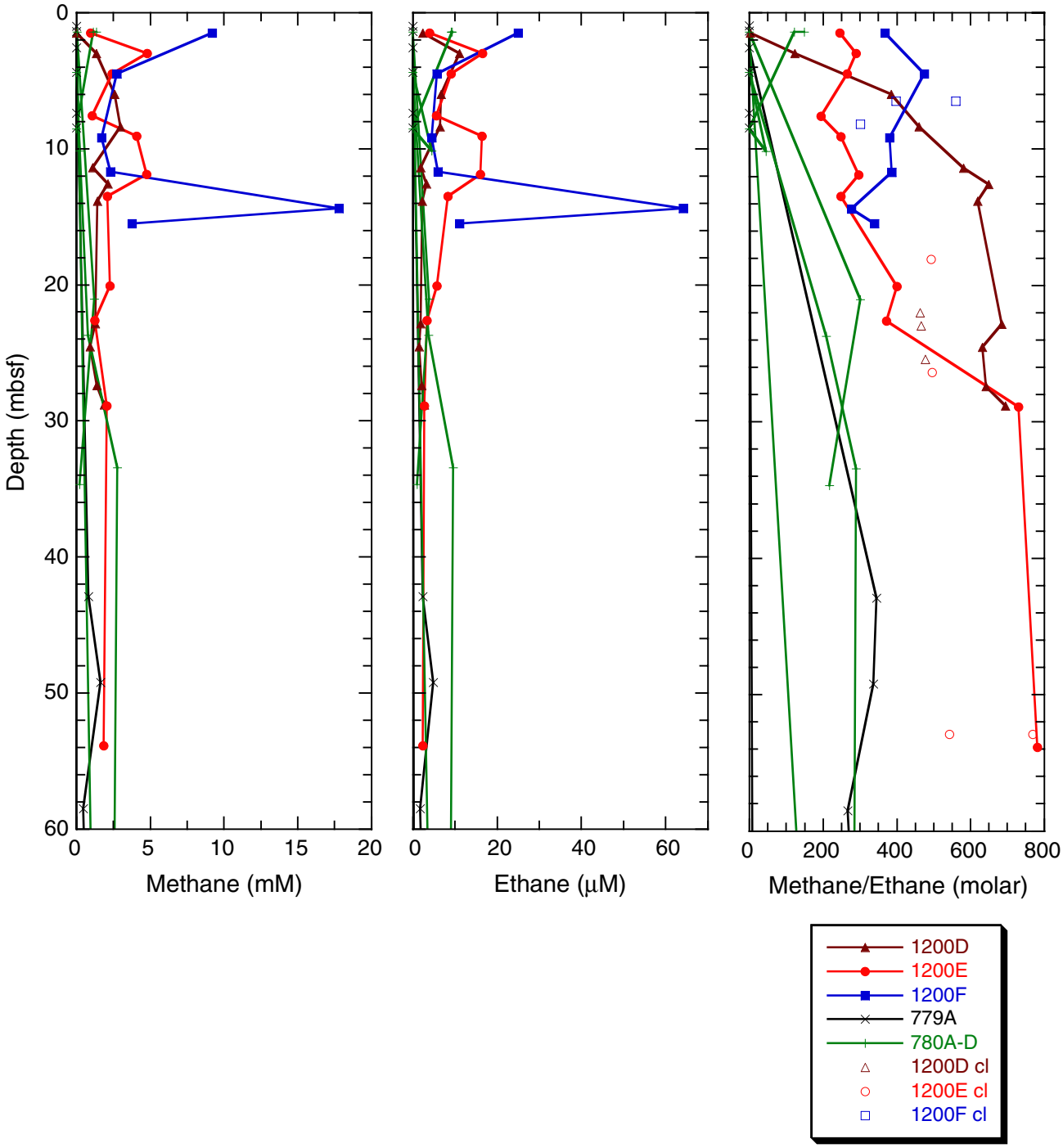

Figure F55. Results of CHNS and coulometric analyses of serpentine mud. **A.** Water. **B.** Calcium carbonate. **C.** Sulfur. **D.** Organic carbon.

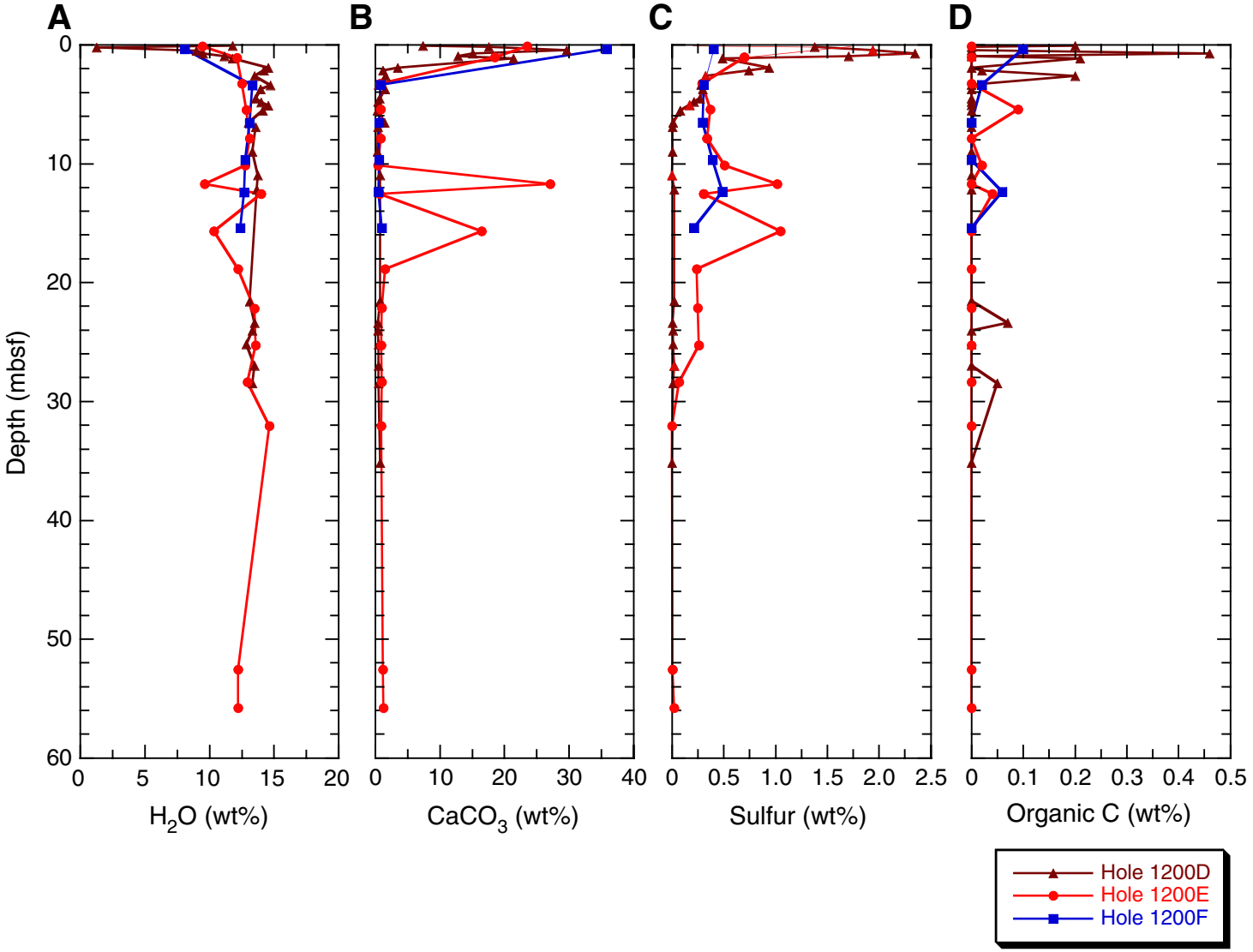

Figure F56. MST results for Hole 1200A. **A.** Volume magnetic susceptibility. **B.** Bulk density; index properties measurements were derived from discrete samples of clast material (solid circles) and matrix material (open circles). Clast samples used for index properties measurements were chosen to contain no fractures; the whole core, measured for bulk density on the MST, contains fractures and has a lower apparent bulk density. **C.** Natural gamma radiation.

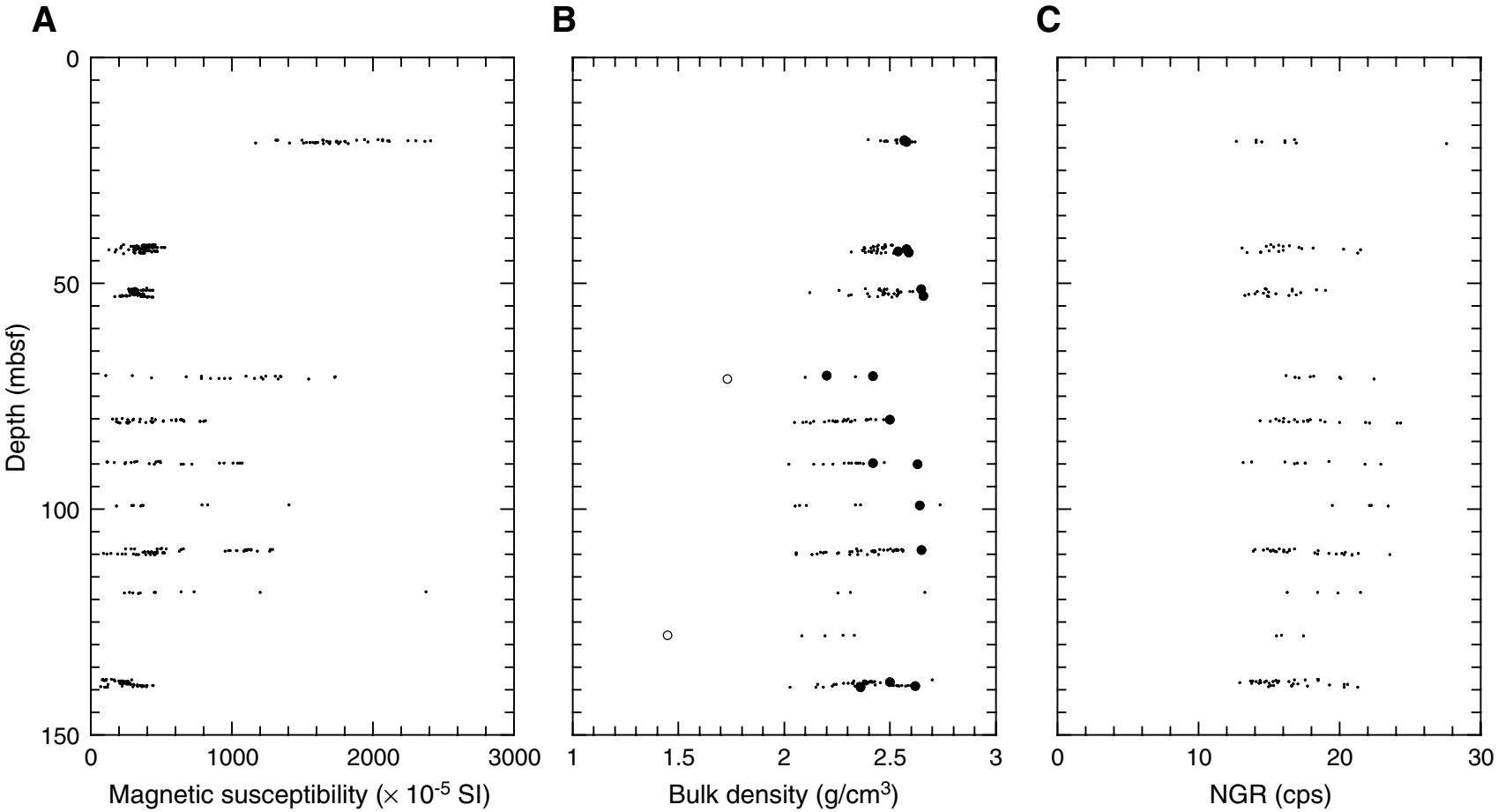

Figure F57. A. *P*-wave velocity for discrete samples of clast material from Hole 1200A. Measurements were made using a pair of contact transducers (PWS3) on samples cut into cubes with faces parallel to the x-, y-, and z-axes of the core. Velocity was measured parallel to each axis. Solid circles = the median velocity; error bars correspond to minimum and maximum velocity. **B.** Distribution of the mean velocity for each sample; the mean velocity from all measurements = 4.89 km/s.

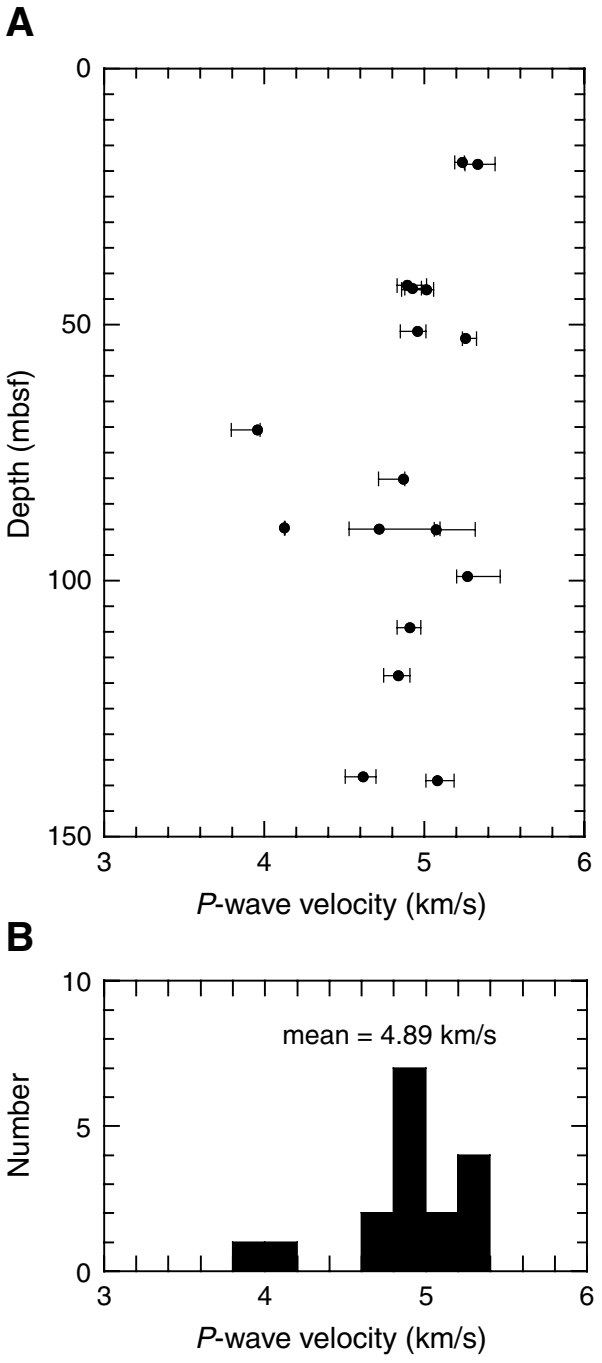

Figure F58. *P*-wave velocity vs. bulk density for serpentinized ultramafic clasts from Hole 1200A. Velocity values are the mean velocity measured for each sample.

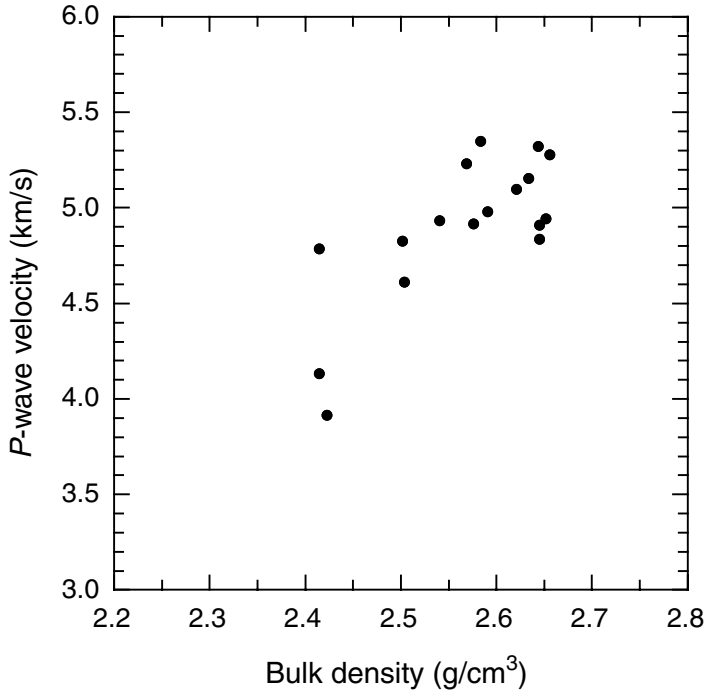

Figure F59. A. Thermal conductivity measurements for clast material (solid circles) and matrix (open circles) from Hole 1200A. **B.** Distribution of thermal conductivity measurements for clast material; the mean value = 2.21 W/(m·K).

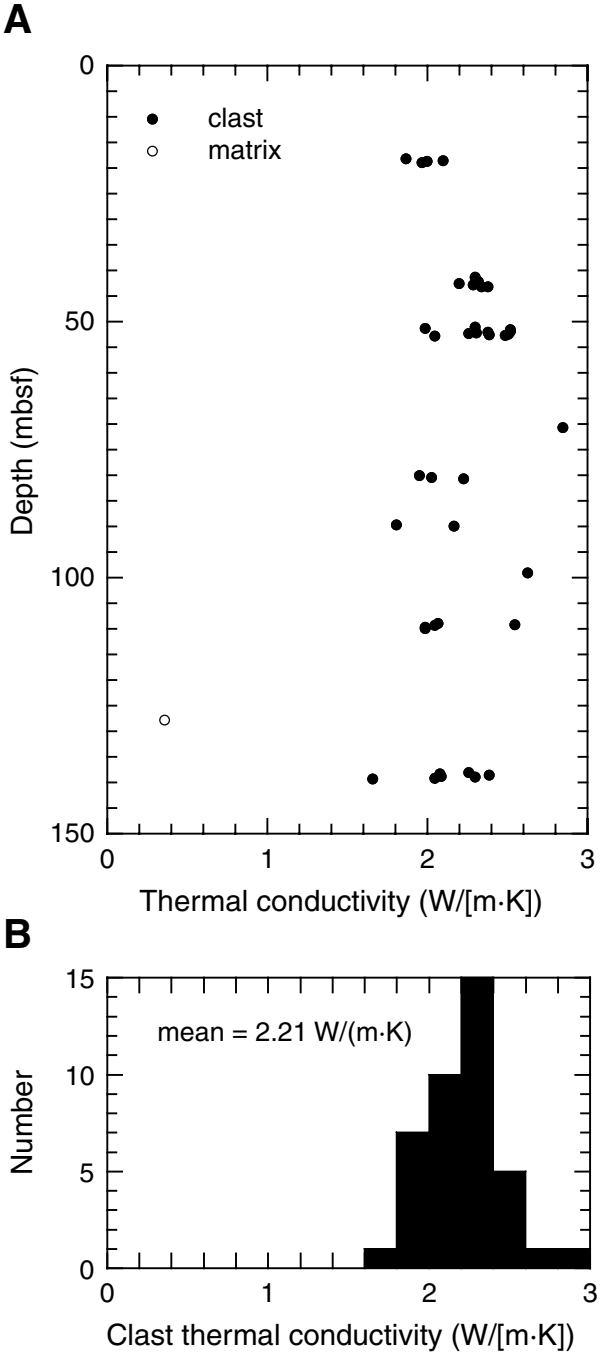

Figure F60. MST results of Hole 1200D. **A.** Volume magnetic susceptibility. Measurements performed on discrete samples are represented by open circles (matrix material) and solid circles (clast material). Arrows = discrete measurements on clast material that are offscale. **B.** Bulk density. Index properties measurements derived from discrete samples are represented by open circles (matrix material) and solid circles (clast material). Ticks on the depth axis indicate where anomalous measurements, caused by voids, have been removed. **C.** Natural gamma radiation.

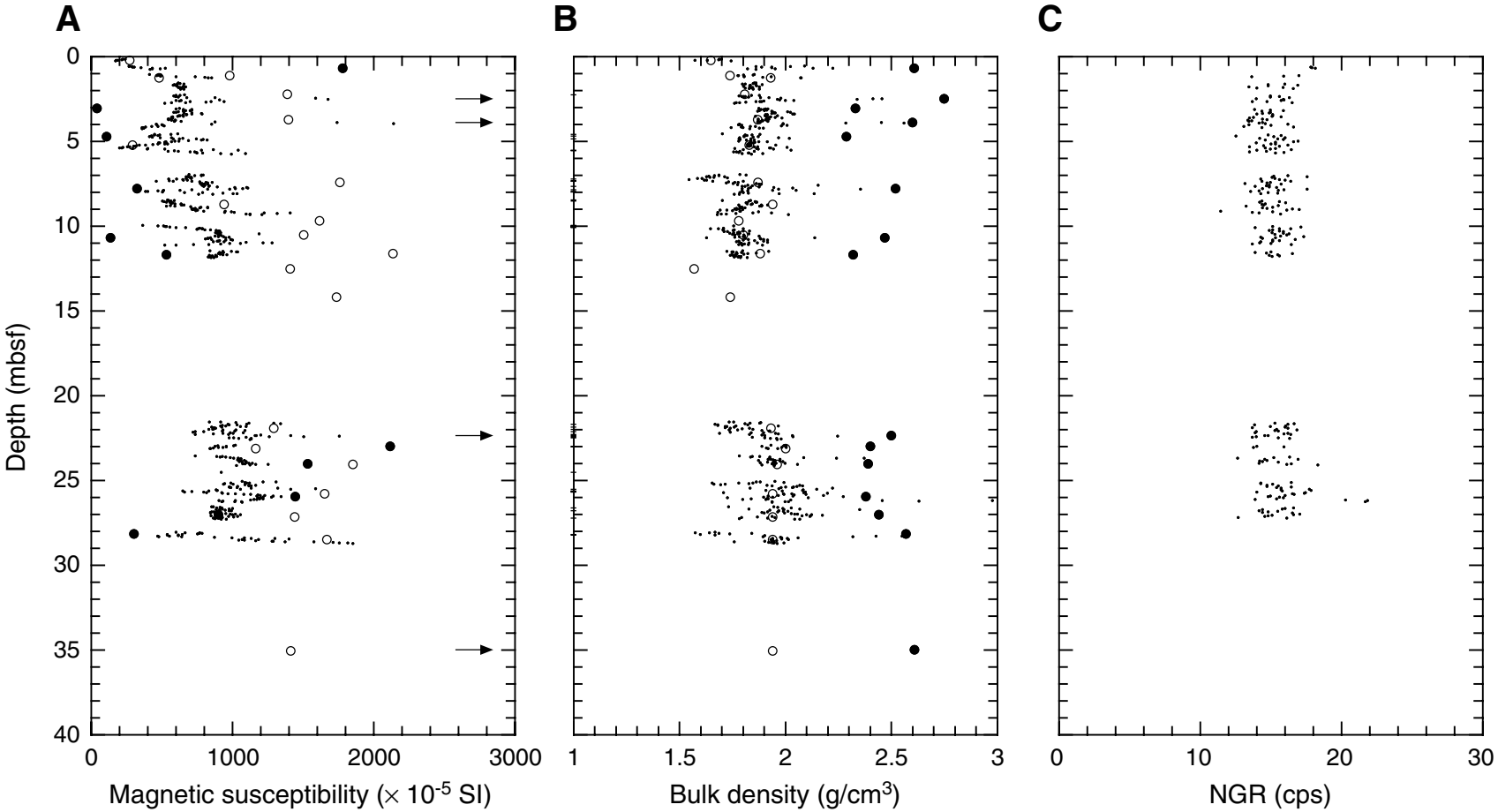

Figure F61. MST results of Hole 1200E. **A.** Volume magnetic susceptibility. Measurements performed on discrete samples are represented by open circles (matrix material) and solid circles (clast material). Arrows = discrete measurements on clast material that are offscale. **B.** Bulk density. Index properties measurements derived from discrete samples are represented by open circles (matrix material) and solid circles (clast material). Ticks on the depth axis indicate where anomalous measurements, caused by voids, have been removed. **C.** Natural gamma radiation. The vertical arrow identifies a small anomaly.

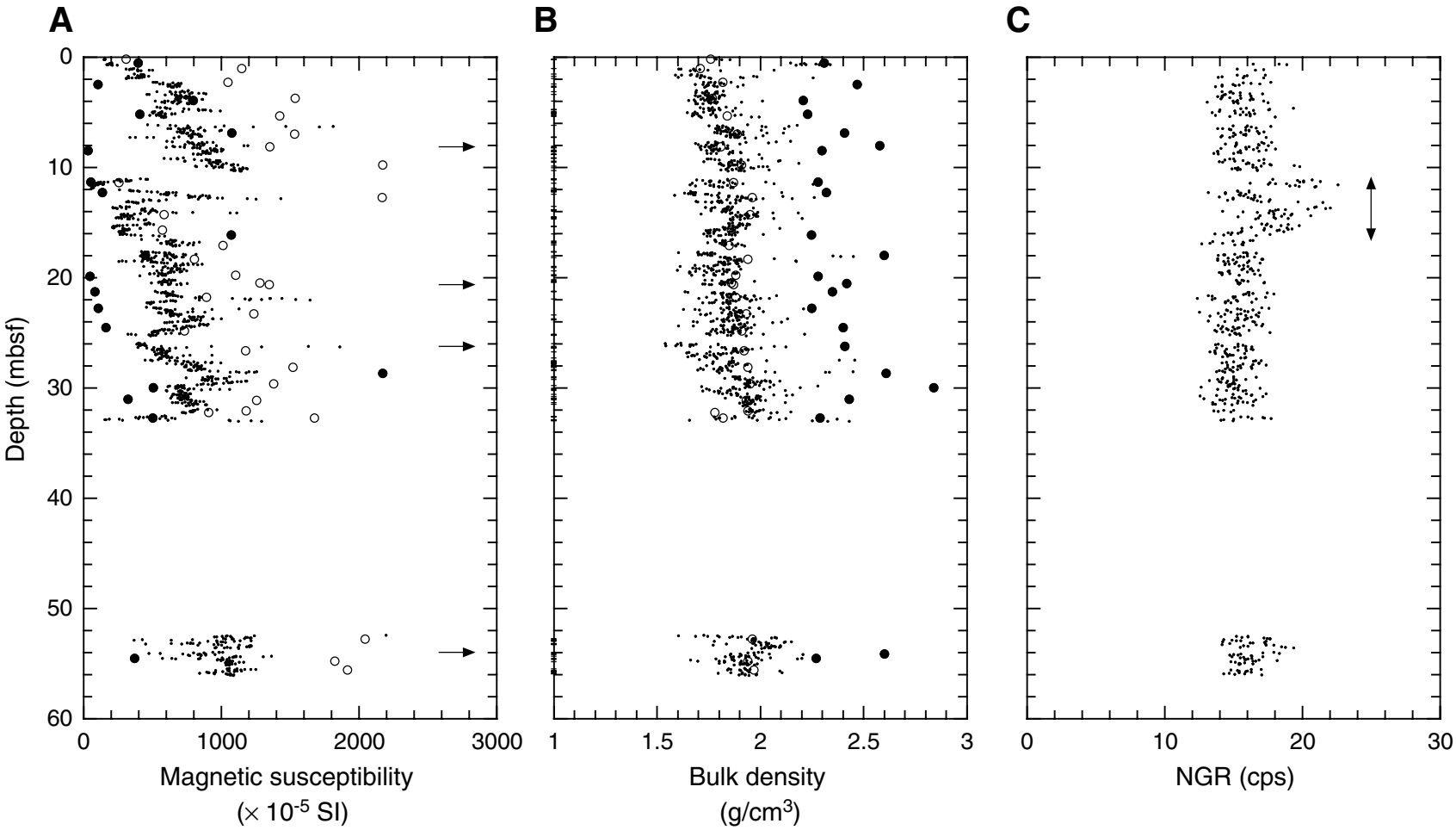

Figure F62. MST results of Hole 1200F. **A.** Volume magnetic susceptibility. Measurements performed on discrete samples are represented by open circles (matrix material) and solid circles (clast material). Arrows = discrete measurements on clast material that are off-scale. **B.** Bulk density. Index properties measurements derived from discrete samples are represented by open circles (matrix material) and solid circles (clast material). Ticks on the depth axis indicate where anomalous measurements, caused by voids, have been removed. **C.** Natural gamma radiation.

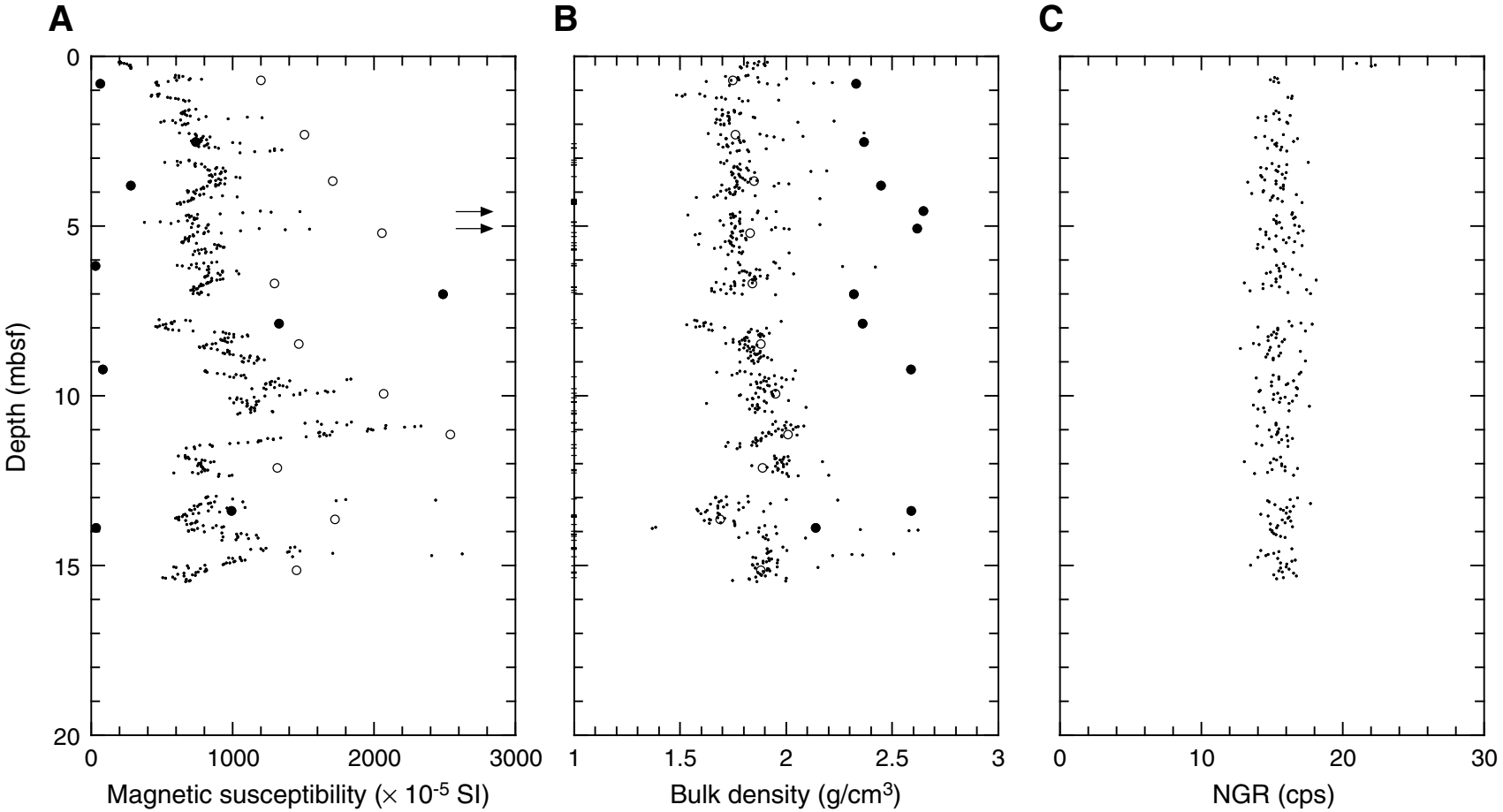

Figure F63. Histogram showing the distribution of magnetic susceptibility of 49 samples of clast material and 61 samples of matrix material taken from Holes 1200D, 1200E, and 1200F. Matrix susceptibilities are corrected to zero porosity.

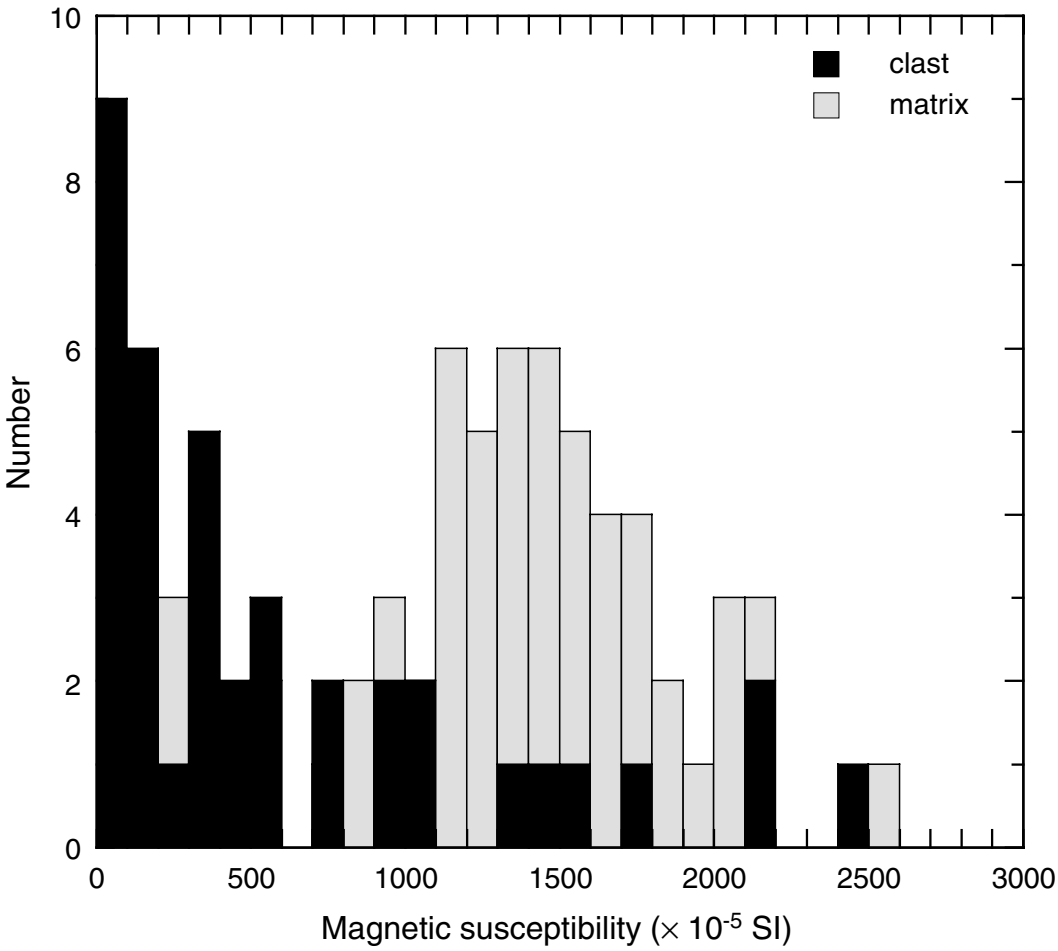

Figure F64. Histogram showing the distribution of grain density for 49 samples of clast material and 61 samples of matrix material taken from Holes 1200D, 1200E, and 1200F.

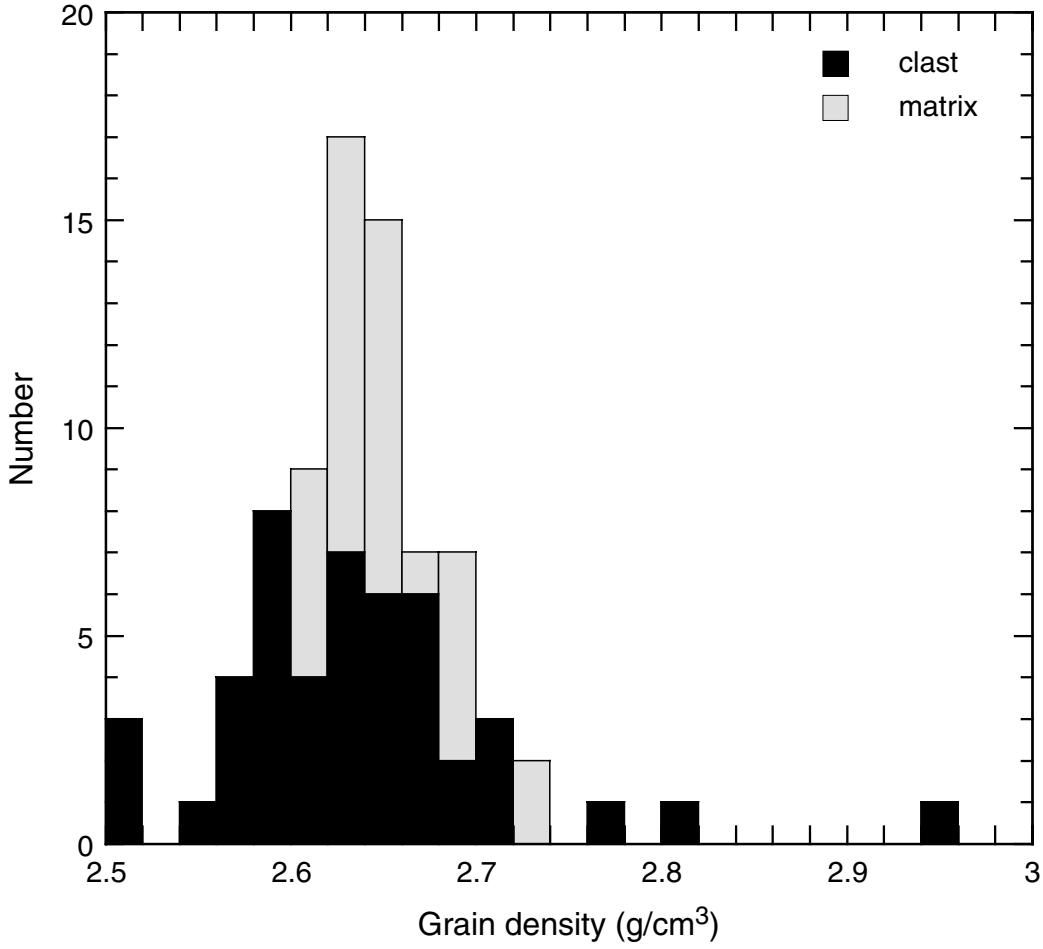

Figure F65. A. Peak shear strength measured in matrix material from Holes 1200D, 1200E, and 1200F using the vane shear apparatus. **B.** Histogram of measured shear strengths. These values exhibit wide scatter about a mean of 52.5 kPa.

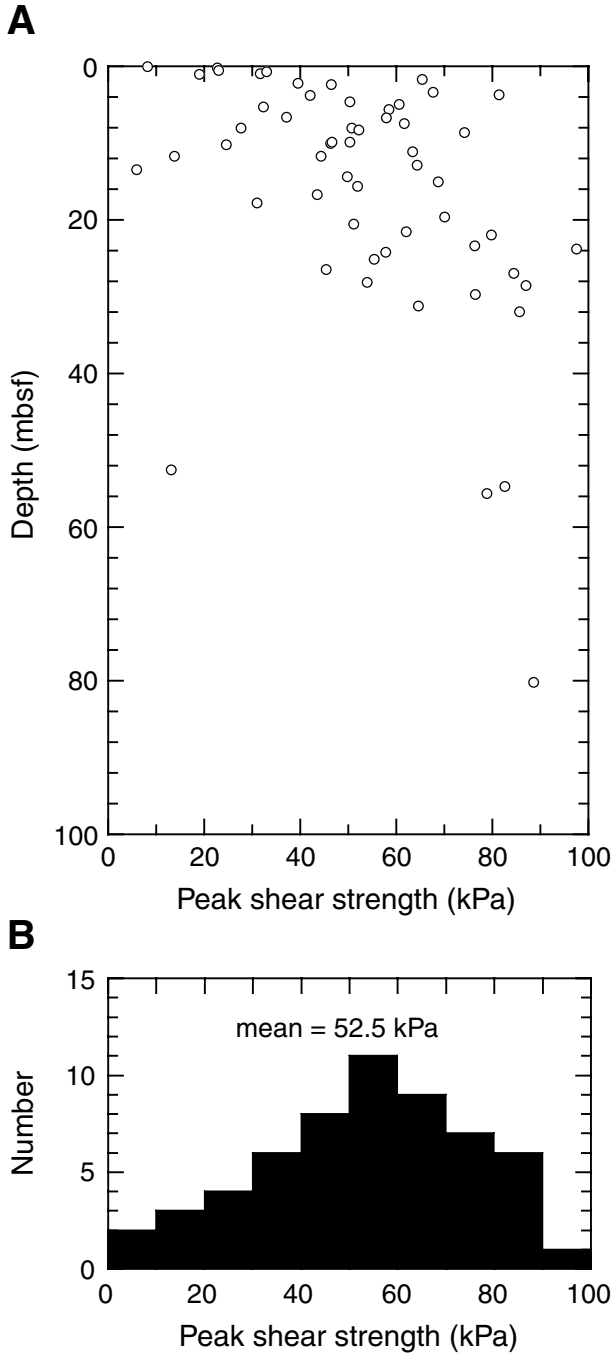

Figure F66. A. Thermal conductivity measured in matrix material from Holes 1200D, 1200E, and 1200F using the needle probe. **B.** Histogram of the thermal conductivities measured in matrix material from Holes 1200D, 1200E, and 1200F.

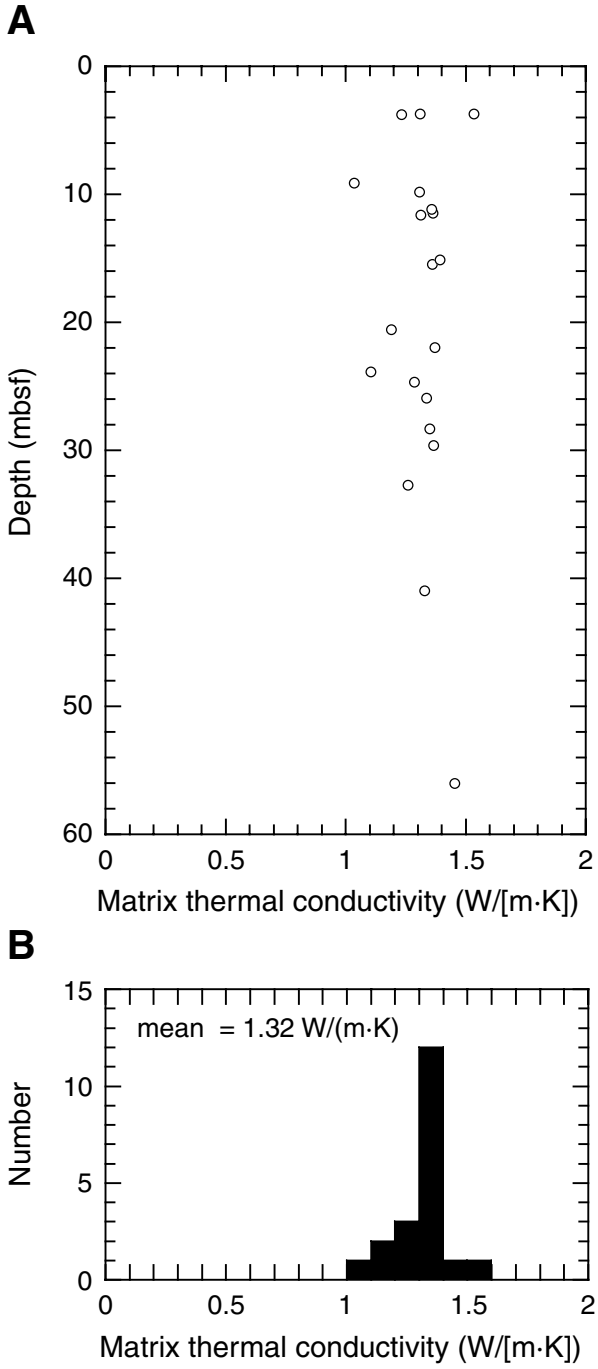

Figure F67. A. Formation factor for Holes 1200D, 1200E, and 1200F, determined from relative resistivity measurements, assuming seawater as the pore fluid. **B.** Porosity determined from index properties measurements on matrix material.

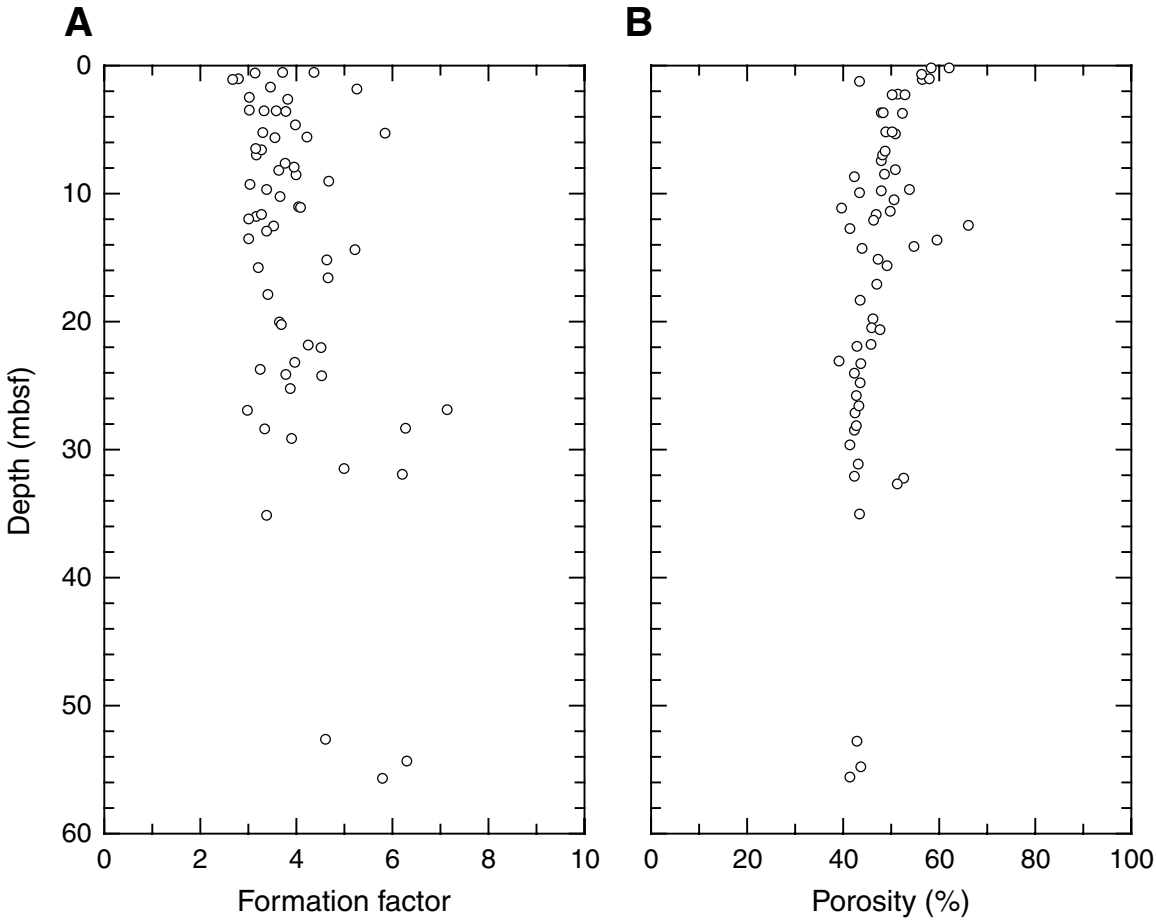

Figure F68. A. Temperature measurement in Hole 1200E at 56.4 mbsf. **B.** Temperature measurement in Hole 1200F at 16.3 mbsf.

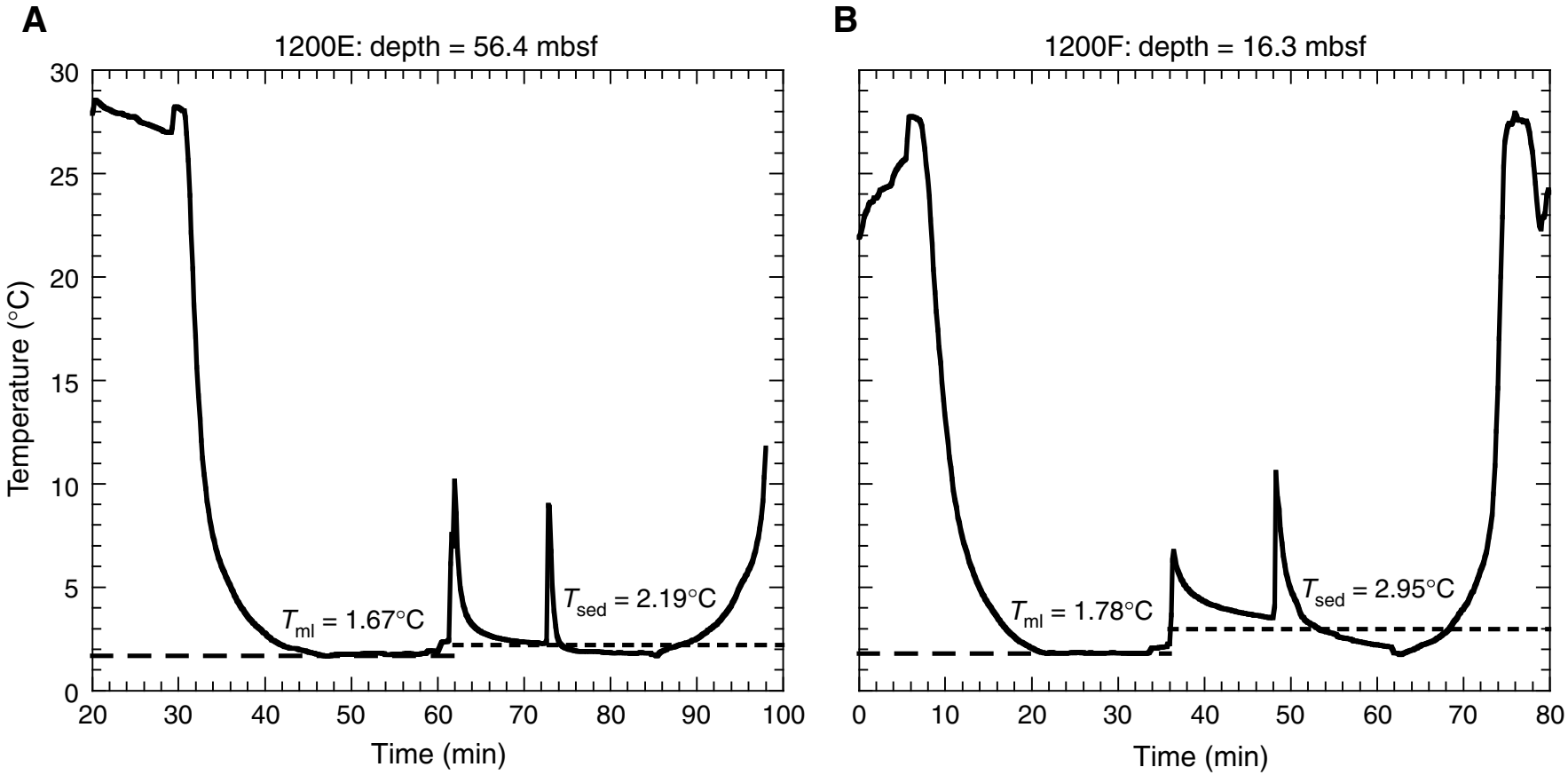

Figure F69. Configuration schematic for circulation obviation retrofit kit (CORK) installed in Hole 1200C. Thermistor T1 was cut off during recovery from an earlier site.

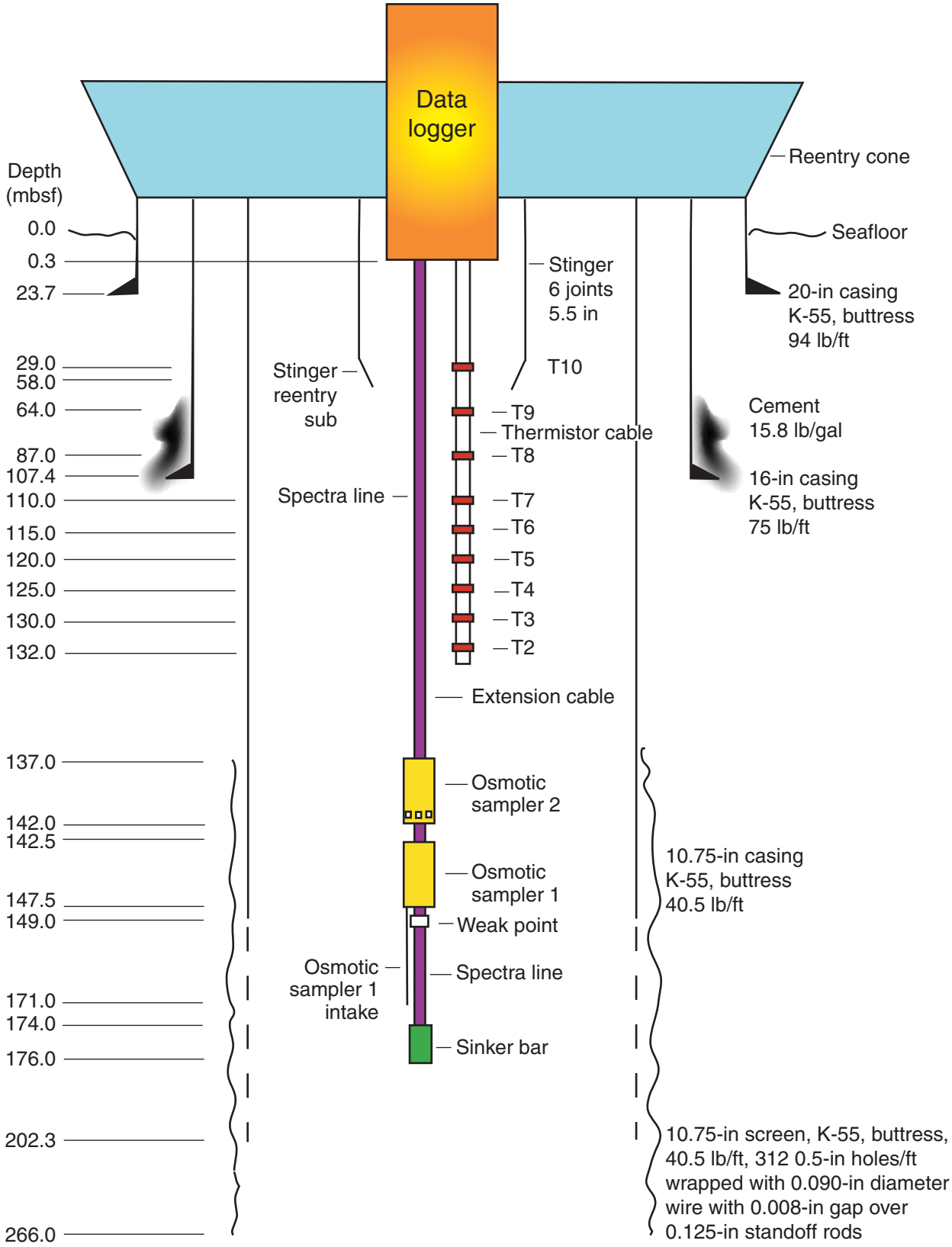

Figure F70. CORK component identification.

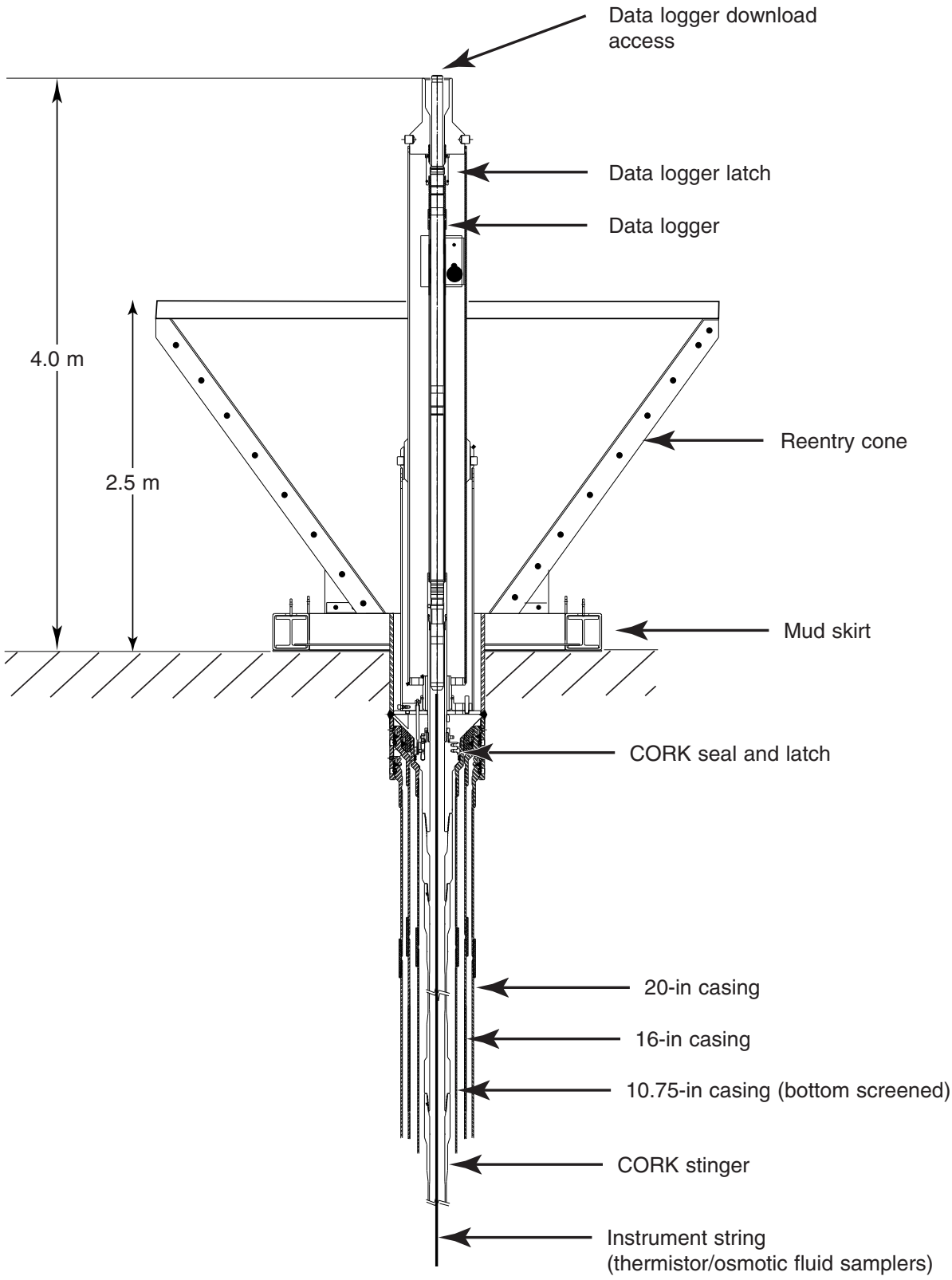

Figure F71. A–E. CORK deployment sequence. ROV = remotely operated vehicle, RH = right hand.

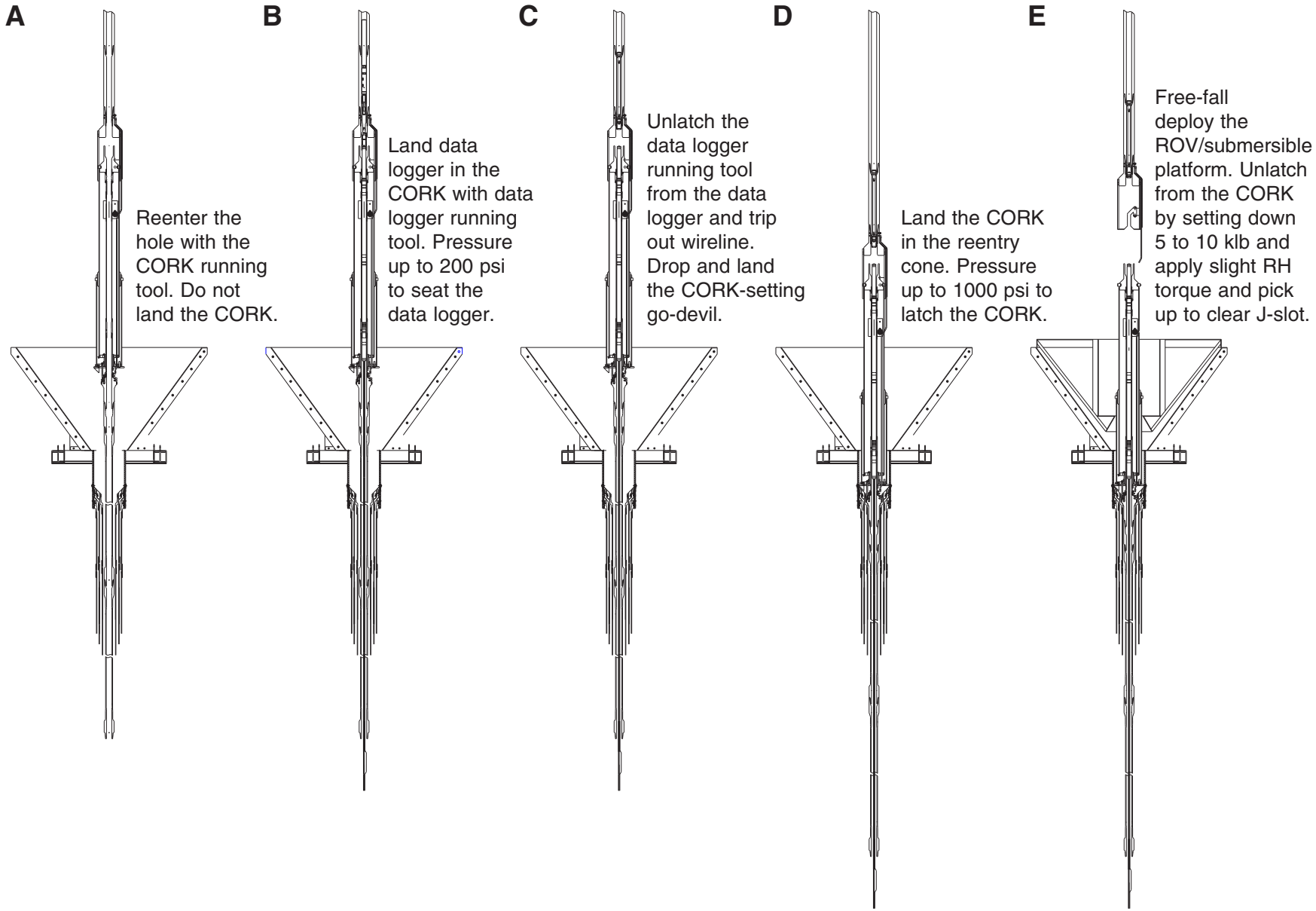

Figure F72. CORK tools.

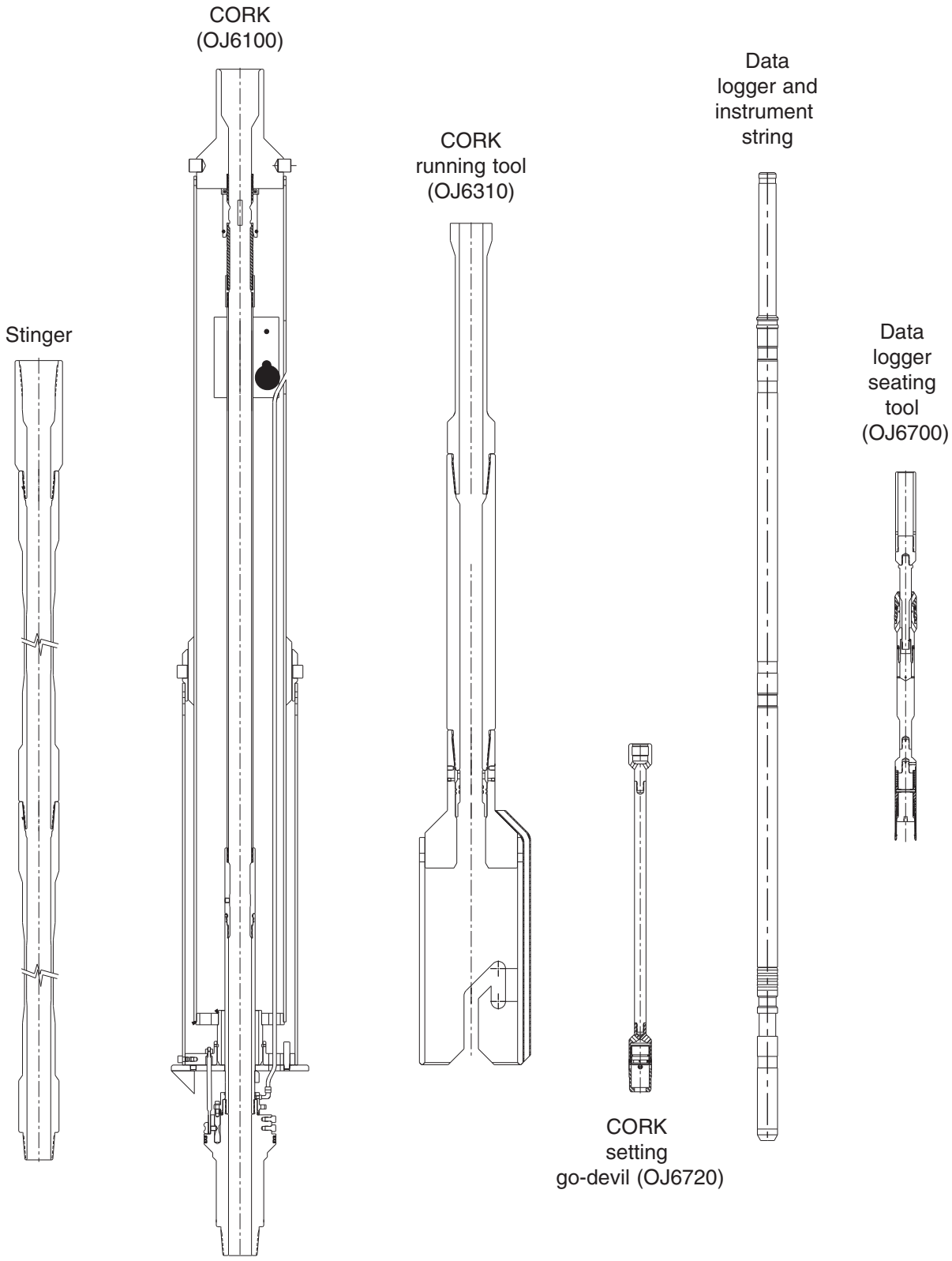

Figure F73. A–D. Data logger seating tool operation.

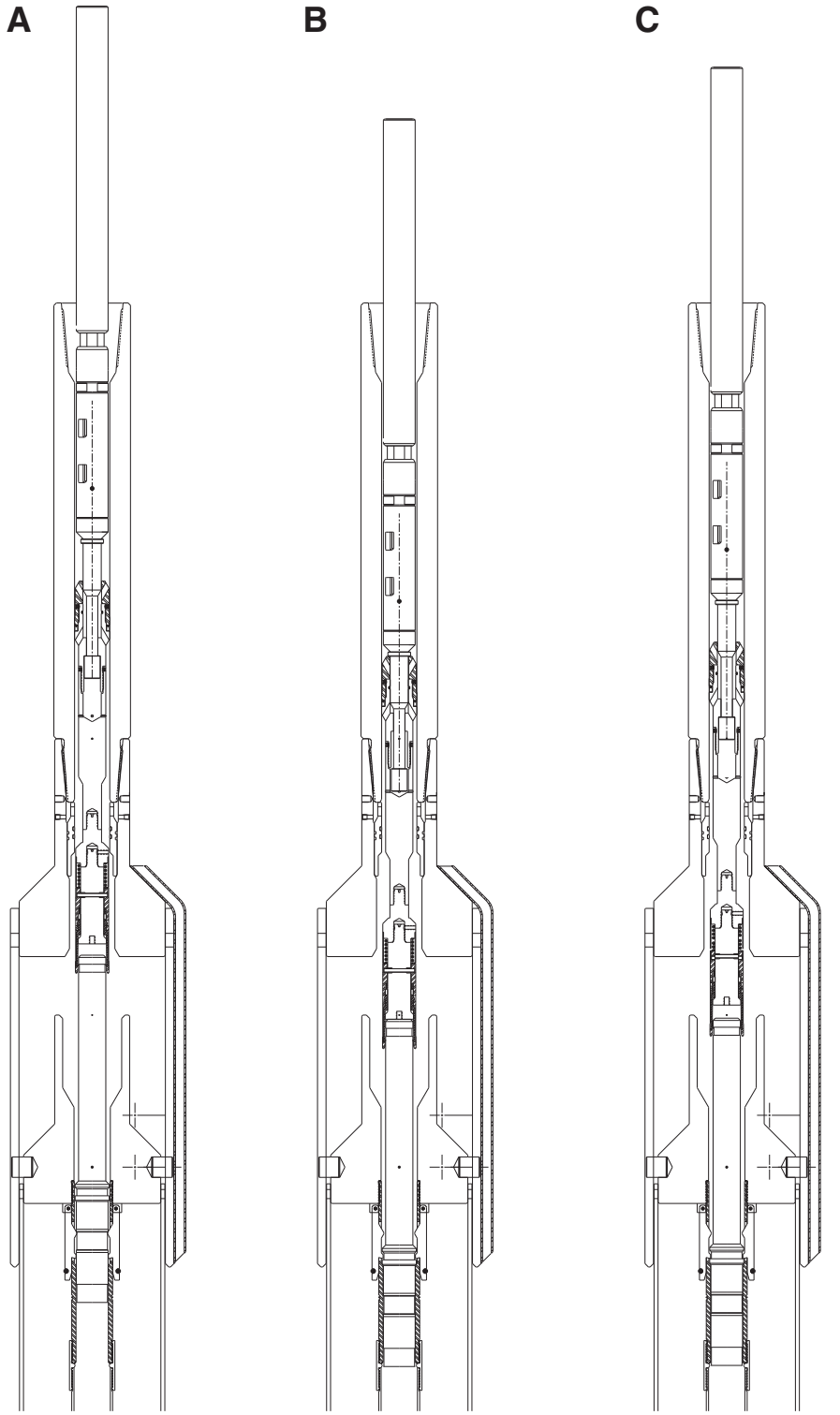

Figure F74. Veins formed during the first serpentinization event. Narrow veins of magnetite-laden serpentine crosscut unserpentinized peridotite along discrete joints.

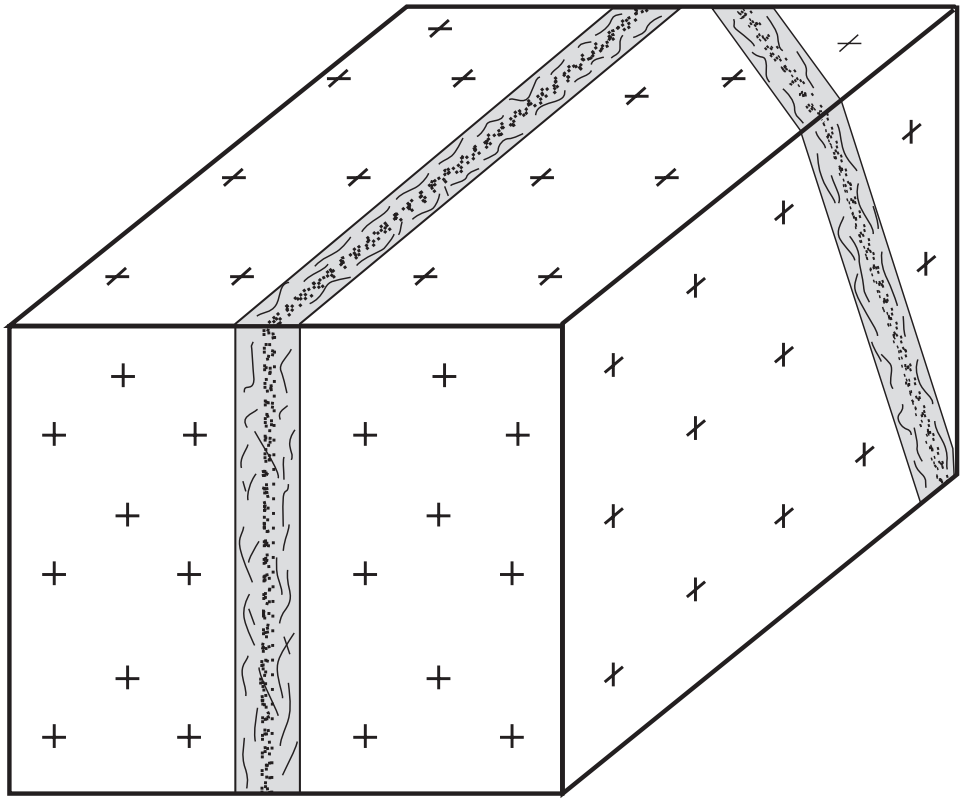

Figure F75. Veins formed during the second serpentinization event, shown intersecting a plane parallel to first serpentine vein set. Second-generation narrow veinlets of pure chrysotile cut the first veins during partial serpentinization and expansion of enclosing peridotite. Arrows indicate direction of dilatory stresses.

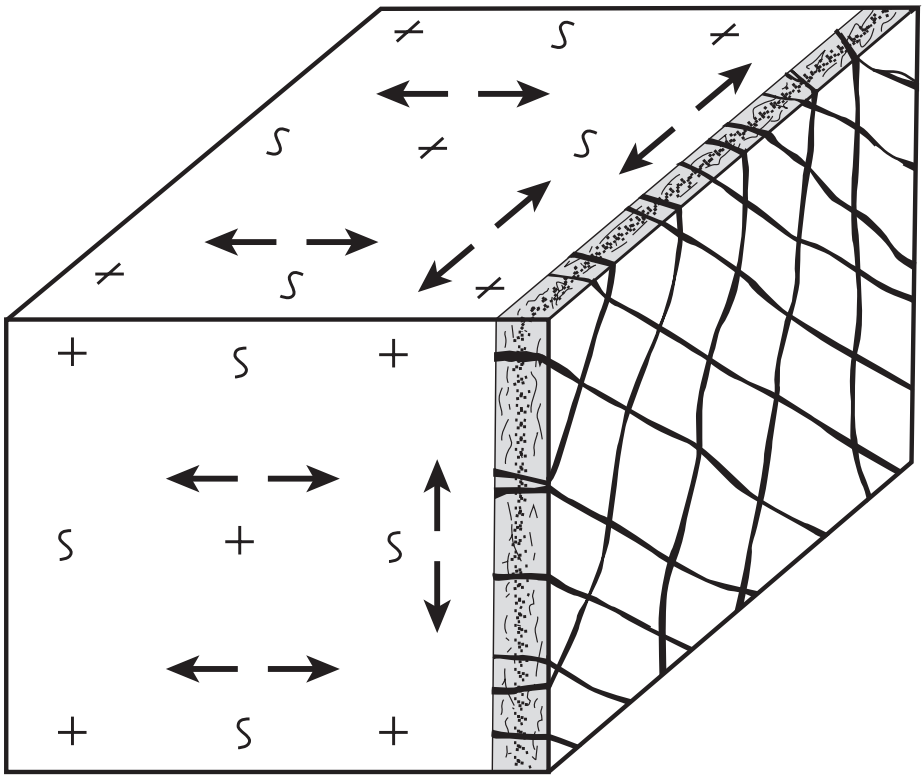

Figure F76. Photograph of a clast margin, showing second-generation chrysotile veinlets crosscutting a first-generation vein (Section 195-1200A-17G-2).

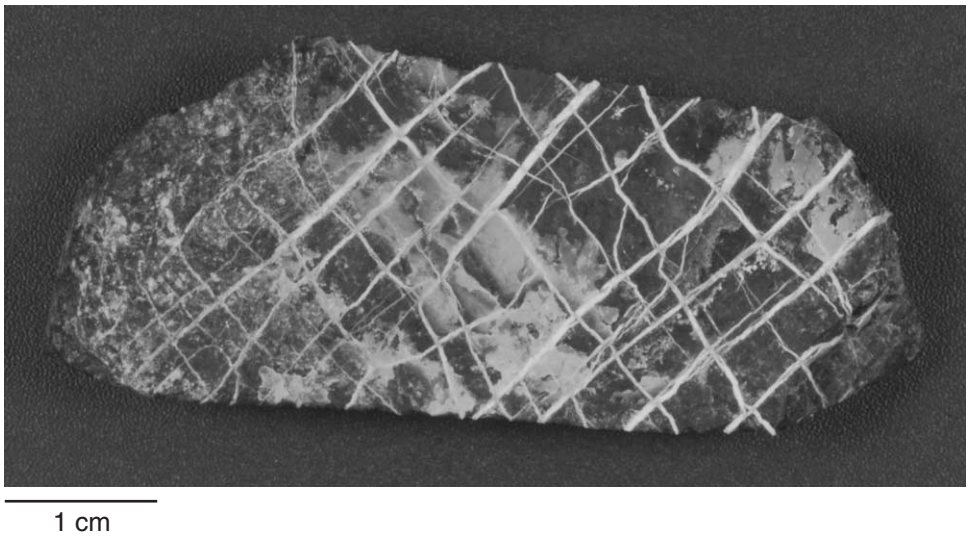

Figure F77. Photograph of a serpentinized clast showing second-generation chrysotile veinlets cutting a first-generation serpentine vein along the clast margin (interval 195-1200A-6R-1, 30–36 cm).

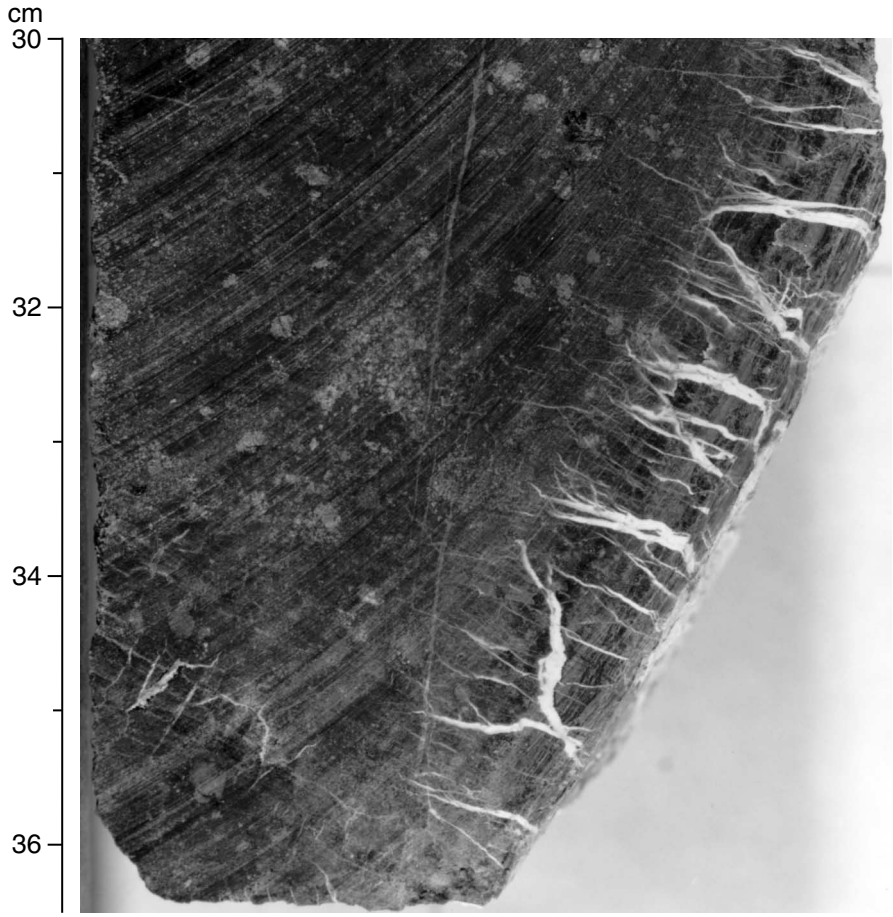

Figure F78. Serpentinite clasts recovered from Hole 1200A. Note the planar margins of most clasts (arrows), where they have broken along joint-controlled serpentine veins, remnants of which are preserved along clast rims. Note also the common bleached selvages along most clasts, indicating reaction with the host serpentine mud.

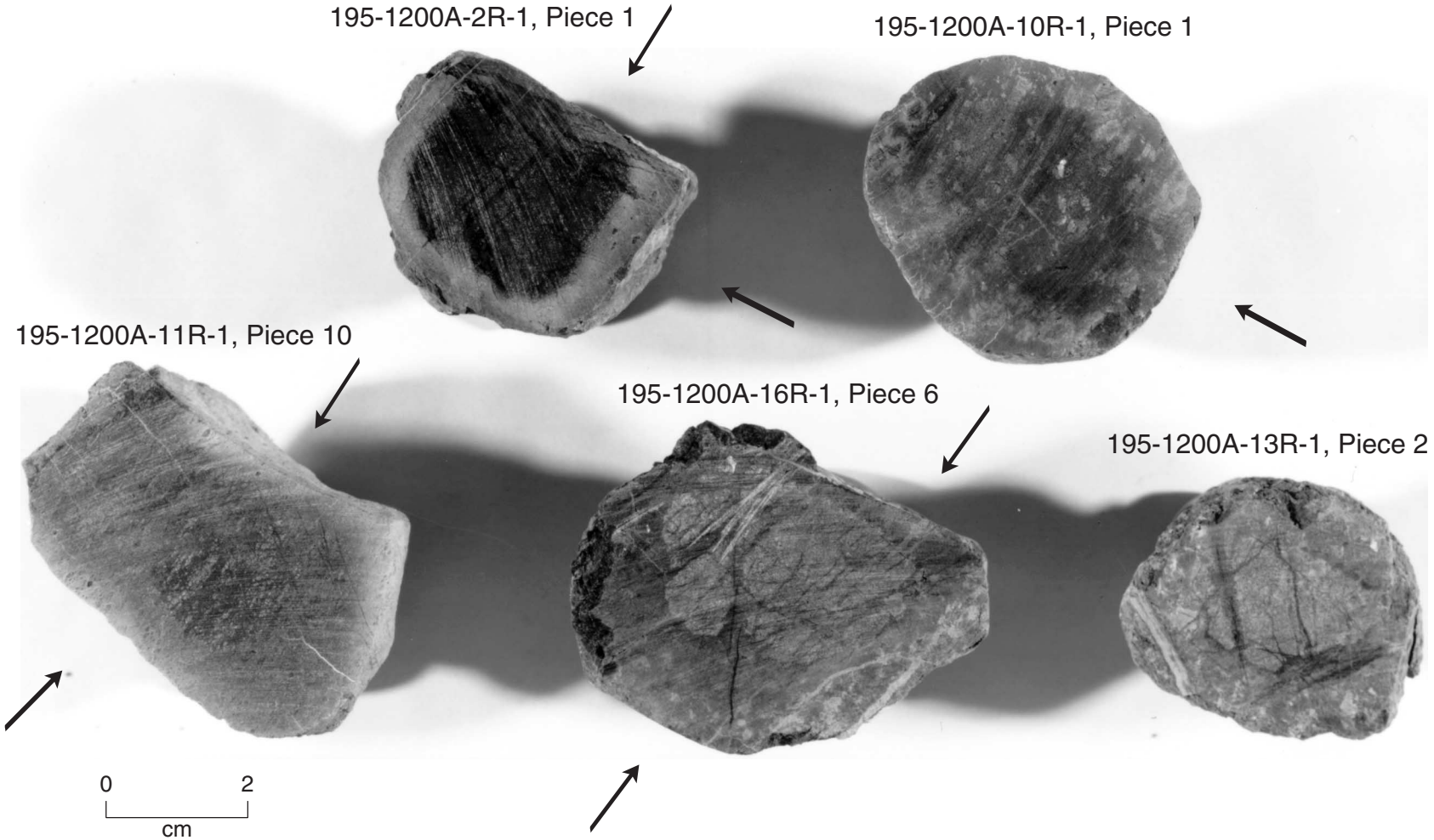

Figure F79. Variation in size, sphericity, and roundness for 250 clasts recovered at Site 1200.

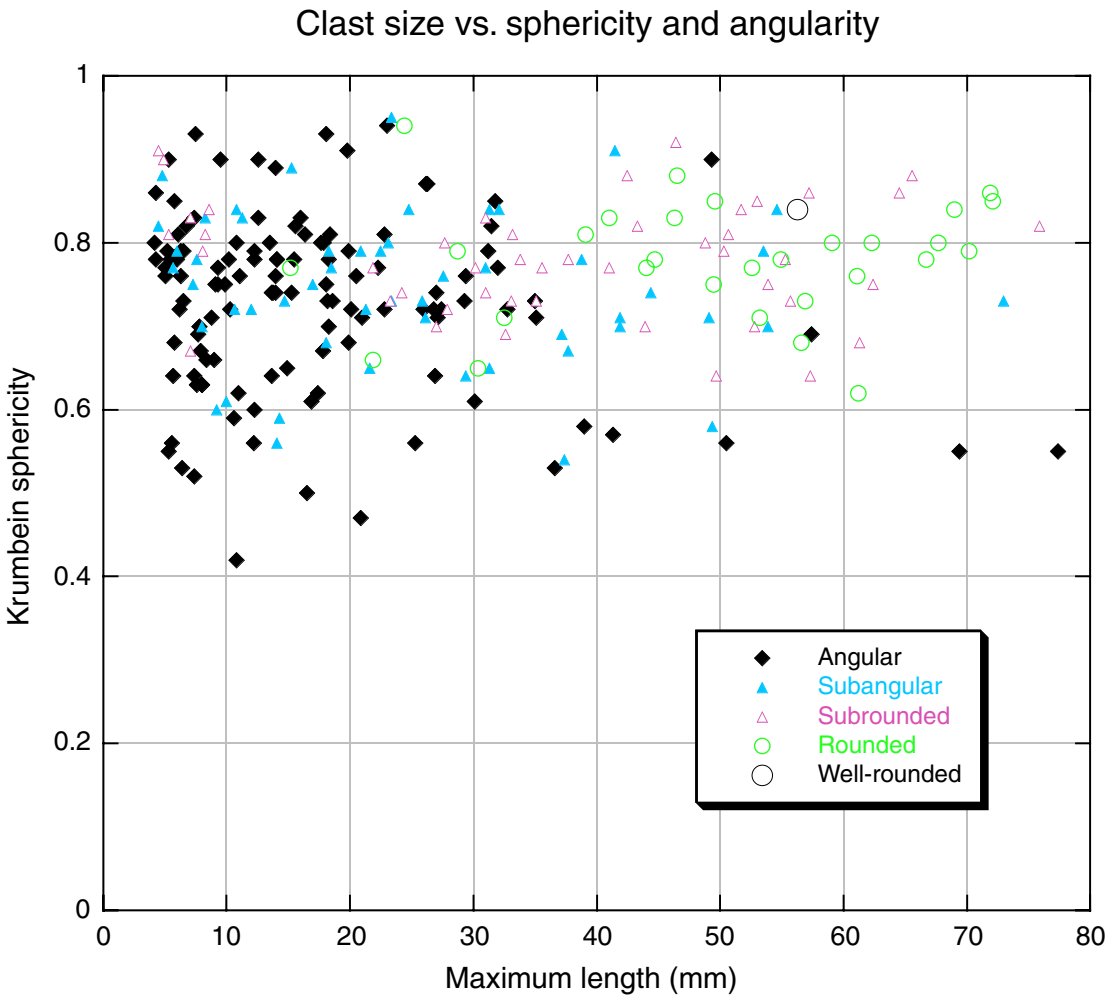

Figure F80. Variation in serpentinite clast shape as a function of size. Pieces were removed for photography from various rotary core barrel cores in Hole 1200A.

Table T1. Coring summary, Site 1200. (See table notes. Continued on next two pages.)

Hole 1200A
Latitude: 13°47.0053′N
Longitude: 146°0.1854′E
Time on site (hr): 446.5 (1130 hr, 10 Mar–0200 hr, 29 Mar 2001)
Time on hole (hr): 76.0 (1130 hr, 10 Mar–1530 hr, 13 Mar 2001)
Seafloor (drill pipe measurement from rig floor, mbrf): 2921.0
Distance between rig floor and sea level (m): 10.7
Water depth (drill pipe measurement from sea level, m): 2910.3
Total depth (drill pipe measurement from rig floor, mbrf): 3068.2
Total penetration (meters below seafloor, mbsf): 147.2
Total length of cored section (m): 147.2
Total core recovered (m): 11.56
Core recovery (%): 7.9
Total number of cores: 17
Comment: Core 195-1200A-17G is a ghost core.

Hole 1200B
Latitude: 13°47.0039′N
Longitude: 146°0.1981′E
Time on hole (hr): 23.0 (1530 hr, 13 Mar–1430 hr, 14 Mar 2001)
Seafloor (drill pipe measurement from rig floor, mbrf): 2922.0
Distance between rig floor and sea level (m): 10.7
Water depth (drill pipe measurement from sea level, m): 2911.3
Total depth (drill pipe measurement from rig floor, mbrf): 3020.0
Total penetration (meters below seafloor, mbsf): 98.0
Total length of cored section (m): 0.0
Total length of drilled intervals (m): 98.0
Total wash core recovered (m): 3.36
Total number of wash cores: 2
Total number of drilled intervals: 2
Comments: Two wash cores were taken between 0.0 and 98.0 mbsf. Core 195-1200B-1W (0.94 m) was taken between 0.0 and 30.7 mbsf. Core 195-1200B-2W (2.42 m) was taken between 30.7 and 98.0 mbsf.

Hole 1200C
Latitude: 13°47.0724′N
Longitude:146°0.1717′E
Time on hole (hr): 278.5 (1430 hr, 14 Mar–0500 hr, 26 Mar 2001)
Seafloor (drill pipe measurement from rig floor, mbrf): 2943.0
Distance between rig floor and sea level (m): 10.7
Water depth (drill pipe measurement from sea level, m): 2932.3
Total depth (drill pipe measurement from rig floor, mbrf): 3083.0
Total penetration (meters below seafloor, mbsf): 140.0
Total length of cored section (m): 0.0
Total length of drilled intervals (m): 140.0
Total core recovered (m): 0.0
Comment: The hole was drilled and cased for downhole CORK installation. No coring was done.

Hole: 1200D
Latitude: 13°47.0443′N
Longitude: 146°0.1715′E
Time on hole (hr): 31.5 (0500 hr, 26 Mar–1230 hr, 27 Mar 2001)
Seafloor (drill pipe measurement from rig floor, mbrf): 2942.0
Distance between rig floor and sea level (m): 11.0
Water depth (drill pipe measurement from sea level, m): 2931.0
Total depth (drill pipe measurement from rig floor, mbrf): 2986.4
Total penetration (meters below seafloor, mbsf): 44.4
Total length of cored section (m): 21.9
Total length of drilled intervals (m): 22.5
Total core recovered (m): 22.0
Core recovery (%): 100.5
Total number of cores: 10
Total number of drilled intervals: 4

Table T1 (continued).

Hole: 1200E
Latitude: 13°47.0014′N
Longitude: 146°0.1858′E
Time on hole (hr): 22.75 (1230 hr, 27 Mar–1115 hr, 28 Mar 2001)
Seafloor (drill pipe measurement from rig floor, mbrf): 2922.0
Distance between rig floor and sea level (m): 11.0
Water depth (drill pipe measurement from sea level, m): 2911.0
Total depth (drill pipe measurement from rig floor, mbrf): 2978.4
Total penetration (meters below seafloor, mbsf): 56.40
Total length of cored section (m): 54.4
Total length of drilled intervals (m): 2.0
Total core recovered (m): 38.06
Core recovery (%): 70.0
Total number of cores: 10
Total number of drilled intervals: 1

Hole: 1200F
Latitude: 13°47.0154′N
Longitude: 146°0.1860′E
Time on hole (hr): 14.75 (1115 hr, 28 Mar–0200 hr, 29 Mar 2001)
Seafloor (drill pipe measurement from rig floor, mbrf): 2922.0
Distance between rig floor and sea level (m): 11.00
Water depth (drill pipe measurement from sea level, m): 2911.0
Total depth (drill pipe measurement from rig floor, mbrf): 2938.3
Total penetration (meters below seafloor, mbsf): 16.30
Total length of cored section (m): 16.3
Total core recovered (m): 16.28
Core recovery (%): 100.0
Total number of cores: 3

Core	Date (Mar 2001)	Time (local)	Depth (mbsf) Top	Depth (mbsf) Bottom	Length (m) Cored	Length (m) Recovered	Recovery (%)	Comments
195-1200A-								
1R	11	2305	0.0	9.7	9.7	0.02	0.2	Whirl-Pak one small piece, all to microbiology and chemistry
2R	12	0130	9.7	18.2	8.5	0.04	0.5	Whirl-Pak
3R	12	0245	18.2	22.2	4.0	0.91	22.8	Whirl-Pak
4R	12	0355	22.2	31.7	9.5	0.00	0.0	Whirl-Pak; no recovery
5R	12	0515	31.7	41.4	9.7	0.00	0.0	Ran DVTP at 41 mbsf (2962 mbsl); no recovery
6R	12	0845	41.4	51.1	9.7	1.86	19.2	Whirl-Pak
7R	12	1105	51.1	60.7	9.6	2.01	20.9	Whirl-Pak
8R	12	1225	60.7	70.4	9.7	0.10	1.0	Whirl-Pak
9R	12	1420	70.4	79.9	9.5	0.75	7.9	AHC; Whirl-Pak
10R	12	1635	79.9	89.4	9.5	1.10	11.6	AHC; Whirl-Pak
11R	12	1920	89.4	99.0	9.6	0.58	6.0	AHC; Whirl-Pak
12R	12	2100	99.0	108.7	9.7	0.28	2.9	AHC; Whirl-Pak
13R	12	2230	108.7	118.3	9.6	1.37	14.3	Whirl-Pak
14R	13	0220	118.3	127.9	9.6	0.23	2.4	Whirl-Pak; hole tight after Core 195-1200A-13R; work pipe 150 klb overpull pipe free
15R	13	0420	127.9	137.6	9.7	0.66	6.8	AHC; Whirl-Pak
16R	13	0700	137.6	147.2	9.6	1.65	17.2	AHC
17G	13	1630	0.0	147.2		2.26	NA	Ghost core
				Totals:	147.2	13.80	9.4	
195-1200B-								
1W	13	2315	0.0	30.7	30.7	0.94	3.1	Wash core; AHC; Whirl-Pak
2W	13	0830	30.7	98.0	67.3	2.42	3.6	Wash core
				Totals:	98.0	3.36	3.4	
195-1200C-								
			*****Drilled from 0.0 to 140.0 mbsf*****					CORK installation hole; no coring was done
195-1200D-								
1H	26	1445	0.0	6.9	6.9	6.90	100.0	PFT
2H	26	1600	6.9	9.9	3.0	3.03	101.0	PFT
3H	26	1915	9.9	12.4	2.5	2.48	99.2	PFT; upper 50 cm disturbed
4H	26	2205	12.4	12.7	0.3	0.35	116.7	PFT; Whirl-Pak, Section 195-1200D-2H-1 disturbed
			*****Drilled from 12.7 to 13.7 mbsf*****					Drilled interval
5H	26	2325	13.7	14.3	0.6	0.60	100.0	PFT; Whirl-Pak
6H	27	0210	21.5	23.5	2.0	1.96	98.0	PFT; Whirl-Pak
7H	27	0300	23.5	25.0	1.5	1.57	104.7	PFT; Whirl-Pak
8H	27	0410	25.0	28.0	3.0	3.04	101.3	PFT; Whirl-Pak

Table T1 (continued).

Core	Date (Mar 2001)	Time (local)	Depth (mbsf) Top	Depth (mbsf) Bottom	Length (m) Cored	Length (m) Recovered	Recovery (%)	Comments
9H	27	0530	28.0	29.5	1.5	1.45	96.7	PFT; Whirl-Pak
			*****Drilled from 29.5 to 34.8 mbsf*****					Drilled interval
10H	27	0830	34.8	35.4	0.6	0.62	103.3	PFT; Whirl-Pak
			*****Drilled from 35.4 to 44.4 mbsf*****					
				Cored totals:	21.9	22.00	100.5	
				Drilled totals:	22.5			
				Total:	44.4			
195-1200E-								
1H	27	1540	0.0	6.1	6.1	6.10	100.0	Whirl-Pak
2H	27	1700	6.1	11.0	4.9	4.94	100.8	Whirl-Pak
3H	27	1830	11.0	12.0	1.0	1.11	111.0	Whirl-Pak
4H	27	1920	12.0	17.6	5.6	5.55	99.1	Whirl-Pak; expanding core
5H	27	2015	17.6	21.2	3.6	3.52	97.8	Whirl-Pak; expanding core
6H	27	2120	21.2	25.9	4.7	4.73	100.6	Whirl-Pak; DVTP; expanding core
7H	28	0150	25.9	32.5	6.6	6.85	103.8	Whirl-Pak stuck core barrel drill over expanding core
8X	28	0355	32.5	40.9	8.4	0.93	11.1	Whirl-Pak
9X	28	0730	40.9	50.4	9.5	0.28	2.9	Drilled out after DVTP
			*****Drilled from 50.4 to 52.4 mbsf*****					
10H	28	0820	52.4	56.4	4.0	4.05	101.3	Whirl-Pak; DVTP at TD = 56.4 mbsf
				Cored totals:	54.4	38.06	70.0	
				Drilled totals:	2.0			
				Total:	56.4			
195-1200F-								
1H	28	1335	0.0	7.7	7.7	7.71	100.1	Whirl-Pak
2H	28	1525	7.7	12.9	5.2	5.17	99.4	Whirl-Pak
3H	28	1645	12.9	16.3	3.4	3.40	100.0	Whirl-Pak; ADARA at TD = 16.3 mbsf
				Total:	16.3	16.28	100.0	

Notes: NA = not applicable. CORK = circulation obviation reentry kit, DVTP = Davis-Villinger temperature probe, AHC = active heave compensator, PFT = perfluorocarbon tracer. TD = total depth.

Table T2. X-ray diffraction (XRD) data for rock pieces and silty clay samples from bulk powder mounts, Site 1200. (**See table note.** Continued on next page.)

Core, section, interval (cm)	Depth (mbsf)	Lithology	Mineral													
			Serpentine	Brucite	Calcite	Aragonite	Opal-CT	Analcime(?)	Forsterite	Orthopyroxene	Clinopyroxene	Amphibole	Chlorite	Talc	Mixed-layer clay	Halite
195-1200A-																
1R-1, 0–1	0.00	Carbonate chimney			D	A										P
3R-1, 9–10	18.29	Fine-grained ultramafic	D	D						P						
3R-1, 81–84	19.01	Fine-grained ultramafic	D	D						C	P					
6R-1, 33–34	41.73	Serpentine vein	D	D												
6R-2, 40–41	43.06	Harzburgite with serpentine vein	D	A					P							
7R-2, 72–73	52.41	Harzburgite	D	A					A	A	C					
9R-1, 30–31	70.70	Serpentine mud	D	C								P	P	P		C
9R-1, 54–55	70.94	Serpentine mud	D	C								P		P		P
9R-1, 75–76	71.15	Serpentine mud	D	C								P		P		C
10R-1, 93–93	80.83	Fine-grained ultramafic	D	A						C	P					
11R-1, 7–8	89.47	Fine-grained ultramafic with SiO_2 veins	C	C			D								C	
11R-1, 21–22	89.61	Fine-grained ultramafic with SiO_2 veins	C	D			A									
11R-1, 45–46	89.85	Fine-grained ultramafic	D	A						P						
11R-1, 66–67	90.06	Harzburgite	D	A					C	C	P					
13R-1, 1–2	108.71	Serpentine mud	D	C								P		P		P
13R-1, 25–26	108.95	Fine-grained ultramafic	D	A						C						
13R-2, 4–5	109.99	Pure fibrous chrysotile	D													
15R-1, 1–2	127.91	Serpentine mud	D	C								C		P		C
15R-CC, 1–2	128.44	Serpentine mud	D	A								P				
16R-2, 47–48	139.42	Fine-grained ultramafic	D	A						P						
17G-2, 29–30		Serpentine vein	D	A						A						
195-1200B-																
2H-1, 124–126	31.94	Greenschist									D		A			
2H-2, 2–6	32.22	Fine-grained ultramafic	D	D												
195-1200D-																
1H-1, 0–1	0.00	Carbonate mud			D											
1H-1, 10–11	0.10	Oxidized mud	A		C	A						P		P		C
1H-1, 20–21	0.20	Light bluish mud	D		C	C						P				C
1H-1, 50–51	0.50	Bluish gray mud	D		P	A							P			P
1H-1, 77–78	0.77	Bluish gray mud	D		P	A						C	P			P
1H-1, 100–101	1.00	Black mud	D			A		C								P
1H-3, 40–41	3.40	Bluish gray mud	A	D								C		P		P
1H-3, 99–100	3.99	Brown streaky flakes in mud	D													
1H-4, 63–64	5.13	Bluish gray mud	D	P												P
1H-CC, 30–31	6.70	Altered clast, greenish	D	D												
2H-1, 60–61	7.50	Bluish gray mud	A	A				P								P
2H-2, 11–12	8.51	Dark mottled mud	D	A								P	P	P		P
2H-2, 40–41	8.80	Bluish gray mud	D	A												
3H-1, 55–56	10.45	Altered clast, light green	D	A												
3H-1, 60–61	10.50	Altered clast, dark green	D	P												
3H-1, 110–111	11.00	Bluish gray mud	A	D												
3H-CC, 10–11	12.22	Bluish gray mud	D	A												P
6H-1, 9–10	21.59	Bluish gray mud	D	A								C	P	P		P
6H-CC, 23–24	23.42	Bluish gray mud	D	A								P		P		P
7H-1, 56–57	24.06	Bluish gray mud	D	A								P				P
8H-1, 20–21	25.20	Bluish gray mud	D	A								P		P		P
8H-2, 49–50	26.99	Bluish gray mud	D	C								P				P
9H-1, 49–50	28.49	Bluish gray mud	D	A								P				P
9H-CC, 0–1	29.10	Fine sand fraction	D	A								P				
195-1200E-																
1H-1, 14–15	0.14	Oxidized mud	A			D						P	P			C
1H-1, 109–110	1.09	Black mud	A	C		D		P				P		P		P
1H-3, 29–30	3.29	Black mud	D	A				P				P	P	P		P
1H-4, 99–100	5.49	Black mud	D	A				P				P		P		P
2H-2, 29–30	7.89	Black mud	D	A				P				C	P	P		P
2H-3, 109–110	10.19	Black mud	D	C								C	P	C		P
3H-1, 74–75	11.74	Contorted greenish mud	A		A	A						P				P
4H-1, 57–58	12.57	Black mud	A	A	P			P				C	P	P		P
4H-3, 70–71	15.70	Black mud	A	P	C	A		P				P	P	P		P
5H-1, 130–131	18.90	Dark bluish mud	D	A				P				P	P	P		P

Table T2 (continued).

Core, section, interval (cm)	Depth (mbsf)	Lithology	Mineral													
			Serpentine	Brucite	Calcite	Aragonite	Opal-CT	Analcime(?)	Forsterite	Orthopyroxene	Clinopyroxene	Amphibole	Chlorite	Talc	Mixed-layer clay	Halite
6H-1, 99–100	22.19	Dark bluish mud	D	A				P				P				P
6H-3, 114–115	25.28	Dark bluish mud	D	A				P				P	P			P
7H-2, 99–100	28.39	Bluish gray mud	D	A								P				P
7H-5, 18–19	32.08	Bluish gray mud	D	A												P
10H-1, 19–20	52.59	Bluish gray mud	D	C								C	P	P		P
10H-3, 40–41	55.80	Bluish gray mud	D	C								P	P	P		P
195-1200F-																
1H-1, 39–40	0.39	Black mud	A	P	P	D						P				P
1H-3, 40–41	3.40	Black mud	D	A				P				P	P	P		P
1H-5, 59–60	6.59	Black mud	D	A				P				P	P	P		P
2H-2, 50–51	9.70	Black mud	D	C				P				C	P	P		P
2H-4, 70–71	12.40	Black mud	D	C				P				C	P	P		P
3H-2, 104–105	15.44	Black mud	D	A				P				P	P	P		P

Note: Semiquantitative estimation of mineral abundance is based on major XRD peak intensities displayed by the various minerals: D = dominant (50%–100%), A = abundant (20%–50%), C = common (5%–20%), P = present (1%–5%).

Table T3. Elemental content, mineral composition, LOI, and Mg# of representative serpentinized ultramafic rocks, Site 1200. (Continued on next page.)

	Hole 1200A											
Core, section:	3R-1	6R-1	7R-2	7R-2	7R-2	10R-1	10R-1	10R-1	11R-1	11R-1	11R-1	12R-1
Interval (cm):	81–84	31–33	27–29	69–71	116–118	13–15	93–95	100–102	20–24	28–30	63–65	3–5
Piece:	2	2	1A	1C	2	3	11	12	6	7	11	1
Depth (mbsf):	19.01	41.71	51.96	52.38	52.85	80.03	80.83	80.90	89.60	89.68	90.03	99.03
Rock type:	Harzburgite	Dunite	Harzburgite	Harzburgite	Harzburgite	Harzburgite	Lherzolite	Harzburgite	Harzburgite	Harzburgite	Harzburgite	Harzburgite
Major element oxides (wt%):												
SiO_2	43.76	41.12	44.05	43.83	44.41	42.90	43.12	44.26	43.98	44.08	43.99	44.42
TiO_2	0.01	0.01	0.01	0.01	0.01	0.01	0.02	0.02	0.02	0.02	0.01	0.01
Al_2O_3	0.56	0.62	0.72	0.74	0.70	0.72	0.95	0.82	0.84	0.68	0.71	0.64
Fe_2O_3T	8.33	8.71	8.26	8.46	8.13	8.32	8.28	8.45	8.62	8.66	8.84	7.95
MnO	0.11	0.11	0.12	0.12	0.12	0.13	0.11	0.12	0.13	0.11	0.12	0.12
MgO	46.50	48.69	47.15	47.43	46.26	47.56	45.30	46.02	46.57	46.64	47.41	46.27
CaO	0.59	0.63	0.75	0.92	0.86	0.49	1.82	0.95	0.53	0.77	0.73	0.71
Na_2O	0.09	0.07	0.08	0.06	0.05	0.11	0.10	0.10	0.15	0.04	0.08	0.07
K_2O	0.04	0.03	0.02	0.03	0.02	0.02	0.03	0.03	0.01	0.02	0.03	0.03
P_2O_5	0.03	0.01	0.04	0.01	0.06	0.06	0.01	0.06	0.04	0.06	0.01	0.01
Total:	100.00	100.00	100.85	101.60	100.57	100.25	99.72	100.77	100.20	101.03	101.92	100.22
Trace elements (ppm):												
Sc	7.7	6.4	8.4	8.9	8.4	6.7	9.4	10.7	11.3	6.7	7.5	9.0
V	28.7	25.3	18.5	18.3	18.9	30.7	42.6	39.5	42.4	27.6	30.7	19.5
Cr	2487	3685	2897	2973	2660	2340	3170	2251	3193	2739	2977	2806
Ni	2342	2558	2524	2384	2464	2721	2403	2541	3339	2588	2503	2432
Sr	19.48	26.82	15.84	16.09	13.31	31.64	34.79	41.72	24.90	9.80	24.54	7.29
Y	1.5	2.2	0.7	2.1	0.4	0.9	1.7	0.5	0.7	0.6	2.1	0.5
Ba	4.8	2.8	3.3	3.4	7.5	8.2	5.6	12.8	6.8	7.6	3.7	10.7
Zr	0.4	2.8	3.8	2.0	1.8	0.3	2.0	0.5	1.9	1.8	2.5	2.3
LOI:	14.54	14.62	12.90	11.29	11.57	16.68	14.50	15.56	11.66	12.50	13.46	12.41
Estimated serpentine (%):	60	81	64	39		61	70		100		85	37
CIPW-normative minerals (wt%):												
or	0.24	0.18	0.11	0.15	0.11	0.13	0.19	0.19	0.07	0.09	0.16	0.19
ab	0.79	0.61	0.65	0.48	0.42	0.89	0.84	0.86	1.24	0.38	0.68	0.57
di	2.13	2.42	2.73	3.55	3.04	1.61	7.06	3.41	1.89	2.71	2.79	2.70
hy	16.22	1.32	15.36	12.84	19.13	11.30	10.21	17.17	16.09	17.08	13.60	19.29
ol	78.44	93.11	79.90	82.13	75.45	83.94	78.87	76.63	79.06	78.23	82.23	75.25
mt	1.00	1.04	0.99	1.01	0.97	1.00	0.99	1.01	1.03	1.04	1.06	0.95
il	0.02	0.02	0.03	0.02	0.02	0.03	0.03	0.03	0.03	0.03	0.02	0.02
ap	0.08	0.02	0.09	0.02	0.15	0.14	0.02	0.14	0.09	0.13	0.02	0.03
Total:	98.91	98.74	99.86	100.22	99.30	99.03	98.22	99.44	99.52	99.70	100.57	99.01
Mg#:	92.34	92.35	92.50	92.37	92.47	92.51	92.20	92.16	92.10	92.08	92.05	92.63

Notes: Element compositions were determined by inductively coupled plasma–atomic emission spectroscopy. LOI = loss on ignition. Mg# = $100 \times Mg^{2+}/(Mg^{2+}+Fe^{2+})$. Calculated CIPW-normative compositions: or = norm orthoclase, ab = norm albite, di = norm diopside, hy = norm hyperthene, ol = norm olivine, mt = norm magnetite, il = norm ilmenite, ap = norm apatite.

Table T3 (continued).

	1200A									1200B	
Core, section:	13R-1	13R-1	14R-1	16R-1	16R-1	16R-2	16R-2	16R-2	17G-2	1W-1	2W-2
Interval (cm):	25–27	90–92	22–24	112–114	133–135	15–17	29–31	48–50	29–31	76–78	2–6
Piece:	6A	8B	6	11B	12	1	2	4	2	5B	1
Depth (mbsf):	108.95	109.60	118.52	138.72	138.93	139.10	139.24	139.43	Unknown	0.76	32.22
Rock type:	Dunite	Harzburgite	Harzburgite	Harzburgite	Harzburgite	Harzburgite	Harzburgite	Harzburgite	Harzburgite	Dunite	Harzburgite
Major element oxides (wt%):											
SiO_2	41.34	43.26	42.81	42.86	43.85	44.63	43.22	44.21	44.23	41.67	42.95
TiO_2	0.01	0.01	0.01	0.01	0.01	0.01	0.01	0.01	0.01	0.01	0.01
Al_2O_3	0.62	0.49	0.62	0.45	0.37	0.72	0.67	0.38	0.70	0.41	0.37
Fe_2O_3T	9.80	8.62	8.70	7.99	7.76	7.78	8.31	8.57	8.15	8.56	7.60
MnO	0.15	0.11	0.12	0.12	0.12	0.12	0.12	0.12	0.12	0.13	0.12
MgO	48.37	47.79	46.81	46.02	47.30	47.12	46.58	47.38	47.20	48.87	46.33
CaO	0.36	0.69	0.82	0.66	0.69	0.93	0.98	0.46	0.78	0.24	0.67
Na_2O	0.08	0.07	0.06	0.07	0.07	0.07	0.07	0.27	0.10	0.09	0.07
K_2O	0.02	0.03	0.03	0.02	0.02	0.03	0.03	0.03	0.03	0.01	0.02
P_2O_5	0.01	0.01	0.01	0.05	0.01	0.06	0.01	0.01	0.05	0.04	0.04
Total:	100.75	101.07	99.97	98.19	101.15	101.40	100.00	101.42	101.32	100.00	100
Trace elements (ppm):											
Sc	7.7	7.7	7.6	7.3	7.2	8.8	9.6	8.9	8.1	8.8	9.6
V	29.5	22.8	19.5	25.6	22.9	19.3	19.4	27.9	32.0	27.2	16.6
Cr	2548	2564	2552	3810	2201	2427	2492	2661	3175	2178	2551
Ni	3706	2437	2580	2483	2761	2412	2524	2829	2673	2983	2879
Sr	18.92	23.70	18.20	21.57	18.01	17.10	16.97	24.23	29.36	12.66	7.90
Y	1.8	3.6	1.9	0.3	0.9	0.7	0.7	0.6	1.2	0.3	0.9
Ba	2.2	3.0	4.7	9.2	5.3	13.1	9.8	7.2	8.7	2.4	2.7
Zr	1.6	2.0	1.9	2.2	3.9	1.8	3.5	1.5	1.7	3.8	2.8
LOI:	18.19	14.48	14.00	15.56	15.94	12.02	13.05	15.96	14.89	16.04	11.42
Estimated serpentine (%):	48	79	62	83		58		100	83	100	72
CIPW-normative minerals (wt%):											
or	0.09	0.15	0.16	0.13	0.10	0.18	0.16	0.16	0.16	0.09	0.09
ab	0.64	0.62	0.53	0.56	0.63	0.57	0.62	1.80	0.85	0.74	0.61
di	1.34	2.63	3.15	2.30	2.66	3.33	3.78	1.72	2.78	0.73	2.43
hy	3.26	10.80	11.11	15.30	15.04	17.16	12.41	12.76	15.33	5.16	14.97
ol	92.82	84.68	82.66	77.81	79.87	77.84	80.71	82.91	79.87	91.14	78.12
mt	1.17	1.03	1.04	0.96	0.93	0.93	0.99	0.81	0.98	1.03	0.91
il	0.02	0.02	0.02	0.02	0.02	0.02	0.02	0.02	0.03	0.02	0.02
ap	0.02	0.02	0.02	0.12	0.01	0.14	0.01	0.03	0.13	0.09	0.09
Total:	99.38	99.95	98.70	97.19	99.26	100.18	98.72	100.22	100.13	99.00	97.25
Mg#:	91.42	92.29	92.08	92.56	92.93	92.90	92.37	92.27	92.59	92.49	92.93

Table T4. Distribution of calcareous nannofossils, Holes 1200D, 1200E, and 1200F. (See table notes. Continued on next page.)

Core, section, interval (cm)	Depth (mbsf)	Zone	Preservation	Group abundance	*Calcidiscus leptoporus*	*Ceratolithus cristatus*	*Coccolithus pelagicus*	*Cyclicargolithus floridanus*	*Emiliania huxleyi/Reticulofenestra* sp.?	*Emiliania huxleyi*	*Gephyrocapsa caribbeanica*	*Gephyrocapsa lumina*	*Gephyrocapsa margarelii*	*Gephyrocapsa oceanica*	*Gephyrocapsa* spp.	*Gephyrocapsa* spp. (small)	*Helicosphaera carteri*	*Neosphaera coccolithomorpha*	*Oolithotus fragilis*	*Pontosphaera* spp.	*Reticulofenestra minutula*	*Reticulofenestra pseudoumbilicus*	*Reticulofenestra* sp.	*Rhabdosphaera clavigera*	*Syracosphaera pulchra*	*Syracosphaera* spp.	*Umbellosphaera* spp.	*Umbilicosphaera sibogae*	Comments
195-1200A-																													
9R-1, 73–75	71.13			B																									
15R-CC, 8–13	128.51		G	B																		R							A well-preserved but contaminated specimen
195-1200D-																													
1H-1, 13–18	0.13	NN21	G	R						A				C			F	R	R	R			R	R		F	C	C	
1H-1, 20–20	0.20	NN21	G	R		R				F				C			F							R		F	C	C	
1H-1, 27–32	0.27	NN21	G	R	R	R				A			R	C			R			R				R	R	F	C	C	
1H-1, 51–51	0.51	NN20	P	T												R													
1H-1, 108–108	1.08			B																									
1H-2, 16–16	1.66			B																									
1H-3, 98–98	3.98			B																									
1H-4, 9–9	4.59			B																									
1H-CC, 45–50	6.85		P	T			R														R		R						
2H-CC, 30–35	9.88		M	T			R					R																	
3H-CC, 21–26	12.33		M	T												R						R							
4H-CC, 8–15	12.68		M	T				R															R						
5H-CC, 13–20	14.23		P	T																									Poorly preserved and unidentifiable coccoliths
6H-CC, 22–27	23.41		M	T																		R							
7H-CC, 22–27	25.02			B																									
8H-CC, 32–37	27.99			B																									
9H-CC, 27–32	29.37			B																									
10H-CC, 16–20	35.38			B																									
195-1200E-																													
1H-1, 0–10	0.05	NN21	G	T	R					C				C			F	R		R							C	C	
1H-1, 12–12	0.12			B																									
1H-1, 13–13	0.13			B																									
1H-1, 26–26	0.26			B																									
1H-1, 50–50	0.50			B																									
1H-1, 74–74	0.74			B																									
1H-CC, 34–40	6.04			B																									
2H-CC, 25–30	10.99			B																									
3H-1, 11–16	11.11	NN20	P	F					F		R			F		C	R								R	R	A	C	
3H-1, 35–40	11.35	NN20	P	F					F		R			F		C									R		C		
3H-1, 77–82	11.77	NN20	P	F					F		R			C		C									R		C	C	
3H-CC, 12–17	12.06	NN20	P	C	R				R		C					R	R		R					R	R	F	A	C	
4H-1, 102–107	13.02	NN20	P	R							C					C								R			R	R	
4H-2, 5–5	13.55			B																									

Table T4 (continued).

Core, section, interval (cm)	Depth (mbsf)	Zone	Preservation	Group abundance	*Calcidiscus leptoporus*	*Ceratolithus cristatus*	*Coccolithus pelagicus*	*Cyclicargolithus floridanus*	*Emiliania huxleyi/Reticulofenestra* sp.?	*Emiliania huxleyi*	*Gephyrocapsa caribbeanica*	*Gephyrocapsa lumina*	*Gephyrocapsa margarelii*	*Gephyrocapsa oceanica*	*Gephyrocapsa* spp.	*Gephyrocapsa* spp. (small)	*Helicosphaera carteri*	*Neosphaera coccolithomorpha*	*Oolithotus fragilis*	*Pontosphaera* spp.	*Reticulofenestra minutula*	*Reticulofenestra pseudoumbilicus*	*Reticulofenestra* sp.	*Rhabdosphaera clavigera*	*Syracosphaera pulchra*	*Syracosphaera* spp.	*Umbellosphaera* spp.	*Umbilicosphaera sibogae*	Comments
4H-2, 18–18	13.68			B																									
4H-2, 30–30	13.80			B																									
4H-2, 46–46	13.96			B																									
4H-CC, 31–36	17.50			B																									
5H-CC, 35–40	21.07			B																									
6H-CC, 35–40	25.88			B																									
7H-CC, 40–43	32.72			B																									
8X-CC, 29–33	33.39			B																									
9X-CC, 24–28	41.14			B																									
10H-CC, 28–33	56.40			B																									
195-1200F-																													
1H-1, 0–5	0.05	NN21	G	F	R					D				C			R		R						F	C	C		
1H-1, 8.5–8.5	0.09	NN21	G	F	R					D				C			R		R	R					F	C	C		
1H-1, 14–19	0.14		M	F	R									C		R	R									C	C		<0.49 Ma
1H-1, 20–20	0.20		M	F										C		R	R									C	C		<0.49 Ma
1H-1, 24–24	0.24			B																									
1H-1, 27–27	0.27			B																									
1H-1, 66–66	0.66		P	T																								R	<0.49 Ma
1H-1, 121–126	1.21		P	T	R																				F	C	C		<0.49 Ma
1H-2, 51–51	2.01			B																									
1H-3, 10–10	3.10			B																									
1H-CC, 46–51	7.66			B																									
2H-CC, 26–31	12.82			B																									
3H-CC, 47–52	16.08			B																									

Notes: Preservation: G = good, M = moderate, P = poor. Abundance: D = dominant, A = abundant, C = common, F = few, R = rare, T = trace, B = barren. Category definitions for abundance and preservation are as defined in **"Biostratigraphy,"** p. 14, in the "Explanatory Notes" chapter.

Table T5. Distribution of planktonic foraminifers, Holes 1200D, 1200E, and 1200F.

Core, section, interval (cm)	Depth (mbsf)	Zone	Preservation	Group abundance	*Beella digitata*	*Candeina nitida*	*Globigerinella aequilateralis*	*Globigerinella calida*	*Globigerinita glutinata*	*Globigerinoides conglobatus*	*Globigerinoides immaturus*	*Globigerinoides quadrilobatus*	*Globigerinoides ruber*	*Globigerinoides sacculifer*	*Globorotalia inflata*	*Globorotalia menardii*	*Globorotalia scitula*	*Globorotalia truncatulinoides*	*Globorotalia tumida*	*Neogloboquadrina dutertrei*	*Orbulina universa*	*Pulleniatina obliquiloculata*	*Sphaeroidinella dehiscens*	*Zeaglobigerina rubescens*	Benthic foraminifers	Comments	Remarks
195-1200D-																											
1H-1, 1–5	0.05	N22	VG	C	R	R	F	R		C	C	C	C	C	R	C	R	R	R	R	F	R	R	R	F	Benthic foraminifers are few but diversified	Excellent preservation
1H-1, 27–29	0.27	N22	G	F		R	R	R		C	C	C	A	A		F	R	R		F	C	R		R			Warm
1H-CC, 45–50	6.85			B																							
2H-CC, 30–35	9.88			B																							
3H-CC, 21–26	12.33			B																							
195-1200E-																											
1H-1, 0–5	0.05	N22	G	F			F			C	C	C	C	C		C			F	F	F		R		F		
2H-CC, 25–30	10.99			B																							
3H-1, 11.5–16.5	11.12	N22	VG	C		F	F		R	C	C	C	C	C		C		F	R	F	C		R	F	F	*C. nitida* unusually abundant; *G. truncatulinoides* D/S = 6/1	Good preservation, cooler
3H-1, 34.5–37.5	11.35	N22	G	F		F	F			F	F	R	A	F		F		R	R	R	C	R	R	R	R	*Orbulina* abundant; *G. truncatulinoides* D/S = 2/0	Cool
3H-1, 77–82	11.77	N22	M	F			R	F	R	C	C	C	C	C		C	R	F	F		F			F	F	*G. truncatulinoides* D/S = 6/0; *Z. rubescens* are abundant	Cooler
3H-CC, 12–17	12.06	N22	M	F			R			C	C	C	C	C		C	R	R	C	R	F	R			F	*G. truncatulinoides* D/S = 4/0; No *Z. rubescens* or *S. dehiscens*	Poor preservation, cool
195-1200F-																											
1H-1, 0–10	0.05	N22	G	C			R			C	C	C	C	C		C	R		R	R	F	R	C	R	R		
1H-1, 14–19	0.14	N22	G	C		F	R			C	C	C	C	C		F	R	R	R	F	C	R	F	R	R		Warm
1H-1, 121–126	1.21	N22	M	F		R	F	R		C	C	C	F	F		R		R		F	A	F	R	R		*G. truncatulinoides* D/S = 1/0	Warm
1H-CC, 46–51	7.66			B																						Only one specimen was found	

Notes: Preservation: VG = very good, G = good, M = moderate. Abundance: A = abundant, C = common, F = few, R = rare, B = barren. D = dextral, S = sinistral. Categories for abundance and preservation are defined in **"Biostratigraphy,"** p. 14, in the "Explanatory Notes" chapter.

Table T6. Rock magnetic and paleomagnetic results, Site 1200.

Core, section, interval (cm)	Depth (mbsf)	*k* (SI)	NRM (A/m)	Q ratio	MDF (mT)	Dec (°)	Inc (°)	MAD
195-1200A-								
3R-1, 15–17	18.35	1.404E–02	1.535	3.43	6.8	–1	–3	2.4
3R-1, 17–19	18.37	1.521E–02	0.749	1.55	12.9			
3R-1, 52–54	18.72	1.273E–02	2.656	6.56	4.1	257	31	1.2
3R-1, 54–56	18.74	1.631E–02	0.646	1.24	11.0			
6R-1, 102–104	42.42	2.746E–03	0.144	1.64	6.1	146	–8	4.4
6R-1, 104–106	42.44	2.411E–03	0.069	0.89	3.7	305	–52	10.0
6R-2, 30–32	42.96	3.365E–03	0.092	0.86	6.3	164	–40	5.0
6R-2, 32–34	42.98	3.803E–03	0.214	1.76	3.8	155	–27	5.3
6R-2, 52–54	43.18	1.649E–03	0.135	2.57	6.8	233	–49	5.9
6R-2, 54–56	43.20	2.888E–03	0.084	0.91	4.4			
7R-1, 25–27	51.35	1.985E–03	0.099	1.56	6.2	223	–52	2.5
7R-1, 30–32	51.40	2.595E–03	0.309	3.74	4.6	208	–22	8.7
7R-2, 112–114	52.81	1.915E–03	0.103	1.69	6.6	218	–60	6.3
7R-2, 114–116	52.83	2.264E–03	0.030	0.42	14.0			
9R-1, 23–25	70.63	1.412E–02	2.586	5.76	3.9	122	58	3.4
10R-1, 33–35	80.23	3.054E–03	0.214	2.20	5.0			
10R-1, 35–37	80.25	6.336E–03	0.170	0.85	4.6	294	–26	6.0
11R-1, 38–40	89.78	8.854E–03	1.002	3.55	5.7	32	–62	3.8
11R-1, 40–42	89.80	7.628E–03	0.366	1.51	3.7			
11R-1, 56–58	89.96	3.169E–03	0.810	8.03	4.5			
11R-1, 68–70	90.08	4.325E–03	0.317	2.30	5.9	198	–38	10.0
12R-1, 20–22	99.20	3.252E–03	0.179	1.73	4.8			
12R-1, 26–28	99.26	3.115E–03	0.514	5.18	4.6	112	–40	8.2
13R-1, 46–48	109.16	8.463E–03	0.341	1.26	3.6			
13R-1, 51–53	109.21	6.991E–03	0.725	3.26	4.7	–64	42	4.7
14R-1, 29–31	118.59	4.924E–03	0.327	2.09	4.5			
16R-1, 76–78	138.36	1.822E–03	0.034	0.59	6.3			
16R-1, 77–79	138.37	1.898E–03	0.099	1.64	5.2	281	43	4.0
16R-2, 22–24	139.17	2.489E–03	0.084	1.06	3.7			
16R-2, 24–26	139.19	3.009E–03	0.111	1.16	8.1			
195-1200D-								
1H-2, 79–81	2.29	5.343E–03	0.945	5.56	3.7			
1H-3, 44–46	3.44	5.986E–03	0.950	4.98	2.8			
2H-1, 52–54	7.42	8.057E–03	0.581	2.26	3.0			
3H-1, 59–61	10.49	1.177E–02	0.739	1.97	2.6			
8H-1, 66–68	25.66	7.100E–03	0.406	1.80	2.6			
9H-1, 44–46	28.44	7.071E–03	0.267	1.19	2.6			
195-1200E-								
1H-2, 37–39	1.87	2.371E–03	0.146	1.94	2.5			
2H-2, 25–27	7.85	6.329E–03	0.176	0.87	2.8			
4H-1, 59–61	12.59	6.357E–03	0.256	1.27	2.7			
7H-1, 64–66	26.54	4.657E–03	0.205	1.39	3.0			
10H-1, 37–39	52.77	9.814E–03	0.176	0.56	2.8			

Notes: *k* = volume magnetic susceptibility; NRM = natural remanent magnetization. Q ratio = J/kH, where J = the NRM intensity, k = the volume susceptibility, and H = the ambient geomagnetic field. MDF = median destructive field. Dec and Inc = stable magnetic declination and inclination. MAD = maximum angular deviation.

Table T7. Interstitial water composition, Site 1200. (**See table notes.** Continued on next two pages.)

Core, section, interval (cm) Method:	IW#	Depth (mbsf)	Volume (mL)	Temperature In situ* (°C)	Temperature Squeeze (°C)	pH ISE	Alkalinity (meq/kg) ET	Chloride (mmol/kg) Used†	Chlorinity (mmol/kg) ET	Chloride (mmol/kg) IC	Sulfate (mmol/kg) IC	Na (mmol/kg) Calc.‡	K (mmol/kg) IC
Surface seawater													
Calc 3/18/01:								540.3	540.3				
Calc 3/23/01:						8.28	2.1	540.2	540.2		27.94	462.4	10.10
195-1200A-													
9R-1, 48–55		70.92	26	2.4	~20	12.47	61.7	512.6	512.6	523.1	28.33	611.2	18.95
15R-1, 38–53		128.33	46	3.0	~20	11.00	5.3	522.5	522.5	531.3	24.49	545.2	15.61
Fraction of SSW admixture required													
195-1200C-													
WSTP-1 prime		30	93	2.7		8.24	2.5	540.2	540.2	539.9	26.83	460.1	10.24
WSTP-1 overflow		30	980	2.7		8.14	2.4	489.2	489.2	481.6	24.91	419.6	9.13
195-1200D-													
1H-1, 40–50	1	0.45	53	1.7	2.7	8.37	2.3	540.2	540.2	543.0	24.38	469.6	10.56
1H-1, 90–100	2	0.95	56	1.7	2.7	8.93	2.6	533.9	535.4	533.9	21.38	484.9	10.93
1H-1, 130–140	3	1.35	51	1.7	1.2	9.53	6.1	530.5	530.5	530.9	17.02	494.0	11.19
1H-2, 60–70	4	2.15	51	1.7	1.8	9.88	19.6	514.7	524.7	514.7	9.21	515.5	11.83
1H-2, 130–140	5	2.85	53	1.7	2.3	10.23	27.7	515.1	522.8	515.1	7.37	540.3	12.30
1H-3, 130–140	6	4.35	46	1.7	2.7	11.66	25.4	522.3	522.3	526.0	12.51	558.9	13.54
1H-4, 130–140	7	5.85	47	1.7	2.4	11.87	23.2	527.3	528.3	527.3	14.09	563.8	14.42
1H-5, 20–30	8	6.25	39	1.7	2.7	11.88	22.8	525.7	529.6	525.7	16.37	566.8	14.37
2H-1, 130–140	9	8.25	41	1.7	3.2	12.02	25.3	526.7	526.7	527.0	17.98	572.0	15.23
2H-2, 98–108	10	9.43	39	1.8	1.2	12.01	23.8	529.6	529.6	533.2	21.46	580.2	15.29
3H-1, 130–140	11	11.25	45	1.8	1.3	12.10	31.0	531.0	531.0	535.5	25.11	594.3	16.22
3H-2, 52–62	12	11.97	41	1.8	2.5	12.30	30.2	531.5	531.5	536.4	26.51	596.4	16.16
5H-1, 30–40	13**	14.05	33	1.8	2.3	10.68	2.7	522.8	522.8	527.8	21.70	533.5	13.75
6H-1, 115–126	14	22.71	29	1.9	2.7	12.35	54.9	526.7	526.7	531.9	24.68	612.6	17.88
7H-1, 120–130	15	24.75	37	1.9	2.5	12.35	52.0	525.2	525.4	525.2	26.10	611.2	17.84
8H-2, 97–107	16	27.52	43	1.9	2.0	12.42	60.8	521.8	521.8	529.3	25.14	614.3	18.14
9H-1, 100–110	17	29.05	43	1.9	3.2	12.37	55.6	520.1	520.1	523.9	24.05	605.5	18.03
195-1200E-													
1H-1, 40–50	1	0.45	66	1.7	2.3	8.49	2.6	533.5	533.5	544.1	26.84	457.9	10.55
1H-1, 90–100	2	0.95	66	1.7	0.0	10.30	42.4	516.5	540.3	516.5	4.12	543.9	14.44
1H-1, 130–140	3	1.35	63	1.7	1.7	12.02	94.2	517.5	550.9	517.5	1.57	597.4	17.17
1H-2, 60–70	4	2.15	41	1.7	2.2	12.22	113.6	521.2	554.8	521.2	0.15	616.7	18.43
1H-2, 130–140	5	2.85	53	1.7	2.5	12.26	123.9	512.9	555.4	512.9	1.62	621.1	18.81
1H-3, 130–140	6	4.35	66	1.7	2.5	12.37	119.3	516.8	527.7	516.8	2.06	620.6	19.63
1H-4, 101–111	7	5.56	55	1.7	2.5	12.35	121.0	519.4	550.9	519.4	0.42	622.3	18.78
2H-1, 130–140	8	7.45	61	1.7	2.5	12.34	125.8	510.8	538.3	510.8	0.02	616.9	19.57
2H-2, 130–140	9	8.95	68	1.8	1.2	12.35	127.2	513.3	532.5	513.3	1.09	623.3	19.16
2H-3, 130–140	10	10.45	47	1.8	0.7	12.29	130.3	516.3	547.0	516.3	0.22	627.5	19.31
4H-1, 130–140	11	13.35	52	1.8	0.7	12.21	126.6	511.5	552.5	511.5	0.64	620.4	18.97
4H-2, 130–140	12	14.85	53	1.8	-0.3	12.28	126.1	514.6	551.7	514.6	0.72	623.0	19.14
4H-3, 130–140	13	16.35	52	1.8	0.0	12.27	126.9	518.8	549.9	518.8	0.87	628.3	19.06
5H-2, 86–96	14	19.96	33	1.9	0.1	12.33	106.8	526.3	526.7	526.3	1.74	617.6	19.06
6H-1, 124–134	15	22.49	39	1.9	2.5	12.37	103.7	523.0	525.8	523.0	3.75	615.6	18.60
6H-3, 119–129	16	25.38	45	1.9	2.0	12.44	79.8	526.0	526.4	526.0	16.99	620.5	19.27
7H-2, 130–140	17	28.75	41	1.9	3.0	12.44	66.1	522.8	526.4	522.8	22.36	614.4	18.91
7H-4, 130–140	18	31.75	38	2.0	1.2	12.47	68.6	515.4	521.6	515.4	21.31	607.0	19.16
10H-1, 130–140	19	53.75	29	2.2	–0.1	12.37	53.5	503.2	507.5	503.2	26.80	592.6	17.06
10H-2, 130–140	20	55.25	25	2.2	2.2	12.44	70.1	516.5	516.7	516.5	23.05	613.2	19.12
195-1200F-													
1H-1, 0–10	1	0.05	67	1.8	2.2	8.18	2.0	539.0	539.0	543.3	27.58	471.6	12.53
1H-1, 40–50	2	0.45	57	1.8	2.9	10.87	48.4	513.5	537.0	513.5	3.36	551.7	15.28
1H-1, 90–105	3	0.98	62	1.9	2.6	11.89	77.8	515.8	543.8	515.8	0.47	578.0	16.19
1H-1, 140–150	4	1.45	42	1.9	1.3	12.02	80.0	522.1	537.0	522.1	2.29	590.0	16.51
1H-2, 60–70	5	2.15	69	1.9	2.2	12.20	99.5	521.3	539.0	521.3	4.06	611.4	17.48
1H-2, 140–150	6	2.95	65	2.0	2.1	12.32	88.8	519.4	521.6	519.4	8.19	606.9	17.67
1H-3, 140–150	7	4.45	70	2.1	1.0	12.35	68.4	510.9	519.6	510.9	13.18	587.0	18.58
1H-4, 140–150	8	5.95	67	2.2	1.8	12.44	93.3	514.3	520.6	514.3	14.55	618.1	18.64
1H-5, 110–120	9	7.15	38	2.3	3.0	12.49	93.8	511.0	520.6	511.0	13.06	611.7	19.22
2H-1, 140–150	10	9.15	60	2.4	2.0	12.36	91.1	510.9	526.1	510.9	7.18	596.6	19.73
2H-2, 140–150	11	10.65	50	2.6	1.2	12.38	110.5	512.6	537.5	512.6	6.65	616.8	19.40
2H-3, 90–100	12	11.65	42	2.6	0.5	12.42	111.6	511.0	536.0	511.0	9.22	621.9	19.05
2H-4, 76–86	13	12.51	48	2.7	2.7	12.37	105.6	510.0	525.3	510.0	7.67	611.5	19.40
3H-1, 140–150	14	14.35	38	2.8	2.8	12.30	92.9	510.0	525.8	510.0	3.27	589.5	19.73
3H-2, 111–121	15	15.56	43	2.9	2.2	12.49	102.9	513.0	521.0	513.0	8.75	613.4	19.83

Table T7 (continued).

Core, section, interval (cm)	Mg (mmol/kg)	Ca (mmol/kg)	Na/Cl (mol/mol)	NH_3 (µmol/kg)	F (µmol/kg)	Sr (µmol/kg)	Ba (mmol/kg)	Mn (µmol/kg)	Fe (µmol/kg)	Al (µmol/kg)	Si (µmol/kg)	B (µmol/kg)	Li (µmol/kg)
Method:	CT	ET	Calculated	Color	ISE	ICP-AES	ICP-AES	ICP-AES	ICP-AES	ICP-AES	ICP-AES	ICP-AES	ICP-AES
Surface seawater 3/18/01 (calc.)													
Surface seawater 3/23/01 (calc.)	52.69	10.16	0.8560	35		90.8	0.1	0.02	0.10	<1	7.9	455	26.0
195-1200A-													
9R-1, 48–55	0.00	0.38	1.1924	216	47.4	11.5	0.5	0.01	1.95	6.6	68.8	3228	0.5
15R-1, 38–53	0.04	7.91	1.0435	150	15.9	96.7	1.4	0.00	0.26	<1	17.0	1223	5.8
Fraction of SSW admixture required													
195-1200C-													
WSTP-1 prime	52.8	10.2	0.8517	39	73.0	88.0	0.2	1.46	1.31	<1	156.7	503	22.6
WSTP-1 overflow	47.39	8.96	0.8576			83.3	0.3	5.17	0.07	<1	119.3	407	22.9
195-1200D-													
1H-1, 40–50	48.27	7.31	0.8692	33	50.9	64.6	0.6	0.45	0.21	<1	193.2	828	24.0
1H-1, 90–100	39.94	1.74	0.9083	39	35.7	14.7	2.0	0.95	0.31	<1	11.7	968	22.6
1H-1, 130–140	32.48	0.25	0.9312	49	23.6	2.6	2.3	0.30	0.80	<1	11.0	914	18.8
1H-2, 60–70	12.41	0.25	1.0017	66	5.4	1.6	1.3	0.12	1.36	<1	17.7	1367	17.1
1H-2, 130–140	2.41	0.06	1.0489	82	2.3	2.8	2.0	0.04	1.36	<1	17.5	1746	14.7
1H-3, 130–140	0.00	0.12	1.0702	106	5.3	2.6	0.4	0.03	1.87	<1	31.9	3031	3.2
1H-4, 130–140	0.00	0.18	1.0693	124	11.0	3.3	1.6	0.08	1.86	0.2	41.2	3082	0.6
1H-5, 20–30	0.00	0.03	1.0782	114	10.9	3.8	0.6	0.02	2.13	3.2	41.2	3346	1.1
2H-1, 130–140	0.00	0.34	1.0861	139	15.0	6.0	1.6	0.00	2.00	2.7	41.4	3177	1.3
2H-2, 98–108	0.00	0.44	1.0955	153	15.4	9.0	2.2	0.02	1.66	0.2	36.6	3519	0.5
3H-1, 130–140	0.00	0.85	1.1193	167	18.1	15.4	0.4	0.02	1.28	<1	27.4	3225	1.3
3H-2, 52–62	0.00	1.07	1.1221	185	16.4	16.7	0.9	0.03	1.61	<1	33.9	3649	1.9
5H-1, 30–40	1.24	9.56	1.0205	106	6.2	83.3	1.8	0.04	1.96	<1	16.4	1015	11.9
6H-1, 115–126	0.00	0.22	1.1631	214	28.4	5.6	0.8	0.02	2.67	9.5	64.8	3054	0.3
7H-1, 120–130	0.00	0.15	1.1638	202	34.7	9.3	0.5	0.04	2.76	6.0	53.9	3009	0.2
8H-2, 97–107	0.00	0.22	1.1772	201	41.2	5.0	1.4	0.02	2.83	15.2	77.9	3149	0.2
9H-1, 100–110	0.00	0.12	1.1642	175	44.0	6.5	0.7	0.07	6.91	10.4	84.6	2997	0.2
195-1200E-													
1H-1, 40–50	51.49	9.19	0.8582	115	60.1	95.9	0.5	1.33	4.86	<1	258.4	687	23.0
1H-1, 90–100	4.36	0.00	1.0532	0	7.1	1.2	0.6	0.42	7.79	<1	21.5	1478	16.5
1H-1, 130–140	0.00	0.15	1.1543	77	59.3	2.9	0.8	0.03	4.79	<1	44.2	3036	2.7
1H-2, 60–70	0.00	0.00	1.1832	329	74.0	3.8	1.7	0.03	6.43	<1	71.2	3226	2.5
1H-2, 130–140	0.00	0.06	1.2110	297	80.0	4.1	6.2	0.01	4.91	3.7	89.8	3511	2.2
1H-3, 130–140	0.00	0.00	1.2009	257	82.7	2.9	2.1	0.02	3.75	1.6	105.6	3301	0.7
1H-4, 101–111	0.00	0.12	1.1980	225	73.4	3.4	0.7	0.00	4.62	1.9	66.0	3342	1.8
2H-1, 130–140	0.00	0.06	1.2078	242	82.0	2.5	3.3	0.01	5.29	2.4	93.8	3365	1.4
2H-2, 130–140	0.00	0.09	1.2143	333	82.7	1.8	1.0	0.01	6.48	<1	62.1	3332	0.7
2H-3, 130–140	0.00	0.12	1.2153	293	80.7	3.5	2.1	0.01	5.40	6.1	86.4	3443	1.3
4H-1, 130–140	0.00	0.00	1.2129	332	109.7	3.6	0.6	0.03	2.26	0.2	68.5	3398	1.3
4H-2, 130–140	0.00	0.00	1.2107	254	105.7	3.4	1.0	0.01	2.95	<1	52.9	3372	1.6
4H-3, 130–140	0.00	0.00	1.2111	292	87.6	3.0	2.4	0.01	3.14	<1	82.6	3419	1.2
5H-2, 86–96	0.00	0.00	1.1734	229	56.0	2.8	3.3	0.02	1.69	<1	67.6	3466	0.9
6H-1, 124–134	0.00	0.03	1.1770	218	54.4	2.5	0.4	0.00	2.06	<1	61.7	3495	1.1
6H-3, 119–129	0.00	0.00	1.1797	167	57.6	2.8	0.7	0.00	3.19	<1	67.5	3665	0.6
7H-2, 130–140	0.00	0.15	1.1752	141	56.2	5.1	0.8	0.04	5.19	0.1	99.5	3392	0.4
7H-4, 130–140	0.00	0.22	1.1777	154	48.7	5.1	1.9	0.05	3.35	1.7	122.6	3438	0.5
10H-1, 130–140	0.00	0.34	1.1775	206	43.3	11.0	1.0	0.00	1.88	20.3	149.2	2918	0.3
10H-2, 130–140	0.00	0.22	1.1871	164	46.0	5.6	2.4	0.01	2.71	47.6	91.3	3094	0.3
195-1200F-													
1H-1, 0–10	48.13	7.91	0.8749	196	49.6	78.0	1.5	1.45	1.27	<1	160.6	588	23.8
1H-1, 40–50	0.78	0.00	1.0745	204	7.8	2.4	1.5	0.01	1.69	<1	19.7	1418	11.0
1H-1, 90–105	0.20	0.00	1.1205	79	53.4	4.2	1.2	0.02	1.47	<1	37.3	2515	2.9
1H-1, 140–150	0.00	0.12	1.1300	144	56.1	5.4	7.0	0.01	0.97	<1	53.1	2589	1.8
1H-2, 60–70	0.00	0.00	1.1728	150	70.2	2.5	1.8	0.01	1.10	0.6	53.0	3109	0.9
1H-2, 140–150	0.00	0.00	1.1684	141	77.0	1.8	0.2	0.01	1.02	1.5	52.0	3111	0.5
1H-3, 140–150	0.00	0.00	1.1491	122	74.4	1.8	1.1	0.02	1.81	2.8	60.1	2691	0.2
1H-4, 140–150	0.00	0.00	1.2017	140	80.3	3.6	0.4	0.03	3.15	2.3	56.7	3318	0.7
1H-5, 110–120	0.00	0.00	1.1970	168	81.7	2.9	0.7	0.02	4.93	2.3	110.7	3235	0.2
2H-1, 140–150	0.00	0.00	1.1677	97	65.9	3.8	2.1	0.02	1.69	2.0	93.0	3078	0.7
2H-2, 140–150	0.00	0.09	1.2034	142	73.2	4.5	0.6	0.00	2.47	0.8	82.2	3261	0.8
2H-3, 90–100	0.00	0.00	1.2171	156	72.3	4.3	0.6	0.02	3.83	1.5	98.0	3266	1.2
2H-4, 76–86	0.00	0.00	1.1990	152	78.0	2.5	1.3	0.02	2.42	2.5	204.0	3242	0.2
3H-1, 140–150	0.00	0.09	1.1558	108	59.8	4.5	2.2	0.01	2.89	0.5	58.8	2996	1.3
3H-2, 111–121	0.00	0.12	1.1956	134	76.0	3.2	0.5	0.03	3.81	0.6	84.9	3382	0.3

Table T7 (continued).

Notes: * = calculated from bottom-water temperatures of 1.67° to 1.78°C and the temperature gradients in Table T18, p. 170. Methods: ISE = ion-specific electrode, ET = electrochemical titration, IC = ion chromatography, Calc. = calculated, CT = colorimetric titration, Color = colorimetric spectrophotometry, ICP-AES = inductively coupled plasma–atomic emission spectroscopy. WSTP = water sampling temperature probe. † = because HS^- in the samples was titrated by $AgNO_3$ along with chlorinity, all values used are chloride as measured by IC, except for the WSTP sample and for those 15 samples (mainly from Hole 1200D) for which the chlorinity by titration was smaller. ‡ = calculated from charge balance; these values average 2% higher than Na by IC, because chloride by IC is 1% too high and Na by IC is 1% too low. See "Chloride, Sulfide, Sodium, Alkalinity, and Sulfate: An Analytical Note," p. 30, in "Interstital Waters" in "Geochemistry." ** = Section 195-1200D-5H-1 was disturbed and obviously contaminated with seawater, probably during recovery. Changes observed relative to seawater should be considered minima.

Table T8. Composition of pore water from three serpentine seamounts vs. seawater.

Seamount:	Conical*	South Chamorro*	Torishima Forearc†	Seawater‡
ODP Site:	780	1200	783, 784	
Analyte (mmol/kg):				
Chloride	270 ± 20	510 ± 5	550 ± 5	542
Sulfate	46 ± 1	28 ± 1	9 ± 3	28.0
Alkalinity	50 ± 10	60 ± 5	1 ± 0.4	2.3
pH	12.5 ± 0.1	12.5 ± 0.1	9.6 ± 0.4	8.1
Na	390 ± 10	610 ± 10	470 ± 20	466
Na/Cl (molar)	1.4 ± 0.1	1.2 ± 0.02	0.86 ± 0.04	0.859
K	15 ± 0.5	19 ± 1	5 ± 1	10.1
Mg	0.01 ± 0.007	<0.01	1 ± 1	52.4
Ca	1 ± 0.5	0.3 ± 0.1	55 ± 5	10.2
CH_4	2 ± 1	2 ± 1		0
Analyte (µmol/kg):				
CH_4			2 ± 1	0
Sr	20 ± 10	10 ± 2	200 ± 50	90
Ba	0.2 ± 0.1	0.4?	1.6 ± 0.7	0.14
Li	1 ± 0.5	0.4 ± 0.1	16 ± 5	26
B	3900 ± 100	3200 ± 200	180 ± 80	410
Si	30 ± 20	70 ± 20	10 ± 8	190
Mn	<0.1	0.01	0.4 ± 0.2	0
Fe	2 ± 1	2 ± 0.5	1 ± 0.9	0
Phosphate	0.3 ± 0.3	0.2?	Not determined	2.8
NH_3	250 ± 20	220 ± 10	140 ± 20	0
HS^-	<250	<250	0	0
C_2H_6	7	2	0	0
C_1/C_2	270	780		

Notes: * = deep upwelling fluid from an active mud volcano (Conical Seamount data from Mottl, 1992; South Chamorro Seamount data from this study). † = product of harzburgite-seawater reaction within an inactive mud volcano (Mottl, 1992). ‡ = estimated composition of local bottom water. ? = error not known.

Table T9. Composition of gas pockets in cores sampled through the core liner, Site 1200.

Core, section, interval (cm)	Depth (mbsf)	GC*	C_1/C_2	Methane (ppmv)	Ethane (ppmv)	Propane (ppmv)	*n*-C_4 (ppmv)	*i*-C_4 (ppmv)	*n*-C_5 (ppmv)	*i*-C_5 (ppmv)	*n*-C_6 (ppmv)	*i*-C_6 (ppmv)
195-1200D-												
6H-1, 50–51	22.00	NGA	464	919,175	1,982	24.3	4.2	1.2	1.2	0.9	0.3	0.2
6H-2, 10–11	22.97	NGA	467	918,456	1,968	24.8	4.3	1.3	1.2	1.0	0.3	0.2
8H-1, 42–43	25.42	NGA	477	944,420	1,979	24.7	4.4	1.3	1.3	1.0	0.3	0.2
195-1200E-												
5H-1, 50–51	18.10	NGA	494	938,905	1,900	22.9	3.5	1.2	0.8	0.7	0.1	0.1
7H-1, 50–51	26.40	NGA	496	955,558	1,927	28.6	5.0	6.2	1.5	1.2	0.4	0.3
10H-1, 50–51	52.90	GC3	770	761,606	990	21.4						
10H-1, 50–51	52.90	NGA	542	776,479	1,432	20.5	3.5	5.2	1.0	0.7	0.2	0.2
195-1200F-												
1H-5, 50–51	6.50	NGA	399	952,983	2,391	42.5	7.4	2.3	2.3	1.8	0.6	0.4
1H-5, 50–51	6.50	GC3	560	937,680	1,675	44.3						
2H-1, 50–51	8.20	NGA	301	904,245	3,005	58.2	9.5	3.1	2.8	2.2	0.7	0.5

Note: GC = gas chromatograph. * = the GC3 is more accurate for C_1/C_2 than the natural gas analyzer (NGA) but does not measure C_4 through C_6.

Table T10. Composition of headspace gas from sediment, Site 1200.

Core, section, interval (cm)	Depth (mbsf)	C_1/C_2*	Methane (µL/L)†	Ethane (µL/L)†	Propane (µL/L)†	Methane (mM)‡	Ethane (µM)‡	Propane (µM)‡
195-1200D-								
1H-2, 0–5	1.5	2.9	78	26.6	0	0.01	2.4	0
1H-3, 0–5	3.0	124	15,294	123.4	0	1.36	11.0	0
1H-5, 0–5	6.0	386	28,982	75.1	0	2.59	6.7	0
2H-2, 0–5	8.4	460	33,232	72.3	0	2.97	6.4	0
3H-2, 0–5	11.4	582	12,189	21.0	0	1.09	1.9	0
4H-CC, 0–5	12.6	651	23,789	36.6	0	2.12	3.3	0
5H-1, 15–20	13.9	620	15,955	25.7	0	1.42	2.3	0
6H-2, 0–5	22.9	686	14,510	21.2	0	1.29	1.9	0
7H-1, 105–110	24.6	633	10,450	16.5	0	0.93	1.5	0
8H-2, 92–97	27.4	642	15,391	24.0	0	1.37	2.1	0
9H-1, 85–95	28.9	695	21,294	30.6	0	1.90	2.7	0
195-1200E-								
1H-2, 0–5	1.5	246	10,980	44.7	0	0.98	4.0	0
1H-3, 0–5	3.0	290	53,992	185.9	0	4.82	16.6	0
1H-4, 0–5	4.5	266	27,070	101.9	0	2.42	9.1	0
2H-2, 0–5	7.6	194	12,086	62.2	0	1.08	5.5	0
2H-3, 0–5	9.1	249	45,990	184.7	0	4.10	16.5	0
3H-1, 89–94	11.9	298	53,497	179.5	0	4.77	16.0	0
4H-2, 0–5	13.5	249	23,482	94.3	0	2.10	8.4	0
5H-3, 0–5	20.1	401	25,483	63.6	0	2.27	5.7	0
6H-2, 0–5	22.6	373	13,962	37.5	0	1.25	3.3	0
7H-3, 0–5	28.9	730	23,182	31.7	0	2.07	2.8	0
10H-2, 0–5	53.9	782	20,557	26.3	0	1.83	2.3	0
195-1200F-								
1H-2, 0–5	1.5	368	103,079	280.1	0	9.20	25.0	0
1H-4, 0–5	4.5	475	30,802	64.8	0	2.75	5.8	0
2H-2, 0–5	9.2	381	19,094	50.1	0	1.70	4.5	0
2H-4, 0–5	11.7	387	25,855	66.8	0	2.31	6.0	0
3H-2, 0–5	14.4	277	199,400	719.2	18.9	17.79	64.2	1.69
3H-2, 110–111	15.5	339	42,398	125.1	0	3.78	11.2	0

Notes: * = measured with GC3. † = microliters of gas per liter of wet unconsolidated serpentinite, assuming a wet bulk density of 1.8 g/cm^3. ‡ = millimoles or micromoles of dissolved gas per liter of pore water, assuming a porosity of 50%.

Table T11. Results of CHNS and coulometric analysis of serpentine mud, Site 1200.

Core, section, interval (cm)	Depth (mbsf)	H_2O^+ (wt%)	$CaCO_3$ (wt%)	C_{org} (wt%)	S (wt%)
195-1200D-					
1H-1, 10–11	0.10	11.79	7.39	0.50	0.200
1H-1, 22–23	0.22	1.26	17.57	0.00	1.380
1H-1, 50–51	0.50	9.00	29.66	0.00	1.940
1H-1, 75–76	0.75	9.54	15.08	0.46	2.350
1H-1, 100–101	1.00	11.16	12.83	0.00	1.710
1H-1, 119–120	1.19	11.79	21.43	0.21	0.490
1H-2, 44–45	1.94	14.58	3.51	0.00	0.940
1H-2, 70–71	2.20	14.22	1.23	0.02	0.740
1H-2, 117–118	2.67	13.50	1.63	0.20	0.320
1H-3, 40–41	3.40	14.76	0.48	0.00	0.280
1H-3, 75–76	3.75	13.95	1.58	0.00	0.300
1H-4, 3–4	4.53	13.59	0.70	0.00	0.270
1H-4, 33–34	4.83	14.04	0.40	0.00	0.210
1H-4, 62–63	5.12	14.58	0.62	0.00	0.170
1H-4, 107–108	5.57	14.13	0.39	0.00	0.080
1H-CC, 16–17	6.56	13.05	1.43	0.00	0.010
2H-1, 6–7	6.96	13.59	0.44	0.00	0.007
2H-2, 60–61	9.00	13.32	0.37	0.00	0.006
3H-1, 110–111	11.00	13.77	0.73	0.00	0.002
3H-CC, 10–11	12.22	13.68	0.72	0.00	0.020
6H-1, 9–10	21.59	13.14	0.77	0.00	0.020
6H-CC, 23–24	23.42	13.50	0.42	0.07	0.004
7H-1, 56–57	24.06	13.32	0.45	0.00	0.010
8H-1, 20–21	25.20	12.87	0.50	0.00	0.010
8H-2, 49–50	26.99	13.50	0.51	0.00	0.020
9H-1, 49–50	28.49	13.32	0.51	0.05	0.010
10H-1, 39–40	35.19	13.41	0.74	0.00	0.000
195-1200E-					
1H-1, 14–15	0.14	9.45	23.48	0.00	1.730
1H-1, 109–110	1.09	12.15	18.56	0.00	0.700
1H-3, 29–30	3.29	12.51	0.79	0.00	0.290
1H-4, 99–100	5.49	12.87	0.84	0.09	0.370
2H-2, 29–30	7.89	13.14	0.86	0.00	0.340
2H-3, 109–110	10.19	12.78	0.48	0.02	0.510
3H-1, 74–75	11.74	9.63	27.07	0.00	1.020
4H-1, 57–58	12.57	14.04	0.65	0.04	0.310
4H-3, 70–71	15.70	10.35	16.52	0.00	1.050
5H-1, 130–131	18.90	12.24	1.54	0.00	0.240
6H-1, 99–100	22.19	13.50	1.01	0.00	0.250
6H-3, 114–115	25.28	13.59	0.92	0.00	0.260
7H-2, 99–100	28.39	12.96	1.06	0.00	0.070
7H-5, 18–19	32.08	14.67	0.94	0.00	0.000
10H-1, 19–20	52.59	12.24	1.17	0.00	0.005
10H-3, 40–41	55.80	12.24	1.29	0.00	0.020
195-1200F-					
1H-1, 39–40	0.39	8.10	35.92	0.10	0.400
1H-3, 40–41	3.40	13.32	0.90	0.02	0.310
1H-5, 59–60	6.59	13.14	0.61	0.00	0.300
2H-2, 50–51	9.70	12.78	0.63	0.00	0.390
2H-4, 70–71	12.40	12.69	0.55	0.06	0.490
3H-2, 104–105	15.44	12.42	1.07	0.00	0.210

Note: CHNS = carbon/hydrogen/nitrogen/sulfur analyzer.

Table T12. Index properties of discrete samples, Hole 1200A.

Core, section interval (cm)	Depth (mbsf)	Density (g/cm³)		Porosity (%)	Water content (%)	Void ratio
		Bulk	Grain			
195-1200A-						
3R-1, 17–19	18.37	2.57	2.58	0.90	0.40	0.01
3R-1, 54–56	18.74	2.58	2.61	1.40	0.60	0.01
6R-1, 104–106	42.44	2.58	2.61	2.10	0.80	0.02
6R-2, 32–34	42.98	2.54	2.57	2.00	0.80	0.02
6R-2, 54–56	43.20	2.59	2.61	1.40	0.50	0.01
7R-1, 25–27	51.35	2.65	2.68	1.80	0.70	0.02
7R-2, 114–116	52.83	2.66	2.68	1.20	0.50	0.01
9R-1, 10–12	70.50	2.20	2.56	23.40	10.90	0.31
9R-1, 20–25	70.60	2.42	2.62	12.10	5.10	0.14
9R-1, 77–79	71.17	1.73	2.61	55.80	33.10	1.26
10R-1, 35–37	80.25	2.50	2.54	2.70	1.10	0.03
11R-1, 40–42	89.80	2.42	2.51	6.40	2.70	0.07
11R-1, 63–65	90.03	2.63	2.69	3.50	1.40	0.04
12R-1, 20–22	99.20	2.64	2.67	1.40	0.50	0.01
13R-1, 46–48	109.16	2.65	2.66	1.00	0.40	0.01
15R-1, 14–16	128.04	1.45	2.62	73.40	51.90	2.76
16R-1, 76–78	138.36	2.50	2.55	2.90	1.20	0.03
16R-2, 24–26	139.19	2.62	2.66	2.20	0.90	0.02
16R-2, 52–54	139.47	2.36	2.62	16.70	7.30	0.20

Note: Samples 195-1200A-9R-1, 77–79 cm, and 15R-1, 14–16 cm, were taken from the mud matrix.

Table T13. Physical properties, Hole 1200A.

Core, section, interval (cm)	Depth (mbsf)	Thermal conductivity (W/[m·K])	Velocity (km/s)			Maximum shear strength (kPa)
			x	y	z	
195-1200A-						
3R-1, 11–29	18.31	1.87				
3R-1, 16–16	18.36		5.19	5.25	5.24	
3R-1, 41–53	18.61	2.10				
3R-1, 53–53	18.73		5.26	5.44	5.34	
3R-1, 55–75	18.75	2.00				
3R-1, 76–95	18.96	1.97				
6R-1, 5–38	41.45	2.30				
6R-1, 85–109	42.25	2.32				
6R-1, 103–103	42.43		5.02	4.90	4.83	
6R-2, 1–20	42.67	2.20				
6R-2, 21–31	42.87	2.29				
6R-2, 31–31	42.97		4.93	4.99	4.88	
6R-2, 53–53	43.19		5.06	4.86	5.02	
6R-2, 53–62	43.19	2.34				
6R-2, 63–80	43.29	2.38				
7R-1, 5–33	51.15	2.30				
7R-1, 31–31	51.41		4.85	4.96	5.01	
7R-1, 33–59	51.43	1.99				
7R-2, 0–27	51.69	2.52				
7R-2, 30–40	51.99	2.52				
7R-2, 41–56	52.10	2.38				
7R-2, 57–69	52.26	2.31				
7R-2, 72–82	52.41	2.26				
7R-2, 83–98	52.52	2.51				
7R-2, 100–109	52.69	2.39				
7R-2, 110–121	52.79	2.49				
7R-2, 113–113	52.82		5.26	5.24	5.33	
7R-2, 127–148	52.96	2.05				
9R-1, 24–24	70.64		3.96	3.80	3.98	
9R-1, 32–44	70.72	2.85				
10R-1, 30–46	80.20	1.95				
10R-1, 34–34	80.24		4.72	4.88	4.87	
10R-1, 59–77	80.49	2.03				
10R-1, 86–98	80.76	2.23				
11R-1, 37–50	89.77	1.81				
11R-1, 39–39	89.79		4.13	4.13	4.13	
11R-1, 57–57	89.97		4.72	4.53	5.10	
11R-1, 61–71	90.01	2.17				
11R-1, 69–69	90.09		5.06	5.08	5.32	
12R-1, 17–29	99.17	2.63				
12R-1, 27–27	99.27		5.20	5.27	5.48	
13R-1, 28–56	108.98	2.07				
13R-1, 52–52	109.22		4.91	4.83	4.98	
13R-1, 58–70	109.28	2.55				
13R-1, 72–83	109.42	2.05				
13R-1, 101–110	109.71	1.99				
13R-2, 11–26	110.06	1.99				
14R-1, 30–30	118.60		4.75	4.84	4.91	
15R-1, 0–33	127.90	0.36				
15R-CC, 4–4	128.47					7.98
16R-1, 51–75	138.11	2.26				
16R-1, 78–78	138.38		4.51	4.70	4.62	
16R-1, 82–101	138.42	2.08				
16R-1, 103–121	138.63	2.39				
16R-1, 124–135	138.84	2.09				
16R-2, 0–29	138.95	2.30				
16R-2, 23–23	139.18		5.01	5.08	5.19	
16R-2, 30–38	139.25	2.05				
16R-2, 45–55	139.40	1.66				

Note: The thermal conductivity measurement for Sample 195-1200A-15R-1, 0–33 cm, was taken in the mud matrix.

Table T14. Index properties, volume magnetic susceptibility, and lithology of clast material, Holes 1200D, 1200E, and 1200F.

Core, section, interval (cm)	Depth (mbsf)	Density (g/cm^3)		Porosity (%)	Water content (%)	Void ratio	Volume magnetic susceptibility ($\times 10^{-5}$ SI)	Lithology
		Bulk	Grain					
195-1200D-								
1H-1, 68–71	0.68	2.61	2.81	11.23	4.41	0.13	1,782.76	Serpentinized harzburgite
1H-2, 100–102	2.50	2.75	2.76	0.74	0.28	0.01	10,369.00	Highly altered gabbro
1H-3, 6–8	3.06	2.33	2.50	12.06	5.31	0.14	40.12	Serpentinized harzburgite
1H-3, 90–92	3.90	2.60	2.63	2.01	0.79	0.02	13,738.30	Basalt
1H-4, 22–24	4.72	2.29	2.61	20.59	9.22	0.26	110.58	Serpentinized harzburgite
2H-1, 90–92	7.80	2.52	2.59	4.84	1.97	0.05	324.51	Serpentinized harzburgite
3H-1, 79–81	10.69	2.47	2.64	10.15	4.20	0.11	138.61	Serpentine-chlorite schist
3H-2, 28–30	11.68	2.32	2.57	16.10	7.10	0.19	531.77	Serpentine-chlorite schist
6H-1, 86–88	22.36	2.50	2.65	9.43	3.87	0.10	8,795.33	Serpentinized peridotite
6H-2, 13–15	23.00	2.40	2.62	13.68	5.84	0.16	2,117.35	Serpentinized peridotite
7H-1, 53–55	24.03	2.39	2.59	12.75	5.46	0.15	1,534.22	Serpentinized peridotite
8H-1, 96–98	25.96	2.38	2.51	8.51	3.66	0.09	1,445.61	Serpentine-chlorite schist
8H-2, 53–55	27.03	2.44	2.64	12.48	5.24	0.14	903.73	Serpentinized peridotite
9H-1, 17–19	28.17	2.57	2.65	5.31	2.12	0.06	300.69	Serpentinized lherzolite
10H-1, 18–20	34.98	2.61	2.71	5.95	2.34	0.06	4,984.24	Serpentinized peridotite
195-1200E-								
1H-1, 52–54	0.52	2.31	2.67	22.13	9.82	0.28	398.20	Serpentinized peridotite
1H-2, 99–101	2.49	2.47	2.56	6.23	2.59	0.07	105.31	Serpentine-chlorite schist
1H-3, 94–96	3.94	2.21	2.59	24.19	11.19	0.32	796.83	Serpentinized peridotite
1H-4, 70–72	5.20	2.23	2.60	23.65	10.86	0.31	409.09	Serpentinized harzburgite
2H-1, 80–82	6.90	2.41	2.63	13.42	5.70	0.16	1,079.11	Serpentinized peridotite
2H-2, 44–46	8.04	2.58	2.67	5.14	2.04	0.05	9,595.28	Serpentine-chlorite schist
2H-2, 90–92	8.50	2.30	2.51	14.43	6.43	0.17	34.62	Serpentinized peridotite
3H-1, 32–34	11.32	2.28	2.71	25.60	11.51	0.34	52.59	Serpentinized peridotite
4H-1, 31–33	12.31	2.32	2.55	14.99	6.61	0.18	138.54	Serpentinized harzburgite
4H-3, 115–117	16.15	2.25	2.67	25.66	11.69	0.35	1,073.04	Serpentinized peridotite
5H-1, 40–42	18.00	2.60	2.62	1.52	0.60	0.02	449.30	Serpentinized harzburgite
5H-2, 84–86	19.89	2.28	2.59	19.82	8.91	0.25	46.93	Serpentinized harzburgite
5H-3, 41–43	20.52	2.42	2.68	15.60	6.60	0.19	4,284.60	Serpentine-chlorite schist
6H-1, 10–12	21.30	2.35	2.64	17.93	7.82	0.22	82.45	Serpentinized mylonite
6H-2, 14–16	22.78	2.25	2.57	21.03	9.59	0.27	104.30	Serpentinized harzburgite
6H-3, 40–42	24.54	2.40	2.59	12.20	5.22	0.14	158.99	Serpentinized harzburgite
7H-1, 33–35	26.23	2.41	2.58	10.54	4.47	0.12	6,271.06	Serpentinized mylonite
7H-2, 127–129	28.67	2.61	2.68	4.40	1.73	0.05	2,173.11	Serpentinized harzburgite
7H-3, 108–110	29.98	2.84	2.96	5.89	2.12	0.06	505.21	Serpentinized harzburgite
7H-4, 65–67	31.05	2.43	2.58	9.47	3.99	0.11	320.73	Serpentinized harzburgite or lherzolite
8X-1, 22–24	32.72	2.29	2.63	21.15	9.46	0.27	503.08	Altered basalt?
10H-2, 26–28	54.16	2.60	2.72	6.79	2.67	0.07	5,291.17	Serpentinized harzburgite
10H-2, 64–66	54.54	2.27	2.61	21.57	9.75	0.28	371.44	Serpentinized harzburgite
195-1200F-								
1H-1, 81–83	0.81	2.33	2.50	11.59	5.09	0.13	64.81	Serpentinite
1H-2, 103–105	2.53	2.37	2.61	15.55	6.73	0.18	742.58	Serpentinite
1H-3, 81–83	3.81	2.45	2.59	9.14	3.82	0.10	280.15	Serpentinized harzburgite
1H-4, 6–8	4.56	2.65	2.68	1.68	0.65	0.02	13,092.09	Amphibolite-chlorite schist
1H-4, 57–59	5.07	2.62	2.69	4.02	1.57	0.04	8,290.70	Serpentinized harzburgite
1H-5, 18–20	6.18	3.16	3.23	3.20	1.04	0.03	29.71	Metabasalt
1H-5, 102–104	7.02	2.32	2.63	19.27	8.50	0.24	2,489.63	Metabasalt
2H-1, 18–20	7.88	2.36	2.65	17.79	7.71	0.22	1,328.18	Serpentine-chlorite schist
2H-2, 3–5	9.23	2.59	2.69	5.95	2.35	0.06	81.48	Serpentinized dunite
3H-1, 49–51	13.39	2.59	2.66	4.30	1.70	0.05	992.13	Serpentinite
3H-1, 100–102	13.90	2.14	2.60	28.95	13.83	0.41	35.53	Serpentinized harzburgite

Table T15. Index properties and volume magnetic susceptibility of matrix material samples, Holes 1200D, 1200E, and 1200F.

Core, section, interval (cm)	Depth (mbsf)	Density (g/cm³)		Porosity (%)	Water content (%)	Void ratio	Volume magnetic susceptibility (×10⁻⁵ SI)
		Bulk	Grain				
195-1200D-							
1H-1, 23–25	0.23	1.65	2.68	62.12	38.55	1.64	274.63
1H-1, 112–114	1.12	1.74	2.67	56.61	33.36	1.30	980.94
1H-1, 124–126	1.24	1.93	2.64	43.50	23.00	0.77	481.85
1H-2, 74–76	2.24	1.81	2.63	51.46	29.18	1.06	1387.37
1H-3, 73–75	3.73	1.87	2.65	48.01	26.31	0.92	1395.21
1H-4, 74–76	5.24	1.83	2.60	48.96	27.43	0.96	293.51
2H-1, 54–56	7.44	1.87	2.65	48.00	26.32	0.92	1761.30
2H-2, 33–35	8.73	1.94	2.62	42.36	22.31	0.74	942.88
2H-CC, 10–12	9.68	1.78	2.67	53.85	30.95	1.17	1617.25
3H-1, 62–64	10.52	1.80	2.60	50.72	28.81	1.03	1506.82
3H-2, 24–26	11.64	1.88	2.64	47.00	25.57	0.89	2137.01
4H-1, 12–14	12.52	1.57	2.64	66.22	43.22	1.96	1411.51
5H-CC, 8–10	14.18	1.74	2.61	54.76	32.24	1.21	1738.67
6H-1, 44–46	21.94	1.93	2.62	42.96	22.77	0.75	1292.05
6H-2, 25–27	23.12	2.00	2.63	39.15	20.02	0.64	1165.77
7H-1, 58–60	24.08	1.96	2.65	42.41	22.16	0.74	1852.10
8H-1, 81–83	25.81	1.94	2.63	42.83	22.56	0.75	1654.66
8H-2, 66–67	27.16	1.94	2.62	42.59	22.46	0.74	1439.93
9H-1, 50–52	28.50	1.94	2.61	42.42	22.39	0.74	1670.35
10H-1, 27–29	35.07	1.94	2.64	43.51	23.01	0.77	1413.78
195-1200E-							
1H-1, 19–21	0.19	1.76	2.81	58.49	33.95	1.41	310.34
1H-1, 104–106	1.04	1.71	2.66	58.07	34.77	1.39	1148.37
1H-2, 81–83	2.31	1.82	2.62	50.25	28.29	1.01	1049.92
1H-3, 74–76	3.74	1.77	2.60	52.41	30.26	1.10	1538.71
1H-4, 84–86	5.34	1.84	2.69	50.94	28.30	1.04	1423.10
2H-1, 91–93	7.01	1.89	2.69	48.25	26.17	0.93	1533.80
2H-2, 55–57	8.15	1.81	2.63	50.91	28.79	1.04	1353.92
2H-3, 68–70	9.78	1.91	2.73	47.97	25.71	0.92	2174.22
3H-1, 38–40	11.38	1.87	2.72	49.84	27.26	0.99	255.23
4H-1, 76–78	12.76	1.96	2.63	41.43	21.62	0.71	2170.31
4H-2, 81–83	14.31	1.95	2.68	44.06	23.15	0.79	584.01
4H-3, 68–70	15.68	1.86	2.67	49.21	27.11	0.97	574.63
4H-4, 60–62	17.10	1.85	2.59	47.07	26.00	0.89	1013.13
5H-1, 76–78	18.36	1.94	2.64	43.56	23.02	0.77	804.82
5H-2, 76–78	19.81	1.88	2.61	46.36	25.29	0.86	1107.09
5H-3, 38–40	20.49	1.86	2.57	45.98	25.30	0.85	1283.19
5H-3, 55–57	20.66	1.87	2.64	47.71	26.11	0.91	1349.19
6H-1, 61–63	21.81	1.88	2.60	45.88	25.06	0.85	894.72
6H-2, 65–67	23.29	1.93	2.64	43.73	23.19	0.78	1238.31
6H-3, 69–70	24.83	1.91	2.60	43.58	23.36	0.77	735.74
7H-1, 73–75	26.63	1.92	2.62	43.40	23.09	0.77	1178.36
7H-2, 74–76	28.14	1.94	2.62	42.88	22.66	0.75	1520.75
7H-3, 75–77	29.65	1.95	2.61	41.53	21.80	0.71	1381.40
7H-4, 75–77	31.15	1.93	2.62	43.22	22.93	0.76	1255.21
7H-5, 20–22	32.10	1.94	2.62	42.47	22.42	0.74	1183.18
7H-5, 34–36	32.24	1.78	2.63	52.70	30.30	1.11	907.70
8X-1, 21–23	32.71	1.82	2.66	51.41	28.92	1.06	1678.34
10H-1, 40–42	52.80	1.96	2.67	42.93	22.40	0.75	2044.89
10H-2, 92–94	54.82	1.94	2.65	43.76	23.13	0.78	1826.43
10H-3, 20–22	55.60	1.97	2.64	41.51	21.59	0.71	1916.76
195-1200F-							
1H-1, 71–73	0.71	1.75	2.69	56.43	33.02	1.30	1199.27
1H-2, 81–83	2.31	1.76	2.59	53.02	30.85	1.13	1507.73
1H-3, 69–71	3.69	1.85	2.62	48.42	26.85	0.94	1709.48
1H-4, 72–74	5.22	1.83	2.64	50.27	28.19	1.01	2055.76
1H-5, 70–72	6.70	1.84	2.62	48.87	27.19	0.96	1295.52
2H-1, 78–80	8.48	1.88	2.69	48.67	26.50	0.95	1468.20
2H-2, 75–77	9.95	1.95	2.65	43.47	22.89	0.77	2067.83
2H-3, 44–46	11.14	2.01	2.66	39.75	20.28	0.66	2540.98
2H-4, 43–45	12.13	1.89	2.63	46.37	25.17	0.86	1317.64
3H-1, 74–76	13.64	1.69	2.68	59.59	36.02	1.48	1724.53
3H-2, 74–76	15.14	1.88	2.64	47.34	25.84	0.90	1453.56

Table T16. Physical properties, Holes 1200D, 1200E, and 1200F. (See table note. Continued on next page.)

Core, section, interval (cm)	Depth (mbsf)	Formation factor	Thermal conductivity (W/[m·K])	Maximum shear strength (kPa)
195-1200D-				
1H-1, 12	0.12			8.32
1H-1, 60–64	0.62	3.14		
1H-1, 77	0.77			33.04
1H-1, 101	1.01			31.71
1H-1, 101–105	1.03	2.80		
1H-2, 17–21	1.69	3.47		
1H-2, 31	1.81			65.53
1H-2, 112–116	2.64	3.82		
1H-3, 43	3.43			67.75
1H-3, 52–56	3.54	3.58		
1H-3, 61–65	3.63	3.79		
1H-3, 75	3.75		1.54	
1H-4, 12–16	4.64	3.99		
1H-4, 48	4.98			60.65
1H-4, 78–82	5.30	5.85		
1H-4, 109–113	5.61	4.22		
1H-4, 115	5.65			58.55
2H-1, 10–14	7.02	3.18		
2H-1, 62	7.52			61.76
2H-1, 73–77	7.65	3.78		
2H-1, 124	8.14			50.90
2H-2, 14–18	8.56	4.00		
2H-2, 30	8.70			74.29
2H-2, 62–66	9.04	4.68		
2H-2, 75	9.15		1.04	
3H-1, 17	10.07			46.46
3H-1, 33	10.23			24.62
3H-1, 34–38	10.26	3.66		
3H-1, 114–118	11.06	4.05		
3H-2, 25	11.65		1.32	
3H-2, 35	11.75			44.47
3H-2, 36–40	11.78	3.17		
4H-1, 15–19	12.57	3.54		
6H-1, 35–39	21.87	3.25		
6H-1, 49	21.99			79.84
6H-1, 52	22.02		1.37	
7H-1, 23–27	23.75	3.79		
7H-1, 30	23.80			97.58
7H-1, 40	23.90		1.11	
7H-1, 62–66	24.14	4.26		
8H-1, 20	25.20			55.44
8H-1, 23–27	25.25	3.88		
8H-1, 94	25.94		1.34	
8H-2, 38–42	26.90	7.14		
8H-2, 48	26.98			84.50
9H-1, 36	28.36		1.35	
9H-1, 37–41	28.39	3.35		
9H-1, 59	28.59			87.05
10H-1, 31	35.13			88.71
10H-1, 34–38	35.16	3.39		
195-1200E-				
1H-1, 24–28	0.24	4.38		
1H-1, 25	0.25			22.84
1H-1, 109–113	1.11	2.68		
1H-1, 110	1.10			19.07
1H-2, 34–38	1.86	5.26		
1H-2, 77	2.27			39.70
1H-3, 51–56	3.54	3.34		
1H-3, 75	3.75		1.31	
1H-3, 80	3.80			42.14
1H-4, 15	4.65			50.45
1H-4, 76–80	5.28	3.32		
2H-1, 49–53	6.61	3.28		
2H-1, 70	6.80			57.99
2H-2, 33–37	7.95	3.96		
2H-2, 49	8.09			27.72
2H-3, 17–21	9.29	3.05		
2H-3, 75	9.85		1.31	
2H-3, 85	9.95			50.34
3H-1, 50	11.50		1.37	
3H-1, 62–66	11.64	3.28		
3H-1, 74	11.74			13.86
4H-1, 92	12.92			64.42
4H-1, 96–100	12.98	3.39		
4H-2, 87–91	14.39	5.23		
4H-2, 96	14.46			49.90
4H-3, 50	15.50		1.36	
4H-3, 73	15.73			52.01
4H-3, 79–83	15.81	3.21		
4H-4, 11–15	16.63	4.67		
4H-4, 24	16.74			43.58
5H-1, 24	17.84			31.05
5H-1, 29–33	17.91	3.42		
5H-2, 65	19.70			70.19
5H-2, 100–104	20.07	3.66		
5H-3, 13–17	20.26	3.69		
5H-3, 46	20.57			51.23
5H-3, 48	20.59		1.19	
6H-1, 36	21.56			62.10
6H-1, 85–89	22.07	4.53		
6H-2, 55–59	23.21	3.98		
6H-2, 79	23.43			76.40
6H-3, 9	24.23			57.88
6H-3, 11–15	24.27	4.54		
6H-3, 57	24.71		1.29	
7H-1, 60	26.50			45.46
7H-1, 106–110	26.98	2.99		
7H-2, 80	28.20			54.00
7H-2, 93–97	28.35	6.29		
7H-3, 23–27	29.15	3.91		
7H-3, 74	29.64		1.37	
7H-3, 83	29.73			76.62
7H-4, 86	31.26			64.65
7H-4, 111–115	31.53	5.01		
7H-5, 5–9	31.97	6.21		
7H-5, 12	32.02			85.72
8X-1, 27	32.77		1.26	
9X-CC, 9	40.99		1.33	
10H-1, 17	52.57			13.20
10H-1, 21–25	52.63	4.61		
10H-2, 41–45	54.33	6.32		
10H-2, 88	54.78			82.72
10H-3, 25	55.65			78.95
10H-3, 31–35	55.73	5.80		
10H-3, 65	56.05		1.46	
195-1200F-				
1H-1, 54–58	0.56	3.72		
1H-1, 64	0.64			23.06
1H-2, 93	2.43			46.57
1H-2, 100–104	2.52	3.03		
1H-3, 50–54	3.52	3.03		
1H-3, 60	3.62			38.03
1H-3, 76	3.76			81.50
1H-3, 80	3.80		1.23	
1H-4, 89	5.39			32.38
1H-4, 115–119	5.67	3.57		
1H-5, 51–55	6.53	3.16		
1H-5, 68	6.68			37.15
2H-1, 51–55	8.23	3.65		
2H-1, 83	8.53			52.23
2H-2, 47–51	9.69	3.39		
2H-2, 70	9.90			46.68
2H-3, 37–41	11.09	4.10		

Table T16 (continued).

Core, section, interval (cm)	Depth (mbsf)	Formation factor	Thermal conductivity (W/[m·K])	Maximum shear strength (kPa)
2H-3, 50	11.20		1.36	
2H-3, 50	11.20			63.54
2H-4, 27–31	11.99	3.02		
2H-4, 39	12.09			74.85
3H-1, 64	13.54			5.99
3H-1, 66–70	13.58	3.02		
3H-2, 70	15.10			68.86
3H-2, 75	15.15		1.40	
3H-2, 81–85	15.23	4.65		

Note: All measurements were made in matrix material.

Table T17. Hydraulic conductivity and specific storage values, Holes 1200D and 1200E.

Core, section, interval (cm)	Depth (mbsf)	Hydraulic conductivity ($\times 10^{-10}$ m/s)	Specific storage ($\times 10^{-5}$ m^{-1})	Sample alignment	Axial load (MPa)	Porosity (%)	Void ratio
195-1200D-							
1H-4, 120–130	5.75	0.56	38.00	Vertical	6.30	49.00	1.00
1H-4, 120–130	5.75	0.17	6.60	Vertical	62.80	49.00	1.00
195-1200E-							
1H-1, 120–130	1.25	2.40	58.00	Vertical	6.30	58.00	1.40
1H-1, 120–130	1.25	2.80	58.00	Horizontal	6.30	58.00	1.40
5H-3, 51–61	20.67	0.56	32.00	Vertical	6.30	48.00	0.90
5H-3, 51–61	20.67	0.58	33.00	Horizontal	6.30	48.00	0.90
7H-5, 30–40	32.25	0.11	6.00	Vertical	6.30	53.00	1.10
7H-5, 30–40	32.25	0.14	12.00	Horizontal	6.30	53.00	1.10

Table T18. In situ temperature, depth, thermal gradient, and heat flow values.

Hole	Temperature (°C)		Depth of measurement (m)	Temperature gradient (°C/m)	Heat flow (mW/m²)
	Mud line	Sediment			
195-					
1200A	1.68	2.09	41.00	0.0100	14
1200E	1.67	2.02	25.90	0.0135	19
1200E	1.67	2.19	56.40	0.0092	13
1200F	1.78	2.96	16.30	0.0724	101

Table T19. String configuration and installation comments.

Drill pipe depth (mbsf)	Description	Comments
0.3	Data logger bottom	
23.7	20-in casing shoe	K-55, buttress, 94 lb/ft, all joints tack welded
29.0	T10	Thermistor 10
58.0	Stinger bottom	5.5-in drill pipe, six joints; string weight = 8500 lb
64.0	T9	Thermistor 9
87.0	T8	Thermistor 8; looped cable between T9 and T8 so that only 23 m, instead of 35 m, remained between them; only had maximum outer diameter of 2.3 in through looped section; each end of loop tapered to prevent hangups; cable shortened by 24 m total to accommodate new well depth
107.4	16-in casing shoe	K-55, buttress, 75 lb/ft, last three joints tack welded
110.0	T7	Thermistor 7; looped cable between T8 and T7 so that only 23 m, instead of 35 m, remained between them; only had maximum outer diameter of 2.3 in through looped section; each end of loop tapered to prevent hangups; cable shortened by 24 m total to accommodate new well depth
115.0	T6	Thermistor 6
120.0	T5	Thermistor 5
125.0	T4	Thermistor 4
130.0	T3	Thermistor 3
132.0	T2	Thermistor 2; during installation of data logger tool string into drill pipe, the cable grip grabbed the thermistor cable, but not the spectra cable; this resulted in the thermistor cable sliding up 3 m with respect to the spectra cable; therefore, spacing between T2 and T3 is only 2 m, instead of the 5 m originally planned
137.0	Osmotic sampler 2 top	
142.0	Osmotic sampler 2 bottom	Intake at bottom and pushed inside drill holes after cutting off portion of tube containing air
142.5	Osmotic sampler 1 top	
147.5	Osmotic sampler 1 bottom	Intake extends 22 m into screened area, 3 m above top of sinker bar; had problems attaching extension to coupling at bottom of osmotic fluid sampler; glued fitting while assuring that tube remained free to flow; while extension tube was vertical and prior to attachment to osmotic sampler 1 (laying horizontally), retention cap fell off bottom of extension tube and fluid dripped continuously
149.0	Weak point	Pull test rated to 4,000 and 56,000 lb
149.0	End of 10.75-in casing	K-55, buttress, 40.5 lb/ft
149.0	Beginning of 10.75-in screen	K-55, buttress, 40.5 lb/ft, screen wrapped, 312 holes/ft, 0.5-in diameter, wrapped with triangular wire with 0.008-in gap over 0.125-in standoff rods
171.0	Osmotic sampler 1 intake	Located 3 m above top of sinker bar
174.0	Top of sinker bar	
176.0	Bottom of sinker bar	156 lb in air, 3-in outer diameter, 2-m long
202.3	End of 10.75-in screen	
208.0	10.75-in shoe	Unable to run casing past ~227 m, so removed three joints to place at current depth
257.0	Top of fill	
266.0	Total depth	

Table T20. Spectra rope specifications.

Diameter (in)	0.375
Work load (lb)	2880
Rope 1 length (m)	149
Rope 2 length (m)	25
Rope 1 attachments	Data logger Osmotic sampler 2 Osmotic sampler 1 Weak point
Rope 2 attachments	Weak point Weight
Rope 1 tied to	Thermistor cable
Rope 2 tied to	Osmotic sampler 1 intake

Note: See Figure F69, p. 133.

Table T21. Installation event times (25 March 2001).

Time (local)	Description
10:00:00	Start rig up
12:40:00	Finished placing data logger tool string in drill pipe and performed data logger final check
14:35:00	Top of data logger at 2933 m (drill pipe) and seated in CORK body; seafloor depth = 2943 m (drill pipe)
15:35:00	End of 1-hr calibration
15:37:00	Latched data logger in CORK
15:59:00	Wireline free from data logger; had to use jars to disconnect after not releasing with 7-klb overpull
19:07:00	CORK landed in casing
19:30:00	CORK latched and tested to 20-klb overpull
22:00:00	CORK landing platform in place
23:15:00	J-slot unlatched; CORK released

Notes: Local time = UTC + 10 hr. CORK = circulation obviation retrofit kit.